

**GEOMETRIC MODELING OF BIOLOGICAL AND ROBOTIC LOCOMOTION
IN HIGHLY DAMPED ENVIRONMENTS**

A Dissertation
Presented to
The Academic Faculty

By

Baxi Zhong

In Partial Fulfillment
of the Requirements for the Degree
Doctor of Philosophy in the
School of Physics
Quantitative Biosciences Graduate Program

Georgia Institute of Technology

December 2022

© Baxi Zhong 2022

**GEOMETRIC MODELING OF BIOLOGICAL AND ROBOTIC LOCOMOTION
IN HIGHLY DAMPED ENVIRONMENTS**

Thesis committee:

Dr. Daniel I. Goldman
School of Physics
Georgia Institute of Technology

Dr. Philip J Bergmann
Department of Biology
Clark University

Dr. Simon N. Sponberg
School of Physics
Georgia Institute of Technology

Dr. Gregory Blekherman
School of Mathematics
Georgia Institute of Technology

Dr. David L. Hu
School of Mechanical Engineering
Georgia Institute of Technology

Dr. Howie Choset
Robotics Institute
Carnegie Mellon University

Date approved: December 8 2022

ACKNOWLEDGMENTS

First, I would like to thank my advisor, Prof. Daniel Goldman. I had many thoughts, reasonable and unreasonable, throughout my PhD years. Prof. Goldman provided invaluable support in educating me to not only think creatively, but logically and carefully. Furthermore, I learned to distinguish between the technical improvement and scientific advancement from various projects. Moreover, I appreciate his support to present my work in different conferences on physics, biology, and robotics. Finally, at the core of the interdisciplinary subject, I learned from him to effectively talk to experts in different community.

I would like to thank the members of my thesis committee for their help in preparation of this work – Prof. Howie Choset, who inspired me to explore the world of locomotion, Prof. Simon Sponberg, with whom I learned the importance to have the biological context in locomotion studies, Prof. Greg Blekherman, who guided me to think mathematically, and Prof. David Hu, who always had golden advice. I would like to thank Prof. Philip Bergmann for the informative discussions on intermediate lizards and their evolutionary background.

Special thanks are due to colleagues from CRAB lab who made this work possible. I would like to thank Erin McCaskey, Eva Erickson, Deniz Kerimoglu, Madison Hales, Kelimar Diaz, Steven Tarr, Aradhya Rajanala, Christopher Pierce, and Andras Karsai for proofreading my papers, specifically adding/removing the articles in most of my writings. I would like to thank Dr. Shengkai Li for helping me with the physics principles behind the analysis. I would like to thank Tianyu Wang for making my theoretical analysis into reality, without whom my projects would have been the theoretical toy models. I would like to thank Juntao He for careful experiments with centipede robot. I would like to thank Kelimar Diaz for always being there for insights on biology, all the way from worms to centipedes. I would like to thank Eva Erickson for the careful tracking of lizards, centipedes, and worms. I would like to thank my postdoc mentor, Prof. Jennifer Rieser, from when I first

came to CRAB lab for her patient guidance. I would like to thank Prof. Chen Li and Prof. Feifei Qian for the useful discussion regarding linking our work to the context of literature. Finally, despite the recent unhappy discussion, I would like to thank Dr. Yasemin Ozkan-Aydin for her help on robot experiments.

I would like to thank my friends at Biorobotics lab from Carnegie Mellon University. I would like to thank Prof. Guillaume Sartoretti for proofreading many of my papers and offering advice on their level of acceptance in the robotics community. I would like to thank Julian Whitman for discussions and suggestions to connect our work to modular controls. I would like to thank Ruijie Fu and Yuelin Deng for performing robot experiments. I would like to thank Dr. Chaohui Gong for introducing the world of geometric mechanics. Finally, I would like to thank Prof. Howie Choset again for all the discussions and educations including academic and non-academic subjects.

I would like to thank my high school physics teacher, Jinsong Yang, for encouraging me to explore the beauty of physics, without whom I would not pursue my career in science. I would like to thank my college research advisor, Yuan Lin, from the University of Hong Kong, for involving me in academic research at early stage.

I would like to thank my friends for all the fun time we had throughout my PhD years. I would like to thank Guanlin Li and Shengkai Li for helping me getting to know the city well. I would like to thank Zhenyu Wang and Xulu Liu for all the drinks we had. I would like to thank Tianyu Wang and Minxi Han for all the double date with my wife and me. I would like to thank Juntao He, Tianyu Wang, Minxi Han, Shengkai Li, Zhaoyuan Gu, Bangyuan Liu for making Atlanta home during all the family-gathering festivals. I would like to thank Xianhan Zhang and Xianla Li for your support and encouragement. I would like to thank Xinming Ye for cheering me up when I am down. I would like to thank Uhall boys: Liwei Hou, Yucheng Hu, Han Bao, Yang Zuo, Wenqing Chen, Changxin Yan, Zeyu Wan for your emotional supports in my hard times.

Finally, I would like to thank my wife, Xiaoxiao Sun for all the support along the way. It

is always love that brings me forward! I would like to thank my parents, Yinbao Chong and Zhili Liu, my uncle Zhiyong Liu, my grandmother, Genyuan Chen for the strong supports so that I can engage to science.

SUMMARY

Biological systems can use seemingly simple rhythmic body and limb undulations to traverse their complex natural terrains. We are particularly interested in the regime of locomotion in highly damped environments, which we refer to as geometric locomotion. In geometric locomotion, the net translation is generated from properly coordinated self-deformation to counter the drag forces, as opposed to inertia-dominated systems where inertial forces dominate over frictional forces (thus coasting/gliding is possible). The scope of geometric locomotion include locomotors with diverse morphologies across scales in various environments. For example, at the macroscopic scale, legged animals such as fire salamanders (*S. salamandra*), display high maneuverability by properly coordinating their body bending and leg movements. At the microscopic scale, nematode worms, such as *C. elegans*, can manipulate body undulation patterns to facilitate effective locomotion in diverse environments. These movements often require proper coordination of animal bodies and/or limbs; more importantly, such coordination patterns are environment dependent. In robotic locomotion, however, the state-of-the-art gait design and feedback control algorithms are computationally costly and typically not transferable across platforms and scenarios (body-morphologies and environments), thus limiting the versatility and performance capabilities of engineering systems. While it is challenging to directly replicate the success in biological systems to robotic systems, the study of biological locomotors can establish simple locomotion models and principles to guide robotics control processes. The overarching goal of this thesis is to (1) connect the observations in biological systems to the optimization problems in robotics applications, and (2) use robotics as tools to analyze locomotion behaviors in various biological systems. In the last 30 years, a framework called “geometric mechanics” has been developed as a general scheme to link locomotor performance to the patterns of “self-deformation”. This geometric approach replaces laborious calculation with illustrative diagrams. Historically, this geometric approach was

limited to low degree-of-freedom systems while assuming an idealized contact model with the environment. This thesis develops and advances the geometric mechanics framework to overcome both of these limitations; and thereby generates insight into understanding a variety of animal behaviors as well as controlling robots, from short-limb elongate quadrupeds to body-undulatory multi-legged centipedes in highly-damped environments.

TABLE OF CONTENTS

Acknowledgments	iii
Summary	vi
List of Tables	xiii
List of Figures	xiv
Chapter 1: Introduction	1
1.1 Overview	1
1.1.1 Conventional legged locomotion	2
1.1.2 Unconventional legged systems	5
1.1.3 Geometric mechanics	8
1.2 Generalizing geometric mechanics to diverse locomotion systems	10
Chapter 2: Geometric mechanics and its application in limbless locomotion . . .	18
2.1 Introduction to geometric mechanics	19
2.1.1 Three link swimmer in viscous environment	19
2.1.2 Shape space	19
2.1.3 Spatial velocity and body velocity	20
2.1.4 Force and torque balance	22

2.1.5	Linearity	23
2.1.6	Gait in the shape space	24
2.1.7	Minimal Perturbation Coordinate	25
2.2	Three link swimmer in granular media	29
2.2.1	Ground reaction force in granular media	29
2.2.2	Linearity	30
2.2.3	Predictions from height functions	32
2.3	N-link swimmer in granular media	33
2.3.1	Two modes in biological locomotors	33
2.3.2	Limbless robot in granular media	39
2.3.3	Summary	42
2.4	N-link sidewinding swimmer: contact function	43
2.4.1	Straight sidewinding	43
2.4.2	Differential Turn	47
2.5	Modulating contact function using geometric mechanics	50
2.5.1	Geometric mechanics with toroidal and cylindrical shape spaces	50
2.5.2	Modulating the contact function	55
2.5.3	General Sidewinding Gait Formula	66
2.6	Obtaining contact functions using geometric mechanics	70
2.6.1	Effect of drag anisotropy on translational locomotion	70
2.6.2	Contact scheduling	72
2.6.3	Optimal Contact Scheduling	76
2.6.4	Applications to more than 3 contact states	80

2.6.5	Application: modulating sidewinding angle of motion	81
2.6.6	Sidewinding of a 6-link Robot	84
2.7	Design gaits for obstacle aided locomotion	86
2.7.1	Modeling Interaction with Obstacles	87
2.7.2	Direction of \dot{y}_1^b	88
2.7.3	Gait Design	89
2.7.4	Numerical Optimization	91
2.7.5	Gait Identification	92
2.7.6	Single Post Experiments	93
2.7.7	Multiple Post Experiments	95
2.7.8	Unevenly Distributed Posts Experiments	96
2.8	Appendix	97
2.8.1	Numerical solution: minimal perturbation coordinate	97

Chapter 3: Coordination of Lateral Body Bending and Leg Movements for Sprawled Posture Quadrupedal Locomotion 101

3.1	Related work on turning	103
3.2	Geometric mechanics	103
3.2.1	Periodic Ground Contacts	103
3.2.2	Cylindrical shape space	106
3.2.3	Granular Resistive Force Theory	107
3.2.4	Gait Design	109
3.2.5	Forward Height Functions	110
3.2.6	Rotational Height Functions	113

3.2.7	Lateral Height Function	117
3.3	Experimental Results	118
3.3.1	Robot Experiment Verification of Forward Height Function Prediction	119
3.3.2	Robot Experiment Verification of Rotational Motions	120
3.3.3	Robot Experiment Verification of Lateral Height Function Prediction	121
3.3.4	Animal Experiment Verification of Forward Height Function Prediction	121
Chapter 4: Coordinating tiny limbs and long bodies: Geometric mechanics of lizard terrestrial swimming		123
4.1	Results	127
4.1.1	Diversity in lizard body movements	127
4.1.2	Wave dynamics are key to body-limb coordination	130
4.1.3	Body weight distribution	136
4.1.4	Terrestrial swimming	137
4.1.5	Robophysical experiments	138
4.2	Discussion and Conclusion	141
Chapter 5: A general locomotion control framework for multi-legged locomotors		143
5.1	Hildebrand Gait Prescription	148
5.1.1	Related work	148
5.1.2	Prescription of Contact Patterns for Arbitrary Robots	149
5.1.3	Prescription of Leg Shoulder Movement	150
5.1.4	Numerical Prediction on Speed and Stability	151
5.1.5	Testing speed and stability predictions in experiments	155

5.2	Body-leg Coordination in Hildebrand Gait Formulation	158
5.2.1	Geometric Mechanics to Coordinate Lateral Body Undulation . . .	158
5.2.2	Numerical Prediction of Speed and Stability	164
5.2.3	Testing predictions for body-leg coordination in experiments	164
5.3	Body-leg Coordination in Biological Locomotors	165
5.4	Discussion and Conclusion	166
5.4.1	Principles of gait modulation	166
5.4.2	Insights from robotics to biological systems	167
5.5	Appendix	168
5.5.1	Numerical Derivation of Local Connection Matrix	168
 Chapter 6: Self propulsion via slipping: frictional resistive force theory for multi-legged locomotors		174
 Chapter 7: A Shannon-inspired framework for multi-legged matter transport		194
 Chapter 8: Conclusion		221
8.1	Summary	221
8.2	Future work	224
8.2.1	Connection morphology to locomotion	224
8.2.2	Coding in matter transportation	225
 References		228

LIST OF TABLES

2.1	Summary of previous work on sidewinder locomotion.	58
-----	--	----

LIST OF FIGURES

1.1	Aerial, aquatic, and terrestrial locomotion (a) Aquatic locomotion of fish swimming [8]. (b) Aerial locomotion of bird flight [9]. In both cases, the reaction force from the interaction between locomotor and environment is continuous temporally and spatially. (c) Terrestrial locomotion of human [10], where appendages (legs) periodically make and break contact with substrate.	2
1.2	Footfall pattern planning on rigid flat terrain Front view of OSU hexapod vehicle and the footfall pattern planning algorithm. Figures are adapted from [18].	3
1.3	Machine learning in legged locomotion (Left) Early work using reinforcement learning to optimize quadruped gait [18]. (Right) Recent work of legged locomotion using deep reinforcement learning [30].	4
1.4	Central pattern generator (CPG) for locomotion (Left) Early work of CPG to study body-limb coordination by oscillation coupling of a salamander robot [35]. (Right) Recent work of CPG to study inter-limb coordination [39].	6
1.5	Template-anchor for locomotion (a) A template (spring-loaded inverted pendulum) for legged locomotion [15]. (b) Application of template-anchor approach to study robot legged locomotion [58]. (c) Application of template-anchor approach to study human locomotion [59]	7
1.6	Resistive Force Theory (RFT) for locomotion (a) Early work in mid 20th century to study self-propulsion in limbless locomotors[61]. (b) Recent work using RFT to study locomotion on granular media [74]. (c) Recent work combining RFT and geometric mechanics [75]	9

1.7	Robotic and biological systems studied in this thesis (a) Body-leg coordination in quadrupedal systems. Two robots were studied: a quadrupedal robot with a single DoF body bending joint and an elongate quadrupedal robot with two DoF body bending joint. We studied five quadrupedal animals: (from top to bottom) <i>Salamandra salamandra</i> , <i>Uma scoparia</i> , <i>Brachymeles kadwa</i> , <i>Brachymeles taylori</i> , and <i>Brachymeles muntingkamay</i> . (b) Body-leg coordination in hexapodal systems. We studied the body-leg coordination of hexapod robot. (c) Body-leg coordination in centipede systems. We studied a centipede robot with 8 pairs of legs and the biological centipede (<i>Scolopendra polymorpha</i>). (d) The undulatory motion in limbless locomotors. We studied limbless locomotors in macroscopic scale (<i>Crotalus cerastes</i>) and in microscopic scale (<i>Caenorhabditis elegans</i>) and use robots to test our analysis. Scale bars are 5 cm unless otherwise labelled.	12
2.1	Geometry of 3-link swimmer (a) The position and orientation of each link. (b) The position of the first link and the joint angles. (c) Spatial velocity, body velocities, and the viscous friction. (d) Body reference frame.	20
2.2	Visualization of $h_\alpha(\dot{\alpha})$: Relationship between body velocities (\dot{x}_1 (left), \dot{y}_1 (mid), and $\dot{\theta}_1$ (right)) and shape velocities ($\dot{\alpha}_1$ and $\dot{\alpha}_2$).	23
2.3	Shape space, vector field, and height function (a) The shape space of 3-link swimmer and an example gait. (b) The vector field and height functions in forward (left), lateral (mid), and rotational directions.	24
2.4	The importance of choices in body reference frame (Left) Forward height function computed with (a) first link and (b) center of mass as body reference frame. (Mid) The comparison between surface integral and numerical computation of circular gaits under different amplitudes. (Right) The illustration of rotational oscillation of body reference frame during the course of a gait period.	26
2.5	Hodge-Helmholtz decomposition of rotational vector field (Left) The original rotational vector field with first link as the body reference frame. (Mid) The curl-free component of the original rotational vector field. (Right) The divergence-free component of the original rotational vector field.	27
2.6	3-link swimmers in granular media (adapted from [75]) (a) (left) The robot resting on a granular medium, a bed of plastic spheres. (Mid) Analytical three-link model. The reaction force from the granular media (F_\perp and F_\parallel) and the attack angle (γ) are labelled. (b) The visualization of $h_\alpha(\dot{\alpha})$ In Equation 2.15. The body velocities are almost linear functions of the shape velocity.	29

2.7	Geometric mechanics analysis for three-link swimmer on granular media (adapted from [75])	(a) Height functions for the three-link swimmer in granular media. The units of the field values are $100\times(\text{body-lengths})$ for forward and lateral height functions; $100\times(\text{radian})$ for rotational height functions. (b) Predictions from geometric mechanics. (Left) Height function estimate of displacement compared to experimental and DEM results as a function of r . Dashed horizontal lines indicate displacements for the butterfly gait in DEM and resistive force theory. (Mid) Illustration of the butterfly gait and the figure-eight gait. (Right) Height function estimate of net rotation for figure-eight gait of different stroke amplitudes. Temporal frequency was 0.5 Hz in (left) and 0.17 Hz in (right)	31
2.8	Low dimensional representation of animal movement through sand.	(Left) Photos of (A) the nematode worm (<i>Caenorhabditis elegans</i>) in S-basal buffer (B) the sandfish lizard (<i>Scincus scincus</i>) 7.6 cm below the surface of and fully immersed in $300\text{-}\mu\text{m}$ glass beads, and (C) <i>Chionactis occipitalis</i> moving on the surface of $300\text{-}\mu\text{m}$ glass beads. (Mid) Solid lines show the two dominant relative curvature ($\kappa\lambda_s$) PCA modes account for (A) 96.7%, (B) 94.7%, and (C) 79.7% of the variation in observed body configurations. Dashed lines show best fits to sin and cos functions (see text). (Right) 2D probability density map of projections of curvatures onto the two PCA modes with the largest eigenvalues. This figure is adapted from [83].	34
2.9	Geometric mechanics of undulatory locomotors.	Columns show the dimensionality reduction for (A) the nematode (B) the sandfish, and (C) the shovelnose snake on the surface of sand. (Top) Dominant two modes of body curvatures determined from PCA. (Bottom) Space of shapes spanned by the two modes. The directed circle on each plot represents a particular gait. This figure is adapted from [83].	35
2.10	Visualization of the connection plane $H_w(\dot{w})$	The body velocities are almost linear functions of the shape velocity, which allows us to approximate Equation 2.18 by Equation 2.19	36

2.11	Geometric mechanics of lateral undulation. (Top) Height functions (contours; here, color scale multiplied by 100) and average animal gait (blue circles); and (bottom) Animal performance (average \pm standard deviation, represented by the blue crosses), geometric mechanics (solid black curve), and RFT (dashed red curve) predictions for (Left) <i>C. elegans</i> in S-basal buffer, (mid) <i>S. scincus</i> in 300- μ m glass beads, and (right) <i>Ch. occipitalis</i> on the surface of 300- μ m glass beads. Crosses in A-(ii) show average animal gaits from different data sets. In [72], curvatures were measured manually once per cycle (dark blue cross); in [122], curvatures were measured throughout time [128] (light blue cross). The light blue cross in B-(ii) represents the postural dynamics as defined by projections onto the two dominant PCs, and the dark blue cross shows postural dynamics measured directly from kinematic data. This figure is adapted from [83].	38
2.12	N-link swimmer (a) A 16-link robot. (b) The waveforms of a <i>N</i> -link swimmer in the shape space are visualized. (c) Snake robot executing a gait. Time interval between each snapshot is five seconds. Figures are adapted from [82, 131].	39
2.13	Geometric mechanics of a N-link swimmer and numerical simulation (a) The height function for a 16-link robot in (a.1) the forward, (a.2) the lateral, and (1.3) the rotational directions. (b) The comparison between the surface integral and RFT simulation for (b.1) circular gaits and (b.2) elliptical gaits with different amplitudes, and (b.3) turning gaits with different offset from origin.	40
2.14	Sidewinder rattlesnake substrate contact. (A) (left) A sidewinding snake <i>Cr. cerastes</i> . Black bar denotes 1 cm. (right) Schematic illustrating sidewinding locomotion. If the animal does not slip, displacements, $\Delta = \lambda_s \cos \phi$, can be predicted from geometry. (B) Time-resolved kinematics are obtained from high-speed cameras. (C) Two relative curvature modes (determined from PCA) account for 42.4% and 37.3% of variance observed in in-plane body configurations of 4 animals throughout 18 trials. (D) 2D probability density map of animal data projected onto two dominant curvature principal components. (E) Depiction of coupling between in-plane and vertical waves (adapted from [16]). (F) Shape space showing body configuration-dependent animal-environment contact model for an animal with 1.5 waves along its body.	45

2.15	Geometric mechanics of sidewinding. (A) Connection vector fields and (B) x - and y - height functions (shown here as contour plots with color scales multiplied by 100) for movement on sand with $n = 1.5$ waves along the body. The blue circle shows average animal performance of <i>Cr. cerastes</i> on sand. (C) Comparisons of RFT simulations (dashed tan curve) and geometric mechanics calculations (solid tan curve) for movement on sand. Biological data: <i>Cr. cerastes</i> on a 7.6-cm layer of sand (blue); <i>N. fasciata</i> on a 5-cm layer of sand (dark purple). <i>Cr. cerastes</i> on an oak board roughened by a layer of adhered glass beads (dark magenta); <i>Cr. cerastes</i> on a smooth oak board (light magenta); <i>Cr. cerastes</i> on a 1.5-cm layer of sand (light purple) [132].	46
2.16	PCA analysis of differential turn Snapshots of <i>Cr. cerastes</i> body configurations performing (A.1) gradual (A.2) sharp differential. (B) One cycle of tracked midline of differential turn colored by time. Rotation (Rot) and displacement are labelled. (B) Two relative curvature modes (determined from PCA) account for 44.7% and 24.5% of variance observed in in-plane body configurations of 4 animals throughout 47 trials. (C) A typical projection of body curvature onto two dominant curvature principal components colored by time.	47
2.17	Geometric mechanics analysis of differential turn (A) x , y , and θ - height functions (shown here as contour plots. Color scales in x , y - height functions are multiplied by 100) for movement with $n = 1.2$ waves along the body. The blue circle typical CW and CCW differential turn in <i>Cr. cerastes</i> (B) The comparison between direct RFT, GM (surface integral in height functions), and animal data (light blue dots) with its linear fit ($p < 0.001$).	49
2.18	Cylindrical shape space (left) Height function on cylindrical shape space. (mid) Height function on the Euclidean parameterization space of the cylindrical shape space. We illustrate two gaits with solid and dashed blue curves. Note that the solid blue gait enclosed three disjoint areas with the assistive lines. The area above the assistive line (solid shadow) and the area below the assistive (dashed shadow) line have different handedness. (right) The illustration of height function on Euclidean shape space of the same system. Note that middle and right panel are identical subject to different parameterization.	51
2.19	Toroidal shape space (left) Height function on toroidal shape space. (mid) Height function on the Euclidean parameterization space of the cylindrical shape space. We illustrated a gait with solid purple curves. Note that the solid purple gait enclosed two disjoint areas with the assistive lines. The area above the assistive line (dashed shadow) and the area below the assistive line (solid shadow) have different handedness	52

2.20	Theoretical Model and Experimental Robot. (a) The theoretical model for the sidewinder robots. The filled black ovals indicate the ground contact phase while the white ovals indicate a no ground contact phase. The contact state is labelled in black ($c(i)$). The joint angle in blue indicates pitch joints and the joint angle in red indicates yaw joints. (b) The serial elastic actuated robot used to test the effectiveness of our stabilization approach.	56
2.21	Examples of Statically Stable and Unstable Configurations. (a) (<i>left</i>) The contact state pattern and an example of a statically stable configuration for gaits with high spatial frequency in both the horizontal wave and the vertical wave. (<i>mid</i>) The contact state pattern and an example of a statically unstable configuration for gaits with low spatial frequency in both the horizontal wave and the vertical wave. (<i>right</i>) Stabilizing the statically unstable configuration by increasing the vertical spatial frequency. The label and the axis are identical. (b) Example of an unstable configuration (<i>left</i>) and an unexpected touchdown (<i>right</i>)	59
2.22	Effect of spatial frequency on static stability in sidewinding. (<i>Left</i>) The figure on top panel shows the relationship between the spatial frequency ($K_v = K_l = K$) and the static stability. Robot experiments showed that significant turning (<i>Left, bottom</i>) was observed in gaits with low static stability (<i>Left, top</i>) and the turning vanished at gaits with high static stability. (<i>right</i>) We directly plotted the relationship between the body rotation and static stability. The curve appeared to be a piece-wise linear function. In the range where the static stability is less than 0.5, the body rotation grows almost linearly with the loss of static stability ($R = 0.99$). Whereas in the range where the static stability is higher than 0.5, the body rotation is almost negligible.	60
2.23	Discrepancy between robot experiments and simulation at low spatial frequency. (<i>left</i>) the trajectories of body motion in 6 gait cycles. The colors represent gait periods. Initial positions of the robot indicated by the black circles. (<i>right</i>) comparisons of time evolution of displacement of the simulation and robot experiments. We compared the low spatial frequency gait (a) and high spatial frequency gait (b). The simulation-experiment discrepancy occurs in low spatial frequency gaits. The unit and the axis labels in all panels are the same.	61
2.24	Temporal frequency dependency of unstable gaits. Dependence of the rotation angle (per cycle) on the temporal frequency of (a) statically unstable translational sidewinding gaits and (b) statically unstable rotational sidewinding gaits on robot experiments. The subplots (i) and (ii) show the snapshots of robot implementing gaits in low temporal frequency (0.2Hz, red) and high temporal frequency (2.0Hz, blue) over three gait cycles. . . .	62

2.25	Height functions to design gaits to produce motion in the desired direction. Height functions on torus (<i>left</i>) and on unfolded Euclidean parameterization space (<i>right</i>) are shown. The height function for (a) horizontal spatial frequency $K_l = 1.5$, V-L ratio $K_v/K_l = 1.3$ in lateral direction (the direction perpendicular to body axis) and (b) horizontal spatial frequency $K_l = 0.9$, V-L ratio $K_v/K_l = 1.2$ in rotational direction. The purple curve in each plot maximizes the surface integral enclosed in the upper left corner (marked in solid lines) minus the surface integral enclosed in the lower left corner (marked in the dashed lines). The assistive lines are shown as lines with green arrows.	64
2.26	Robustness of statically stable gaits as a function of temporal frequency. Dependence of the rotation angle (per cycle) on the temporal frequency of (a) the stabilized translational sidwinding gaits and (b) the stabilized rotational sidwinding gaits on robot experiments. In both cases, the rotation angle is steady over a range of temporal frequencies. The unit and the axis labels in all panels are the same. The subplots (i) and (ii) show the snapshots of robot implementing gaits in low temporal frequency (0.2Hz, red) and high temporal frequency (2.0Hz, blue) over three gait cycles.	66
2.27	Extended sidwinding gait formula. (a) Height functions for different V-L ratio with fixed $K_l = 1.0$. We show that while we change the V-L ratio, the optimal phase ϕ_0 emerged to increase linearly from height function predictions. We then ran regression and find that $\phi_0/2\pi$ linearly correlates with V-L ratio K_v/K_l , under slopes $a = -0.44$ and intercept $b = 1.2$. (b) We then test how the slopes and intercept correlates with the horizontal spatial frequency K_l . It turns out that both the slope a and the intercept b linearly correlate with K_l ($a \sim -0.439K_l + 0.001, b \sim 0.439K_l + 0.750$). (c) A model to explain the empirical equations. We develop our model in CoM frame, neglecting the forward displacement (along the direction) of body segments, and only investigate the effect of lateral displacement.	67
2.28	Vector fields and height functions for an 8-link robot on granular media and frictional ground with continuous contact. (a) A schematic sketch, vector field, and height function for an 8-link robot moving on granular media (poppy seeds). The height function has a large magnitude. (b) The sketch, vector field, and height function for a 8-link robot moving on frictional ground. The axes of all shape space are identical. The color bar of height functions in (a) and (b) are identical. The units of the color bar in the height functions are BL/π^2	71

2.29	Example of a mixed contact pattern. (a-c) The vector fields and height functions for three contact states I_1 , I_2 , and I_3 . Corresponding robot links which are in contact with the environment are denoted by red, black and grey. The color bar of height functions in (a), (b), and (c) are identical. (d.1) The contact pattern prescribed by (Equation 2.43). (d.2) The vector field prescribed by (Equation 2.44). (d.3) The corresponding height function. The axes of all shape space are identical. The units of the color bar in all height functions are BL/π^2	73
2.29	Example of a mixed contact pattern (continued) (d.3) The corresponding height function. The axes of all shape space are identical. The units of the color bar in all height functions are BL/π^2	74
2.30	Illustration of a contact pattern optimization. (a) The vector field and its curl-free component and divergence-free component by the Hodge Helmholtz decomposition.	74
2.30	Illustration of a contact pattern optimization (continued). (b) The potential functions for P_1 , P_2 and P_3 . Note that, in curl-free components, the line integral is path independent, allowing us to compute the potential function to estimate the line integral between any points. (c) The potential function difference for $P_\gamma = P_2 - P_1$, $P_\alpha = P_3 - P_2$, and $P_\beta = P_1 - P_3$. The axes of all shape spaces are identical. The units of the color bar in all potential function differences are BL/π^2	75
2.31	Experiments on angle of motion modulation. (a.1) Snapshots of robot implementing sidewinding gaits with different amplitudes using sinusoidal templates ((Equation 2.33,Equation 2.33)). The solid yellow arrow indicates the direction of motion l_t and the dashed blue line, l_c indicate the central body axis. The angle between l_c and l_t is then defined as the angle of motion. (a.2) For the sidewinding gaits using sinusoidal templates, the angle of motion is almost independent of the amplitude for robot moving in isotropic environments. The blue solid line represents simulation and the black line with error bars is robophysical experimental data. (b.1) Comparison of snapshots of the robot experiment and the simulation implementing the gait to modulate the angle of motion. (b.2) Modulation of the motion angle by controlling the convex coefficient ϵ	78

2.32	Modulating the angle of motion using contact pattern optimization. The potential function difference (PFD) in forward (a), lateral (b) and rotational (c) directions. The black circle indicate our joint angle limit: $\ [r_1, r_2] \ _2 \leq \pi/3$. The set of extreme points ($Q^x = \{q_\gamma^x, q_\alpha^x, q_\beta^x, \}$) are chosen to maximize the sum of PFD in forward directions. The set of extreme points ($Q^y = \{q_\gamma^y, q_\alpha^y, q_\beta^y, \}$) are chosen to maximize the sum of PFD in lateral directions. The axes of all shape spaces are identical. The color bar of PFD in (a) are identical. The units of the color bar in all PFDs are BL/π^2	80
2.32	Modulating the angle of motion using contact pattern optimization (continued). The potential function difference (PFD) in forward rotational directions. The units of the color bar in all PFDs are BL/π^2	81
2.33	Sidewinding with fewer number of links. (a) Snapshots of a 6-link robot implementing the sidewinding gait with the sinusoidal templates ((Equation 2.33), (Equation 2.33)). (b) Snapshots of a 6-link robot implementing the sidewinding gait with our optimization method. (c) The sidewinding speed (in unit BL per cycle) as a function of link numbers (sidewinding gait is prescribed using the sine wave template). The blue solid line represents simulation and the black line with error bars is robophysical experimental data. The speed decreases as the link number decreases until $N = 10$. For $N < 10$, the configuration is unstable and turning emerged. The speed of the gait with our optimization method is highlighted as a diamond marker.	82
2.34	Designing sidewinding gaits for a 6-link robot. (a) Three stable contact patterns and their corresponding vector fields.	83
2.34	Designing sidewinding gaits for a 6-link robot (continued). (b) The PFD of lateral and rotational directions. The color bars of PFD are identical in three illustrations. The black circle indicates the robot's joint angle limit: $\ [r_1, r_2] \ _2 \leq \pi/3$	84
2.34	Designing sidewinding gaits for a 6-link robot (continued). (c) The boundary of each contact state, the vector field, and the height function with the optimal contact pattern, determined from the obtained transitional points. The units of color bar in height function are BL/π^2	85
2.35	Modeling interactions between robot and obstacles (a) (Left) The vector field V_1 assuming the obstacle has interactions with the head link ($i_o = 1$). (Right) Force relationship illustrations for interactions between robot and obstacle. (b) (Left) The vector field V_2 assuming the obstacle has interactions with the head link ($i_o = 1$). (Right) The two conditions (Sec.subsubsection 2.7.1 and Sec.subsubsection 2.7.1)	87

2.36	Identification of gaits (a) Numerically computed effective gait paths for $i_0 = \{1, 2, 3\}$. In (left) and (mid) panels, we showed the effective gait paths with weight higher than 0.1 body length. In (right) panel, we showed the gait path with the highest weight (0.06 body length). (b) Comparison between circular-wave (ϕ_c), elliptical-wave (ϕ_e), and standing-wave (ϕ_s) gaits.	89
2.37	Single post experiments (a) The half-cycle displacements for different gaits are measured. We illustrated configurations before and after interaction with the obstacle. The net forward displacement d (net displacement along the direction of motion) is labelled with a dashed arrow. The net displacement (forward and lateral) is labeled with a solid arrow. BL denotes body length. The purple arrows indicate the direction of motion over the half gait cycle. (b) The ranges of beneficial obstacles are measured. We illustrated the starting and ending configuration where the interaction with the obstacle is beneficial. γ is measured to quantify the ranges of beneficial obstacles.	90
2.38	Multiple posts experiments We illustrated snapshots of robots implementing (a) circular, (b) elliptical, and (c) standing wave gaits on wide-distributed posts (0.3 BL) and narrow-distributed posts (0.2 BL). Elliptical-wave gait outperformed standing-wave and circular-wave gaits in both posts. Purple arrows indicate the direction of motion over two gait cycles. On the right panel, we illustrated the definition of attack angle ψ and contact duration τ .	93
2.39	Experiment data for multiple post experiments (Left panel) The speeds of standing-wave ($\sigma = 0.1$), elliptical-wave ($\sigma = 0.5$), and circular-wave ($\sigma = 1$) gaits are compared in (a) wide-distributed posts and (b) narrow-distributed posts. (Right panel) The attack angle and contact duration for all cases are measured and compared. ** denotes $p < 0.01$	94
2.40	Unevenly distributed post experiments A sequence of video frames of the robot executing the elliptical-wave gait in an unevenly arranged planar peg board over two gait cycles.	95
3.1	The animal, robot and theoretical models studied in the chapter. (a) top view of a Fire salamander. The body angle, α_b , is defined as an angle between the center lines that are parallel to the front and the back part of the body. (b) top view of the robo-physical model. It has two body parts connected with a servo, four 2 DoF legs, and a tail. The metal part at the center is used to pick up the robot with an electromagnetic gripper. All legs and tail have the same foot geometry (24X24 mm cube shape). (c) the theoretical model with shape variables and body velocities labeled.	102

3.2	<p>The connection vector field and the height functions in the cylindrical shape space. The connection vector field (top) and the height function (bottom) in a cylindrical shape space corresponding to the forward motion of a quadruped robot moving with a four-beat walking gait on the surface of ~ 1 mm poppy seeds. We show the vector field and height function on a cylindrical space and on the Euclidean parameterization of a cylindrical space. The blue curve represents a sample gait in the corresponding cylindrical shape space. Orange lines represent the assistive lines to form closed loops with the gait path in the unfolded cylindrical shape space. The area in the blue shading represents the area where the gait path and the assistive line form a clockwise loop; the area in the green shading represents the area where the gait path and the assistive line form a counterclockwise loop. Red, white, and black colors indicate positive, zero and negative values in the height function respectively.</p>	104
3.3	<p>The leg contact variables c_i and joint angles β_i prescribed by gait phase τ for (a.1) (forward) slow walk, (a.2) (forward) fast walk, (a.3) (forward) trot (b.1) (rotational) lateral sequence with no modulation (LS NM), (b.2) (rotational) lateral sequence with differential drive modulation (LS DDM), (b.3) (rotational) rotary sequence with no modulation (RS NM), (b.4) (rotational) rotary sequence with differential drive modulation (RS DDM), and (c) (lateral) sideways leg movements. The “cartoon sequence” shows the leg joint angles and contact states (solid means contact; open in air) at different gait phases. A row of eight boxes indicates the contact state of a leg at eight different phases of the gait, where filled gray color represents contact and open white color represents non contact state. The blue curves indicate the joint angles of the leg “shoulders” (shoulder for fore-legs and hip for hind legs). The initials F, H, L, R represent front, hind, left and right leg, respectively. All the panels have the same ordinate range (from $-\frac{\pi}{3}$ to $\frac{\pi}{3}$) as in (a.1). The dashed lines in (a.2) and (a.3) indicate two legs are simultaneously in the air, which could only occur for diagonal leg pairs.</p>	106
3.4	<p>The flow chart of our gait design process</p>	110

3.5 **Height functions** (a) Forward height functions associated with trot (a.1), fast walk (a.2) and slow walk (a.3) leg movements. The units of the colorbars are cm per step, i.e., $cm/4\pi^2$. (b) Rotational height functions associated with lateral sequence no modulation (**LS NM**) (b.1), lateral sequence differential drive modulation (**LS DDM**) (b.2), rotary sequence no modulation (**RS NM**) (b.3) and rotary sequence differential drive modulation (**RS DDM**) (b.4) leg movements. The units of the colorbars are rad per step, i.e., $rad/4\pi^2$. (c) Lateral height function associated with sideways leg movements. The blue curves are the identified “optimal” gait paths. Red, white and black indicate positive, zero and negative values respectively. The ordinate range is the same for all panels. The units of the colorbars are cm per step, i.e., $cm/4\pi^2$ 111

3.6 Snapshots of robot experiment (b and d), RFT simulation (a and c) and animal experiments (e). Body bending coordinated with leg movements (a-b) changes the orientation of the body or increases forward displacement. In (a) and (c), the green dots identify the head and the solid blue line represents the trajectory of center of mass. In (b) and (d), the module connected to hanging tail (not making contact with the ground) indicates the hind body module. We compared our designed forward gaits (c and d) with the forward locomotion observed in animal experiments (e) 112

3.7 Sample trajectories of robot experiments and RFT simulations implementing (a) fast walk gait, (b) rotary sequence no modulation gait, and (c) sideways gait, showing close agreement between RFT simulations and robot experiments. In these gaits, body undulations are properly designed to improve (a) forward, (b) rotational, and (c) lateral displacements. 113

3.8 Comparison of displacement in RFT simulations (blue bars) and robot experiments (orange bars with error bar, representing 1 standard deviation) results of (a) forward, (b) rotational and (c) lateral gaits, showing close agreement between RFT simulations and robot experiments. Each gait is tested for ~ 3 experiment trials; each trials containing at least ~ 3 gait periods. The “optimal”, “neutral” and “worst” respectively represent the optimal body bending, no body bending (fixed straight back) and the worst body bending. We indicate statistically significant improvement comparing the ‘optimal’-‘neutral’, as well as ‘optimal’-‘worst’ gaits. The gait comparison with a horizontal bracket with *** represents statistically significant improvement ($p < .001$); the gait comparison without a horizontal bracket represents no statistically significant improvement ($p > .05$). For rotational gaits in (b), we show both transitional and rotational displacement values for completeness only: body bending is optimized with respect to rotation only, and displacement changes are not optimized. 115

3.9	(a) Snapshots of robot simulation following a circle. Rotation with forward motion will lead to an arc in center of mass trajectory. R is the curvature radius of the center of mass trajectory; θ is the stride rotation and D is the stride displacement. (b) Body undulation amplitude vs. robot turning radii (the curvature radius of the center of mass motion trajectory). We hypothesize that by modulating the body undulation amplitude, we can control the turning radius of the robot. Robot experimental data (blue) and RFT simulation data (black) validate our hypothesis.	116
3.10	Height functions for salamanders, namely experimentally-measured gaits for (a) slow walk, (b) fast walk and (c) trot, with salamander gait in blue curves and geometric mechanics predicted gait in green curves overlaid. All the panels have the same body angle range as in the middle panel. . . .	118
4.1	Target and model systems for understanding the role of body undulation in the lizard body elongation and limb reduction continuum (Left) (from top to bottom) fully limbed lizards (<i>U. scoparia</i> and <i>S. olivaceus</i>) in comparison with extant short limbed, elongate lizards (<i>B. kadwa</i> , <i>B. taylori</i> , and <i>B. muntingkamay</i>) and limbless/almost limbless species (<i>L. praepedita</i> and <i>C. occipitalis</i>). Scale bars indicate 2 cm. (Right) An illustrative diagram of the thrust generation in short limbed, elongate lizards: the thrust generated by limb retraction is labeled in red arrows, the thrust generated by body undulation is labeled in yellow arrows.	124
4.2	The diversity of body waves in the body elongation and limb reduction continuum. (top) Photos of species and the snapshots of their body motion during one period (at a scale of seconds) of locomotion. Seven species were studied (from left to right): <i>U. scoparia</i> , <i>S. olivaceus</i> , <i>B. kadwa</i> , <i>B. taylori</i> , <i>B. muntingkamay</i> , <i>L. praepedita</i> , and <i>C. occipitalis</i> . The relative limb size (l : the hind limb length normalized by SVL) and number of presacral vertebrae (V) for each species are labeled [173, 105]. (bottom) The projections of body curvature into the reduced shape space and the estimation of σ for each animal. Units of axes are identical to the left panel.	125
4.2	The diversity of body waves in the body elongation and limb reduction continuum. (top) Photos of species and the snapshots of their body motion during one period (at a scale of seconds) of locomotion. Seven species were studied (from left to right): <i>U. scoparia</i> , <i>S. olivaceus</i> , <i>B. kadwa</i> , <i>B. taylori</i> , <i>B. muntingkamay</i> , <i>L. praepedita</i> , and <i>C. occipitalis</i> . The relative limb size (l : the hind limb length normalized by SVL) and number of presacral vertebrae (V) for each species are labeled [173, 105]. (bottom) The projections of body curvature into the reduced shape space and the estimation of σ for each animal. Units of axes are identical to the left panel.	126

4.3	From standing wave to traveling wave	(a) Comparison between the original body curvature profile of <i>B. taylori</i> and the reconstructed body curvature profile over a gait cycle from the estimated wavelength λ and flatness σ . The units of the colorbar are SVL^{-1} . (b) The relationship between the locomotion parameters (σ and λ) and morphology parameter (the relative hind limb length l). Red points with error bars correspond to the locomotion parameters of <i>U. scoparia</i> and <i>S. olivaceus</i> on an aerated granular medium to reduced the resistive force of the media. Note that we use $l = 0.01$ for <i>L. praepedita</i> on the plot and that the abscissa is reversed (descending left to right) to correspond to Fig. 2.	127
4.4	Geometric mechanics analysis of the body-limb coordination in short limbed, elongate lizards	(a) The limb movement in short limbed, elongate lizards follows the lateral couplet sequence (FR-HL-FL-HR). The phase relationship of hip bending and hind limb movements are plotted in the right side panels.	128
4.4	Geometric mechanics analysis of the body-limb coordination in short limbed, elongate lizards	(b) The shape space for short limbed, elongate lizards. The body movements are prescribed by the reduced shape variable w_1 and w_2 , and the limb contact states are inferred from the body movements. Gaits can be represented by closed-loop paths in the shape space. A standing wave gait path, a traveling wave gait path, and an intermediate wave gait path are compared.	129
4.4	Geometric mechanics analysis of the body-limb coordination in short limbed, elongate lizards	(c) Height functions to investigate the body undulation in lizards with intermediate limbs. (left) Two strips emerged in the height function for short limbed, elongate lizards, such that a circular gait path can enclose significantly more surface than a flattened elliptic gait path. To further understand the two stripes, we calculated the height function for hypothetical lizards with one pair of limbs near the head (middle panel) and near the tail (right panel). Each stripe is associated with a pair of limbs, in which case a flattened elliptic gait path can enclose sufficient surface in the height function. The units of the colorbar are $(10^{-3} \times \text{SVL}^{-1} / \text{rad}^2)$. 129	129
4.5	The weight distribution role of limbs in lizard locomotion	(a) The body weight can be supported by the limbs and the body; γ indicates the fraction of body weight supported by limbs. (b) Three typical gaits: the pace gait (duty factor = 0.5, leg phase shift = 0) implemented by lizards with short limbs, the LS (lateral sequence: duty factor = 0.5, leg phase shift = 0.25) gait implemented by lizards with intermediate limbs, and the trot gait (duty factor = 0.5, leg phase shift = 0.5) implemented by lizards with long limbs.	131

4.5	The weight distribution role of limbs in lizard locomotion (c) The relationship between γ and speed for (solid black curves) pace, (dashed blue curves) LS, and (dashed red curves) trot gaits on lizards with (c.1) short, (c.2) intermediate, and (c.3) long limbs. Potential tip-overs are indicated by a red cross.	131
4.6	Traveling wave in fully limbed lizards induced by substrate variation Comparison of the body wave dynamics of <i>Uma scoparia</i> (a) on sandpaper and (b) on a loosely packed granular medium, and (c) on an aerated granular medium. An almost perfect standing wave is observed for <i>Uma scoparia</i> on sandpaper and on the loosely packed granular medium, while features of a traveling wave emerge for <i>Uma scoparia</i> on the aerated granular medium. Resulting σ and λ are shown in Fig. Figure 4.3b. The units of the colorbar are SVL^{-1} for all panels.	132
4.7	Geometric mechanics modeling for the robophysical experiments (a) The definition of α_1 and α_2 and the body-limb coordination in the 3-link swimmer and 4 leg contacts. ψ is the phase lag between the upper back and lower back actuators. Right panel demonstrates how leg contact patterns are coupled to the shape variables (α_1 and α_2). On the lower right half of the shape space, the contact patterns are counter-diagonal; on the upper left half of the shape space, the contact patterns are diagonal. Examples of the standing wave ($\psi = 0$) and the traveling wave ($\psi = \pi/2$) are compared in the shape space. (b) Vector field and height functions for modelling the robophysical experiments on poppy seeds. The displacement can be approximated by the surface integral enclosed by the gait path over the height function (right panels). The units of the colorbar are $(10^{-3} \times SVL^{-1}/rad^2)$. Units of axes in (b) are identical to the shape space in (a).	133
4.8	Robophysical experiments (a) Snapshots of robots (top panel: belly thrust; bottom panel: no belly thrust) implementing standing wave ($\psi = 0$) and traveling wave ($\psi = \pi/2$) gaits. (b) The effect of ψ on locomotion performance for robot with no belly thrust (blue curve) and robot with belly thrust (orange curve).	134
5.1	Legged and limbless robotic models studied in the paper. a. Quadrupedal robot [176] b. Hexapod robot c. Myriapod robot with eight pairs of legs d. Sidewinder robot [134]. All scale bars are 5 cm.	144

- 5.2 **Modelling multi-legged systems and sidewinders.** The contact patterns of some well-known gaits: (a.1) lateral sequence walking, (a.2) trotting, and (a.3) pacing in quadrupeds; (b) alternating tripod in hexapods, (c.1) retrograde-wave and (cc.2) direct-wave gaits in myriapods, and (d) sidewinding in snake-like limbless robots,. For each system, these diagrams show the variables included in the model, such as leg joint angles θ_N , and body joint angles $\alpha_{(N-1)}$, where N is the number of leg pairs for legged systems or joint sets in the sidewinder. In the contact sequence diagrams, filled blocks represent stance phase, and open blocks represent swing phase. (e) A general contact pattern table. The blue arrow represents the duty factor D . The red arrow represents the lateral phase lag, Φ_{lat} . τ denote gait phase. (f) Hildebrand plots with two parameters D and Φ_{lat} to characterize the motions in the vertical plane. We labeled the region associated with walking, running, lateral sequence (LS) and diagonal sequence (DS) gaits. 147
- 5.3 **An example of gait design for a hexapod using Hildebrand gait principles and geometric mechanics.** From the parameter space (a.1), we select the duty factor D and lateral phase lag Φ_{lat} . We prescribe the contact by its phase ϕ_c (a.2), and the lateral body undulation by its phase ϕ_b (a.3). (b) The gait parameters determine the equations of motion, which in turn are used to derive a height function, and design a gait. The gait path (the purple curve) shown maximizes the volume enclosed in the lower right corner (in solid shadow) minus the volume enclosed in the upper left corner (in dashed shadow). The left panel is the toroidal visualization of the height function, the right panel is the Euclidean visualization of the height function. (c) Typical configurations in which the robot is statically stable (c.1), statically unstable (c.2) and unstable (c.3) 152
- 5.4 **Snapshots of the numerical simulation showing examples of two prescribed myriapod gaits.** (a) statically unstable, $\Phi_{lat} = 0.92$, $D = 0.5$ and (b) statically stable $\Phi_{lat} = 0.5$, $D = 0.5$. We compared the gait with straight fixed body (top) and gaits with coordinated body undulation (bottom). The displacement, in body length (BL) per cycle, are labeled with a red arrow. The black/white circles show the stance/swing phase of the feet. 153

5.5	Trade-off between speed and static stability in quadruped, hexapod, myriapod, and sidewinding systems.	Theoretically predicted static stability (left column), displacement in body lengths per cycle (BLC) with fixed straight back (middle column), and displacement with coordinated lateral body undulation (right column) over the space of Hildebrand parameters D and Φ_{lat} , for the quadruped (a), hexapod (b), myriapod (c) and sidewinder (d). White space in all panels represents the regions where unstable configurations exist (Figure 5.3c.3); we defined static stability to be zero in those regions. Note that static stability of the quadruped, hexapod and myriapod is numerically calculated for configurations with a straight backbone. The static stability of the sidewinder is numerically calculated for gaits with coordinated lateral body undulation. Note that we only consider gaits where unstable configurations (Figure 5.3c.3) do not occur. Axes in each sub-figure are identical. The color-maps in each column are identical. 155
5.5	Trade-off between speed and static stability in quadruped, hexapod, myriapod, and sidewinding systems.	Theoretically predicted static stability (left column), displacement in body lengths per cycle (BLC) with fixed straight back (middle column), and displacement with coordinated lateral body undulation (right column) over the space of Hildebrand parameters D and Φ_{lat} , for the myriapod (c) and sidewinder (d). 156
5.6	Verification of the theoretically generated gaits in the robotic models	(left column) Gait cycle of each robot (a: quadruped, $D = 0.75$ and $\Phi_{lat} = 0.5$; b: hexapod, $D = 0.5$ and $\Phi_{lat} = 0.3$). The arrows show the direction of locomotion and T is one gait cycle. The center of mass trajectories (yellow) are given in the last snapshots. (Middle column) The comparison of simulations (solid curves) and experimental data (curves with error bar) of displacement over time for each system. Two gaits with body undulation coordinated with geometric mechanics (GM) are illustrated for each system. (Right column) The relationship between the lateral phase lag, Φ_{lat} , and the displacement for the same system either with fixed straight backbone (red) or with coordinated lateral body undulation (blue). The color scheme and axes in (b, c, d) are the same as in (a). 157
5.6	Verification of the theoretically generated gaits in the robotic models	(left column) Gait cycle of each robot (c: myriapod, $D = 0.5$, $\Phi_{lat} = 0.1$; d: sidewinder). The color scheme and axes in (b, c, d) are the same as in (a). . 158

5.7 **The effect of static stability on locomotion performance.** In the left column (a.), the body roll and pitch over the course of the hexapod experiments are recorded as a function of gait fraction. Three gaits ($D = 0.5$, $\Phi_{lat} = 0.65$ in purple; $D = 0.5$, $\Phi_{lat} = 0.45$ in red; and $D = 0.5$, $\Phi_{lat} = 0.15$ in yellow) in Hildebrand gait space are compared. In the middle row, we show the theoretical prediction of static stability as a function of lateral phase lag. In the bottom row, we show the average \pm SD experimental body roll and pitch as a function of the lateral phase lag. In the right column, (b.), a similar analysis is performed for the sidewinder experiments. The top-right shows the trajectory of body motion over six gait cycles, where the color scale represents the evolution of time. We marked the initial position of the robot in the black circles. In the middle row, we showed the theoretical prediction of static stability as a function of lateral phase lag. In the bottom panel of Fig 7b, The body yaw angle is recorded as a function of lateral phase lag. 159

5.8 **Physical intuition in body-leg coordination** (a) The relationship between Φ_{lat} , lateral phase lag, and ϕ_{bc} , the optimal phasing between body and leg. ϕ_{bc} is numerically calculated from a height function (Figure 5.3). The empirical data for the hexapod (blue circle) and myriapod (red circle) are compared. (b) Consider a quadrupedal “sub-unit” consisting of two pairs of legs and one body-joint. The Hildebrand prescription allows us to write the phase relation of each leg and the body bending with respect to the fore right leg (FR). (c) To maximize locomotive performance with body-bending, at FL (fore left) and HR (hind right) touchdown, the body is bent clockwise; and at FR (fore right) and HL (hind left) touchdown, the body is bent counterclockwise [176]. Given this empirical relation $\phi_{bc} \sim (\Phi_{lat} + 1/2)\pi$, the HL/FR and HR/FL touchdown phases are symmetrically distributed around the peaks of the bending trajectory, which we use to coordinate body-bending with foot contacts. 160

5.9 **Analysis of salamander (*Salamandra salamandra*) locomotion using the Hildebrand framework and geometric mechanics** (a.1) Estimation of the duty factor, D , and lateral phase lag, Φ_{lat} from animal joint angle trajectories. Curves with error bars are the average leg shoulder (hip) angle over three cycles. The lighter-color solid curves are piece-wise linear sinusoidal functions (defined in Equation 5.3) fit to the tracked data. (a.2) Estimated D and Φ_{lat} for animal locomotion under different speeds. (b.1) Estimating ϕ_{bc} from body bending angle trajectories. (b.2) Relationship between ϕ_{bc} and speed, measured in body lengths (BL) per cycle. The prediction made with geometric mechanics is shown as dashed curves. The measured salamander data are shown as crosses in the same color as their corresponding prediction curves, where the length and height of the crosses denote the standard deviation of the measured animal data. The scale bar near the salamander photo indicates 30 mm. 161

5.10	Analysis of centipede (<i>Scolopendra polymorpha</i>) locomotion using the Hildebrand framework and geometric mechanics (a.1) Estimation of the duty factor, D , and lateral phase lag, Φ_{lat} from animal joint trajectories. The colorbar here denotes the shoulder joint angle for each leg on right-hand side. (a.2) Estimated gait parameters D and Φ_{lat} for the centipede's locomotion. (b.1) Estimating ϕ_{bc} from body phase and leg phase. (b.2) Relationship between ϕ_{bc} and the speed, measured in body lengths per cycle. The prediction made with geometric mechanics is shown as solid curves. The measured centipede data is presented by crosses in the same color as their corresponding prediction curves, where the length and height of the crosses denote the standard deviation of the measured animal data. The scale bar near the centipede photo indicates 30mm.	162
5.11	Supporting force distribution (a) An example of the myriapod model. In this example, the robot is supported by eight legs. For a leg i , it provides supporting force N_i . Its location is labeled as $[x_i y_i]$. The location of center of mass is labeled $[x_c y_c]$. (b) The robots with hybrid contact with environments. The body segments in stance phase are labelled by red circle. (c) The illustration of the force-velocity relationship. (Left) The vector of body velocity (ξ) and GRF f on the body segment in contact with environments (red cube). (Right) The decomposition of body velocity and GRF in the direction of body orientation.	171
6.1	Swimming in terrestrial environments (a) Top view of a robophysical device swimming on frictional ground.	175
6.1	Swimming in terrestrial environments (b) The patterns of lifting and landing of contralateral feet. Each row represents the contact states of i -th link. Shadow region represents right foot in stance phase, open region presents left foot in stance phase. (right) Front view of the robophysical device lifting (i) left and (ii) right feet of the first module	175
6.1	Swimming in terrestrial environments (c) Trajectory of backbone during terrestrial swimming ($\Theta_{body} = \pi/3$, $\Theta_{leg} = 0$, $n = 6$) colored by time. (d) (left) Displacement and (Right) velocity profile of terrestrial swimming. We compared the experimental data with dynamical simulation (brown curve) and quasi-static simulation (blue curve) for body-dominated terrestrial swimming. After the transient development, both experiments dynamical simulation converge to a limit cycle similar to quasi-static simulation.	176

6.2	The geometric nature of terrestrial swimming (a) Robot ($n = 6$) implementing the same gait ($\Theta_{body} = \pi/3, \Theta_{leg} = 0$) under different temporal frequencies. (<i>Left</i>) The development of displacement as a function of time under different temporal frequencies. (<i>Right</i>) The step length is stable over a range of temporal frequencies. Dashed lines represent prediction from quasi-static simulation.	177
6.2	The geometric nature of terrestrial swimming (b) Robot implementing the same gait under different substrate (different friction coefficients, μ). (<i>Left</i>) The development of velocity as a function of time. Despite the initial high-magnitude oscillation, robots on low-friction surfaces converged to quasi-static velocity profiles after one gait cycle. (<i>Right</i>) The saturated step length is stable over a range of friction coefficient.	177
6.2	The geometric nature of terrestrial swimming (c) Experimental verification of force-velocity relationship ($\Theta_{body} = \pi/3, \Theta_{leg} = 0, n = 8$). We test the relationship between the whole body drag force and the velocity by measuring the speed of robots on slopes. We compared two spatial frequencies, $\xi = 1$ and $\xi = 1.3$. In both experiments, we observed that there exists a linear relationship between force and velocity near equilibrium.	178
6.3	Direction of limb slipping (i) Typical trajectories of foot tips of robophysical device ($n = 6$) during stance phase for (a) body-dominated ($\Theta_{body} = \pi/3, \Theta_{leg} = 0$) and (b) leg-dominated ($\Theta_{body} = 0, \Theta_{leg} = \pi/6$) terrestrial swimming. x -axis is the direction of motion. We quantify the slipping of a foot by its direction (Ψ unit: rad) and magnitude (unit: BL/cycle).	178
6.3	Direction of limb slipping (ii) The simulation prediction (red curves) and experimental measured (black dots) time series of slipping angles.	179
6.3	Direction of limb slipping (iii) The slipping profiles from simulation. We illustrate (<i>top</i>) the slipping direction profile and (<i>bottom</i>) the slipping magnitude profile.	179

- 6.4 **Performance space of multi-legged terrestrial locomotion.** We characterize the terrestrial locomotion using a performance space consisting of the amplitudes of body undulation and leg movement. (a) The heat map of velocity (v , unit: cm/cycle) over the performance space for robophysical model with (*left*) 4, (*right*) 8 pairs of limbs. n is the number of limb pairs. Note that optimal terrestrial locomotion (the highest velocity) occurs at “hybrid” region when $N = 4$ and at body-dominated when $N = 8$. (*bottom*) We showed the snapshots of body configurations over a cycles for (i) $N = 4$, $\Theta_{body} = 60^\circ$, $\Theta_{leg} = 15^\circ$, (ii) $N = 4$, $\Theta_{body} = 0^\circ$, $\Theta_{leg} = 45^\circ$, and (iii) $N = 8$, $\Theta_{body} = 60^\circ$, $\Theta_{leg} = 0^\circ$. (b) The transition of optimal terrestrial locomotion from leg-dominated to body-dominated as the number of leg pairs increases. 180
- 6.5 **Advantage of body-dominated terrestrial swimming in obstacle-rich environments** (a.1) A snapshot of robot ($n = 6$) moving on obstacle-rich environments ($\rho = 0.06$). Cartoon illustration of interaction between robot and obstacles subject to different slipping directions (*top*: typical body-dominated; *bottom*: typical leg-dominated). Red blocks represents obstacles, legs from darker color to lighter color represents progression of time. (a.2) We choose three isoheight lines on the velocity heat-map over the performance space: $v = 12$ cm/cycle, $v = 16$ cm/cycle, and $v = 18$ cm/cycle. We quantify the degree of body and leg use by $\beta = \tan^{-1}(\Theta_{leg}/\Theta_{body})$. (b) Comparison of locomotion performance in homogeneous (curves with error bar in green colors), heterogeneous environments (curves with error bar in black color), and theoretical predictions from Equation 6.6 (curves and areas in light brown color). From top to bottom the flat line descended from isoheight lines with $v = 18$ cm/cycle, $v = 18$ cm/cycle, and $v = 18$ cm/cycle. . 182
- 6.6 **Analysis of centipede locomotion** (a) (*left*) Snapshots of a trial of (i) body-dominated and (ii) leg-dominated centipede locomotion. (*right*) The trajectory of foot slipping colored by time. The stance phase spans 0.4 seconds. Trajectory of centipede body during terrestrial swimming colored by time. (b) The (*top*) displacement and (*bottom*) velocity profiles. Measured animal data is presented in cycles and the predictions from quasi-static model is presented in blue curve. 183
- 6.6 **Analysis of centipede locomotion** (c) The transition from leg-dominated gaits to swimming dominated gaits as speed increases. In each centipede locomotion trial, we extract amplitude of body undulation and leg retraction, and represented it as a cross (colored by its speed) on performance space. 184

7.1	<p>An analogy between signal transmission and matter transportation. (a) The flowchart of signal transmission. We compare analog and digital signal transmission through noisy wires. Digital redundant signal allows reliable transmission through a noisy wire via either redundancy or a re-transmission channel. (b) Matter transportation with both continuous and discrete active contacts can be effective on perfect tracks. Discrete redundant contacts enable robust matter transportation over rugose tracks via redundancy or environmental awareness. (c) Multi-legged robophysical locomotors traverse noisy landscapes: (c.1.<i>left</i>) pebbles, (c.1.<i>middle</i>) stairs and slopes, (c.1.<i>right</i>) entangled granular media, and (c.2) a laboratory model of rugose terrain.</p>	196
7.2	<p>Encoding and decoding of signal transmission and matter transportation. (a) The analogy of (a.1) signal transmission (adapted from [112]) and (a.2) locomotion (matter transportation). (b.i) The matter to be transported to a destination D. (b.ii) The desired bac sequence to reach the locomotion destination. (b.iii) Noisy landscapes can introduce contact errors such as delaying bacs and shortening the duration of bacs. We labeled the desired bac (spans the duration of τ) and two terrain-contaminated bacs (starts at c_1 with duration τ_u). (b.vi) The actual bac sequence (contaminated by contact errors). (b.v) The actual locomotion destination \hat{D}.</p>	197
7.3	<p>Numerical verification of the sufficiency to bound contact errors via redundancy. (a.1) (<i>Left</i>) An illustration of thrust generation from bacs. (<i>Right</i>) Illustrations of the relationship between thrust and velocity. Self-propulsion with (i) nominal contact and (ii) contact errors are compared. (a.2) (<i>Left</i>) The instantaneous thrust $f(t)$ as a function of time, derived from [235]. (<i>mid</i>) The cumulative distribution function of τ_u. (<i>Right</i>) The thrust-velocity (normalized by nominal velocity) relationship. (b.1) The numerical histogram of terrain-disturbed thrust for robots with different combinations of temporal (T) and spatial (N) redundancy. (b.2) Numerically calculated $N_{95\%}$, the minimal number of leg pairs to facilitate successful locomotion with 95% confidence interval (CI), plotted against noise level (b). (c.1) The numerical distribution of velocity for robots with different spatial and temporal redundancy. The color schemes are identical to (b.1). (c.2) The numerically calculated expected average velocity plotted as a function of the number of leg pairs.</p>	199

7.4	Experimental verification of the sufficiency to bound contact errors via redundancy. (a) Rugose terrains with rugosity (a.1) $R_g = 0.17$ and (a.2) $R_g = 0.32$. The block height distribution is shown on the right panel. (b) The correlation between bac duration and locomotion velocity of a 12-legged robots on rugose terrains. Color schemes are identical to (a). (c) For robot with different number of leg pairs N , we recorded $T_{[D=60]}$, the number of periods required to transport $D = 60\text{cm}$ on terrains with (blue) $R_g = 0$, (green) $R_g = 0.17$, and (black) $R_g = 0.32$. The error bar was calculated from at least 10 trials. $T_{[D=60]}$ for contact modulated gaits are illustrated in the purple rectangle. (d) The empirical distribution of velocity on terrains with (d.1) $R_g = 0.17$ and (d.2) $R_g = 0.32$. Effect of temporal redundancy on (<i>Top</i>) the 6-legged robot and (<i>Bottom</i>) the 12-legged robot. Non-negligible locomotion failure is observed when there is not sufficient redundancy. The empirical distributions were obtained from 30 trials.	204
7.5	Robophysical model. (a) CAD of one module of the robot. The legs are out-of-phase and their up/down and fore/aft positions are controlled by two AX 12A motors. The body motor (2XL 430) controls the lateral undulation of the body. Body angle and legs are coupled to each other with a hip and a undulation connector. Inset shows the max lifting angle (60°) of the leg. (c) Overall sketch of a 12-legged robot.	209
7.6	Leg compliance design. (a) Working principle of inward compliance. Return rubber bands connect legs and the hip connector. Drag forces from rubber bands support the weight of each module of the robot. Rubber bands also recover the lifted leg to its neutral position when the leg up/down motor stops lifting. (b)Working principle of the directional flexible (bends from head to tail) leg with a return rubber band. The leg approaches the obstacle, pivots around the tip, and bends. After it passes the obstacle, the rubber band returns the leg to its neutral position. Black arrow indicates the moving direction of the robot.	210
7.7	Robot connection. The PC input control signals to the robot via a Robotis U2D2 USB communication converter. A DC power supply HY3050E provides power for the motors.	211
7.8	Tracking system setup. (a). Four 4 OptiTrack prime 13w cameras are fixed on tripods and placed at each corner of the testing arena for tracking. (b). A 12-legged robot mounted with markers.	212
7.9	Contact error. (<i>Top</i>) Side view of robot on rugose terrain. Missing steps are identified in blue arrows. (<i>Bottom</i>) Cumulative distribution functions of empirically measured contact duration for (green) lower rugose terrain with $R_g = 0.17$ and (black) higher rugose terrain with $R_g = 0.32$	212

7.10 **Contact modulation.** Snapshots of (a) top view and (b) side view of contact modulated gaits. Note that for modules in the concave part of the vertical wave (labelled in red arrow), both legs are not in contact with substrate because of contact modulation. We also label the modules in concave part of vertical wave in the top view. 215

CHAPTER 1

INTRODUCTION

1.1 Overview

The transport of physical matter is an important aspect in human society and biological systems. Locomotion as a means of matter transport has been thoroughly studied in various forms [1, 2, 3, 4], where a core concept is to actively generate thrust against drag to develop “self-propulsion”. In aerial and aquatic environments, locomotors are often submerged in a continuous medium where the thrust is generated from continuous interaction between the locomotor and the media [5, 6]. In other words, the thrust is continuous with respect to both time and position on a locomotor body [7]. In those cases, inertial forces typically dominate over the frictional forces, a regime we will refer to as the *inertia-dominated locomotion*.

Terrestrial locomotion is particularly interesting because it occurs at the interfaces among multiple media [11] where the heterogeneous spatial terrestrial structures can interfere with thrust generation. To counter the terrestrial heterogeneity and its effects on locomotion, humans have built costly flat platforms, such as tracks and roads. In particular, the conveyance arising from wheels on tracks/roads is believed to be one of the most efficient terrestrial matter transportation schemes [5]. This wheeled terrestrial locomotion, however, shares a property of continuous thrust akin to aerial and aquatic locomotion, where thrust generation relies heavily on the homogeneity of the established platforms [12] and lacks generality towards more complex terrestrial environments [13]. In environments where construction of homogeneous platforms is inconvenient, researchers have either increased the size of the wheels [14] or have developed appendage based self-propulsion, such as legs [15] and vertical waves of contact in limbless locomotors [16].

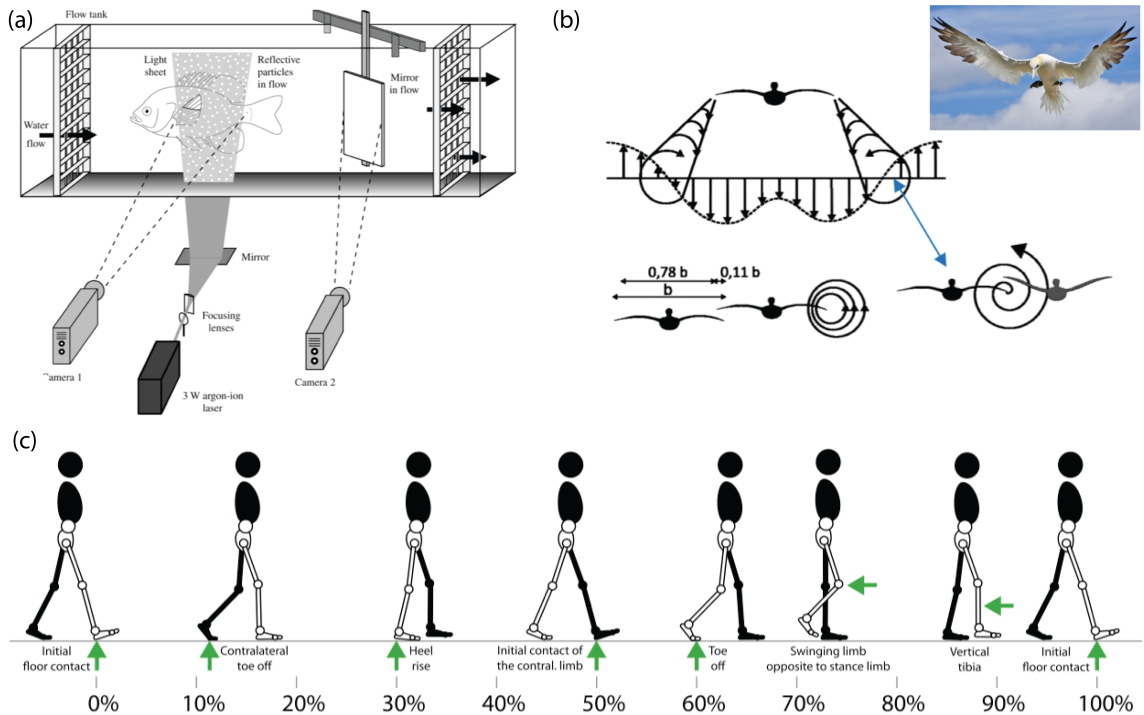


Figure 1.1: **Aerial, aquatic, and terrestrial locomotion** (a) Aquatic locomotion of fish swimming [8]. (b) Aerial locomotion of bird flight [9]. In both cases, the reaction force from the interaction between locomotor and environment is continuous temporally and spatially. (c) Terrestrial locomotion of human [10], where appendages (legs) periodically make and break contact with substrate.

1.1.1 Conventional legged locomotion

A simple self-propulsion principle to govern conventional legged locomotion (e.g., bipeds or quadrupeds) is to protract¹ during stance phase (which makes contact) and retract² during swing phase (which breaks contact) [17, 15]. The challenges of conventional legged locomotion then lie in properly controlling the dynamics of appendages to avoid potentially catastrophic loss of stability and thereby execute such self-propulsion principles. Given the importance of stability in legged locomotion, legged locomotion is stereotyped as *stability-driven locomotion*, where the coordination of body inertia can be important for balance and self-righting [18, 19, 20, 21, 22, 23, 4, 24]. State-of-art legged systems tend to be classified into one of several categories, including planning for appropriate foot contacts to maintain

¹Limbs generate thrust by swinging from anterior to posterior.

²Limbs restore their positions from posterior to anterior.

static stability during each phase of the step [18, 19, 20, 21, 22], or relying on dynamical stability by proper inertia management [23, 4, 24].

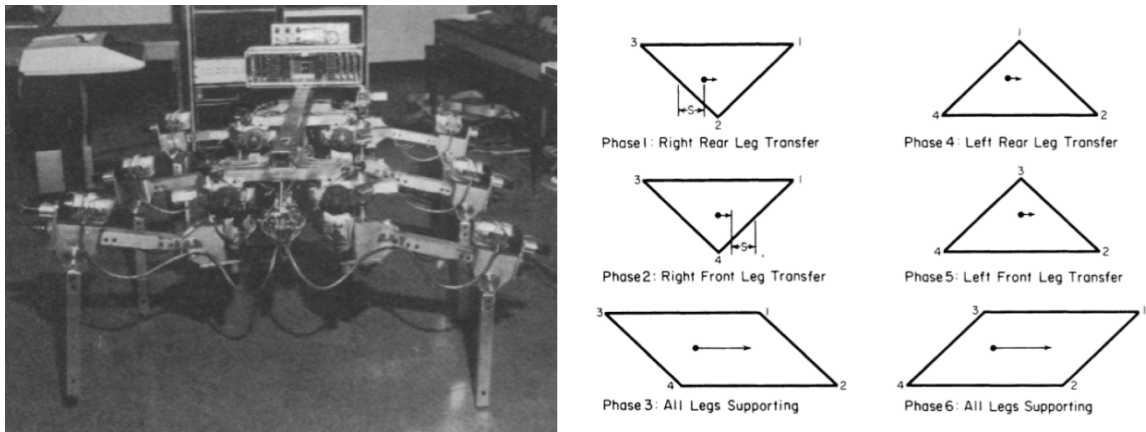


Figure 1.2: **Footfall pattern planning on rigid flat terrain** Front view of OSU hexapod vehicle and the footfall pattern planning algorithm. Figures are adapted from [18].

One of the most popular approaches is to plan for foot contacts to enforce the static stability of the locomotor. Foot placement determines a sequence of locations on the ground where a system places the distal-most portion of its limbs. McGhee and Iswandhi [18] introduced a heuristic gait-planning algorithm for legged robots by maximizing the stability margin (the distance from the center of mass to the supporting polygon in the direction of travel) and minimizing kinematic margin (the distance that the foothold of a given leg can travel in the opposite direction of motion before reaching the boundary of its workspace). Although this algorithm was adequate for hexapods, it is not as well suited to quadrupeds because quadrupeds have more strict stability criteria. Bai et al. [25] applied a similar approach to quadrupeds, which took a lateral sequence walk (leg lifting follows the sequence: left hind leg, left front leg, right hind leg, right front leg [17]) as a primary gait and successfully adapted it to the environment. These ideas were applied to the Little Dog platform [19, 22], where the footsteps are planned and implemented across rough terrain in the presence of disturbances.

More recently, machine learning tools and algorithms have been applied to design leg movements during locomotion. Kim et al. [26] applied Powell’s minimization method [27]

to design a periodic footfall pattern for quadrupedal robots that was faster and more stable than previous hand-optimized gaits in the RoboCup soccer competition. Kohl and Stone [28] parameterized leg movements based on *locus* foot trajectory [29], then optimized these parameters to improve locomotion speed by some established machine learning algorithms. With improved physical simulator and learning robust policies, Tan et al. [30] trained robot control policy in simulation and successfully implemented trotting and galloping gaits on agile quadrupedal robots in real world.

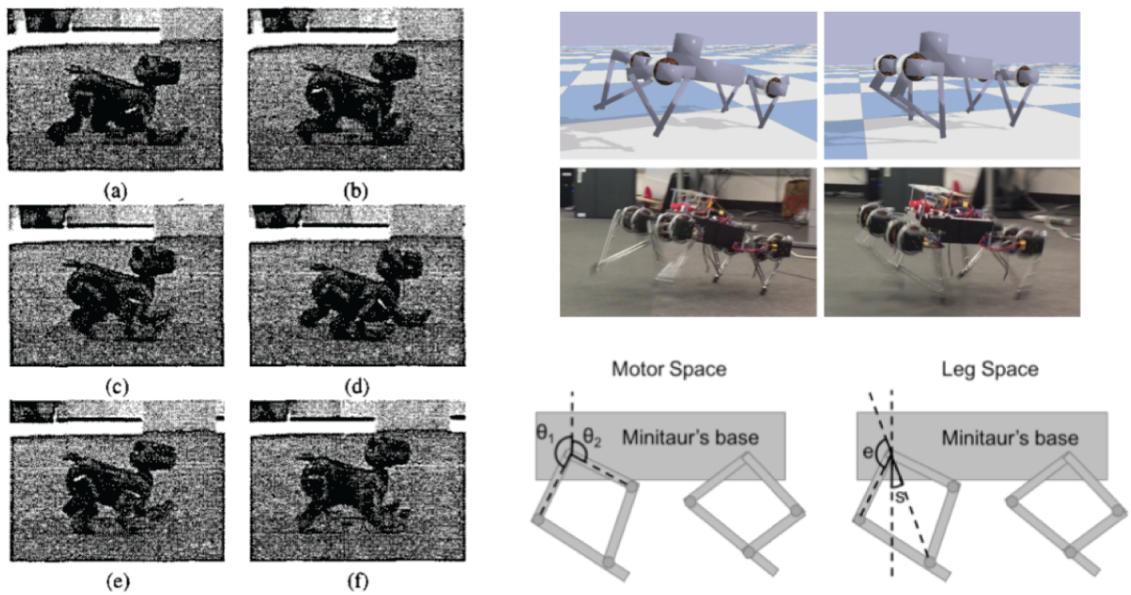


Figure 1.3: **Machine learning in legged locomotion** (Left) Early work using reinforcement learning to optimize quadruped gait [18]. (Right) Recent work of legged locomotion using deep reinforcement learning [30].

Inspired by analogous ideas from biology, the central pattern generator (CPG) approach uses periodic signals to drive body joint trajectories in shape space for locomotion or other repetitive tasks [1, 31, 32, 33, 34] to augment the performance of an existing footfall pattern. Ijspeert et al. [35] showed that CPGs can produce body-limb coordinated movements for the locomotion of a salamander robot, as well as generate gait transitions among different forward gait motions of varying speed. Using CPG analytic tools, prior work [36, 37, 38] demonstrated that the body-limb coordination used by salamanders optimizes their

forward speed and produces turning motion. Following this idea, Owaki et al. [39] investigated the mechanisms of inter-limb coordination which exhibited good adaptability to changes in walking speed of a quadrupedal robot.

1.1.2 Unconventional legged systems

Locomotion is also an essential behavior observed in biological systems [40, 41, 42]. Animals can use seemingly simple rhythmic body (and/or leg) movements to traverse their natural terrains. In organisms as diverse as galloping horses [17], fast-walking centipedes [43], sidewinding snakes [44, 45], and undulatory lizards [46], properly coordinated self-deformation can generate thrust through interactions with substrates and cause self-propulsion. A major challenge in locomotor biology (which is echoed in design of robots with life-like capabilities [47, 48]) is to discover general principles of self-propulsion which govern how organisms generate and control fast, stable, or energetically efficient locomotion.

However, aside from extensive studies on conventional bipedal and quadrupedal locomotors, the principles of unconventional locomotors, such as centipedes and sidewinders as we listed earlier, are less studied. Specifically, because of additional legs or belly contact, the stability of centipedes or sidewinders have limited impact on the overall locomotion behavior. It remains unclear how centipedes or sidewinders coordinate their body appendages to generate thrust.

To explore such principles, researchers divide general locomotion control into templates and anchors [15, 49, 50, 51, 52, 53, 54]. Specifically, a template is the simplest locomotion model with the least number of variables and parameters and an anchor is the elaborated model with morphological and physiological details. The template approach ignores the complexity of organisms and seeks to discover broad (cross taxa) and relatively simple patterns of dynamics. For example, the spring-loaded inverted pendulum is a template for legged locomotion, which guided the development of various agile legged robots [55, 56,

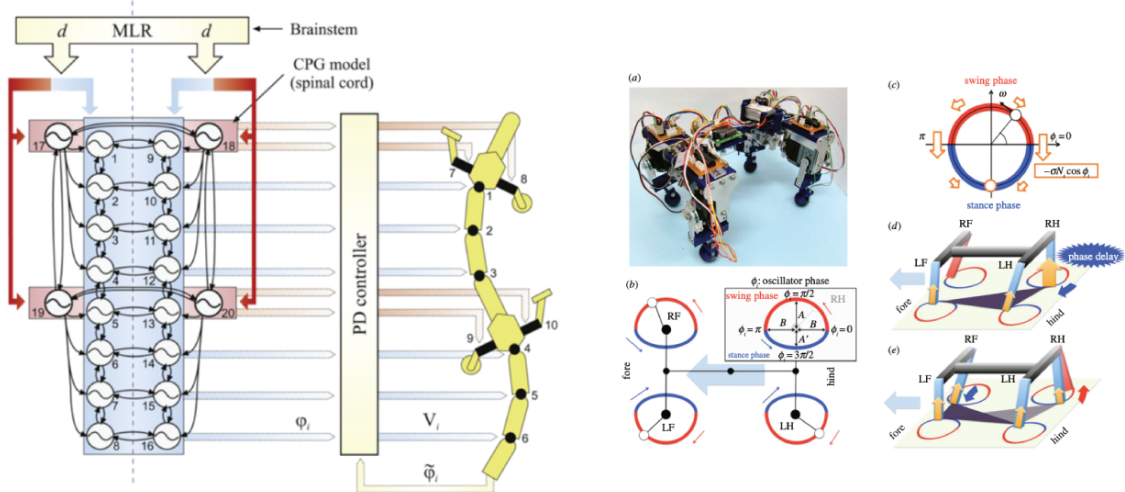


Figure 1.4: **Central pattern generator (CPG) for locomotion** (Left) Early work of CPG to study body-limb coordination by oscillation coupling of a salamander robot [35]. (Right) Recent work of CPG to study inter-limb coordination [39].

57, 58] and generate insight into biological legged locomotion [59].

Despite the simplicity of the template-anchor approach, in some cases, the morphological features can also affect the overall locomotion strategy/performance. For example, stereotyped snakes and lizards have distinct body movement patterns: snakes primarily use traveling wave body undulations to generate thrust [60, 61, 62, 63]. Lizards use a standing wave to assist limb retraction [64, 65]; and employ traveling waves of axial body undulation at high speed [66, 67, 65], believed to help the limbs in transmitting forces along the axis of progression [65]. Notably, the body morphology in lizards spans from fully limbed and short bodied to elongate and limbless [68]. In lizards with short limbs and elongate bodies, because of the proximity to the substrate, both the body and limbs directly contribute to generating thrust and overcoming drag [65]. Since the short limbs of elongate lizards typically cannot support the animal's body weight, the two propulsive mechanisms (limb retraction and body undulation) can coexist, requiring proper coordination. Further, the support of body weight must be properly distributed between the ventral surface of the body and the limbs to facilitate effective thrust-generation mechanics. In other words, the morphological features (anchors) of lizards can in turn affect the coordination between the

self-propulsion templates of body undulation and limb retraction.

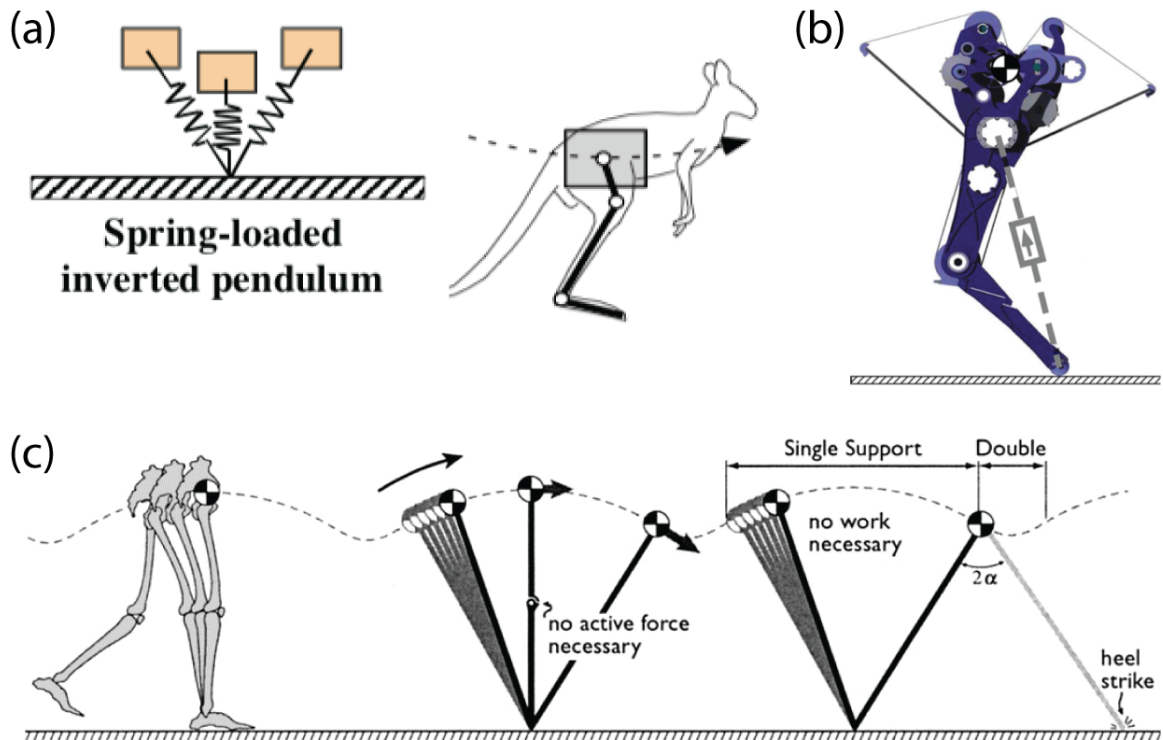


Figure 1.5: **Template-anchor for locomotion** (a) A template (spring-loaded inverted pendulum) for legged locomotion [15]. (b) Application of template-anchor approach to study robot legged locomotion [58]. (c) Application of template-anchor approach to study human locomotion [59]

To elaborate our argument, we illustrate another example. Locomotion is typically separately studied in continuous media where bodies and legs experience forces generated by the flowing medium, or on solid substrates dominated by friction. In the former, centralized whole-body coordination is believed to facilitate appropriate slipping through the medium for self-propulsion. In the latter, slip is often assumed minimal and thus avoided by (locally) intra-limb coordination. While the bulk of prior work on terrestrial locomotors [69] focused on systems with two or four legs, many biological, and increasingly robotic device, possess multiple sets of limbs (e.g., cockroaches have six and centipedes can have up to 40 legs). In contrast to the few-legged systems in which an assumption of no-slip contact is often feasible [70], for systems with more than four legs, there is a high possibility that some slip has to occur during locomotion [71] because of kinematic constraint violations,

(e.g., the BigAnt [71]). As we will discuss in Chapter 6, instead of avoiding slipping, multi-legged locomotors can actively coordinate slips for effective propulsion. In other words, as the number of legs increases (changes in anchors), locomotion in myriapods shifts from slipping-avoidance to slip-driven (changes in templates).

In this way, on top of the sequential template-anchor hypothesis, there should also be a reverse anchor-to-template adaptation where we can systematically explore the relationship between the detailed morphology (what they have) and the governing locomotion principles (how they move). In this thesis, we seek to elaborate such reverse anchor-to-template adaptation using a comparative biological, robophysical, and theoretical modeling approach. Such comparative analyses allow us to predict and analyze animal and robot locomotion behaviors according to their “anchors” (morphological and physiological features).

1.1.3 Geometric mechanics

To simplify the self-propulsion modeling, we assumed that the frictional forces dominate over the inertial forces, which we will refer to as *highly-damped locomotion*. Here, cyclic patterns of self-deformations solely dictate performance, in contrast to inertia dominated systems where gliding (movement without shape changes) and stored/returned elastic energy can be utilized. An approach for analyzing such highly-damped locomotion, which integrates thrust and drag forces over the body, was introduced in the early-to-mid 20th century and goes by Resistive Force Theory (RFT). This method has successfully modeled the kinematics of organisms in highly damped hydrodynamic and granular terradynamic environments, like microorganisms and sand-swimmers [72, 63, 73, 11].

Despite the effectiveness of the RFT framework, its analysis typically involves laborious calculations. For example, even in simple artificial systems [76, 77, 78] to identify parameters that result in optimal performance requires considerable computational effort, comparing movements arising from an infinite combination of shape change sequences. In the last 30 years, a framework referred to as “geometric mechanics” has been devel-

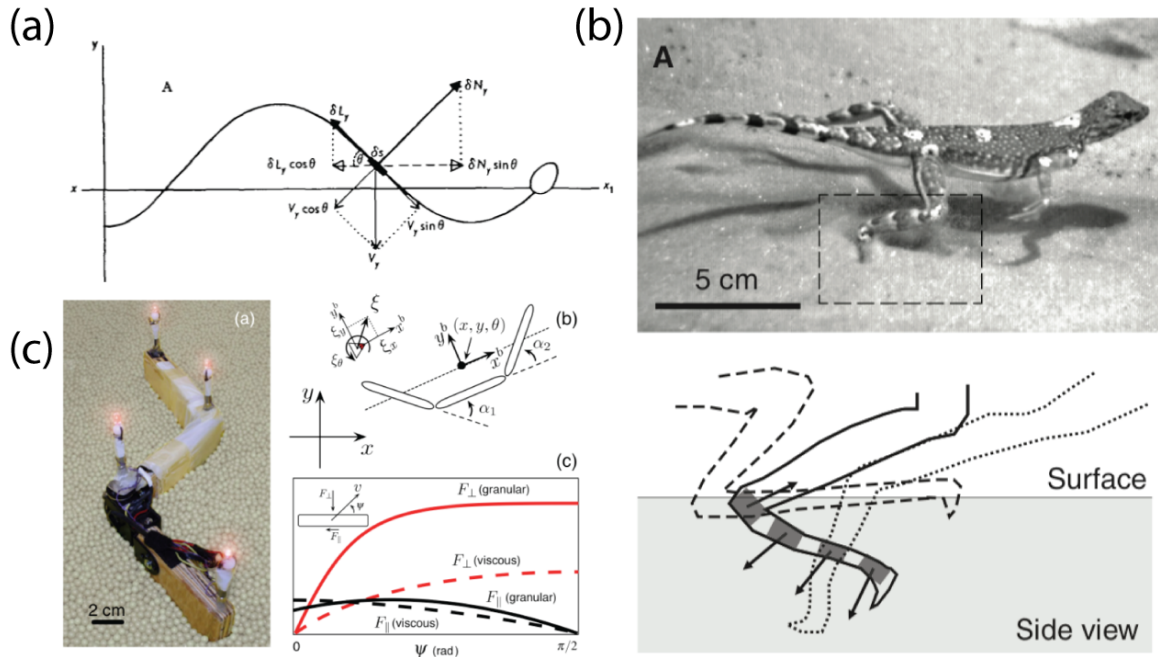


Figure 1.6: **Resistive Force Theory (RFT) for locomotion** (a) Early work in mid 20th century to study self-propulsion in limbless locomotors[61]. (b) Recent work using RFT to study locomotion on granular media [74]. (c) Recent work combining RFT and geometric mechanics [75]

oped [79, 80, 81] as a general scheme to link locomotor performance to patterns of “self-deformation”. This scheme replaces the laborious calculation with a geometric approach to gain qualitative and quantitative insights into how animals and robots can generate optimal high level control templates to affect a desired behavior. In the geometric mechanics framework, the motion of a self-propelling system is separated into a shape space³ and a position space (position and orientation of the locomotor in the world frame). The relationship between velocities in a shape space (joint angle velocities) and velocities in a position space (body velocities of the locomotor) is called the local form of the *connection*. A gait then maps a periodic path in the shape space to a displacement in the position space. A visualization tool known as height functions (the curl of the connection) [75, 82] is used to analyze and design gaits. Prior work successfully advanced this scheme to enable gait design for a limbless undulatory swimming system (a 3-link simmer) in highly damped

³Shape space describes the collection of all possible body-postures. Example of shape space include joint angle space for limbless locomotors.

situations like dry, frictional granular media [75]. Importantly, the theoretical predictions are in quantitative agreement with experimental measurements [75], demonstrating that the geometric mechanics framework can be accurately and successfully applied to real-world systems.

Height functions from geometric mechanics enable a comparatively simple, diagrammatic approach. That is, the key utility of height functions is that they simplify the gait design problem: providing ready identification of gaits that maximize performance in the desired directions (e.g., forward speed or turning rate) in diverse systems. Height functions also give a geometric understanding of benefits and trade-offs of different self-deformation patterns, without need for significant calculation. Most relevant to our interests, height functions can aid the search in finding and optimizing control templates in the form of families of closed curves in the configuration space.

1.2 Generalizing geometric mechanics to diverse locomotion systems

This thesis is organized in the following manner.

- Chapter 2, which advances and uses geometric mechanics to study general limbless locomotion, and
- Chapter 3, which advances geometric mechanics to study body-leg coordination in sprawled posture quadrupedal locomotion, and
- Chapter 4, which applies geometric mechanics to study the lizard terrestrial swimming in the context of lizard limblessness, and
- Chapter 5, which uses geometric mechanics to study body-leg coordination in the general multi-legged locomotor, and
- Chapter 6, which advances geometric mechanics to study the slipping in multi-legged locomotors.

- Chapter 7, which takes inspiration from information theory to illustrate the sufficiency of using redundant legs to counter terrain roughness.

The 3-link swimmer is one of the simplest systems that can generate self-propulsion. In biological systems, swimmers can have many more internal degrees of freedoms [46]. In Chapter 2, we will advance concepts and tools within geometric mechanics to study limbless locomotion. From principal component analysis (PCA) of forward motion in diverse biological limbless locomotors, we show that the essence of limbless locomotion can be reduced to a two-dimensional configuration space. Aided by this low dimensional representation, we can numerically calculate the height functions. Interestingly, parameters governing the animals' chosen amplitude (of undulatory wave) nearly maximize the forward speed according to our geometric analysis, which indicates that the animals are controlling their self-deformation patterns to achieve near-optimal locomotor performance.

Although mathematically elegant, the use of geometric methods presumes idealized constant contact between the system and the environment. In reality, many biological limbless locomotors are observed to lift a portion of their body, and therefore periodically make and break contacts during locomotion [45]. In Chapter 2, we further introduce the concept of contact function to couple the body-environment contact to shape space. With a proper contact function [16], we can use geometric mechanics to explain a variety of limbless locomotion behaviors, from straight sidewinding, to gradual differential turns, and to sharp differential turns. Furthermore, using robot experiments, we show that the modulation of contact function can lead to novel behaviors such as stable in-place turning. Towards the end of Chapter 2, we will also discuss using geometric mechanics to design contact patterns.

However, geometric mechanics has been mainly limited to study limbless locomotion [83]. Legged animals, and increasingly robots, can use limbs to propel themselves to maneuver across a variety of terrains [18, 19, 22, 23, 4]. In addition to these appendages, undulatory body motions can also contribute to locomotor propulsion, even when not di-

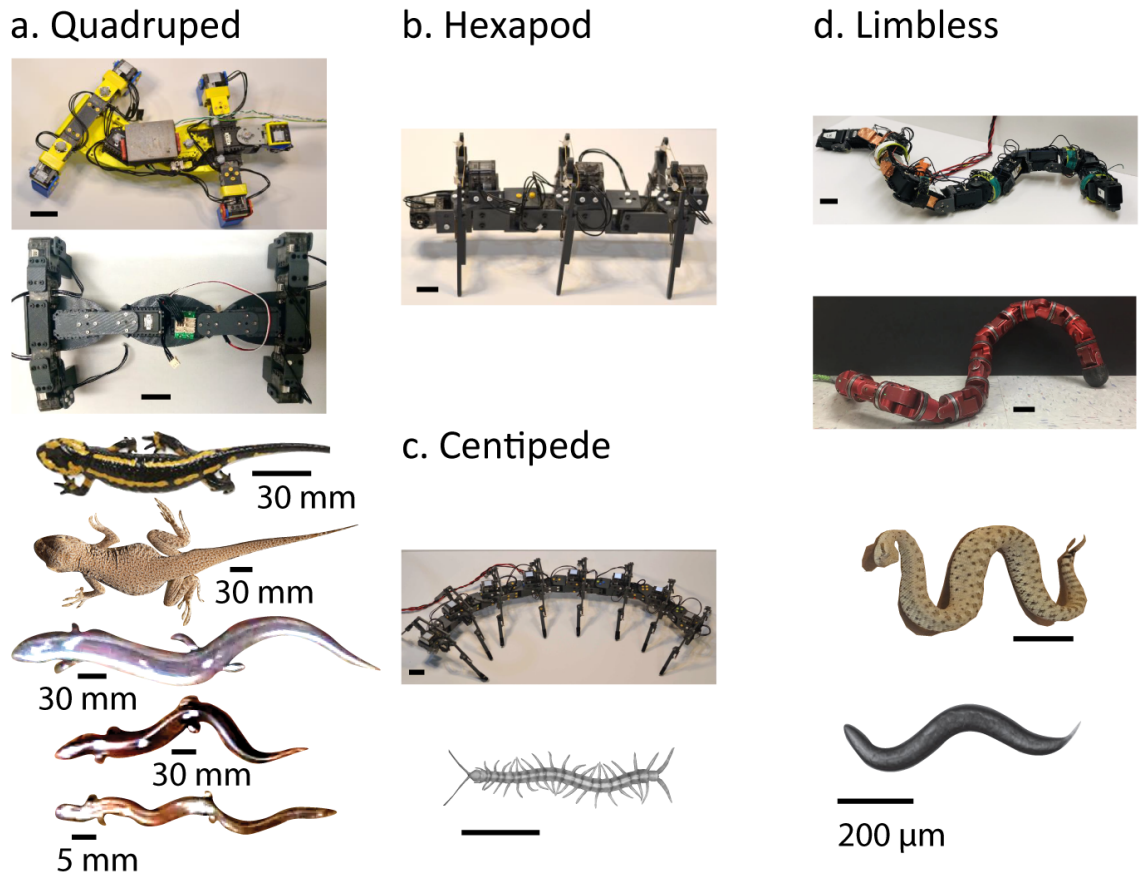


Figure 1.7: **Robotic and biological systems studied in this thesis** (a) Body-leg coordination in quadrupedal systems. Two robots were studied: a quadrupedal robot with a single DoF body bending joint and an elongate quadrupedal robot with two DoF body bending joint. We studied five quadrupedal animals: (from top to bottom) *Salamandra salamandra*, *Uma scoparia*, *Brachymeles kadwa*, *Brachymeles taylori*, and *Brachymeles muntingkamay*. (b) Body-leg coordination in hexapodal systems. We studied the body-leg coordination of hexapod robot. (c) Body-leg coordination in centipede systems. We studied a centipede robot with 8 pairs of legs and the biological centipede (*Scolopendra polymorpha*). (d) The undulatory motion in limbless locomotors. We studied limbless locomotors in macroscopic scale (*Crotalus cerastes*) and in microscopic scale (*Caenorhabditis elegans*) and use robots to test our analysis. Scale bars are 5 cm unless otherwise labelled.

rectly in contact with the environment. For example, salamanders [84, 66, 85, 86], lizards [87], and some mammals [88] use lateral body undulation in coordination with their legs for effective locomotion. While previous studies have elucidated the benefits of using lateral body undulation in conjunction with quadrupedal limb motion for individual tasks such as walking, running, or turning [66, 85, 35, 88], no general framework yet exists to system-

atically explore coordination and performance in quadrupedal systems that employ body undulatory motion, or more specifically back bending. The challenge lies in the fact that it requires not only coordinating many degrees of freedom (DoF), but also coordinating different types of DoF (i.e., body bending and the leg movements) in different types of behaviors (i.e., forward, turning and sideways motion).

To address these challenges, we require a dimensionality reduction scheme to prescribe the complicated quadrupedal behaviors. One method used over the last century to understand legged locomotion is a gait classification scheme called “Hildebrand diagrams”. Hildebrand [17] developed schemes to study symmetric gaits⁴ observed in quadrupedal animals (e.g., horses). These gaits have two key variables: *duty factor*, the fraction of a period that each leg is on the ground over a full gait cycle, and *lateral phase lag*, the fraction of a period that the hind leg leads the foreleg on the same side. Both key variables are modulated in response to speed changes in biological systems [89, 90, 91]. Using these gait principles as a reference, a multitude of algorithms have been developed for quadrupedal robot locomotion, or to explain why living quadrupeds choose certain gaits [92, 25, 39, 93, 94, 95].

In Chapter 3, we prescribe the leg contact states by their phase according to Hildebrand analysis [17, 96, 97, 89, 98]; this phase, together with the body-bending angle, forms the shape space, in which we can apply geometric mechanics tools. We demonstrate that proper body undulation, obtained from geometric mechanics, can improve the locomotion performance of our quadrupedal robots in forward, rotational and lateral directions. Furthermore, experimental data collected from Fire salamanders (*Salamandra salamandra*) reveal that our geometric-based approach closely predicts motion observed in this biological system.

Note that we only consider a single DoF body bending in Chapter 3, partially because the animals of interests (salamanders and lizards) are stereotyped to have short bodies and thus use one DoF standing-wave body bending. However, lizards and salamanders have

⁴In symmetric gaits, the contralateral (left and right pair) of legs are 180° out of phase.

evolved diverse body plans including elongate trunks with tiny limbs which are hypothesized to aid locomotion in cluttered/fossorial environments [99, 100, 101, 99].

Such transitions in body morphology are just one of many aspects of evolutionary adaptations for cluttered or fossorial habitats. Another crucial but less studied aspect in such adaptation is how animals can use these diverse morphologies during locomotion. In Chapter 4, we will investigate the role of body movements for a spectrum of lizard morphologies in field and laboratory environments. In particular, we will show that there is a diversity of body movements in lizards, exhibiting a linear combination of standing wave body bending and traveling wave body undulation. Species with more elongate bodies and reduced limbs used a greater ratio of traveling wave. The fact that these animals move in highly damped environments, where frictional forces dominate over inertial forces, allows the use of the geometric mechanics framework to explain body wave dynamics and body-limb coordination. The geometric mechanics theory rationalizes the advantage of using traveling waves in short limbed elongate lizards, and predicts that such advantages emerge when the primary thrust generation source shifts from the limbs to the body. We will illustrate the verification of our hypothesis by numerical/biological/robophysical experiments. In this way, our geometric analysis not only establishes a relationship between what they have (the body morphology) and how they move (the body-limb coordination) [32, 102, 103, 104], but also facilitates our understanding of the locomotion implications of the evolution of snake-like forms [105, 106].

So far, the power of Hildebrand analysis and therefore the application of geometric mechanics were limited to systems with up to 4 appendages. For multi-legged locomotors, there is a lack of a systematic gait description framework that allows us to modulate the balance between locomotion metrics such as speed and stability. In multi-legged animals and increasingly in robots, appendages that make direct contact with substrates are not the sole contributor to locomotion. As discussed earlier, undulatory body motions play an important role in generating propulsive forces in many systems [88, 87, 84, 43]. We aim to use

geometric mechanics to investigate the role of body undulatory motion in the general multi-legged locomotors. However, geometric mechanics has limitations. In particular, it is not directly applicable to systems with a large number of appendages. Furthermore, despite some recent efforts [83, 107], application of geometric mechanics in frictional environments (e.g., rate-independent isotropic Coulomb dry friction) has not been systematically studied. In Chapter 5, we develop dimensionality reduction and physical modelling methods and we use geometric mechanics to design gaits for serially connected multi-legged robots.

We integrate extended Hildebrand analysis with tools from geometric mechanics to develop locomotion control schemes for multi-legged locomotors. Our analysis reveals empirical rules to balance the trade-off between speed and static stability, and the potential benefit of body undulation in multi-legged robot locomotion. In this way, our framework offers the potential to modulate gaits for different tasks by switching between fast gaits and stable gaits. Further, we show that our scheme can generate control hypotheses for diverse living systems including salamanders and centipedes, thereby offering new insights on the functional role of body-leg coordination from a biomechanical and robophysical perspective.

Centipede robots serve as alternative agile robots to quadrupedal and bipedal robots. However, up to this point, our analysis of centipede robots was limited to low-speed quasi-static locomotion. In geometric mechanics framework, one of the major assumptions is that the inertia is negligible compared to frictional forces. In other words, we assume that there is no acceleration (instantaneous force and torque balance) throughout the course of locomotion. Prior work showed that in viscous environment, because of the negative linearity between velocity and reaction force, viscous swimming can converge to quasi-static locomotion even when operated at high speed [108, 109, 110]. However, in frictional environment (rate-independent Coulomb friction), it is controversial whether the assumption of geometric locomotion still holds.

In Chapter 6, we investigate the terradynamics of multi-legged locomotors on rigid hard terrains. From robophysical experiments, we will show that the multi-legged locomotion has a property of geometric locomotion (the effect of inertia is negligible) even when operated at high frequency on a low-friction substrate. We use resistive force theory to study the slipping and ground reaction forces in multi-legged systems and propose a new principle of effective viscous friction. Specifically, by periodic lifting and landing of body appendages, the nonlinear and isotropic Coulomb friction experienced on each limb can be simplified into a velocity-dependent whole-body drag, similar to that of organisms at low Reynolds number. This effective viscous friction can then allow us to use geometric mechanics to analyze centipede locomotion without the concern of inertial effects. Similar to our study in intermediate lizards, centipedes also have two self-propulsion mechanisms: body undulation and leg retraction. In an effort to unify the body-driven and leg-driven mechanism, we establish a performance space, and discuss the relative advantage (i.e., higher speed and less sensitivity to obstacle-rich environments) of body-driven over leg-driven centipede locomotion by robophysical experiments. Finally, we use our scheme to analyze the locomotion of a biological multi-legged system. Similar to our predictions on robophysical experiments, we observe a smooth gait transition from leg-dominated to body-dominated locomotion as speed increases.

In Chapter 6, we notice that myriapod robots with up to 16 legs demonstrate remarkable progress towards robust open-loop operations in diverse environments. It is different from state-of-the-art legged robots (mostly bipedal and quadrupedal systems), whose increasingly agile locomotive performance relies heavily on accurate sensors and properly designed control frameworks [3, 111]. However, it remains unclear what mechanism drives such robustness and, more importantly, whether redundancy in leg numbers can be generally sufficient to counter the terrain noise for self-propulsion.

During the last century, Shannon predicted that signals could be reliably transmitted over noisy channels based on digital redundant coding in the form of binary bit se-

quences [112]. Such prediction has become increasingly critical in modern communication. Inspired by the principles which facilitate signal transmission on noisy channels, we hypothesize that there exist general principles of matter transportation by which, for a complex terradynamic task, we can “guarantee” that multi-legged robots can self-transport over distance with error rate (e.g., loss of stability or thrust deficiency) arbitrarily close to zero, even without environmental awareness. The key idea is to digitize thrust-generation via basic active contacts. In Chapter 7, from theory and experimental analysis, we demonstrate that appropriate gait design can facilitate reliable transport of multi-legged systems on laboratory and field rugose terrains without the need for complex sensing/control. We hypothesize that the analogy between signal and matter transportation can accelerate development of devices with mobility approaching that of living systems.

CHAPTER 2

GEOMETRIC MECHANICS AND ITS APPLICATION IN LIMBLESS LOCOMOTION

In this chapter, we will extend the geometric mechanics to study the general limbless locomotion. Specifically, we will use basis function to describe the locomotion of N-link swimmer. Further, we will illustrate that, by properly coupling the contact function, we can increase the maneuverability of limbless locomotors, and enable behaviors including sidewinding, steering, and in-place turning. Then, we will introduce a geometric mechanics framework to design the contact function. Finally, we will briefly discuss the use of geometric mechanics in heterogeneous environments (obstacle-aided locomotion).

Part of this chapter is adapted from an arXiv preprint¹, two peer reviewed conference papers^{2 3}, a journal article⁴, and a journal article under review⁵.

Note that the core of this chapter is based on the mathematical tool of geometric mechanics. We provide a concise overview of the geometric tools needed for this chapter below:

¹“Geometric phase predicts locomotion performance in undulating living systems across scales” (1906.11374)

²“Geometric motion planning for systems with toroidal and cylindrical shape spaces.” Dynamic Systems and Control Conference. Vol. 51913

³“Optimizing coordinate choice for locomotion systems with toroidal shape spaces.” 2020 IEEE/RSJ International Conference on Intelligent Robots and Systems

⁴“Frequency modulation of body waves to improve performance of sidewinding robots.” The International Journal of Robotics Research 40.12-14 (2021): 1547-1562

⁵“Optimizing contact patterns for robot locomotion via geometric mechanics” The International Journal of Robotics Research

2.1 Introduction to geometric mechanics

2.1.1 Three link swimmer in viscous environment

In this section, we will briefly introduce geometric mechanics and its applications. Note that most content in this section is adapted from prior works [75]. Specifically, we will introduce the concepts of the shape space, the local connection and the height function using 3-link-swimmer locomotion as an example.

2.1.2 Shape space

Consider a planar three link swimmer (Figure 2.1). The configuration (position and orientation) of each link (with respect to the world reference frame) can then be characterized by $g_i = [x_i, y_i, \theta_i]$. The configuration of a three link swimmer is then the collection of positions and orientation in each link⁶: $\{g_i, i = \{1, 2, 3\}\}$ (Figure 2.1a).

Each module is connected by a rotational joint. Thus, one can relate the configuration of a link g_i to the next link g_{i+1} by:

$$\begin{bmatrix} \cos(\theta_{i+1}) & -\sin(\theta_{i+1}) & x_{i+1} \\ \sin(\theta_{i+1}) & \cos(\theta_{i+1}) & y_{i+1} \\ 0 & 0 & 1 \end{bmatrix} = \begin{bmatrix} \cos(\theta_i) & -\sin(\theta_i) & x_i \\ \sin(\theta_i) & \cos(\theta_i) & y_i \\ 0 & 0 & 1 \end{bmatrix} DR(\alpha_i)D \quad (2.1)$$

where

$$D = \begin{bmatrix} 1 & 0 & L/2 \\ 0 & 1 & 0 \\ 0 & 0 & 1 \end{bmatrix}, \quad R(\alpha) = \begin{bmatrix} \cos(\alpha) & -\sin(\alpha) & x_i \\ \sin(\alpha) & \cos(\alpha) & y_i \\ 0 & 0 & 1 \end{bmatrix};$$

L is the length of a link, and α_i is the joint angle between two links. Because of Equation 2.1, there are only 5 independent variables in the configuration of a three link swim-

⁶Each link is considered as a rigid body

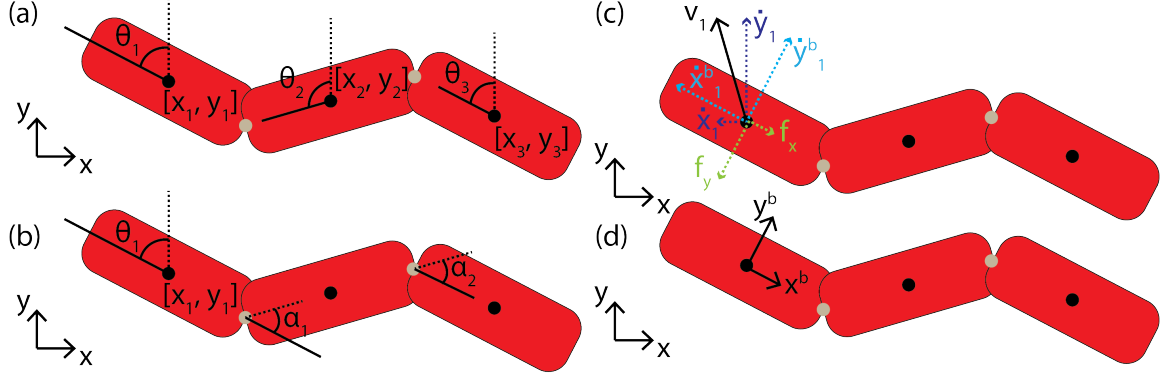


Figure 2.1: **Geometry of 3-link swimmer** (a) The position and orientation of each link. (b) The position of the first link and the joint angles. (c) Spatial velocity, body velocities, and the viscous friction. (d) Body reference frame.

mer, $\{[x_i, y_i, \theta_i], i = \{1, 2, 3\}\}$: the position and orientation of the first link⁷ (g_1), and the joint angles ($[\alpha_1, \alpha_2]$) (Figure 2.1b). Geometric mechanics separates these independent variables into two groups, the position variable (g_1) and the shape variable ($\alpha = [\alpha_1, \alpha_2]$). The former determines the relative position of the 3-link swimmer with respect to the world reference frame, and the latter determines the internal shape of the locomotor. The shape space is then defined as the collection of all possible shape variables.

2.1.3 Spatial velocity and body velocity

Consider the position and orientation of each link being time-dependent

$$g_i(t) = [x_i(t), y_i(t), \theta_i(t)],$$

which indicates that there is a velocity associated with each link. Naturally, the velocity is considered with respect to the world reference frame. The spatial velocity is defined as $\dot{g}_i(t) = [\dot{x}_i(t), \dot{y}_i(t), \dot{\theta}_i(t)]$, meaning the velocity of each link expressed in the world reference frame (Figure 2.1c). From definition, one can relate the spatial velocity to instantaneous position changes by:

⁷As suggested by Equation 2.1, the information of position variables of the first link is equivalent to that of the second link, third link, or any arbitrary chosen body reference frame.

$$\begin{bmatrix} x_i(t + dt) \\ y_i(t + dt) \\ \theta_i(t + dt) \end{bmatrix} = \begin{bmatrix} x_i(t) \\ y_i(t) \\ \theta_i(t) \end{bmatrix} + \begin{bmatrix} \dot{x}_i(t) \\ \dot{y}_i(t) \\ \dot{\theta}_i(t) \end{bmatrix} dt \quad (2.2)$$

The instantaneous velocity profile of the 3-link swimmer is defined as the collection of spatial velocities of all links: $\{\dot{g}_i(t), i = \{1, 2, 3\}\}$. From geometry, $\dot{g}_i(t)$, the spatial velocity of link i , can be separated into two components: the spatial velocity of the first link ($\dot{g}_1(t)$), and the relative velocity from link i to the first link (v_{1i}). The relative velocity v_{1i} is then invariant to the choices of world reference frame, thus is only dependent on the shape variable (α) and shape velocities ($\dot{\alpha}$):

$$\dot{g}_i(t) = \dot{g}_1(t) + J(\alpha)\dot{\alpha}. \quad (2.3)$$

where J is the spatial Jacobian matrix⁸ [113]. Given Equation 2.3, there are only 7 independent variables of velocity profiles: the spatial velocity of the first link, $\dot{g}_1(t)$, the shape variables, α , and the shape velocity $\dot{\alpha}$.

In addition to spatial velocity, it is also important to analyze the velocity in the body reference frame. The body reference frame of a link is defined from the position and orientation of the link (Figure 2.1d). The body velocity is then defined as the projection of spatial velocity into the body frame: $\dot{g}_i^b(t) = [x_i^b(t), y_i^b(t), \dot{\theta}_i^b(t)]$ (Figure 2.1c). Note that angular velocity is invariant to frame transformation: $\dot{\theta}_i^b(t) = \dot{\theta}_i(t)$. Similar to Equation 2.2, the one can also calculate the instantaneous changes in configuration of a link from its body velocity. However, because of the reference frame transformation, the simple linear formula in Equation 2.2 becomes:

⁸Jacobian matrix provides the relation between angular velocities of joints to link velocities

$$\begin{aligned}
& \begin{bmatrix} \cos(\theta_i(t+dt)) & -\sin(\theta_i(t+dt)) & x_i(t+dt) \\ \sin(\theta_i(t+dt)) & \cos(\theta_i(t+dt)) & y_i(t+dt) \\ 0 & 0 & 1 \end{bmatrix} \\
& = \begin{bmatrix} \cos(\theta_i(t)) & -\sin(\theta_i(t)) & x_i(t) \\ \sin(\theta_i(t)) & \cos(\theta_i(t)) & y_i(t) \\ 0 & 0 & 1 \end{bmatrix} \exp\left(\begin{bmatrix} 0 & -\dot{\theta}_i^b(t) & \dot{x}_i^b(t) \\ \dot{\theta}_i^b(t) & 0 & \dot{y}_i^b(t) \\ 0 & 0 & 0 \end{bmatrix} dt\right) \quad (2.4)
\end{aligned}$$

2.1.4 Force and torque balance

Consider a viscous environment where the frictional force is linearly related to the body velocity:

$$\begin{bmatrix} f_x \\ f_y \end{bmatrix} = \begin{bmatrix} \gamma_x & 0 \\ 0 & \gamma_y \end{bmatrix} \begin{bmatrix} \dot{x}_i^b \\ \dot{y}_i^b \end{bmatrix}, \quad (2.5)$$

where γ_x and γ_y are frictional coefficient in parallel and perpendicular directions respectively (Figure 2.1c). Consider the environment to be isotropic if $\gamma_x = \gamma_y$, where translational locomotion can be challenging [114, 115]. The essential physical property for locomotors to translate in viscous fluid is the drag anisotropy: $\gamma_x > \gamma_y$ [115]. In the analysis in this section, we will assume $\gamma_x = 2\gamma_y$ unless otherwise stated, because it is a reasonable approximation in low Reynolds number system [116, 117].

In quasi-static motion, there is no net force and torque (thus no linear and angular acceleration) acting on the center of mass throughout the course of locomotion. In other words, there are three equality constraints in the equation of motion: the force balance in x direction and in y direction, and the torque balance. From force and torque balance, one can numerically calculate the body velocity of the first link (3 independent variables) from the shape variable α and the shape velocity $\dot{\alpha}$:

$$\begin{bmatrix} \dot{x}_1^b \\ \dot{y}_1^b \\ \dot{\theta}_1^b \end{bmatrix} = h(\alpha, \dot{\alpha}) = h_\alpha(\dot{\alpha}) \quad (2.6)$$

2.1.5 Linearity

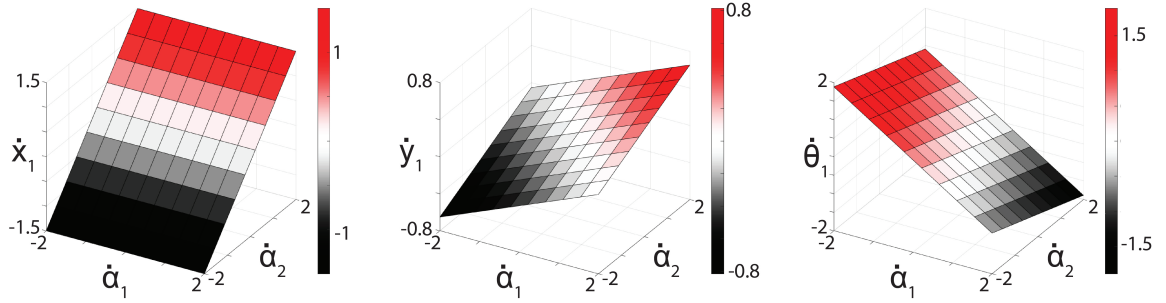


Figure 2.2: **Visualization of $h_\alpha(\dot{\alpha})$:** Relationship between body velocities (\dot{x}_1 (left), \dot{y}_1 (mid), and $\dot{\theta}_1$ (right)) and shape velocities ($\dot{\alpha}_1$ and $\dot{\alpha}_2$).

In Equation 2.6, one can obtain a function relating the shape variable and shape velocity to the body velocity. With fixed shape variable $\alpha = [-0.85, -1.14]$, the relationship between the body velocity \dot{g}_1^b and the shape velocity $\dot{\alpha}$ is plotted. From Figure 2.2, one can notice that function between \dot{g}_1^b and $\dot{\alpha}$ is linear:

$$\begin{bmatrix} \dot{x}_1^b \\ \dot{y}_1^b \\ \dot{\theta}_1^b \end{bmatrix} = A(\alpha)\dot{\alpha}, \quad (2.7)$$

where $A(\alpha) \in \mathbb{R}^{3 \times 2}$ is called the local connection matrix. Each row of the connection matrix can be viewed as a vector field in the shape space. In Figure 2.3b, the local connection matrix is displayed in the x (forward, first row of $A(\alpha)$), y (lateral, second row of $A(\alpha)$), and θ (rotational, third row of $A(\alpha)$) directions, respectively.

2.1.6 Gait in the shape space

A gait is a periodic sequence of shape changes. In geometric mechanics framework, a gait can be viewed as a simple closed curve in \mathbb{R}^2 in the shape space. An example of a gait is shown in Figure 2.3a. During locomotion, a periodic change in shape variables (implementation of a gait) can lead to net translation in world reference frame. One then seek to predict the net displacement that results from one period of the gait.

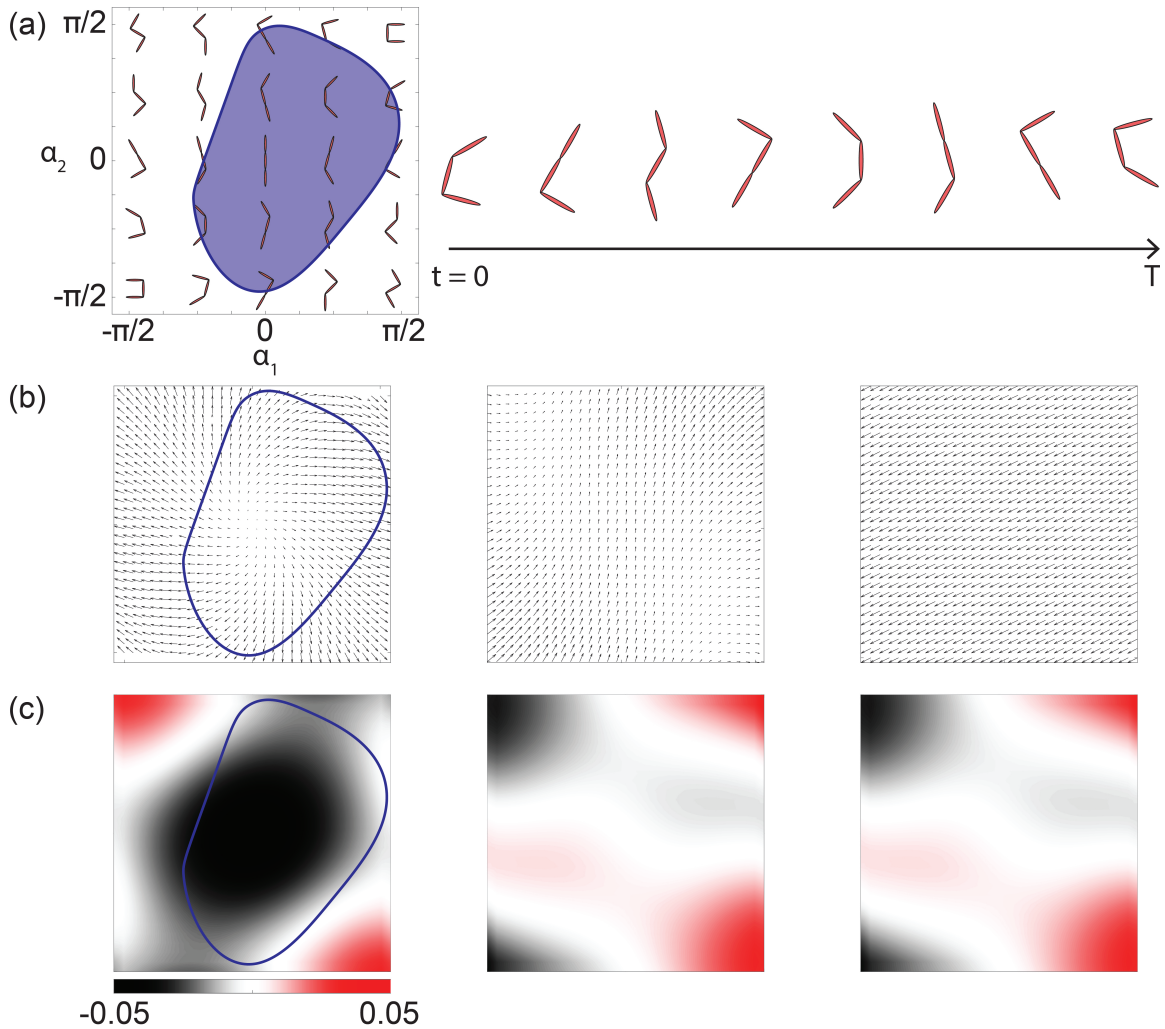


Figure 2.3: **Shape space, vector field, and height function** (a) The shape space of 3-link swimmer and an example gait. (b) The vector field and height functions in forward (left), lateral (mid), and rotational directions.

Unfortunately, the nonlinearity in Equation 2.4 makes such predictions complicated and

computationally expensive. To simplify the problem, the spatial velocity can be approximated by body velocity. In other words:

$$\begin{aligned} \begin{bmatrix} x_i(t+dt) \\ y_i(t+dt) \\ \theta_i(t+dt) \end{bmatrix} &\approx \begin{bmatrix} x_i(t) \\ y_i(t) \\ \theta_i(t) \end{bmatrix} + \begin{bmatrix} \dot{x}_i^b(t) \\ \dot{y}_i^b(t) \\ \dot{\theta}_i^b(t) \end{bmatrix} dt \\ &= \begin{bmatrix} x_i(t) \\ y_i(t) \\ \theta_i(t) \end{bmatrix} + A(\alpha)\dot{\alpha} \end{aligned} \quad (2.8)$$

Given Equation 2.8, the displacement from a gait ($\partial\phi$) can then be formulated as a line integral along the vector field:

$$\begin{bmatrix} \delta x_i \\ \delta y_i \\ \delta \theta_i \end{bmatrix} \approx \int_{\partial\phi} A(\alpha)\dot{\alpha}. \quad (2.9)$$

According to Stokes' theorem, the line integral of a vector field over a loop is equal to the surface integral of its curl through an enclosing surface:

$$\begin{bmatrix} \delta x_i \\ \delta y_i \\ \delta \theta_i \end{bmatrix} \approx \iint_{\phi} \nabla \times A(\alpha) d\alpha, \quad (2.10)$$

where ϕ is the area bounded by the gait $\partial\phi$, and $\nabla \times A(\alpha)$ is then called the height function. Therefore, one can directly use the height function to estimate the net displacement resulted from one period of gait cycle.

2.1.7 Minimal Perturbation Coordinate

Height functions, discussed in subsection 2.1.6, offer an intuitive and visual tool to analyze the locomotion. However, one of major assumptions in the analysis is to approximate the

complicated nonlinear equation (Equation 2.4) by a linear equation (Equation 2.8). In this section, we will show that the accuracy of this approximation and illustrate a framework to optimize the accuracy of the approximation.

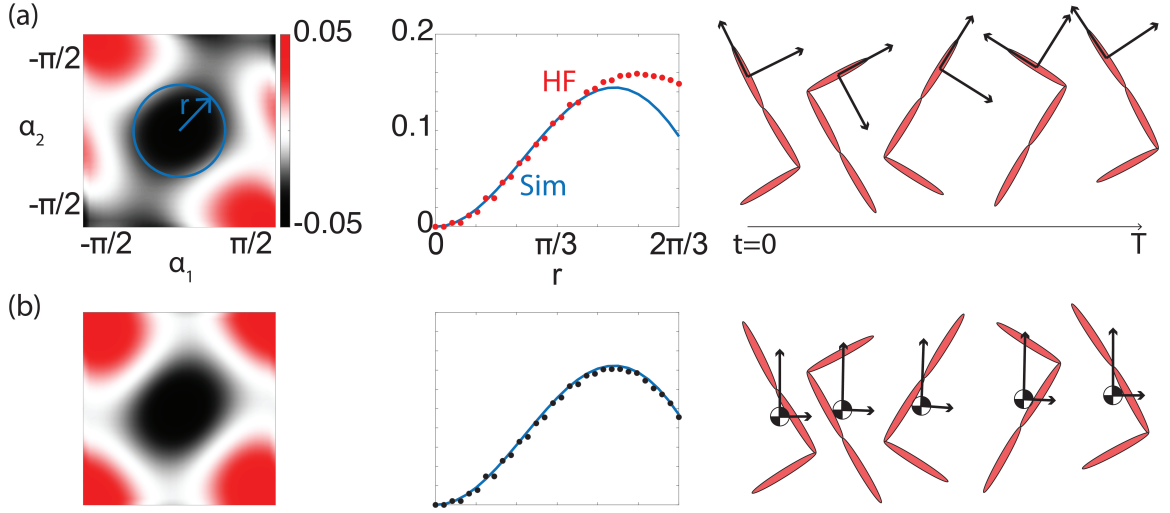


Figure 2.4: **The importance of choices in body reference frame** (Left) Forward height function computed with (a) first link and (b) center of mass as body reference frame. (Mid) The comparison between surface integral and numerical computation of circular gaits under different amplitudes. (Right) The illustration of rotational oscillation of body reference frame during the course of a gait period.

Consider predicting the optimal amplitudes for circular gaits that can lead to highest forward displacements. In circular gaits, the gait path follows the following trajectories:

$$\partial\phi(r) = \{[\alpha_1, \alpha_2] \mid \alpha_1 = r \sin(\tau), \alpha_2 = r \cos(\tau), \tau \in [0, 2\pi)\}, \quad (2.11)$$

where r is the amplitude of the gait path and τ is the phase of the gait trajectory. As shown in Figure 2.4, one can numerically calculate displacement (per gait cycle) of different amplitudes using the nonlinear equation Equation 2.4, and then compared it to the surface integral over the height function. Surprisingly, one can only obtain accurate predictions at low amplitude regime (Fig.Figure 2.4).

In Equation 2.8, the spatial velocity is approximated by body velocity. In other words,

the line integral in Equation 2.9 can only give us the integral of forward, lateral, and rotational velocity in the body reference frame instead of the net displacement (in world reference frame).

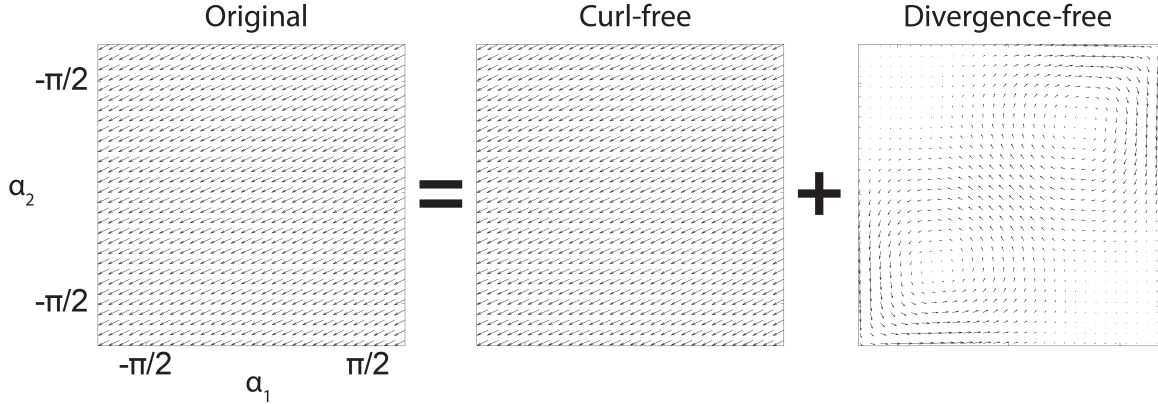


Figure 2.5: **Hodge-Helmholtz decomposition of rotational vector field** (Left) The original rotational vector field with first link as the body reference frame. (Mid) The curl-free component of the original rotational vector field. (Right) The divergence-free component of the original rotational vector field.

To better understand the approximation, we take the parallel parking car as an example. The body velocity of a car has constantly zero lateral velocity: $\dot{y}^b = 0$. However, with proper combination of the forward and rotational velocities, it is possible to have lateral translation in the world reference frame. More formally, the sequenced combination of rotational body velocity and forward velocity can cause translation in lateral direction; and similarly the sequenced combination of rotational body velocity and lateral velocity can cause translation in forward direction. In other literature, such effect is called the *Lie bracket effect* [118].

In an effort to minimize the Lie bracket effect, one should aim to minimize the net rotational oscillation throughout the gait. Notably, the choice of body reference frame can have a significant effect on the magnitude of rotational oscillation. Figure 2.4a illustrates that while the first frame experienced significant rotation throughout the gait, the body reference frame of CoM (center of mass) has almost a steady orientation (Figure 2.4b).

The body reference frame is defined as:

$$g_{com} = \frac{1}{3} \sum_{i=1}^3 g_i \quad (2.12)$$

Thus, in prior work [118], it is posited that by properly choosing the body reference frame, one can minimize the rotational oscillation and improve the accuracy of the linear approximation in Equation 2.4. To identify the optimal body reference frame, prior work investigated the vector field in the rotational direction. The rotational vector field can be vastly different depending on the choice of body reference frame. The rotational height function, however, is invariant to the choices of body reference frame because the rotational body velocity is identical to the rotational spatial velocity, $\dot{\theta}_i(t) = \dot{\theta}_i^b(t)$, as discussed earlier. In other words, the rotational vector field obtained from different body reference frames has the same curl; and the difference between rotational vector fields is curl-free.

To minimize the rotational oscillation throughout the gait, any addition of curl-free vector field will only contribute to higher rotational oscillation. In this way, one can find the optimal body reference frame by removing the curl-free component of the rotational vector field. Hodge-Helmholtz decomposition [119] is used to to remove the curl-free component of the vector field and then use it to identify the optimal body reference frame (Figure 2.5).

The height functions obtained in the original body reference frame and the optimal reference frame are compared in Figure 2.4. Surprisingly, the optimal reference frame can give us accurate predictions on displacement across different amplitudes, which then allows us to analyze gait with reasonable amplitudes and effective locomotion performance.

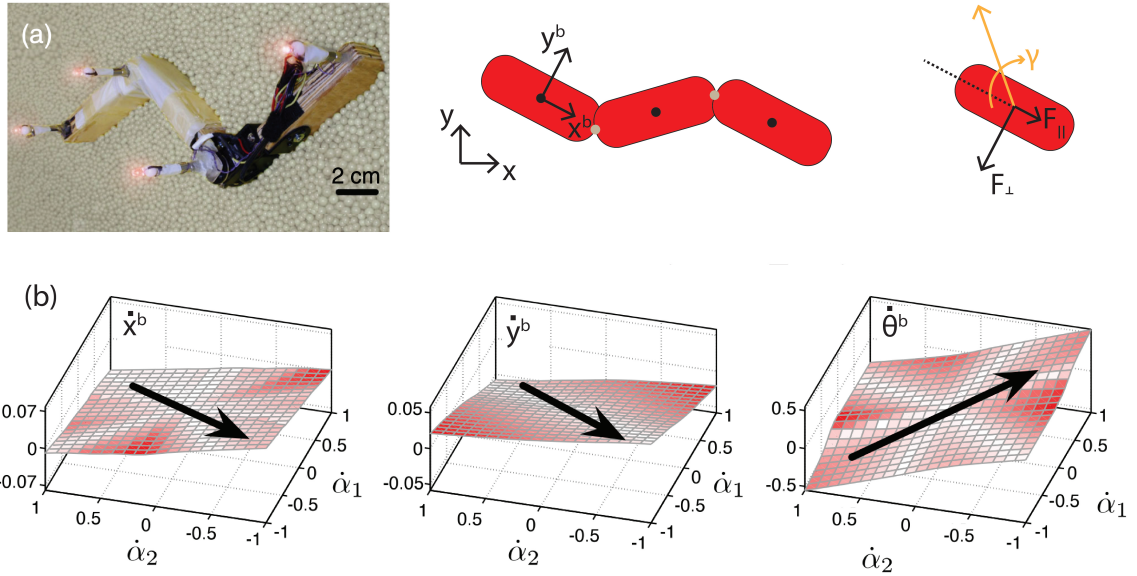


Figure 2.6: **3-link swimmers in granular media (adapted from [75])** (a) (left) The robot resting on a granular medium, a bed of plastic spheres. (Mid) Analytical three-link model. The reaction force from the granular media (F_{\perp} and F_{\parallel}) and the attack angle (γ) are labelled. (b) The visualization of $h_{\alpha}(\dot{\alpha})$ in Equation 2.15. The body velocities are almost linear functions of the shape velocity.

2.2 Three link swimmer in granular media

2.2.1 Ground reaction force in granular media

While the geometric analysis of 3-link swimmer in viscous fluid is elegant, it has limited real-world applications. Specifically, the ground reaction force is often much more complicated than the linear relationship as in Equation 2.5. In this section, we will introduce the granular resistive force (RFT) theory and extend geometric mechanics to study the locomotion of a three-link swimmer in granular media. Note that most content in this section is adapted from prior works [75].

RFT [120, 72, 121] assumes that environmental disturbances induced by the movement of a single body segment are highly localized, therefore decoupled from interactions with neighboring body segments. Prior work showed that granular RFT can successfully describe movement in highly-dissipative dry granular environments [72, 121, 122]. In particular, RFT assumes that a swimmer can be divided into different segments (in this example,

the three links in the 3-link swimmer) that can be analyzed independently. Similar to Equation 2.5, the reaction force on a link can be decomposed to \mathbf{F}_\perp and \mathbf{F}_\parallel , acting perpendicular and parallel to the surface of the link respectively (Figure 2.6a). The reaction forces are then determined from experimental measurements as a function of the attack angle γ , the angle between the direction of movement and the link orientation. For example, on 6 mm diameter spherical glass beads, the following empirical functions are used to approximate \mathbf{F}_\perp and \mathbf{F}_\parallel :

$$\begin{aligned}\mathbf{F}_\perp &= C_s \sin(\beta_0) \\ \mathbf{F}_\parallel &= C_F \cos \gamma + C_L(1 - \sin \gamma)\end{aligned}\tag{2.13}$$

where $\tan(\beta_0) = c \sin(\gamma)$, $C_s = 3.21$, $C_F = 1.34$, $C_L = -0.82$, $c = 2.79$ are the empirically [123] fitted function to characterize the granular media resistive force.

2.2.2 Linearity

In highly-damped environments where inertial effects are negligible, the net force on a body is assumed to be zero at every moment in time, giving

$$\mathbf{F} = \sum_{i=1}^3 (\mathbf{F}_\perp^i + \mathbf{F}_\parallel^i) = 0.\tag{2.14}$$

Similar to analysis in subsection 2.1.4, one can numerically calculate the body velocities from shape variable and shape velocity:

$$\begin{bmatrix} \dot{x}_1^b \\ \dot{y}_1^b \\ \dot{\theta}_1^b \end{bmatrix} = h_\alpha(\dot{\alpha})\tag{2.15}$$

Figure 2.6b visually shows the shape of the function $h_\alpha(\dot{\alpha})$. To simplify the calculation,

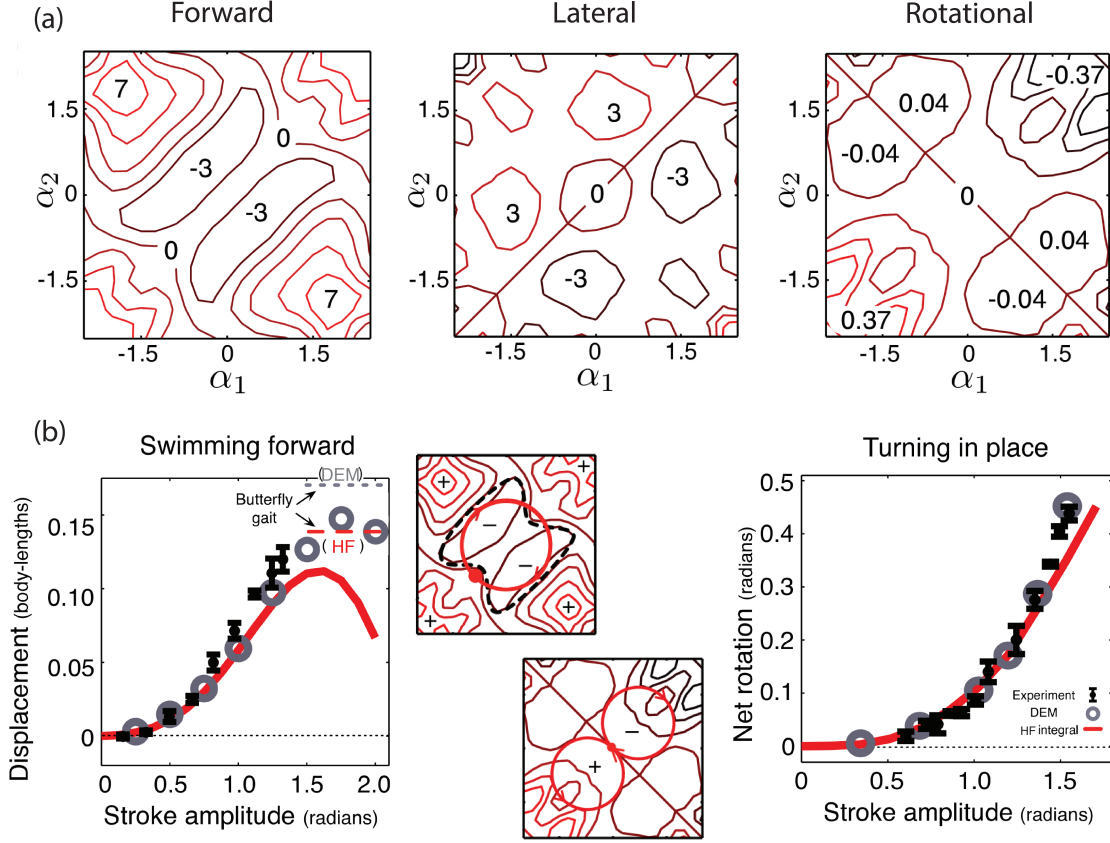


Figure 2.7: **Geometric mechanics analysis for three-link swimmer on granular media (adapted from [75])** (a) Height functions for the three-link swimmer in granular media. The units of the field values are $100 \times (\text{body-lengths})$ for forward and lateral height functions; $100 \times (\text{radian})$ for rotational height functions. (b) Predictions from geometric mechanics. (Left) Height function estimate of displacement compared to experimental and DEM results as a function of r . Dashed horizontal lines indicate displacements for the butterfly gait in DEM and resistive force theory. (Mid) Illustration of the butterfly gait and the figure-eight gait. (Right) Height function estimate of net rotation for figure-eight gait of different stroke amplitudes. Temporal frequency was 0.5 Hz in (left) and 0.17 Hz in (right)

it is assumed reasonable to approximate Equation 2.15 using a linear plane despite the nonlinear relationship between velocity and reaction forces:

$$\begin{bmatrix} \dot{x}_1^b \\ \dot{y}_1^b \\ \dot{\theta}_1^b \end{bmatrix} \approx A(\alpha)\dot{\alpha}, \quad (2.16)$$

where $A(\alpha) \in \mathbb{R}^{3 \times 2}$ is the local connection matrix which can be numerically approximated

by fitting a plane to Equation 2.15.

2.2.3 Predictions from height functions

Circular gaits for forward motion

Figure 2.7 shows the forward and rotational height functions. By visualizing gaits as paths in the shape space, the height functions provide an intuitive and visual overview of how gait patterns can cause net displacements. Similar to analysis in subsection 2.1.7, good agreement are observed between numerically calculated displacement and the surface integral from the height function. For low-amplitude circular gaits, the net forward displacement scales approximately quadratically with amplitude. At high amplitudes, the gait includes negative regions near the corners of the height functions, which reduces the area integral. These observations suggest the best forward locomotion performance occurs at intermediate amplitude.

To verify the theoretical predictions, robophysical experiments and DEM simulation were conducted [75]. Specifically, the robot (0.56 kg) consists of three wooden segments connected by two motors (Hitec, HSR 5980SG). The segments are covered by a thin latex sleeve giving the robot a body-particle coefficient of friction of 0.4. The robot is fully immersed in a large bed of $5.7 \pm 0.06\text{mm}$ diameter plastic beads. Robot locomotion is tracked using the lit masts at the ends of the links as markers. Each link of the robot has dimension: $5.4 \times 2.8 \times 14.7 \text{ cm}^3$. Details of DEM simulation can be found in [123]. Good agreements are observed between robot experiments, DEM, and theory, specially at low-amplitude regime.

Further, one can also identify the zero-height contour on the height function such that it will have the highest surface integral. The zero-height contour has the shape of a butterfly, thus it is referred to as the butterfly gait. As confirmed by DEM simulation, such butterfly gaits produce more displacement than any circular gaits.

Circular gaits for turning motion

The height functions can also bring insights to movements that are relatively less studied, such as turning in place. To design this gait, it requires zero surface integral in the forward height function and finite surface integral in rotational height function. From the symmetry of the height functions, it is posited that the figure-eight gait (Figure 2.7) can produce a net rotation by connecting two loops enclosing oppositely signed regions from opposite directions (therefore uni-direction contribution). The hypothesis was tested using robophysical experiments and DEM simulation.

2.3 N-link swimmer in granular media

The content in this section is adapted from a collaborative project with Dr. Jennifer M Rieser. My role in this section is to assist Dr. Jennifer M Rieser for the analysis.

2.3.1 Two modes in biological locomotors

Shape basis function

The 3-link swimmer is one of the simplest system that can generate self-propulsion. In biological systems, swimmers can have many more internal degrees of freedoms. Now we consider a general N -link swimmer. Similar to our analysis in the three-link swimmer, the shape variable of a N -link swimmer has $(N - 1)$ degrees of freedom (DoF). In the extreme case where the swimmer has continuous body ($N \rightarrow \infty$), we can represent the shape of the swimmer by its curvature: $\kappa(s)$, $s \in [0, 1]$, where $\kappa(s)$ is the curvature at position s , and s is the position along the body (Figure 2.8). In this way, we can consider the shape variable of the N -link swimmer as the discretization of $\kappa(s)$ into $N - 1$ curvatures.

Despite some recent efforts to extend geometric mechanics to higher dimensions [124, 125], the two dimensional shape space can offer more visual and intuitive insights than the higher dimensional shape spaces. For example, the visualization of curls as flux [125] in 3-

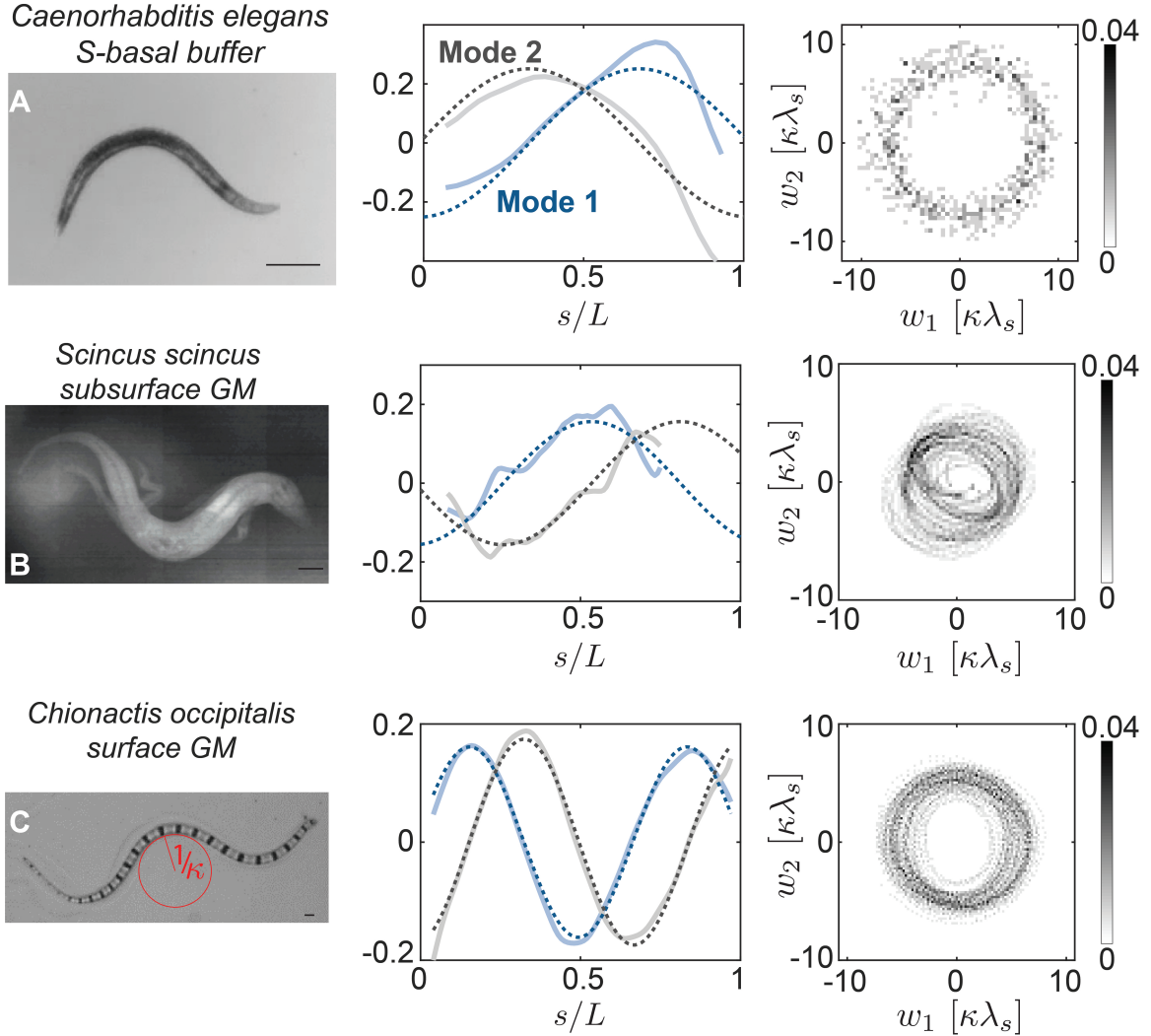


Figure 2.8: **Low dimensional representation of animal movement through sand.** (Left) Photos of (A) the nematode worm (*Caenorhabditis elegans*) in S-basal buffer (B) the sand-fish lizard (*Scincus scincus*) 7.6 cm below the surface of and fully immersed in 300- μm glass beads, and (C) *Chionactis occipitalis* moving on the surface of 300- μm glass beads. (Mid) Solid lines show the two dominant relative curvature ($\kappa\lambda_s$) PCA modes account for (A) 96.7%, (B) 94.7%, and (C) 79.7% of the variation in observed body configurations. Dashed lines show best fits to sin and cos functions (see text). (Right) 2D probability density map of projections of curvatures onto the two PCA modes with the largest eigenvalues. This figure is adapted from [83].

dimensional shape space can often be abstract and counter-intuitive to interpret in comparison to the height functions in 2-dimensional shape space. Thus we seek a dimensionality reduction framework for the general N -link swimmer.

Lateral undulation is one of the most commonly observed modes locomotion in these

swimmers. Previous studies of biological elongate locomotors revealed relatively simple wave patterns behind the seemingly complicated behaviors [46, 126]. For example, to describe the shapes during *C. elegans* locomotion, [46] used Principal Components Analysis (PCA) to identify a set of orthonormal basis functions. We refer to this set of orthonormal basis functions as the Principal Components (PCs). The time series of weights in PCs can be used to capture observed animal posture changes. For steady-state forward motion, Stephens et. al. [46] showed that it is sufficient to capture most of the shape changes using two PCs and the essence of forward motion could be represented in a two-dimensional space by projecting time series of body postures profiles onto these PCs. Inspired by the dimensionality reduction methods in *C. elegans*, we studied a variety of elongate swimmers (the sandfish lizard *Scincus scinus* [122], the shovel-nosed snake, *Chionactis occipitalis*, [122, 127], and the mm-scale locomotor *C. elegans*), and seek to represent the body shape changes using a low dimensional shape space.

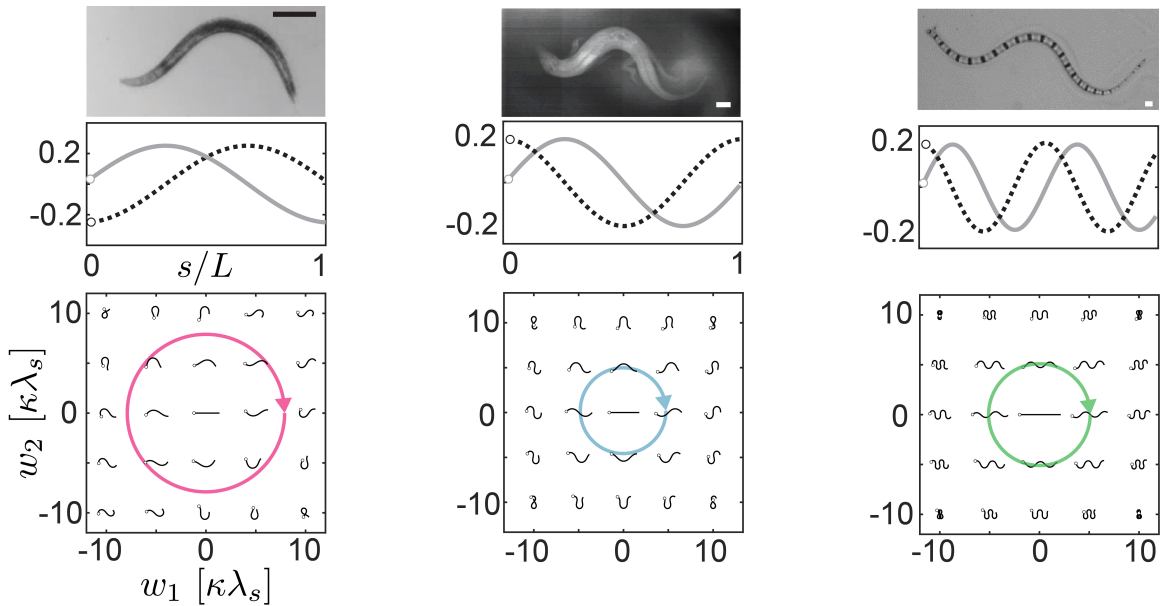


Figure 2.9: **Geometric mechanics of undulatory locomotors.** Columns show the dimensionality reduction for (A) the nematode (B) the sandfish, and (C) the shovelnose snake on the surface of sand. (Top) Dominant two modes of body curvatures determined from PCA. (Bottom) Space of shapes spanned by the two modes. The directed circle on each plot represents a particular gait. This figure is adapted from [83].

We apply PCA to the entire data set to identify an orthonormal set of curvature basis functions (Figure 2.8). We observe that two PCs capture most of the variation in the body postures of each species for the forward motion of lizards, snakes, and nematodes. Therefore, we can use the space spanned by the first two PCs as our two-dimensional representation for each animal.

Further, we find that the two dominant PCs in the lizards, snakes, and nematodes are well-fit by sinusoidal functions: $\kappa_1(s) = \sin(2\pi s/\lambda_s)$ and $\kappa_2(s) = \cos(2\pi s/\lambda_s)$, where λ_s is the wavelength of the PC. Within each two-dimensional shape space, the body postures are represented by a linear superposition of PCs:

$$\kappa(s, t) = w_1(t)\kappa_1(s) + w_2(t)\kappa_2(s). \quad (2.17)$$

We defined $w = [w_1, w_2]$ as the new shape variable. The new shape space is then defined as the collection of all feasible w . Notably, a circular path (centered at origin) in the new shape space can be prescribed as: $w_1 = w_m \cos \omega t$, $w_2 = w_m \sin \omega t$, where w_m is the amplitude of the wave, and ω is the temporal frequency. Combined with Equation 2.17, we have $\kappa(s, t) = w_m \sin(2\pi s/\lambda_s + \omega t)$, a standard traveling wave of body curvatures (Figure 2.9).

Linearity

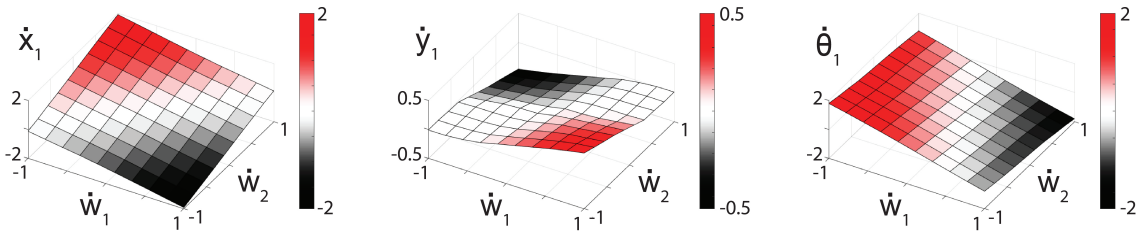


Figure 2.10: **Visualization of the connection plane $H_w(\dot{w})$** The body velocities are almost linear functions of the shape velocity, which allows us to approximate Equation 2.18 by Equation 2.19

From Equation 2.17, we can rewrite Equation 2.15 as:

$$\begin{bmatrix} \dot{x}_1^b \\ \dot{y}_1^b \\ \dot{\theta}_1^b \end{bmatrix} = h_w(\dot{w}). \quad (2.18)$$

Similar to our analysis in prior sections, we visualized $h_w(\dot{w})$ in Figure 2.10. The detailed force formula can be found in [83]. Interestingly, from the structure Figure 2.10, it is reasonable to assume the linearity in local connection matrix:

$$\begin{bmatrix} \dot{x}_1^b \\ \dot{y}_1^b \\ \dot{\theta}_1^b \end{bmatrix} = A(w)\dot{w}, \quad (2.19)$$

where $A(w)$ is the new local connection matrix.

Height function predictions

We show the height functions for lizards, snakes, and nematodes in Figure 2.11. Note that the unit of axis in the height function is $\kappa\lambda_s$, a dimensionless quantity to measure the magnitude of body curvatures. We calculate the surface integral over a range of circular gaits with different amplitudes. We also perform the direct simulations for each system to compare with surface integrals in our geometric framework (Figure 2.11).

For the subsurface movement of the sandfish lizard *S. scincus* in a frictional fluid and for swimming of *C. elegans* in buffer, comparisons of animal performance, direct RFT simulations, and height function surface integrals reveal that displacements per cycle are close to predictions (Figure 2.11). It is important to note here that because of power limitations in living (or synthetic) systems, displacement per cycle is not necessarily equivalent to speed. Since power generation capabilities of a swimmer are finite (e.g., muscles are not infinitely strong), larger shape changes (and therefore larger amplitude cycles) require more time to execute [129]. As a result, in the case of the sandfish, the peak power-limited speed occurs

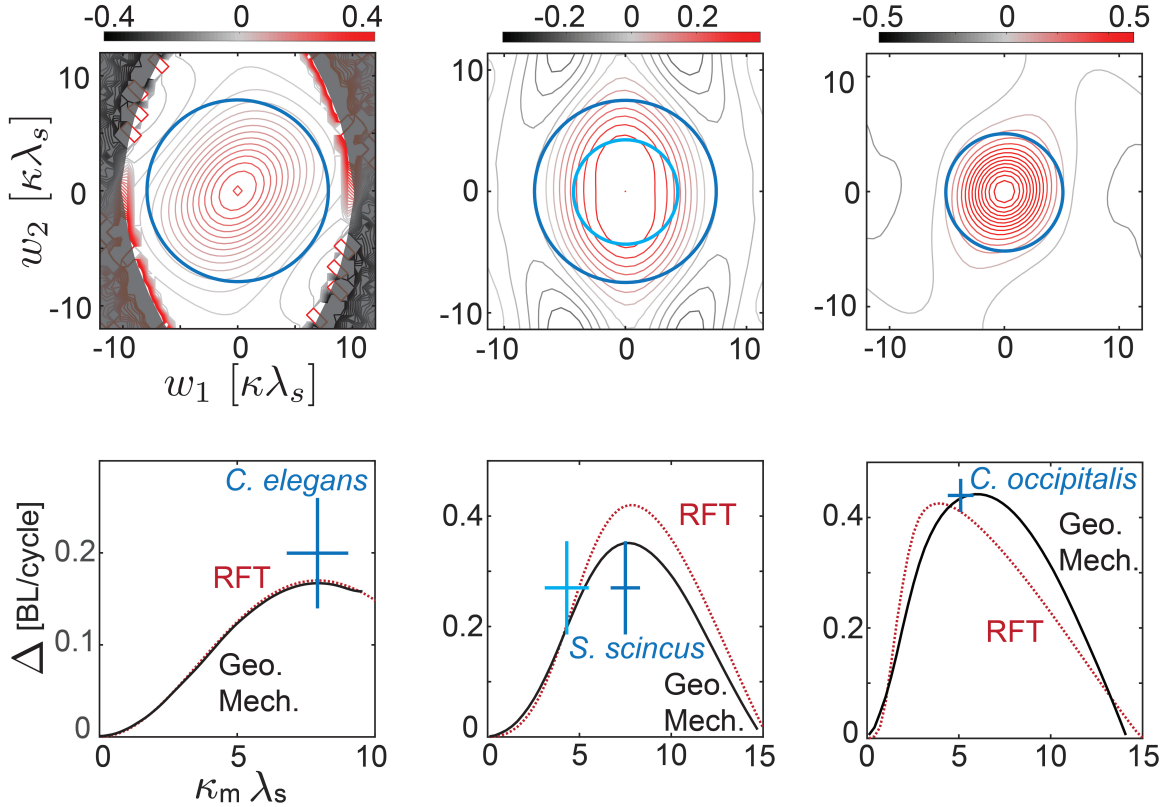


Figure 2.11: **Geometric mechanics of lateral undulation.** (Top) Height functions (contours; here, color scale multiplied by 100) and average animal gait (blue circles); and (bottom) Animal performance (average \pm standard deviation, represented by the blue crosses), geometric mechanics (solid black curve), and RFT (dashed red curve) predictions for (Left) *C. elegans* in S-basal buffer, (mid) *S. scincus* in 300- μm glass beads, and (right) *Ch. occipitalis* on the surface of 300- μm glass beads. Crosses in A-(ii) show average animal gaits from different data sets. In [72], curvatures were measured manually once per cycle (dark blue cross); in [122], curvatures were measured throughout time [128] (light blue cross). The light blue cross in B-(ii) represents the postural dynamics as defined by projections onto the two dominant PCs, and the dark blue cross shows postural dynamics measured directly from kinematic data. This figure is adapted from [83].

at a slightly smaller amplitude. In contrast, in low viscosity regimes *C. elegans* is not power limited [130].

The surface waveform used by *Chionactis occipitalis*, which has more waves and lower curvatures, produces low-slip movement that leaves behind a well-defined track of depth ≈ 5 mm [127]. Given that RFT measurements for movement at the surface used a flat plate intruder, we added an additional term to the measured RFT relations to account for the kinetic Coulomb friction drag that opposes the motion of the local segment. Predictions

from direct RFT simulation and height function surface integrals are in agreement with animal performance (Figure 2.11).

2.3.2 Limbless robot in granular media

Inspired by the biological elongate locomotors, we used shape basis function to design gaits for snake robots (with more than 3 links). Similar to our analysis in biological systems, we consider the shape variable of N -link snake robot to be:

$$\alpha(i, t) = w_1(t) \sin\left(\frac{2\pi K_s i}{N-1}\right) + w_2(t) \cos\left(\frac{2\pi K_s i}{N-1}\right), \quad (2.20)$$

where $i = \{1, 2, \dots, N-1\}$ is the joint index; K_s is the number of spatial waves; $w_1(t)$ and $w_2(t)$ are the reduced shape variables. In this way, we can represent the original $N-1$ dimensional shape space by a 2 dimensional shape space. Note that we use sinusoidal shape basis functions similar to our analysis in biological systems; the identification of other useful shape basis functions can be found in [82].

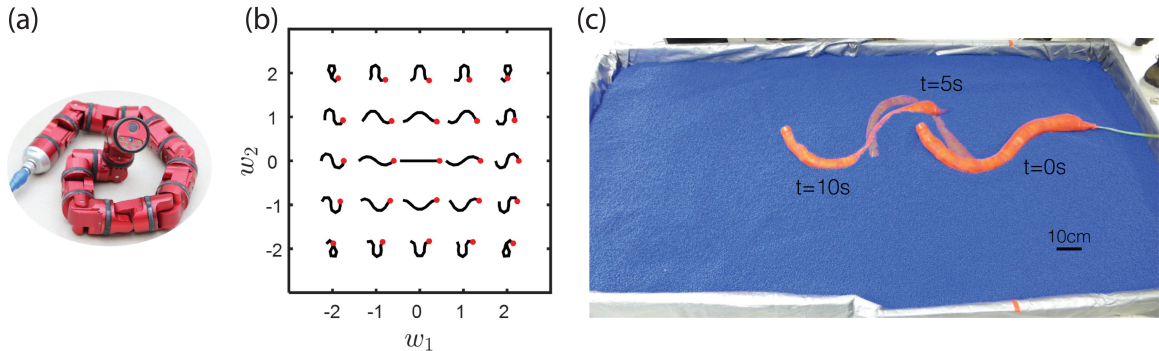


Figure 2.12: **N-link swimmer** (a) A 16-link robot. (b) The waveforms of a N -link swimmer in the shape space are visualized. (c) Snake robot executing a gait. Time interval between each snapshot is five seconds. Figures are adapted from [82, 131].

We consider the case of a snake robot swimming in granular materials (6 mm plastic particles) (Figure 2.12). The number of spatial waves, K_s is chosen to be 1. From our prior analysis, we numerically approximate the relationship between body velocity and the shape velocity with a linear function:

$$\begin{bmatrix} \dot{x}_1^b \\ \dot{y}_1^b \\ \dot{\theta}_1^b \end{bmatrix} = A(w)\dot{w},$$

The resultant height functions are shown in Figure 2.13.

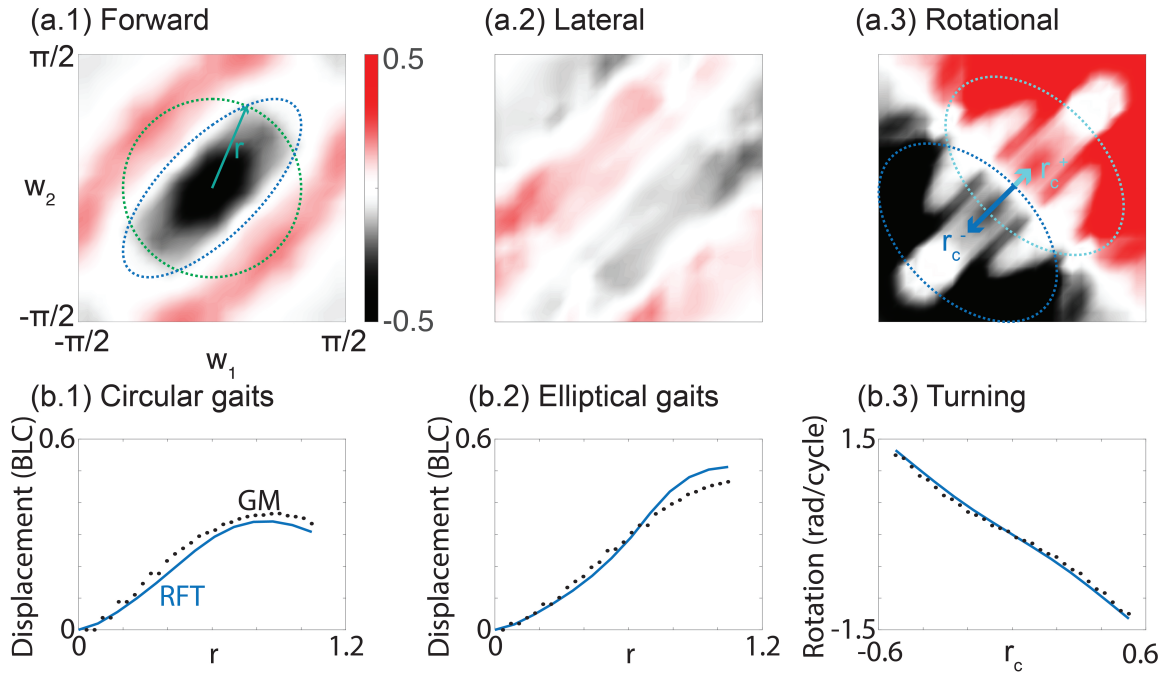


Figure 2.13: **Geometric mechanics of a N-link swimmer and numerical simulation** (a) The height function for a 16-link robot in (a.1) the forward, (a.2) the lateral, and (a.3) the rotational directions. (b) The comparison between the surface integral and RFT simulation for (b.1) circular gaits and (b.2) elliptical gaits with different amplitudes, and (b.3) turning gaits with different offset from origin.

Circular gaits

We first consider circular gaits centered at the origin of the shape space with different amplitudes. Figure 2.13 plots the displacement of each gait as a function of its amplitude. Note that the surface integral from geometric mechanics agrees with RFT simulation.

Elliptical gaits

From the structure from the forward height function, we noticed that an elliptical gait path could better bound the positive areas on the height function. To verify our hypothesis, we tested gaits with different eccentricity. Specifically, we parameterized the elliptical gaits as:

$$\begin{aligned}\alpha_1(t) &= r \sin(t) \\ \alpha_2(t) &= r \sin(t + \psi),\end{aligned}\tag{2.21}$$

where r is the amplitude of the elliptical gaits, and ψ determines the eccentricity of the gait path. For example, $\psi = \pi/2$ denotes a circle (thus a traveling wave) and $\psi = 0$ denotes a flattened ellipse (and thus a standing wave). Note that our parameterization prescribed a family of elliptical gaits with long axis oriented with an angle 45° from the w_1 axis, which aligns with the structure in the forward height function.

From the structure of the height function, we notice that an ellipse with $\psi = \pi/4$ optimally bounds the positive areas. We then tested the effect of amplitudes while fixing $\psi = \pi/4$. Similar to our analysis in circular gaits, we observed good agreements between surface integral and RFT simulations. Interestingly, we noticed that the peak displacement from elliptical gaits outperformed those in circular gaits, which agrees with our observation from the structure in height functions.

Turning gaits

Finally, we consider rotation in the limbless robot (from numerical simulation). From the structure of rotational height functions, we noticed that an oriented ellipse off-center from the origin can cause the highest rotation per cycle. We posited to modulate turning by controlling the center of the gait path. Specifically, we parameterize the gait path as:

$$\begin{aligned}\alpha_1(t) &= \pi/3 \sin(t) + r_c \\ \alpha_2(t) &= \pi/3 \sin(t + 0.65\pi) + r_c,\end{aligned}\tag{2.22}$$

where r_c is the offset from center of elliptical gait to the origin. We verified our prediction by numerical RFT simulation, and robophysical experiments. Surface integral prediction from the height function have good agreement with both RFT simulation and robophysical experiments.

2.3.3 Summary

In this section, we introduced the shape basis function such that we can apply geometric mechanics to systems with higher DoF. Specifically, from PCA analysis at biological elongate locomotors, we showed that the essence of lateral undulation in these animals can be prescribed by a two dimensional shape space spanned by two shape basis functions. The linearity of local connection is preserved in such dimensionality reduction, which allows us to use geometric mechanics.

While we are confined with the two dimensional representation of the original high DoF locomotion systems, there can still be many novel and interesting observations. With the help of height functions, we can identify the optimal amplitude for the undulatory motion; further, by investigating the structures in the forward and rotational height functions, we can analyze forward motion, turning, and steering in a continuous spectrum; finally, in the application to robot (robophysical) systems, we showed that the elliptical gait (intermediate between traveling wave and standing wave) outperformed the pure traveling wave. All combined, geometric mechanics can offer intuitive and visual insights to practical biological and robotics locomotion systems instead of laborious calculation.

2.4 N-link sidewinding swimmer: contact function

The content in this section is adapted from a collaborative project with Dr. Jennifer M Rieser. My role in this section is to assist Dr. Jennifer M Rieser for straight sidewinding analysis and leads the differential turn analysis.

2.4.1 Straight sidewinding

Thus far in the chapter, the systems studied maintain continuous full-body contact with the environment during self-propulsion. However, many animals lift limbs or body portions as they move, changing their contact state throughout a gait cycle [17, 132]. Here, we chose an organism that modulates environmental contact while using lateral traveling waves and inhabits a flowable environment, the sidewinder rattlesnake, *Crotalus cerastes* (Figure 2.14), which encounters sandy substrates in its native North American desert habitat. Sidewinders locomote on homogeneous substrates [133, 134] by propagating a wave of lateral body undulation coupled to an offset wave of body lifting, resulting in each body segment being cyclically lifted clear of the substrate, moved forwards, placed into a nearly static contact, then lifted again, with a slight phase offset between successive segments [135, 136, 137, 132]. Thus, the snake generates multiple head-to-tail propagating regions of lifted movement and nearly static ground contact (Figure 2.14) [135, 136, 137, 132, 107].

Despite the apparent complexity of these movements, our previous work indicated that the self-deformation pattern of *Cr. cerastes* could be characterized as a template consisting of a superposition of a lateral and vertical traveling wave [16], with a phase shift of $\pm\pi/2$ between them (Figure 2.14). The modulation (e.g., changes in the maximum amplitude) of these waves can lead to diverse behaviors such as turning [45, 16, 107]. However, sidewinders tend to use relatively consistent horizontal waves during forward motion and are typically thought to regulate forward speed using temporal frequency changes of the wave [133, 132, 45].

Indeed, when we applied PCA analysis to horizontal wave dynamics of previously collected *Cr. cerastes* data, we discovered that across trials, the dynamics of the horizontal wave consist of a circular path in a two sinuous mode configuration space (Figure 2.14) of a characteristic radius (and therefore maximal body curvature). We thus posit that this circle forms a control template enabling these animals to move rapidly over loose granular surfaces.

Although the vertical body dynamics have not been carefully experimentally resolved [45], they are assumed to be a traveling wave (and thus described by two modes) that sets the periodic contact pattern (Figure 2.14A-B). On level granular media [45, 16], parameters describing the vertical template remained approximately constant. Therefore, to model the vertical wave interaction, as in [16, 103, 107] we introduced a weighting prefactor, c , that specified how much of the environmental force each infinitesimal segment experienced. Specifically, we modify the resistive force balance in Equation 2.14 as:

$$\mathbf{F} = \int_{body} (cd\mathbf{F}_{\perp} + cd\mathbf{F}_{\parallel}) = 0. \quad (2.23)$$

Previous work [16] revealed that the three-dimensional pose of *Crotalus cerastes* could be represented by a horizontal wave coupled to a phase-shifted vertical wave that sets the environmental contact condition. To properly couple the vertical wave to the in-plane shape, we introduced $\delta(s)$

$$\delta(s) = \sin \left[\frac{2\pi ns}{L} + \tan^{-1} \left(\frac{w_2}{w_1} \right) - \frac{\pi}{2} \right], \quad (2.24)$$

where s is the position along the body, n is the number of waves on the body, L is the total length of the body, and w_1 and w_2 describe the in-plane wave shape. To set the contact using the vertical wave description, δ , we defined the smoothly-varying function, c

$$c(\delta(s)) = \frac{1}{1 + \exp[a(\delta(s) + b)]}. \quad (2.25)$$

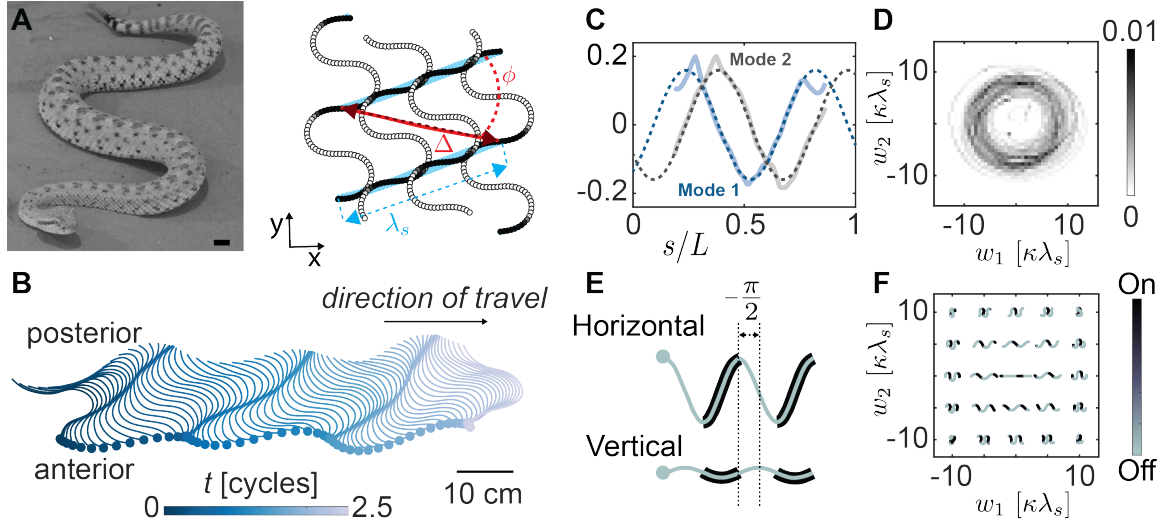


Figure 2.14: **Sidewinder rattlesnake substrate contact.** (A) (left) A sidewinding snake *Cr. cerastes*. Black bar denotes 1 cm. (right) Schematic illustrating sidewinding locomotion. If the animal does not slip, displacements, $\Delta = \lambda_s \cos \phi$, can be predicted from geometry. (B) Time-resolved kinematics are obtained from high-speed cameras. (C) Two relative curvature modes (determined from PCA) account for 42.4% and 37.3% of variance observed in in-plane body configurations of 4 animals throughout 18 trials. (D) 2D probability density map of animal data projected onto two dominant curvature principal components. (E) Depiction of coupling between in-plane and vertical waves (adapted from [16]). (F) Shape space showing body configuration-dependent animal-environment contact model for an animal with 1.5 waves along its body.

Here, $c \in [0, 1]$ sets the local fraction of the environmental force experienced as a function of position, s , along the body, b sets contact width, and a sets the sharpness of the on/off ground transition along the body. To be consistent with previous observations, $a = 15$ and $b = 0.5$ are chosen so that, when averaged over a completed gait cycle, approximately 34% of the animal's body is on the ground [45].

Figure 2.14 shows four RFT simulation snapshots throughout one undulation cycle. Contact patches (dark regions) originate near the head and are propagated toward the tail. As shown in previous work [16, 103], the prefactor c can be coupled to the in-plane shape, which allows us to use geometric mechanics to make sidewinding predictions. Given the experimentally observed oblique direction of travel (relative to the head-to-tail body axis), we expect the kinematics in our modeling to produce significant displacements in both the x - (forward) and y (lateral) directions. We therefore numerically computed height functions

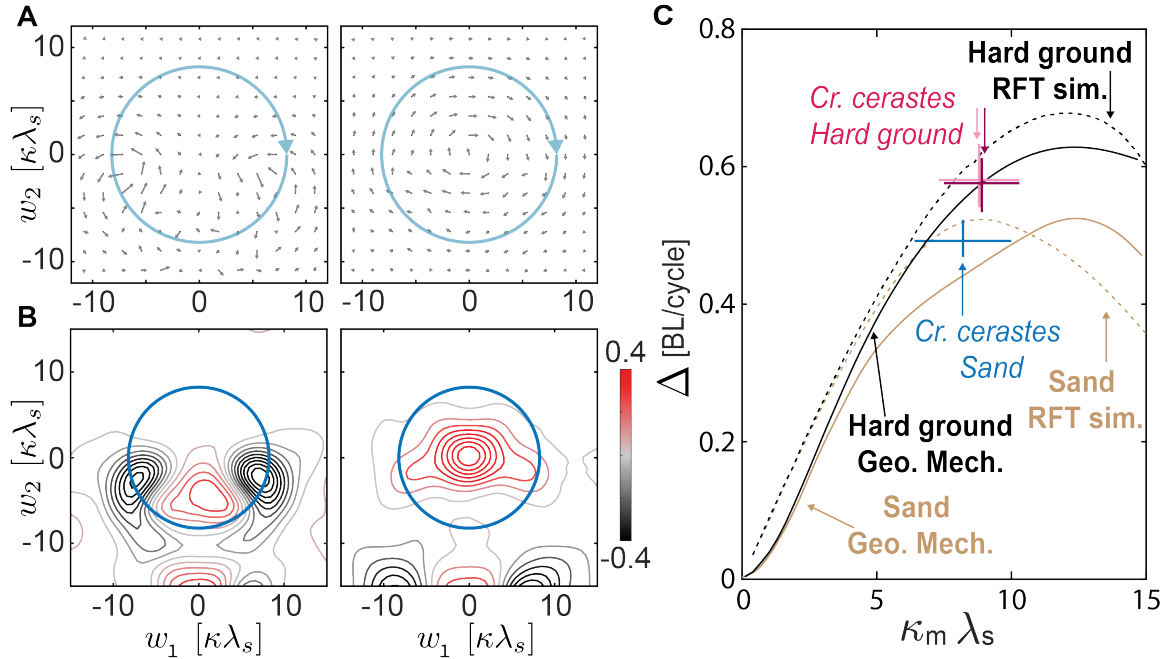


Figure 2.15: **Geometric mechanics of sidewinding.** (A) Connection vector fields and (B) x - and y - height functions (shown here as contour plots with color scales multiplied by 100) for movement on sand with $n = 1.5$ waves along the body. The blue circle shows average animal performance of *Cr. cerastes* on sand. (C) Comparisons of RFT simulations (dashed tan curve) and geometric mechanics calculations (solid tan curve) for movement on sand. Biological data: *Cr. cerastes* on a 7.6-cm layer of sand (blue); *N. fasciata* on a 5-cm layer of sand (dark purple). *Cr. cerastes* on an oak board roughened by a layer of adhered glass beads (dark magenta); *Cr. cerastes* on a smooth oak board (light magenta); *Cr. cerastes* on a 1.5-cm layer of sand (light purple) [132].

describing motions along both the x and y directions (Figure 2.15), and we define the total predicted displacement is given as $\Delta = (\Delta_x^2 + \Delta_y^2)^{1/2}$, where Δ_x and Δ_y are displacements predicted from x - and y - height functions, respectively.

Figure 2.15C shows that, for movement on granular media, direct RFT simulations (dashed tan curve) and geometric computations (solid tan curve) predict similar maximal displacements. Despite the differences in predicted gait amplitude, the displacement curves predicted are not highly sensitive to gait amplitude variation over a broad range. Note that the discrepancy between RFT simulation and geometric mechanics for sidewinding on sand can be a result of the non-commutativity of body velocities. As shown in Figure 2.15B, the body velocity in x - and y - directions have comparable magnitudes, which can lead to

relatively large non-commutativity effects in body velocities [138].

2.4.2 Differential Turn

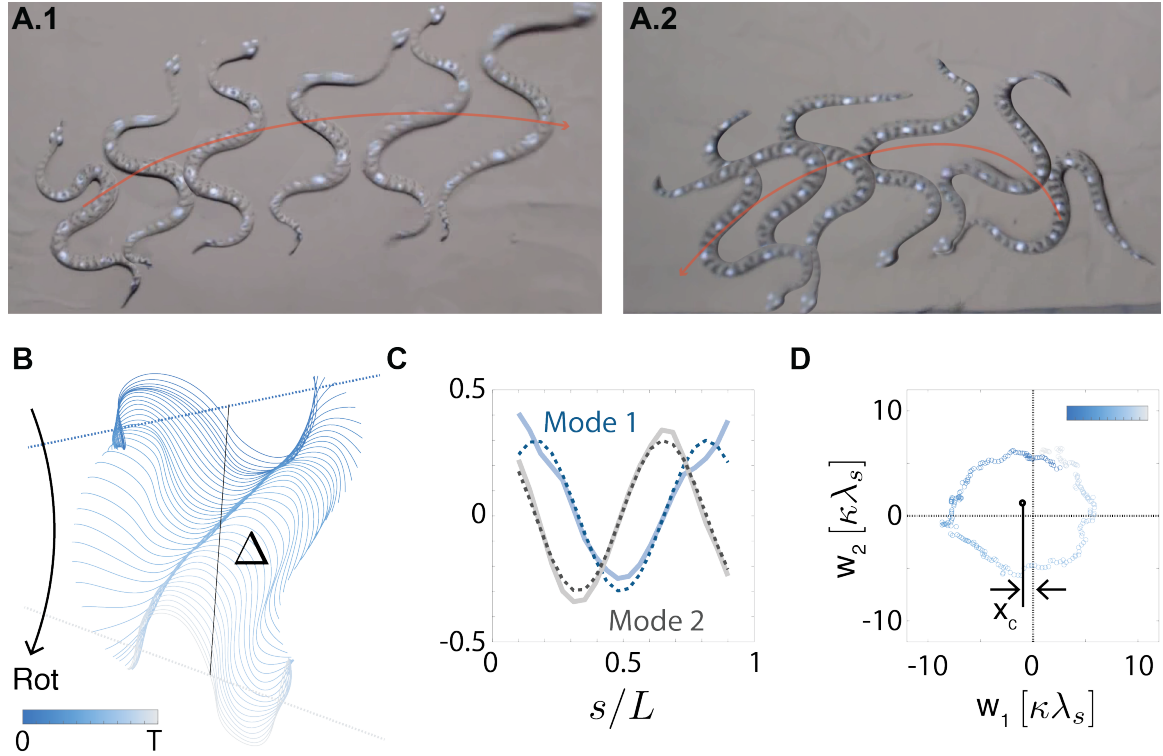


Figure 2.16: **PCA analysis of differential turn** Snapshots of *Cr. cerastes* body configurations performing (A.1) gradual (A.2) sharp differential. (B) One cycle of tracked midline of differential turn colored by time. Rotation (Rot) and displacement are labelled. (B) Two relative curvature modes (determined from PCA) account for 44.7% and 24.5% of variance observed in in-plane body configurations of 4 animals throughout 47 trials. (C) A typical projection of body curvature onto two dominant curvature principal components colored by time.

To navigate in complex terrains, effective turning behaviors are as important as the translation. However, turning behaviors in animals are less studied than translational behaviors. Often, the turning behaviors are thought to be distinct from translational behaviors, and therefore would require additional analytical tools. Here, we used geometric mechanics as a unified framework to study a spectrum of behaviors from translation to turning. Specially, we studied the differential turn observed in *Cr. cerastes*.

During differential turn [16], the animals imposed an amplitude modulation in the hori-

zontal wave (Figure 2.16a). Depending on the magnitude of amplitude modulation, animals can thus control the degree of turning. Moreover, animals also modulate the net translational displacement associated with the degree of turning. Specifically, sharp turns are often accompanied by reduced translational displacement, and gradual turns by large translation. Therefore, unlike in straight sidewinding where the animals use relatively consistent horizontal waves, animals exhibit a variety of horizontal waves during differential turns. We used PCA to analyze the modes during differential turns. We noticed that the two modes of sidewinding were preserved in differential turns: the first two principle components can account for over 69.1% of the variance (Figure 2.16b); and the two modes for straight sidewinding are almost identical to those for differential turns.

We then project curvatures (of differential turn) onto the first two PC modes. We noticed that the trajectory in PC space emerged as a circle, and the center of the circle is off from the origin. We posited that the offset of center from the origin can serve as an indicator of the degree of turning and translation. We then measured the rotation for each cycles (95 cycles over 47 trials) and plotted the (Figure 2.17B, left) translation and the (Figure 2.17B, right) rotation as a function of w_1 offset of the trajectory center (arithmetic average) from the origin. We ran a linear regression between w_1 offset and rotation, and observed significant relationships (translation: $r^2 = 0.20$, $p < 0.0001$; rotation: $r^2 = 0.50$, $p < 0.0001$).

We used the geometric mechanics to explain such correlation. We numerically computed the height functions using the same contact function as described in Equation 2.24- Equation 2.25. We observed that the clusters of positive and negative volumes are distributed along the axis of $w_2 = 0$ in θ - height function, indicating that the introduction of offset in w_1 direction can indeed lead to rotation. We used the following equations to prescribe the off-centered circle in geometric mechanics calculation:

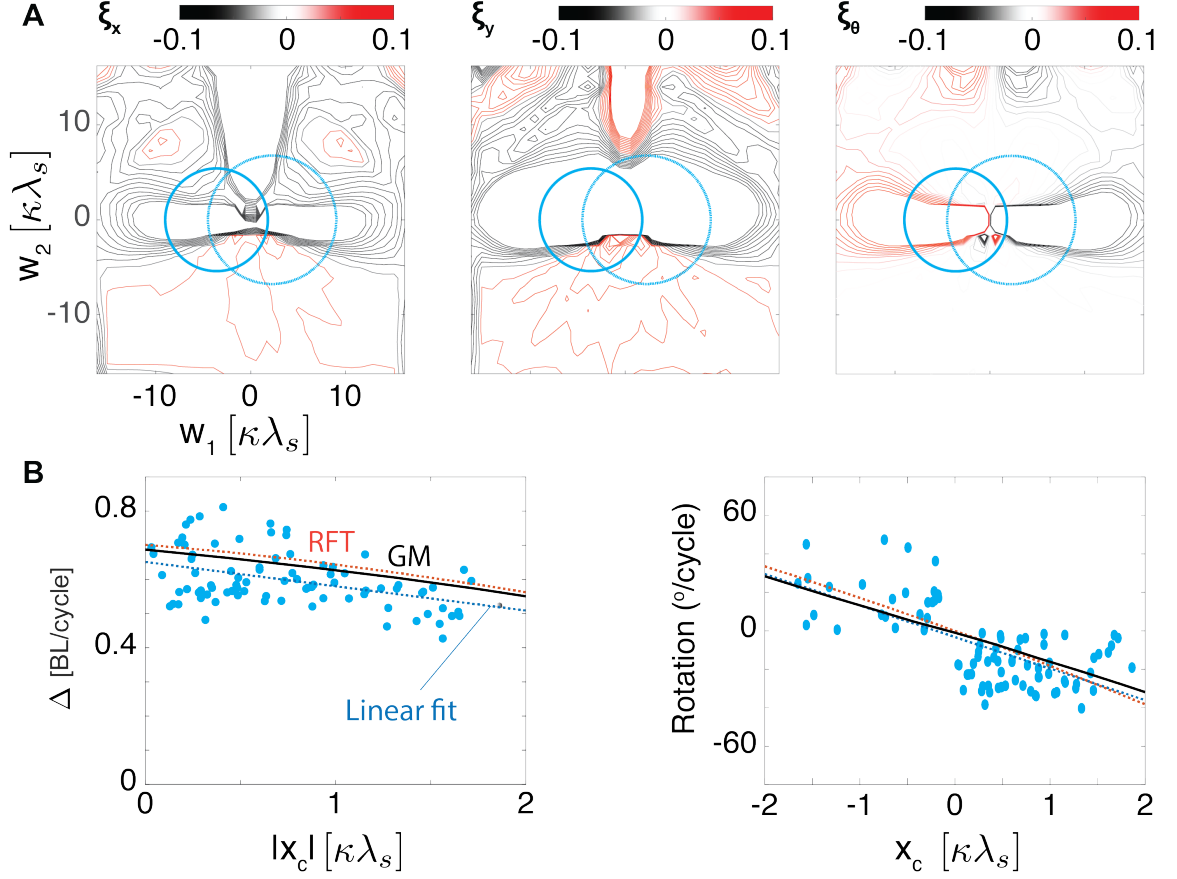


Figure 2.17: **Geometric mechanics analysis of differential turn** (A) x , y , and θ - height functions (shown here as contour plots. Color scales in x , y - height functions are multiplied by 100) for movement with $n = 1.2$ waves along the body. The blue circle typical CW and CCW differential turn in *Cr. cerastes* (B) The comparison between direct RFT, GM (surface integral in height functions), and animal data (light blue dots) with its linear fit ($p < 0.001$).

$$\begin{aligned}
 \lambda_s \kappa(t, s) &= w_1(t)v_1(s) + w_2(t)v_2(s) \\
 w_1(t) &= (\kappa_m \lambda_s - |x_c|) \sin(t) + x_c \\
 w_2(t) &= (\kappa_m \lambda_s - |x_c|) \cos(t).
 \end{aligned} \tag{2.26}$$

We then performed surface integrals of circular gaits over height functions and compared it with direct RFT simulation and the fitted linear regression, and observed good

agreement.

2.5 Modulating contact function using geometric mechanics

2.5.1 Geometric mechanics with toroidal and cylindrical shape spaces

The content in this subsection is adapted from a collaborative project with Dr. Chaohui Gong and Dr. Bo Lin. My contribution in this subsection is to identify the importance of minimal perturbation coordinate in toroidal and cylindrical shape spaces, and formulate the minimal perturbation coordinate problem as a mathematical problem.

Kinematic motion planning using geometric mechanics tends to prescribe a trajectory in a shape space and determine its displacement in a position space. So far, we only considered Euclidean shape space. However, in many cases, the shape space can be non-Euclidean either because the robotic joints can spin over a full cycle (i.e., has an \mathbb{S}^1 configuration space component), or its parameterization has an \mathbb{S}^1 dimension.

Consider a shape space that is a cylinder; gaits that “wrap” around the full range of a shape variable and return to its starting configuration are valid gaits in the shape space. Existing geometric mechanics methods cannot properly evaluate the displacement partially because there is no obvious area enclosed by these gaits. Here, we derive geometric tools to consider systems with toroidal and cylindrical shape spaces by explicitly analyzing the topology of the underlying shape space.

Cyclic shape variables

We first consider the locomotion of an N -link planar swimmer in viscous fluid. As discussed earlier, we can relate the body velocity to shape velocity with a linear mapping (repeating Equation 2.19)

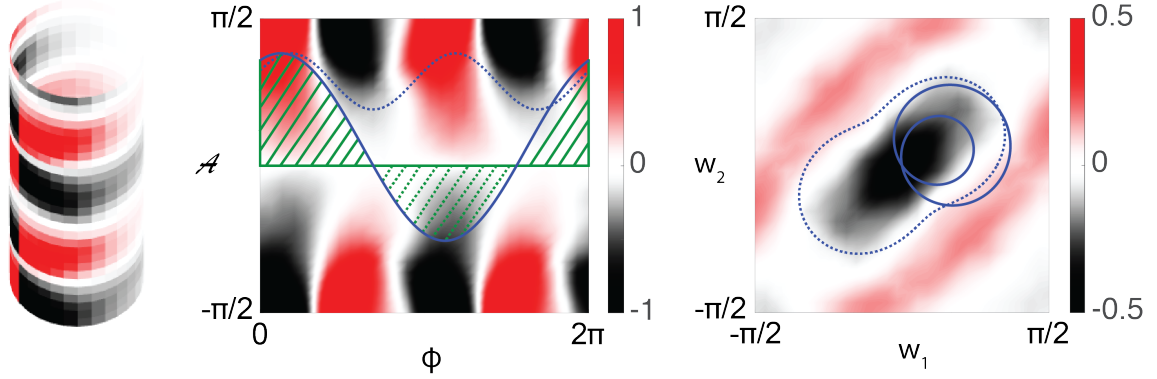


Figure 2.18: **Cylindrical shape space** (left) Height function on cylindrical shape space. (mid) Height function on the Euclidean parameterization space of the cylindrical shape space. We illustrate two gaits with solid and dashed blue curves. Note that the solid blue gait enclosed three disjoint areas with the assistive lines. The area above the assistive line (solid shadow) and the area below the assistive (dashed shadow) line have different handedness. (right) The illustration of height function on Euclidean shape space of the same system. Note that middle and right panel are identical subject to different parameterization.

$$\begin{bmatrix} \dot{x}_1^b \\ \dot{y}_1^b \\ \dot{\theta}_1^b \end{bmatrix} = A(w)\dot{w},$$

where $w = [w_1, w_2]^T$ is the reduced shape variable, prescribing the overall shape from the shape basis function:

$$\alpha(i) = w_1\beta_1(i) + w_2\beta_2(i) \quad (2.27)$$

where $\alpha(i)$ is joint angle between link i and $i + 1$ for the N -link swimmer; $\beta_1(i)$ and $\beta_2(i)$ are the shape basis functions. When the weights, w_1 and w_2 , are varied cyclically, a travelling wave gait can be created and the system swims forward. For instance, a gait with a constant amplitude is represented as a circle in this shape space. A gait with two shape variables can also be parameterized by a phase and an amplitude [139]:

$$\alpha_i = \mathcal{A} \sin(\phi) \beta_1(i) + \mathcal{A} \cos(\phi) \beta_2(i) \quad (2.28)$$

with amplitude $\mathcal{A} = \sqrt{w_1^2 + w_2^2}$ and phase $\phi = \tan^{-1}(w_2/w_1)$. In this form, the shape space is $r = [\phi, \mathcal{A}]^T$. The phase can be viewed as cyclical; $\alpha_i(0, \mathcal{A}) = \alpha_i(2\pi, \mathcal{A})$ so we can consider $\phi \in \mathbb{S}^1$.

From Equation 2.28, we can rewrite Equation 2.19 as:

$$\begin{bmatrix} \dot{x}_1^b \\ \dot{y}_1^b \\ \dot{\theta}_1^b \end{bmatrix} = \underbrace{A(r)}_{A'(r)} \begin{bmatrix} \sin(\phi) & \mathcal{A} \cos(\phi) \\ \cos(\phi) & -\mathcal{A} \sin(\phi) \end{bmatrix} \begin{bmatrix} \dot{\mathcal{A}} \\ \dot{\phi} \end{bmatrix}, \quad (2.29)$$

where we established new local connection matrix between the body velocity and shape velocity where the shape space has cyclic structure. Similarly, there could also be cases where both shape variables are cyclic (i.e., $r = [\phi_1 \ \phi_2]^T, \phi_1, \phi_2 \in \mathbb{S}^1$), and therefore the shape space is toroidal.

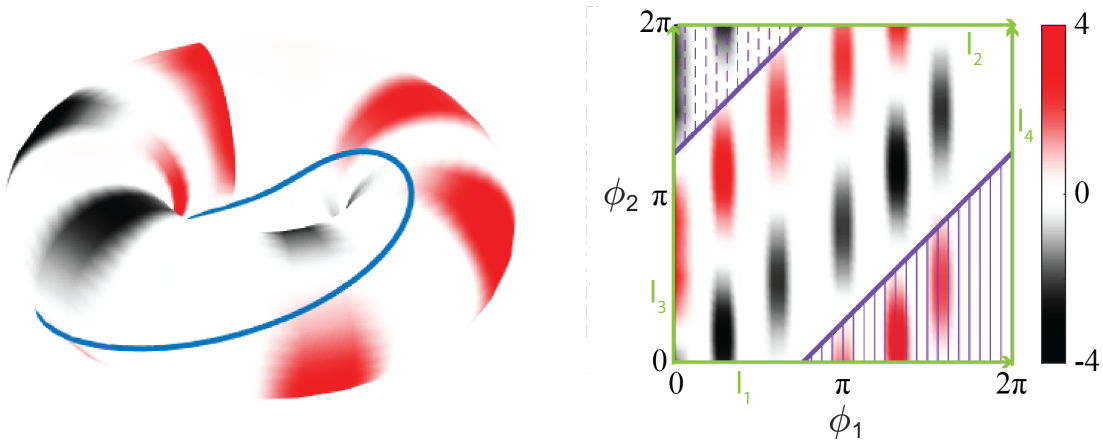


Figure 2.19: **Toroidal shape space** (left) Height function on toroidal shape space. (mid) Height function on the Euclidean parameterization space of the cylindrical shape space. We illustrated a gait with solid purple curves. Note that the solid purple gait enclosed two disjoint areas with the assistive lines. The area above the assistive line (dashed shadow) and the area below the assistive line (solid shadow) have different handedness .

Since we are considering gaits that wind around the \mathbb{S}^1 component of the shape space, we need to establish terminology that measures the number of winds. Conventionally, a

winding number is defined by the number of revolutions a closed loop curve makes in the plane [140]. With a slight abuse of notation, we define the winding number, $\mathbf{w}^n \in \mathbb{Z}^m$ for an m -dimensional space to be the integer set of times that a path wraps around each \mathbb{S}^1 dimension of that space. This notion of winding number is similar to that which is defined in [141]. For gaits that have a zero winding number, the use of height function is straightforward, as described in [75]. However, gaits with non-zero winding numbers do not have a closed curve representation on the shape space, so do not enclose a well defined area. Consequently, the height function cannot be directly used for such gaits.

Assistive lines

To better visualize the shape spaces with cyclic shape variables, we unfold the cylinder ($\mathbb{S}^1 \times \mathbb{R}^1$) or torus ($\mathbb{S}^1 \times \mathbb{S}^1$) into its Euclidean parameterization space (cylindrical: $\mathbb{R}^1 \times [0, 2\pi]$, toroidal $[0, 2\pi] \times [0, 2\pi]$, Figure 2.19). To form an enclosed area in the Euclidean parameterization space, we introduce the notion of an assistive line ([142]). The assistive lines are defined to be fixed paths in shape space and are used to form a closed loop with the gait path in the shape space. Note that, in principle, the choice of assistive line is arbitrary with respect to the same winding number. In practice, we often choose the assistive line with a physical meaning. For example, in the cylindrical shape space, we choose the assistive line to be $\partial\phi_0 : \mathcal{A} = 0$ (green line in Figure 2.18). The net displacement can be approximated by the path integral along the assistive line $\partial\phi_0$ plus the surface integral of the area enclosed by the gait path $\partial\phi$ and the assistive line ([142]):

$$\int_{\partial\phi} \mathbf{A}(\mathbf{r})d\mathbf{r} = \int_{\partial\phi_0} \mathbf{A}(\mathbf{r})d\mathbf{r} + \iint_{\phi-\phi_0} \nabla \times \mathbf{A}(\mathbf{r})d\alpha_b d\tau, \quad (2.30)$$

where $\phi - \phi_0$ is the area enclosed by assistive line $\partial\phi_0$ and gait path $\partial\phi$. Note that when the gait path and the assistive line enclose disjointed areas in the shape space, the handedness (the direction of the curl) of the area enclosed can be different. For example, as shown in our example in Figure 2.18, the assistive line (green curve) and our gait path (blue curve)

form three disjoint areas: the area where $\partial\phi_0$ is above (solid shading area) and below (dashed shading area) $\partial\phi$. Thus, taking the handedness of enclosed area into consideration, the second term in (Equation 2.30) is computed as the surface integral of area where $\partial\phi$ is above $\partial\phi_0$ subtracted from the surface integral of area where $\partial\phi$ is below $\partial\phi_0$.

In the toroidal shape space, we choose the assistive lines to be a collection of two line segments $\partial\phi_0 : \{[\phi_1, \phi_2], \text{mod}(\phi_1, 2\pi) = 0\} \cup \{[\phi_1, \phi_2], \text{mod}(\phi_2, 2\pi) = 0\}$. Note that lines $l_1 = \{[\phi_1, \phi_2], \phi_1 = 0\}$ and $l_2 = \{[\phi_1, \phi_2], \phi_1 = 2\pi\}$ (similarly $l_3 = \{[\phi_1, \phi_2], \phi_2 = 0\}$ and $l_4 = \{[\phi_1, \phi_2], \phi_2 = 2\pi\}$) are identical in the toroidal shape space, but appeared as two disjoint lines in the Euclidean parameterization space. Therefore, we are free to partition l_1 and l_2 (similarly l_3 and l_4) in the Euclidean parameterization space without changing its physical meaning. In practice, we choose to partition the lines such that it can enclose areas with the gait path. An example of assistive line partition Figure 2.19. Two areas are enclosed by assistive lines and the gait path. Because of the handedness of enclosed areas, the surface integral is the area within solid lines subtracted from the area of the surface enclosed in the upper left corner.

Minimal Perturbation Coordinate on toroidal shape space

As discussed in [138], the Lie bracket effect can be important as we approximate the spatial velocity with body velocity. Hatton et. al. showed that the Lie bracket effect can be minimized when the designated body reference is properly chosen [138]. The transformation of body frame orientation can be interpreted as, replacing the vector field $A_\theta(\mathbf{r})$ by a new vector field, $A'_\theta(\mathbf{r})$ such that the line integral of $A'_\theta(\mathbf{r})$ should be equal to the one of $A_\theta(\mathbf{r})$ along any closed curve in the shape space. However, the existing framework is not directly applicable to cylindrical or toroidal shape spaces because of the cyclic constraints. In this section, we will briefly introduce the algorithm to identify the minimal perturbation coordinate on toroidal shape space.

By the linearity of line integrals, $A_\theta(\mathbf{r}) - A'_\theta(\mathbf{r})$ is a vector field whose line integral

along any closed curve is zero. By [143, Thm 2.1, p.362], $\mathbf{A}_\theta(\mathbf{r}) - \mathbf{A}'_\theta(\mathbf{r})$ is the gradient of some potential function, $P(\mathbf{r}) = P(r_1, r_2)$, defined on the shape space.

It is shown in [138] that in the optimal orientation of the body frame, the norm of the vector field \mathbf{A}'_θ is minimized. Let the vector field $\mathbf{A}_\theta(\phi_1, \phi_2) = (f_1(\phi_1, r_2), f_2(r_1, r_2))$ be the third row of $\mathbf{A}(\mathbf{r})$. Since the shape space of ϕ_1, ϕ_2 is the standard 2-torus T^2 , which we identify with $(\mathbb{R}/2\pi\mathbb{Z}) \times (\mathbb{R}/2\pi\mathbb{Z}) = [0, 2\pi) \times [0, 2\pi)$. Now we need to minimize the ‘distance’ between F and the gradient $\nabla P(r_1, r_2)$ of a potential function $P(r_1, r_2)$ defined on T^2 . For the efficiency of computations, we choose the L^2 -norm, and thus our problem becomes:

Problem 1. *Given continuous functions f_1, f_2 defined on T^2 , find a differentiable function $P(r_1, r_2)$ defined on T^2 such that the integral*

$$\int_{T^2} \left[\left(f_1(r_1, r_2) - \frac{\partial P}{\partial r_1}(r_1, r_2) \right)^2 + \left(f_2(r_1, r_2) - \frac{\partial P}{\partial r_2}(r_1, r_2) \right)^2 \right] dr_1 dr_2 \quad (2.31)$$

is minimal.

The detailed numerical solution can be found in Appendix and [144].

2.5.2 Modulating the contact function

The content in this subsection is adapted from a collaborative project with Tianyu Wang, who performed robophysical experiments. My contribution in this project includes (1) designing the experiments, (2) conducting the numerical analysis, (3) writing the manuscript.

Prior work on wave modulation

Many recent works are dedicated to replicate the success of biological sidewinding in their robotic counterparts [45, 16, 126, 145]. Typically limbless robots are constructed with adjacent rotary motors rotated by 90° such that successive modules can achieve rotation in

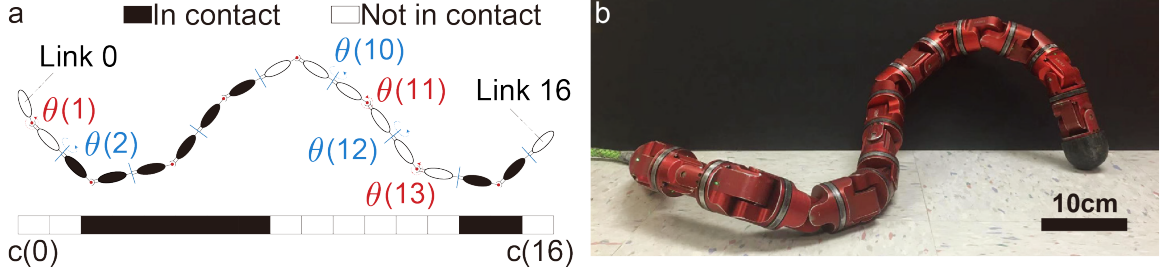


Figure 2.20: **Theoretical Model and Experimental Robot.** (a) The theoretical model for the sidewinder robots. The filled black ovals indicate the ground contact phase while the white ovals indicate a no ground contact phase. The contact state is labelled in black ($c(i)$). The joint angle in blue indicates pitch joints and the joint angle in red indicates yaw joints. (b) The serial elastic actuated robot used to test the effectiveness of our stabilization approach.

the horizontal and vertical planes alternatively. In this way, the robot can have 3 dimensional configurations by a superposition of a vertical wave and a horizontal wave. For an N -joint limbless robot, joints are labeled 1 to N , and links are labeled from 0 to N , where joint j connects link $j - 1$ and link j . Odd numbered joints are *yaw* joints and therefore produce motion in the horizontal plane (their rotation axes are vertical). Even numbered joints are *pitch* joints and therefore produce motion in the vertical plane (their rotation axes are horizontal). The joint angles were often prescribed using the following functions:

$$\theta(2j - 1, t) = A_l \sin\left(2\pi K_l \frac{2j - 1}{N} + 2\pi f t\right), \quad (2.32)$$

$$\theta(2j, t) = A_v \sin\left(2\pi K_v \frac{2j}{N} + 2\pi f t + \phi_0\right), \quad (2.33)$$

where $\theta_l(2j - 1, t)$ and $\theta_v(2j, t)$ refer to the yaw (odd) joint angles and the pitch (even) joint angles respectively; K_l and K_v are the spatial frequency of the horizontal wave and the vertical wave respectively; A_l and A_v are the amplitude of the horizontal wave and the vertical wave respectively; f defines the temporal frequency; and ϕ_0 is the phase lag between the horizontal and the vertical wave.

The contact state of link i is represented by $c(i)$, where $c(i) = 1$ indicates that link i is in contact and $c(i) = 0$ indicates that link i is not in contact. The links between two consecutive vertical joints have the same contact state, i.e., $c(2j) = c(2j - 1)$. Therefore, the contact state in robots can be approximated by ([83]):

$$\begin{aligned} c(2j - 1, t) &= c(2j, t) \\ &= \sigma \left[\sin \left(2\pi K_v \frac{j}{2N} + 2\pi f t + \phi_0 \right) \right], \end{aligned} \quad (2.34)$$

where $\sigma[x] = 1/(1 + e^{ax+b})$. Equation 2.34 has a similar structure as those described in Equation 2.24 and Equation 2.25. As demonstrated in prior works [16], certain sidewinding parameters (specifically, $K_l = K_v$ and $\phi_0 = \pm\pi/2$) can lead to translational sidewinding (which we will refer to as ‘‘T-sidewinding’’) motion, where the locomotor displays translational displacement with no significant turning. Similarly, the modulation of the horizontal wave can also cause differential turn, closely resembling our observation in biological systems.

In addition to the modulation in the horizontal wave, [16] showed that modulating the ratio of the spatial frequency in the vertical and horizontal directions (K_v/K_l) yields turning gaits (*frequency turning*). Either increasing ($K_v = 1.3K_l$) or decreasing ($K_v = 0.6K_l$) the vertical spatial frequency will lead to clockwise (CW) turning. Here, we refer to the frequency turning as the rotational sidewinding (which we will refer to as ‘‘R-sidewinding’’) motion. Beyond sidewinding, the sinus lifting gait is another snake gait using horizontal and vertical waves. [146] showed that snakes lift body portions with the largest curvatures during lateral undulation (slithering) locomotion. In the scheme defined in Equation 2.32 and Equation 2.34, this form of locomotion has $K_v = 2K_l$ and $\phi_0 = 0$. We summarize previous work on wave modulation in Table 1.

K_l	K_v	ϕ_0	Behavior	Source
1.5	1.5	$\pi/2$	T-sidewinding	[45]
2	2	$\pi/2$	T-sidewinding	[16]
1.5	0.9	$\pi/2$	R-sidewinding	[16]
1.5	1.95	$\pi/2$	R-sidewinding	[16]
1.5	3	0	Slithering	[146]

Table 2.1: **Summary of previous work on sidewinder locomotion.**

Statically unstable gaits

As discussed in [16], sidewinding gaits with 1.5 and 2 spatial waves ($K_l = \{1.5, 2\}$, $K_v/K_l = 1$) can be successfully implemented in robophysical platforms, partially because of their property of gait stability. To explore the effects of stability, we defined static stability as the fraction of a temporal undulation period in which the center of mass is inside the support polygon. The support polygon is defined as the convex hull of all links in contact with the substrate. In Figure 2.21, we show examples of stable (Figure 2.21 *left*) and unstable configurations (Figure 2.21 *right*). We observed that in both cases ($K_l = \{1.5, 2\}$), the gaits are statically stable. With this knowledge, we proceed to study the locomotion performance of the statically unstable sidewinding gaits.

We calculate the static stability for sidewinding gaits with different spatial frequencies ($K_v = K_l = K$) in Figure 2.22. High spatial frequencies lead to a dense distribution of short contact patches and are often statically stable. In contrast, low spatial frequencies lead to sparse distribution of long contact patches and are often not statically stable.

To investigate the behavior of statically unstable sidewinding gaits, we perform experiments on sidewinding gaits with 0.9 spatial wave and 1.5 waves on our robot (Figure 2.23). We set horizontal amplitude $A_l = 40K_l$ (unit of amplitudes: degree), vertical amplitude $A_v = 8.5K_v$, and a temporal frequency $f = 2.0$ Hz for all the robot experiments unless otherwise stated. Snapshots of the robot implementing such gaits are shown in Figure 2.23. Good agreement between experiment and theory is observed in the sidewinding gait with

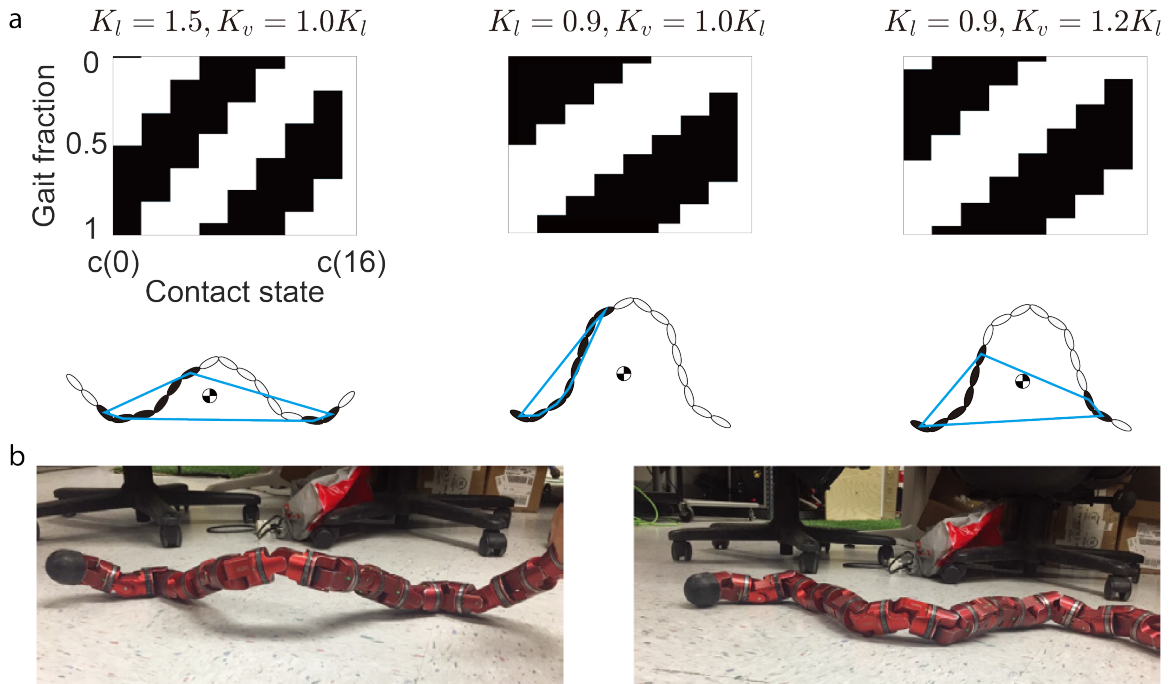


Figure 2.21: **Examples of Statically Stable and Unstable Configurations.** (a) (*left*) The contact state pattern and an example of a statically stable configuration for gaits with high spatial frequency in both the horizontal wave and the vertical wave. (*mid*) The contact state pattern and an example of a statically unstable configuration for gaits with low spatial frequency in both the horizontal wave and the vertical wave. (*right*) Stabilizing the statically unstable configuration by increasing the vertical spatial frequency. The label and the axis are identical. (b) Example of an unstable configuration (*left*) and an unexpected touchdown (*right*)

1.5 spatial waves. However, we observe significant discrepancies between the simulation and robot experiments for the sidewinding gait with 0.9 spatial waves (see Figure 2.23). We hypothesize that at low spatial frequency, the configuration of the robot is not statically stable (static stability = 0.34 for 0.9 spatial wave, static stability = 0.83 for 1.5 spatial waves), which leads to the robot falling down and causes contact patterns different from expectation. The unexpected touchdown can change the distribution of ground reaction forces and

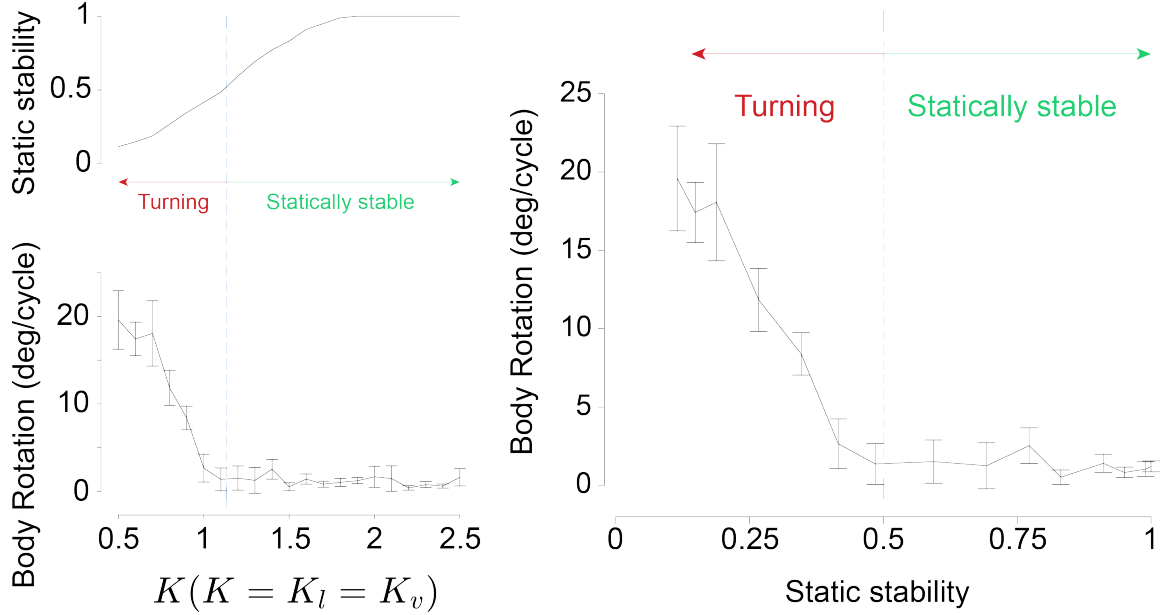


Figure 2.22: **Effect of spatial frequency on static stability in sidewinding.** (*Left*) The figure on top panel shows the relationship between the spatial frequency ($K_v = K_l = K$) and the static stability. Robot experiments showed that significant turning (*Left, bottom*) was observed in gaits with low static stability (*Left, top*) and the turning vanished at gaits with high static stability. (*right*) We directly plotted the relationship between the body rotation and static stability. The curve appeared to be a piece-wise linear function. In the range where the static stability is less than 0.5, the body rotation grows almost linearly with the loss of static stability ($R = 0.99$). Whereas in the range where the static stability is higher than 0.5, the body rotation is almost negligible.

therefore lead to motions in other directions (in this case, turning).

We further conducted robot experiments across a range of spatial frequencies. Those robot experiments showed that the undesired rotation vanished at high spatial frequencies. We observed that, the cut-off static stability that leads to unexpected behavior is around 0.5. In this way, we use 0.5 as the threshold to determine the static stability in later analysis. Moreover, in the regime of unstable gaits, the degree of rotation is highly correlated with the static stability, which further validates our hypothesis on stability-driven turning.

Temporal Frequency Dependency

Despite being statically stable, it is possible that, when operated at high temporal frequency, the acquired dynamic stability can compensate for the loss of static stability. Following this

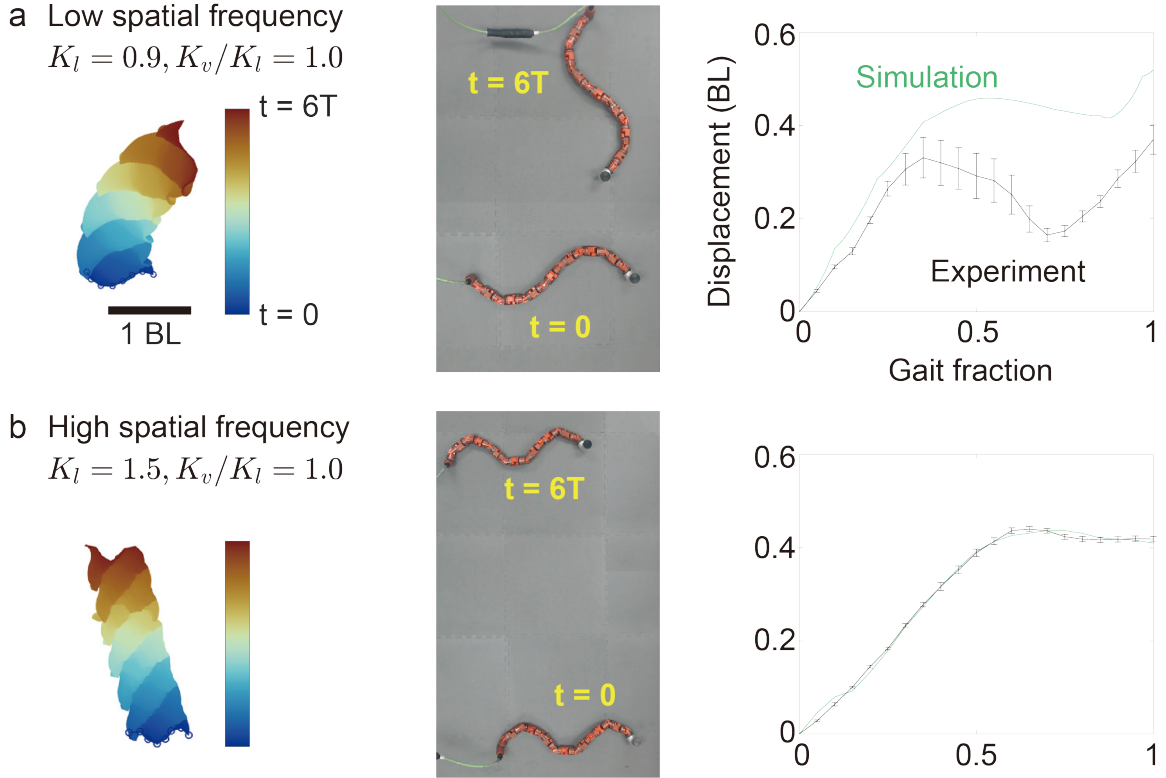


Figure 2.23: **Discrepancy between robot experiments and simulation at low spatial frequency.** (*left*) the trajectories of body motion in 6 gait cycles. The colors represent gait periods. Initial positions of the robot indicated by the black circles. (*right*) comparisons of time evolution of displacement of the simulation and robot experiments. We compared the low spatial frequency gait (a) and high spatial frequency gait (b). The simulation-experiment discrepancy occurs in low spatial frequency gaits. The unit and the axis labels in all panels are the same.

idea, we test the effect of the temporal frequency on the performance of gaits.

We first evaluate the effect of temporal frequency on the translational sidewinding gait with 0.9 spatial wave ($K_l = 0.9, K_v/K_l = 1$). We set $A_l = 50^\circ$ and $A_v = 75^\circ$ for all robot experiments. From our static stability analysis, this translational sidewinding gait is not statically stable (static stability = 0.35). At low temporal frequency (see Figure 2.24), significant rotations are observed in robot experiments, whereas at high temporal frequency, the magnitude of rotation reduces but the robot rotates in a different direction. Our experiments show that the locomotion performance for statically unstable gaits is not predictable and controllable when operated at different temporal frequencies. However, the magnitude

of rotation significantly decreases when robot was operated at high temporal frequency, which suggests that the loss of static stability can be compensated by emergent dynamic stability at high speeds.

a $K_l = 0.9, K_v/K_l = 1.0$

b $K_l = 1.5, K_v/K_l = 0.6$

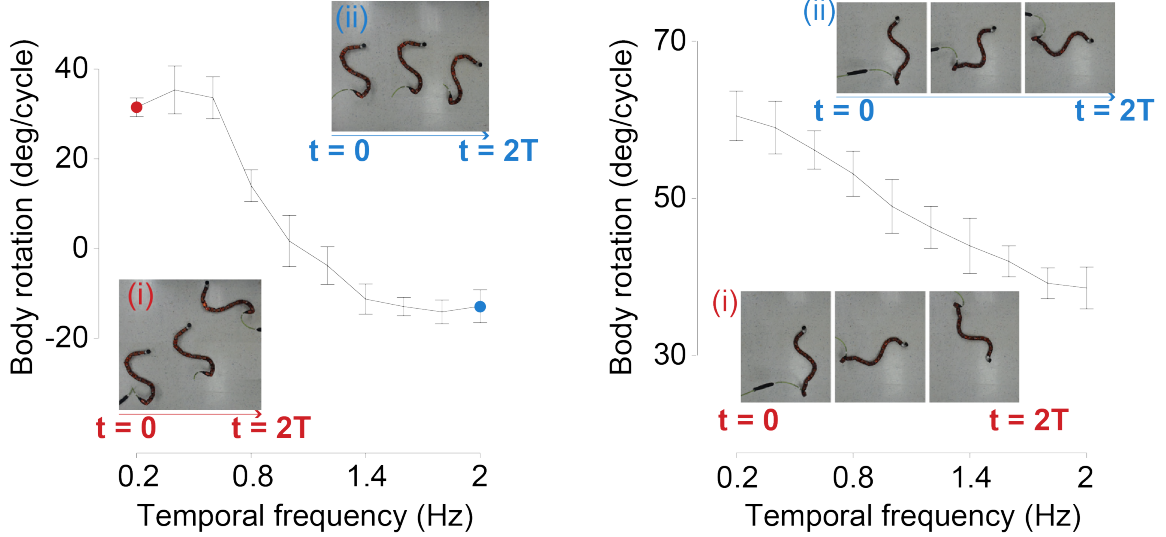


Figure 2.24: **Temporal frequency dependency of unstable gaits.** Dependence of the rotation angle (per cycle) on the temporal frequency of (a) statically unstable translational sidewinding gaits and (b) statically unstable rotational sidewinding gaits on robot experiments. The subplots (i) and (ii) show the snapshots of robot implementing gaits in low temporal frequency (0.2Hz, red) and high temporal frequency (2.0Hz, blue) over three gait cycles.

Next, we evaluate the temporal frequency dependence of the rotational sidewinding gait from ([16]): $K_l = 1.5, K_v/K_l = 0.6, \phi_0 = \pi/2$. From our static stability analysis, the rotational sidewinding gait is not statically stable (static stability = 0.46). In addition, numerical simulation predicts that the rotational sidewinding gaits should lead to counter-clockwise rotation, in contrast with the results in ([16]). Therefore we suspect that the rotational sidewinding gait is driven by the unexpected touchdowns and therefore will be strongly temporal frequency dependent. Robot experiments verified that locomotion performance (Figure 2.24) in the rotational sidewinding gait is strongly correlated with the temporal frequency. Higher rotation angles are achieved when robot operated at low temporal frequency.

Stabilizing sidewinding using geometric mechanics

We observe that gaits with large vertical spatial frequencies have more distinct body-environment contact patches, and are therefore more statically stable than gaits with low spatial frequency in the vertical wave. Inspired by this observation, we will stabilize the originally unstable gaits by increasing the spatial frequencies of the vertical wave (*frequency modulation*). In other words, we gradually increase the V-L ratio, K_v/K_l , until the satisfactory static stability is reached. As discussed earlier, we consider a gait as statically stable when its static stability is greater than 0.5. Note that this threshold is selected for our experiments on flat terrain. If necessitated by conditions such as uneven terrain, the static stability threshold may be raised to improve the capability of the robot to remain statically stable even when some modules fail to follow the prescribed contact states (e.g., perturbed by the environment).

We then use geometric mechanics to coordinate the horizontal and vertical waves subject to different spatial frequency. We decomposed the internal shape of sidewinder robots into two independent traveling waves: a horizontal traveling wave and a vertical traveling wave. The horizontal traveling wave is prescribed by:

$$\theta_l(j, \tau_1) = A_l \sin\left(2\pi K_l \frac{j}{N} + \tau_1\right), \quad (2.35)$$

where τ_1 is the phase of the horizontal wave. Similarly, the contact state is prescribed as:

$$c(2i - 1, \tau_2) = c(2i, \tau_2) = \sigma\left(\sin\left(2\pi K_v \frac{i}{2N} + \tau_2\right)\right), \quad (2.36)$$

where τ_2 is the phase of the vertical wave that can uniquely determine the contact pattern. $c(i, \tau_2) = 0$ represents swinging-state and therefore no ground reaction force appears at link i at phase τ_2 .

The phases of the horizontal wave and the vertical wave then comprise the shape

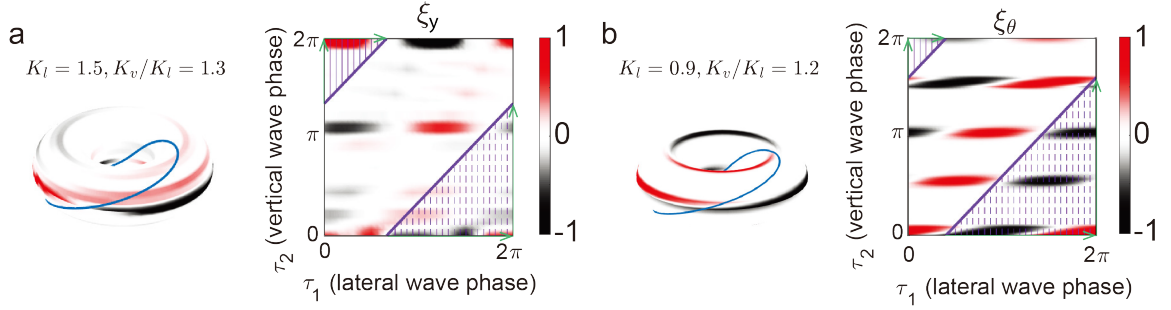


Figure 2.25: **Height functions to design gaits to produce motion in the desired direction.** Height functions on torus (*left*) and on unfolded Euclidean parameterization space (*right*) are shown. The height function for (a) horizontal spatial frequency $K_l = 1.5$, V-L ratio $K_v/K_l = 1.3$ in lateral direction (the direction perpendicular to body axis) and (b) horizontal spatial frequency $K_l = 0.9$, V-L ratio $K_v/K_l = 1.2$ in rotational direction. The purple curve in each plot maximizes the surface integral enclosed in the upper left corner (marked in solid lines) minus the surface integral enclosed in the lower left corner (marked in the dashed lines). The assistive lines are shown as lines with green arrows.

variable, $\tau = [\tau_1, \tau_2]^T$. Using the geometric mechanics gait design tools mentioned in Sec.subsection 2.5.1, we can calculate the height function and visualize the kinematics in the desired directions (translational and rotational).

A gait that coordinates the horizontal and vertical wave can be described as a function that maps τ_1 to τ_2 . From the structure of the height functions (see Figure 2.25), we observed that in the Euclidean parameterization space of the torus (where the edges are properly identified with each other at 0 and 2π), a straight line path gives rise to an optimal path; this is seen by the integral of the surface in the upper left minus the integral of the surface in the lower right being maximized. In this way, we characterize the coordination of the horizontal and the vertical wave by the relative phase lag: $\phi_0 := (\tau_2 - \tau_1 \bmod 2\pi)$.

We summarize our steps to stabilize the sidewinding gaits in Algorithm 1.

Stable sidewinding

We use our gait stabilization algorithms to stabilize the statically unstable translational and rotational sidewinding gaits. As discussed earlier, the translational sidewinding gait with 0.9 spatial wave is not statically stable. We show that we can stabilize this gait by increasing

Algorithm 1: Stabilizing sidewinding and turning gaits

```
1 Initialization:  $K_v/K_l = 1.0$ ;  
2 while Static Stability < 0.5 do  
3    $K_v/K_l \leftarrow K_v/K_l + 0.1$ ;  
4   CPR;  
5   Calculate height function (HF);  
6   Take  $\phi_0$  to maximize HF surface integral;  
7 end  
8 Perform numerical simulation  
9 Implement robot experiments
```

the V-L ratio K_v/K_l to 1.2. From the lateral height function (Figure 2.25), we take $\phi_0 = 1.076$ to optimize the surface enclosed in the lateral height function. The static stability analysis suggests that this gait is statically stable (static stability = 0.5). We implement this gait on robot experiments (Figure 2.26), which show that no significant turning was observed over our range of temporal frequencies.

Note that the stabilized translational sidewinding gait ($K_l = 0.9$, $K_v/K_l = 1.2$) exhibited effective lateral displacement. Robot experiments demonstrate that the average lateral displacement per gait cycle is 0.69 ± 0.02 body lengths per cycle, significantly greater than the displacement (0.42 ± 0.01 body length per gait cycle) of the translational sidewinding gait with 1.5 spatial waves ($K_l = 1.5$, $K_v/K_l = 1$).

We next stabilize the rotational sidewinding gait with 1.5 spatial waves, $K_l = 1.5$. We show that we can stabilize this gait by raising the V-L ratio K_v/K_l to 1.3. From the rotational height function (Figure 2.25), we take $\phi_0 = 1.02$ to optimize the surface enclosed in the rotational height function. The static stability analysis suggests that this gait is statically stable (static stability = 0.62). We implement this gait on robot (Figure 2.26), revealing that the locomotion performance (rotation per gait cycle) is robust over a range of temporal frequencies.

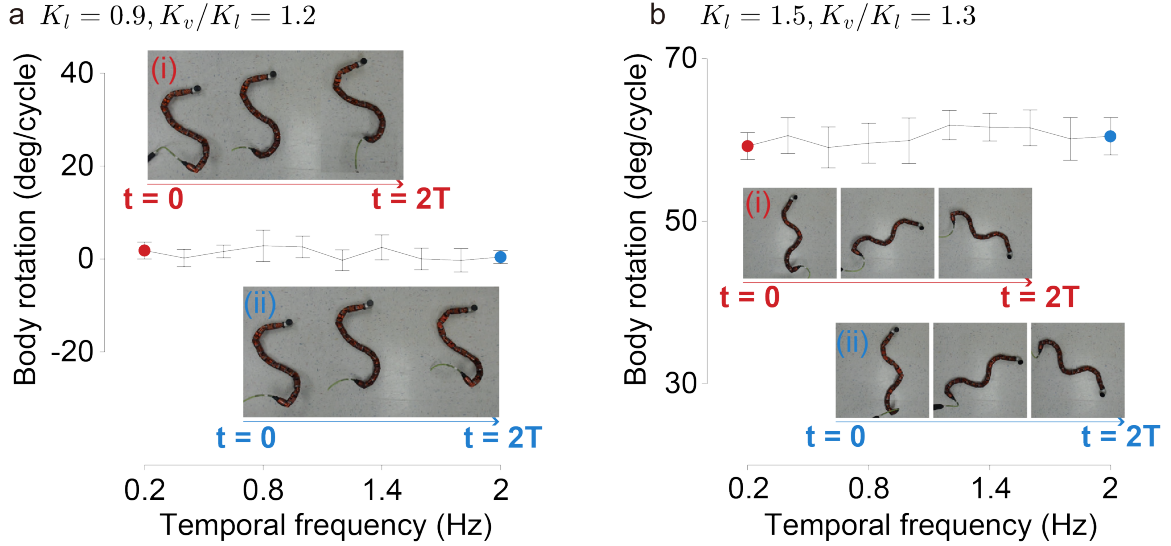


Figure 2.26: **Robustness of statically stable gaits as a function of temporal frequency.** Dependence of the rotation angle (per cycle) on the temporal frequency of (a) the stabilized translational sidewinding gaits and (b) the stabilized rotational sidewinding gaits on robot experiments. In both cases, the rotation angle is steady over a range of temporal frequencies. The unit and the axis labels in all panels are the same. The subplots (i) and (ii) show the snapshots of robot implementing gaits in low temporal frequency (0.2Hz, red) and high temporal frequency (2.0Hz, blue) over three gait cycles.

2.5.3 General Sidewinding Gait Formula

Empirical Sidewinding Governing Equation

As discussed earlier, the coordination pattern of horizontal and vertical waves in sidewinding locomotion has been well studied and documented ([146, 45, 16, 83, 126]). Some of the well-known sidewinding gaits are summarized in Table Table 2.1. In previous sections, we showed that there is a broad range of gait parameters that can produce pure translation or pure rotation. In this section, we explore the question of whether empirical equations governing sidewinding gait parameters exist and can be identified. Such equation can help us better understand the kinematic principles behind the seeming complex sidewinding motion.

First, we show in Figure 2.27 that when we fix the horizontal spatial frequency K_l and modulate the V-L ratio, the patterns of height functions change accordingly. Surprisingly,

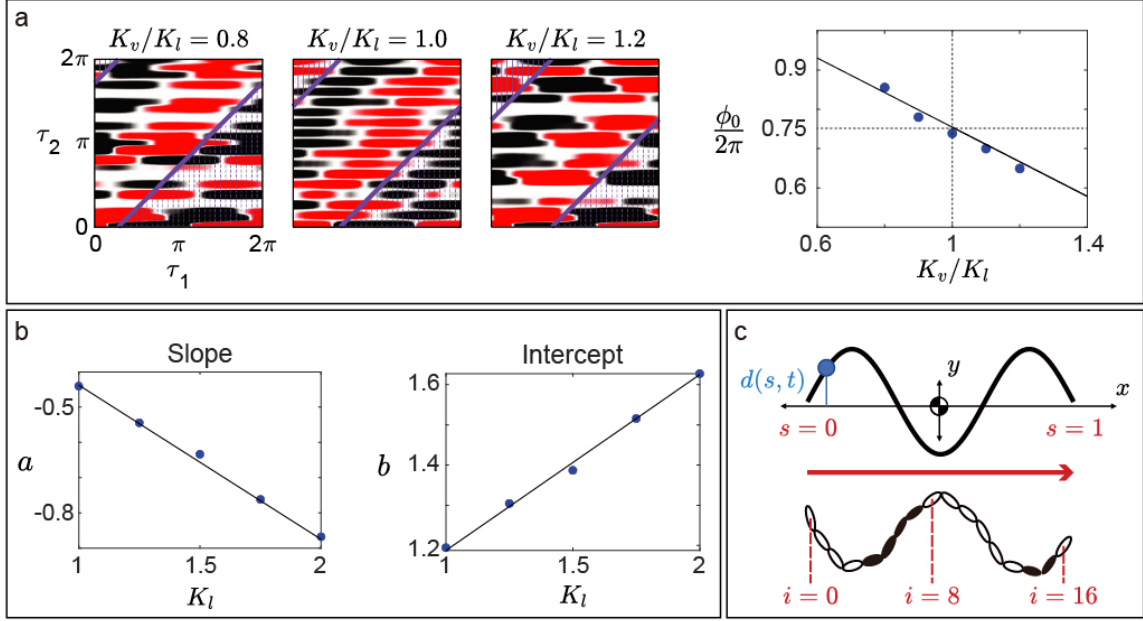


Figure 2.27: **Extended sidwinding gait formula.** (a) Height functions for different V-L ratio with fixed $K_l = 1.0$. We show that while we change the V-L ratio, the optimal phase ϕ_0 emerged to increase linearly from height function predictions. We then ran regression and find that $\phi_0/2\pi$ linearly correlates with V-L ratio K_v/K_l , under slopes $a = -0.44$ and intercept $b = 1.2$. (b) We then test how the slopes and intercept correlates with the horizontal spatial frequency K_l . It turns out that both the slope a and the intercept b linearly correlate with K_l ($a \sim -0.439K_l + 0.001, b \sim 0.439K_l + 0.750$). (c) A model to explain the empirical equations. We develop our model in CoM frame, neglecting the forward displacement (along the direction) of body segments, and only investigate the effect of lateral displacement.

we notice that the emerging ϕ_0 linearly correlates with the V-L ratio K_v/K_l , with slope $a = -0.44$ and intercept $b = 1.2$ ($R^2 = 0.96$). We then investigate how the slope and intercept are related to the horizontal spatial frequency K_l . From Figure 2.27, we see that both slope a and intercept b linearly correlate with K_l . Therefore, we can formulate an empirical function that governs the sidwinding gait parameters for the pure sideways translational motion ($R^2 = 0.98$):

$$\frac{\phi_0}{2\pi} = -0.438(K_v - K_l) + 0.750. \quad (2.37)$$

Similarly, we can obtain an empirical equation that governs the sidwinding gait parameters for backwards translation (enables pure sideways translation in the opposite direction

to the motion enabled by Equation 2.37, $R^2 = 0.98$):

$$\frac{\phi_0}{2\pi} = -0.438(K_v - K_l) + 0.250, \quad (2.38)$$

clockwise in-place turning (maximal area in rotation height function, $R^2 = 0.98$):

$$\frac{\phi_0}{2\pi} = -0.438(K_v - K_l) + 0.498, \quad (2.39)$$

and counterclockwise in-place turning (minimal area in rotation height function, $R^2 = 0.98$):

$$\frac{\phi_0}{2\pi} = -0.438(K_v - K_l) + 0.001. \quad (2.40)$$

Simple Model for Sidewinding Governing Equations

In this section, we develop a model to derive the conditions for sidewinding gaits that exhibit T-sidewinding and R-sidewinding.

Consider a continuous traveling wave (Figure 2.27) in the center of mass frame. The lateral displacement of a body segment can be expressed as:

$$d(s, t) = d_m \sin(\omega t - 2\pi K_l s)$$

where d_m is the amplitude of undulation. Its non swinging-state spans the period

$$\{t | t \in [\phi_0 + 2\pi K_v s, \phi_0 + 2\pi K_v s + \pi]\}.$$

To simplify the derivation, we use a linear expression $F = \beta v$ to model the ground reaction force instead of the discontinuous Coulomb friction. Although this linear expression differs from the Coulomb friction, it can offer reasonably good approximations, especially when v is small ([147]). In addition, the linear expression can also allow us to study the

kinematics analytically. In this way, the ground reaction force can be calculated as:

$$F(s, t) = \beta \frac{\partial d(s, t)}{\partial t} = f_m \cos(\omega t - 2\pi K_l s),$$

where f_m is the amplitude of ground reaction force. Then we can calculate the angular momentum contribution (w.r.t. CoM frame) at position s over a period as:

$$\begin{aligned} L(s) &= \int_{\phi_0 + 2\pi K_v s}^{\phi_0 + 2\pi K_v s + \pi} \left(s - \frac{1}{2}\right) f_m \cos(\omega t - 2\pi K_l s) \\ &= L_m \left(s - \frac{1}{2}\right) \sin(\phi_0 + 2\pi s(K_v - K_l)), \end{aligned}$$

where L_m is the amplitude of angular momentum. We then propose a sufficient condition for pure translation without rotation in locomotion as $L(s) + L(1 - s) = 0$, meaning that the angular momentum contributions from two body segments symmetric about the CoM cancel. Solving for $L(s) + L(1 - s) = 0$, we obtain:

$$\frac{\phi_0}{2\pi} = -\frac{1}{2}(K_v - K_l) + \frac{1}{4} + \frac{1}{2}k,$$

where $k \in \mathbb{Z}$.

In the discrete case, where in a N -link robot (or, a $(N - 1)$ -joint robot, N as an odd number), the central link is located at $i = \frac{N-1}{2}$, therefore the governing equation should be modified to:

$$\frac{\phi_0}{2\pi} = -\frac{N-1}{2N}(K_v - K_l) + \frac{1}{4} + \frac{1}{2}k. \quad (2.41)$$

In our case, $N = 17$, the analytic equation (Equation 2.41) and empirical equation ($k = 1$ for Equation 2.37 and $k = 0$ for Equation 2.38) are close in numerical values.

Similar to the pure translation without rotation situation, the maximal clockwise or counterclockwise in-place rotation situation can be expressed as: $L(s) = L(1 - s)$, where the angular momentum contribution from two body segments symmetric to CoM have the

same direction. Solving for $L(s) = L(1 - s)$, we can obtain the continuous case

$$\frac{\phi_0}{2\pi} = -\frac{1}{2}(K_v - K_l) + \frac{1}{2}k,$$

and discrete condition:

$$\frac{\phi_0}{2\pi} = -\frac{N-1}{2N}(K_v - K_l) + \frac{1}{2}k, \quad (2.42)$$

where $k \in \mathbb{Z}$. Notice that in our case, $N = 17$, Equation 2.42 are close to the empirical equations ($k = 1$ for Equation 2.39 and $k = 0$ for Equation 2.40).

2.6 Obtaining contact functions using geometric mechanics

The content in this subsection is adapted from a collaborative project with Tianyu Wang, who performed robophysical experiments, and Dr. Bo Lin, who performed mathematical derivation. My contribution in this project includes (1) designing the experiments, (2) conducting the numerical analysis, (3) writing the manuscript.

Earlier in this chapter, we showed that properly coordinated contact patterns allow for computationally tractable gait design and efficient gait performance. However, so far, we prescribed the contact functions from observations in biological systems. In other words, our capability to coordinate contact patterns are limited to the availability of biological insight. To explore beyond the observations from biological experiments, we need a framework to systematically design the contact patterns and their coordination with the internal shape changes. In this section, we will extend the geometric mechanics framework to design contact patterns.

2.6.1 Effect of drag anisotropy on translational locomotion

Locomotion effectiveness can be highly dependent on the ground reaction force. Specifically, while terrestrial limbless robots can achieve good mobility on granular media using lateral undulation, they often struggle on frictional ground [148]. We compare the height

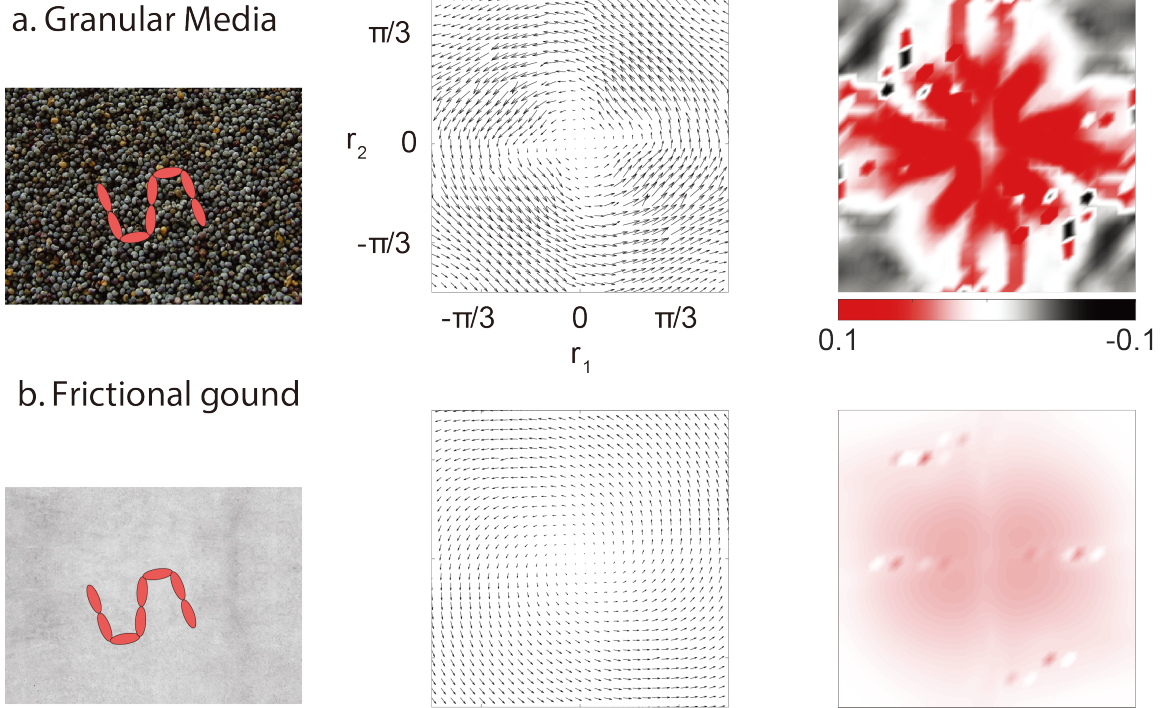


Figure 2.28: **Vector fields and height functions for an 8-link robot on granular media and frictional ground with continuous contact.** (a) A schematic sketch, vector field, and height function for an 8-link robot moving on granular media (poppy seeds). The height function has a large magnitude. (b) The sketch, vector field, and height function for a 8-link robot moving on frictional ground. The axes of all shape space are identical. The color bar of height functions in (a) and (b) are identical. The units of the color bar in the height functions are BL/π^2 .

function for an 8-link snake robot (with $K_s = 1.5$) moving on surface of a model granular media (poppy seeds) and frictional ground (Figure 2.28).

The ground reaction forces governing the interaction of body segments and granular media are well studied when moving on a granular surface. The forces F_{\perp} and F_{\parallel} [104] can be approximated by:

$$f_{\perp} = C \sin(\chi), f_{\parallel} = A \cos(\chi) + B(1 - \sin(\chi)) + F_0,$$

where χ is the attack angle; $C = 0.66$, $A = 0.27$, $B = -0.32$, $F_0 = 0.09$ is the empirically fitted function to characterize the granular media resistance force [149, 73]. From the structure and magnitude of its height function (Figure 2.28.a), we see that, with proper

gaits, the robot can move effectively on granular media as discussed in [73].

The ground reaction force between the body segments and the frictional ground can then be modelled by dry Coulomb kinetic friction:

$$f_{\perp} = f_0 \sin(\chi), f_{\parallel} = f_0 \cos(\chi),$$

where $f_0 = \mu F$ is the magnitude of the Coulomb kinetic friction, μ is the coefficient of friction and F is the magnitude of the normal supporting force. The height function (Figure 2.28.b) suggests that the robot has almost negligible speed regardless of the choices of gaits. However, it is important for limbless robots to move effectively on frictional ground. Inspired by the sidewinding snakes [103], limbless robots can greatly improve maneuverability by properly controlling their contact patterns [16].

2.6.2 Contact scheduling

Single Contact State

Consider a 12-link limbless robot moving on frictional ground. We assign a binary variable to each link, $c(i)$, such that $c(i) = 0$ denotes link i in swing phase (no contact) and $c(i) = 1$ denotes link i in stance phase (full contact). As we discussed earlier, the structure of the robot restricted that $c(2i) = c(2i - 1)$. I is the collection of all the links that are instantaneously in contact with the environment, $I = \{i \mid c(i) = 1\}$. For illustration purpose, we consider three examples of contact states: I_1 , I_2 , and I_3 :

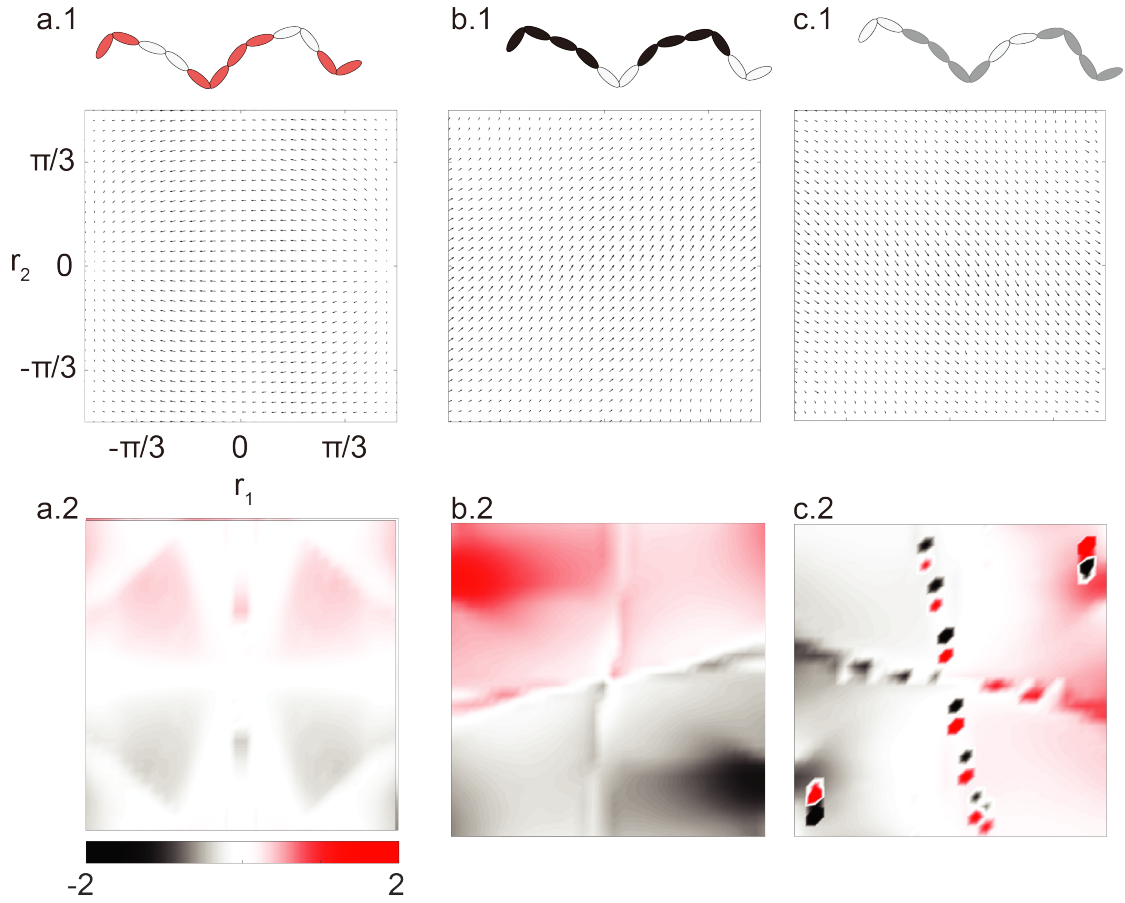


Figure 2.29: **Example of a mixed contact pattern.** (a-c) The vector fields and height functions for three contact states I_1 , I_2 , and I_3 . Corresponding robot links which are in contact with the environment are denoted by red, black and grey. The color bar of height functions in (a), (b), and (c) are identical. (d.1) The contact pattern prescribed by (Equation 2.43). (d.2) The vector field prescribed by (Equation 2.44). (d.3) The corresponding height function. The axes of all shape space are identical. The units of the color bar in all height functions are BL/π^2 .

Contact state	$c(1)$	$c(3)$	$c(5)$	$c(7)$	$c(9)$	$c(11)$
	$c(2)$	$c(4)$	$c(6)$	$c(8)$	$c(10)$	$c(12)$
I_1	1	0	1	1	0	1
I_2	1	1	0	1	1	0
I_3	0	1	1	0	1	1

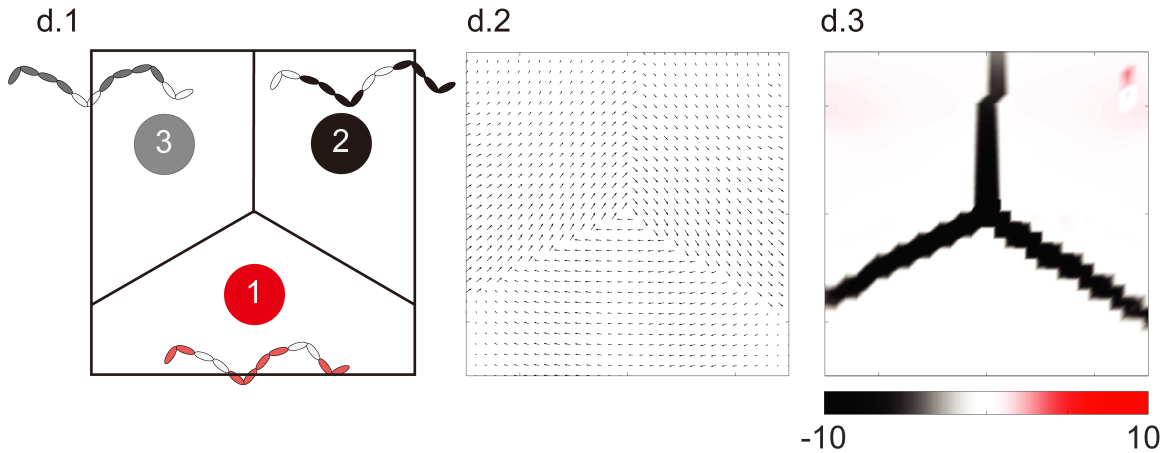


Figure 2.29: **Example of a mixed contact pattern (continued)** (d.3) The corresponding height function. The axes of all shape space are identical. The units of the color bar in all height functions are BL/π^2 .

Note that none of these contact states are dependent on r . Their realizations can be visualized in Figure 2.29.(a-c). For each contact state, we compute its vector field and height function in the lateral direction (Figure 2.29.(a-c)). We observe that in all cases, the height functions do not have regular patterns and their magnitude is low, which indicates limited mobility when a limbless robot uses a single contact state.

Mixed Contact State

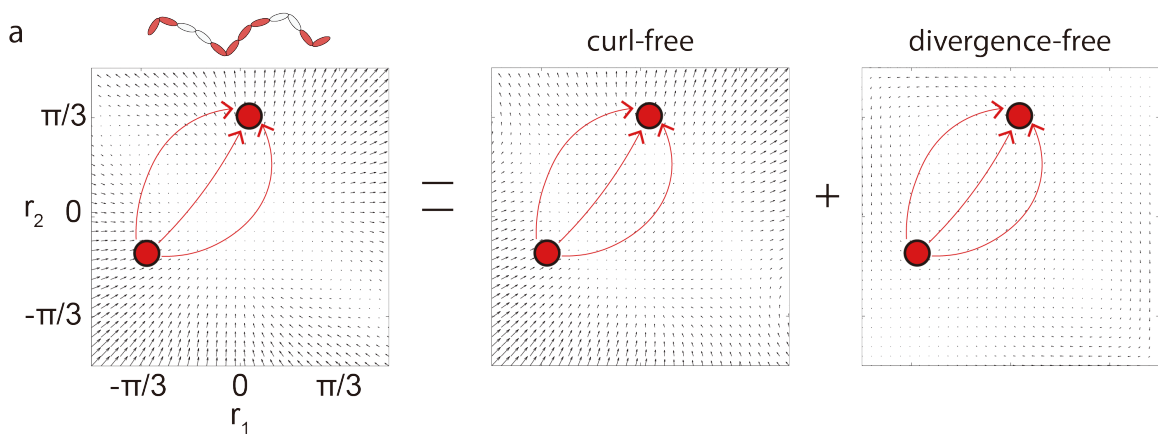


Figure 2.30: **Illustration of a contact pattern optimization.** (a) The vector field and its curl-free component and divergence-free component by the Hodge Helmholtz decomposition.

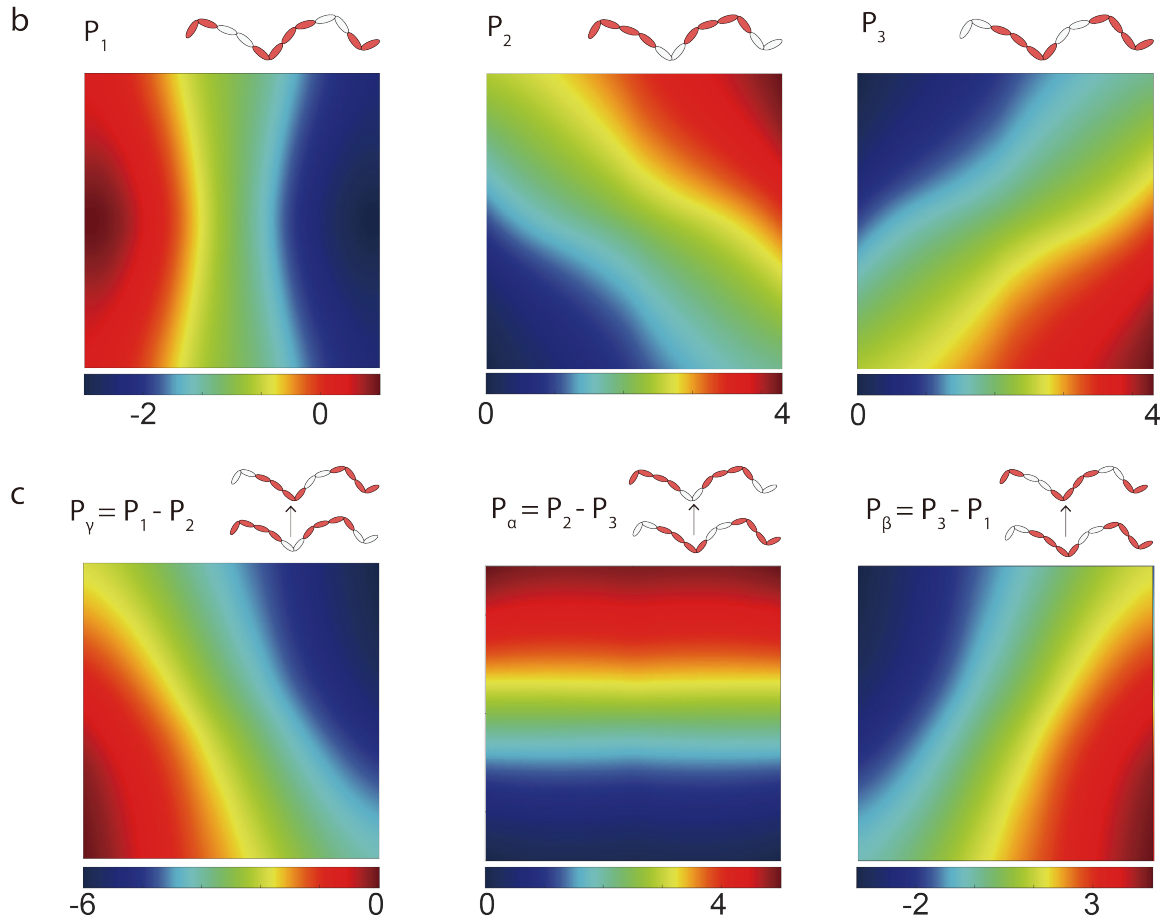


Figure 2.30: **Illustration of a contact pattern optimization (continued).** (b) The potential functions for P_1 , P_2 and P_3 . Note that, in curl-free components, the line integral is path independent, allowing us to compute the potential function to estimate the line integral between any points. (c) The potential function difference for $P_\gamma = P_2 - P_1$, $P_\alpha = P_3 - P_2$, and $P_\beta = P_3 - P_1$. The axes of all shape spaces are identical. The units of the color bar in all potential function differences are BL/π^2 .

Although each individual contact state cannot lead to effective displacement, we showed earlier that their combination can enable new motion behaviors. In this section, we evaluate the locomotion performance of mixed contact states. For example, we construct the contact state as:

$$I(r_1, r_2) = \begin{cases} I_1, & \text{if } \text{atan2}(r_2, r_1) \in (7\pi/6, 11\pi/6] \\ I_2, & \text{if } \text{atan2}(r_2, r_1) \in (\pi/2, 7\pi/6] \\ I_3, & \text{if } \text{atan2}(r_2, r_1) \in (-\pi/6, \pi/2] \end{cases} \quad (2.43)$$

where atan2 is the four-quadrant inverse tangent operator. In this way, we can rewrite the local connection as:

$$\mathbf{A}(r_1, r_2) = \begin{cases} \mathbf{A}_1, & \text{if } \text{atan2}(r_2, r_1) \in (7\pi/6, 11\pi/6] \\ \mathbf{A}_2, & \text{if } \text{atan2}(r_2, r_1) \in (\pi/2, 7\pi/6] \\ \mathbf{A}_3, & \text{if } \text{atan2}(r_2, r_1) \in (-\pi/6, \pi/2] \end{cases} \quad (2.44)$$

Its realization is shown in Figure 2.29.d.1. We then obtain the vector field and height function using (Equation 2.43) in Figure 2.29.d(2-3). Interestingly, the new height function has high magnitude and exhibits regular patterns (dark region along the boundary).

2.6.3 Optimal Contact Scheduling

Note that (Equation 2.43) is manually designed, inspired by biology and empirical experience [16, 83, 150]. Thus, the optimality of (Equation 2.43) remains unclear. To explore the optimization of contact patterns, we formulate the following optimization problem. To simplify our problem, we limit the number of contact states to be 3.

Problem 2. *Given 3 vector fields $\mathbf{A}_1^x, \mathbf{A}_2^x, \mathbf{A}_3^x$ in a shape space M , let p be any partition $M = M_1^p \cup M_2^p \cup M_3^p$ and it induces the vector field $\mathbf{A}_p^x(\mathbf{r})$ such that for $i = 1, 2, 3$,*

$$\mathbf{A}_p^x(\mathbf{r}) = \mathbf{A}_i^x(\mathbf{r}) \text{ if } \mathbf{r} \in M_i^p.$$

Let L^p be the set of closed loops l in M such that for $i = 1, 2, 3$, and assume that the intersection $l \cap M_i^p$ is simply connected. The objective function is

$$\max_{l,p} \oint_l \mathbf{A}_p^x(\mathbf{r}) d\mathbf{r} \quad \forall l \in L^p.$$

Since each region $l \cap M_i^p$ is simply connected, any two of them have a unique intersection point. We may define the following:

$$\begin{aligned} l_1 &= l \cap M_1^p, & l_2 &= l \cap M_2^p, & l_3 &= l \cap M_3^p \\ \{q_\beta\} &= l_1 \cap l_3, & \{q_\gamma\} &= l_1 \cap l_2, & \{q_\alpha\} &= l_2 \cap l_3. \end{aligned} \quad (2.45)$$

Then

$$\oint_l \mathbf{A}(\mathbf{r}) d\mathbf{r} = \sum_{i=1}^3 \int_{l_i} \mathbf{A}_i^x(r_1, r_2) d\mathbf{r}. \quad (2.46)$$

Note that in (Equation 2.46), each component is path-dependent, which is not desirable. From the Hodge-Helmholtz theorem, any vector field can be decomposed into the sum of a curl-free component, $(\mathbf{A}_1^x)_c$, and a divergence-free component, $(\mathbf{A}_1^x)_d$. In other words,

$$\mathbf{A}_1^x = (\mathbf{A}_1^x)_c + (\mathbf{A}_1^x)_d.$$

Note that in our applications, the curl-free component has a much greater magnitude than the divergence-free component (Figure 2.30.a). Therefore, we approximate the line integral in the original vector field by the line integral in the curl-free component from the Hodge-Helmholtz decomposition. Note that in the case where the divergence-free component has comparable magnitude as the curl-free component, we can use the divergence-free components to determine the paths connecting the intersections once we determine the partition.

For curl-free vector fields the line-integral is path-independent. Suppose the corresponding potential functions of the curl-free components are P_1^x, P_2^x, P_3^x , respectively (Fig-

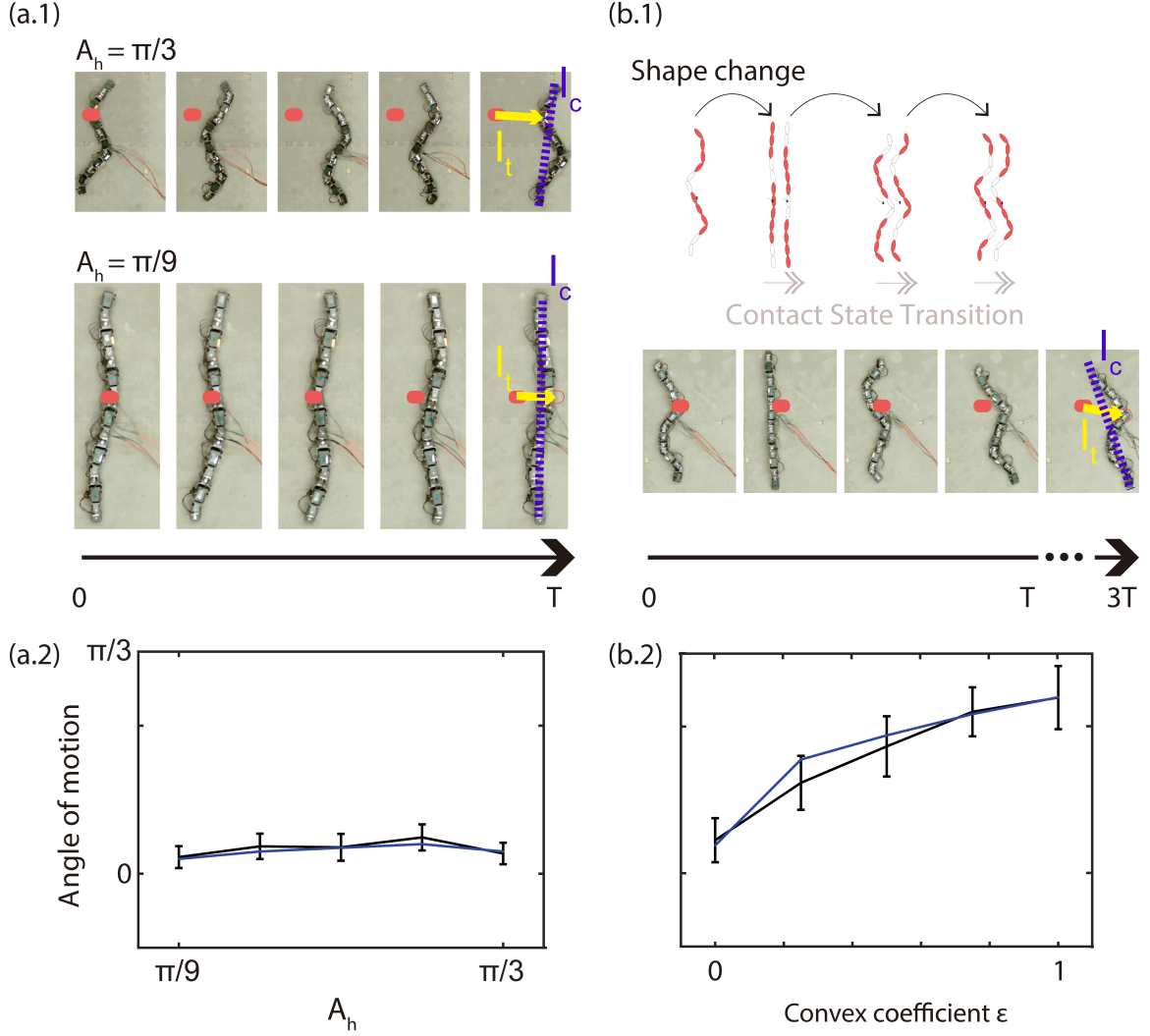


Figure 2.31: **Experiments on angle of motion modulation.** (a.1) Snapshots of robot implementing sidewinding gaits with different amplitudes using sinusoidal templates (Equation 2.33, Equation 2.33). The solid yellow arrow indicates the direction of motion l_t and the dashed blue line, l_c indicate the central body axis. The angle between l_c and l_t is then defined as the angle of motion. (a.2) For the sidewinding gaits using sinusoidal templates, the angle of motion is almost independent of the amplitude for robot moving in isotropic environments. The blue solid line represents simulation and the black line with error bars is robophysical experimental data. (b.1) Comparison of snapshots of the robot experiment and the simulation implementing the gait to modulate the angle of motion. (b.2) Modulation of the motion angle by controlling the convex coefficient ϵ .

ure 2.30.b). By the Fundamental Theorem of Calculus, we have

$$\int_{l_1} A_1^x(r_1, r_2) dr \approx \int_{l_1} (A_1^x)_c(r_1, r_2) dr = P_1^x(q_\beta) - P_1^x(q_\gamma).$$

The other two terms in (Equation 2.46) are decomposed similarly. Then our objective function becomes

$$\begin{aligned}
\oint_l \mathbf{A}(\mathbf{r})d\mathbf{r} &\approx (P_1^x(q_\beta) - P_1^x(q_\gamma)) + (P_2^x(q_\gamma) - P_2^x(q_\alpha)) \\
&\quad + (P_3^x(q_\alpha) - P_3^x(q_\beta)) \\
&= (P_3^x - P_2^x)(q_\alpha) + (P_1^x - P_3^x)(q_\beta) + (P_2^x - P_1^x)(q_\gamma) \\
&= P_\alpha^x(q_\alpha) + P_\beta^x(q_\beta) + P_\gamma^x(q_\gamma), \tag{2.47}
\end{aligned}$$

where $P_\alpha^x := P_3^x - P_2^x$, $P_\beta^x := P_1^x - P_3^x$, and $P_\gamma^x := P_2^x - P_1^x$ are the potential function difference (PFD) (Figure 2.30.c). Note that our objective function has separated parameters - the coordinates of $q_\alpha, q_\beta, q_\gamma$. In addition, the choices of p and l imply that all three intersection points could be arbitrary points in M . As a result, when (Equation 2.47) is optimized, so are the three individual terms in (Equation 2.47). Therefore, q_α is the point in M that optimizes the univariate function P_α^x . Parameters q_β, q_γ are characterized similarly.

Since the vector fields $\mathbf{A}^x(r)$ are given, so are the PFDs $P_\alpha^x, P_\beta^x, P_\gamma^x$. Thus we can find the optimal contact scheduling by solving these three individual optimization problems. In practice, if we discretize the values of $P_\alpha^x, P_\beta^x, P_\gamma^x$, we can apply numerical algorithms to solve these optimization problems.

Once $q_\alpha, q_\beta, q_\gamma$ are found, we can then choose a generic point q_0 in M (in practice, q_0 can be chosen to be the origin), and extend a curve connecting q and q_α to the boundary of M , which serves as the boundary between M_2^p and M_3^p . The other two boundaries are obtained by connecting and extending q, q_β and q, q_γ , and we obtain the partition p , which leads to the optimal contact scheduling.

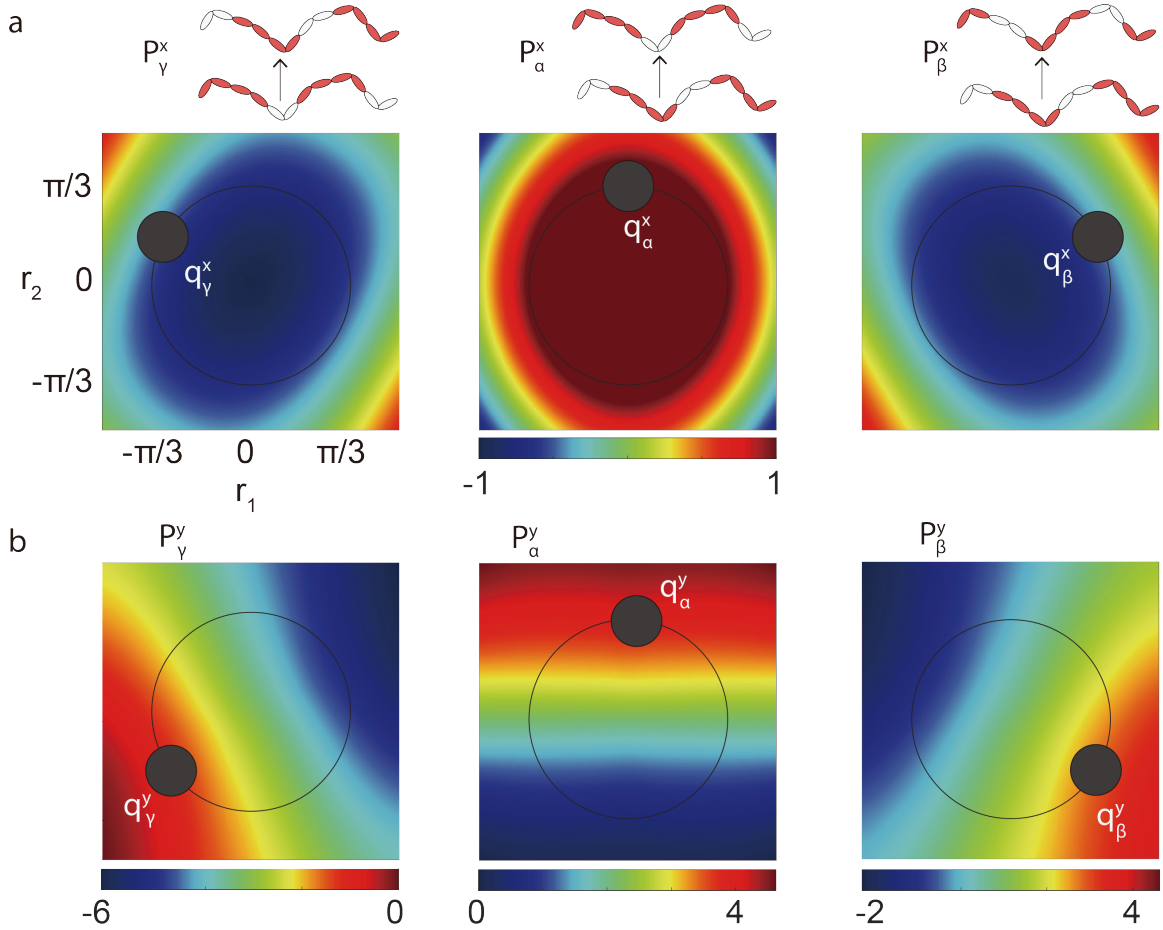


Figure 2.32: **Modulating the angle of motion using contact pattern optimization.** The potential function difference (PFD) in forward (a), lateral (b) and rotational (c) directions. The black circle indicate our joint angle limit: $\|[r_1, r_2]\|_2 \leq \pi/3$. The set of extreme points ($Q^x = \{q_y^x, q_\alpha^x, q_\beta^x, \}$) are chosen to maximize the sum of PFD in forward directions. The set of extreme points ($Q^y = \{q_y^y, q_\alpha^y, q_\beta^y, \}$) are chosen to maximize the sum of PFD in lateral directions. The axes of all shape spaces are identical. The color bar of PFD in (a) are identical. The units of the color bar in all PFDs are BL/π^2 .

2.6.4 Applications to more than 3 contact states

Our methods can be applied to systems with more than three states. However, in practice, it is surprisingly challenging to directly applying our methods to systems with more than three contact states. In fact, the contact pattern design problem is an NP-hard problem which can be reduced to the *longest path problem* from discrete optimization [151, p. 114]. We refer the readers to [152] for a detailed discussion on the applications to systems with

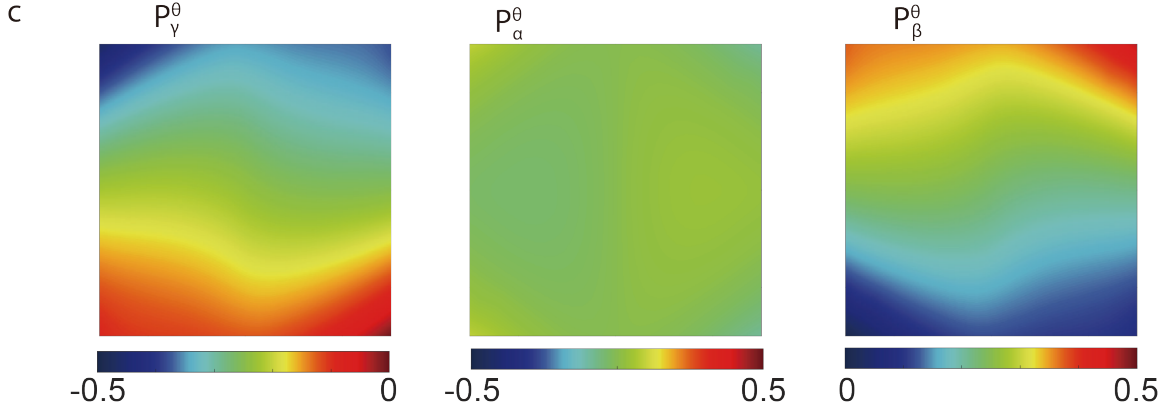


Figure 2.32: **Modulating the angle of motion using contact pattern optimization (continued)**. The potential function difference (PFD) in forward rotational directions. The units of the color bar in all PFDs are BL/π^2 .

more than 3 contact states.

2.6.5 Application: modulating sidewinding angle of motion

As discussed earlier, the track angle (the angle between the direction of motion and the trajectories of the “tracks” made by body-environment contact) can be modulated by the amplitude of the horizontal wave, A_l . On granular media, the measurement of track angle can give an approximation to the angle of motion (the angle between the direction of motion and the central axis of snake body) [83]. Here, we tested the sidewinding gaits with a range of amplitudes of the horizontal wave A_l , from 20 to 60 degrees, on a 12-link limbless robot moving on frictional ground. We found through experiments that the angle of motion is almost independent of the amplitude (Figure 2.31.a). Given the low effectiveness of altering the horizontal amplitude on the motion angle modulation, we sought to design a general control scheme that would modulate this angle of motion in isotropic environments.

We then applied our method to design sidewinding gaits for a 12-link robot. Following the method introduced in Sec. II, we computed the potential function difference in forward, lateral, and rotation directions (Figure 2.32). First, we identified the three transitional points that maximized the displacement in lateral directions, $Q^y = \{q_\alpha^y, q_\beta^y, q_\gamma^y\}$. Note that we limited the joint angle to $\pi/3$, i.e., $\| [r_1, r_2] \|_2 < \pi/3$. We then identified the three

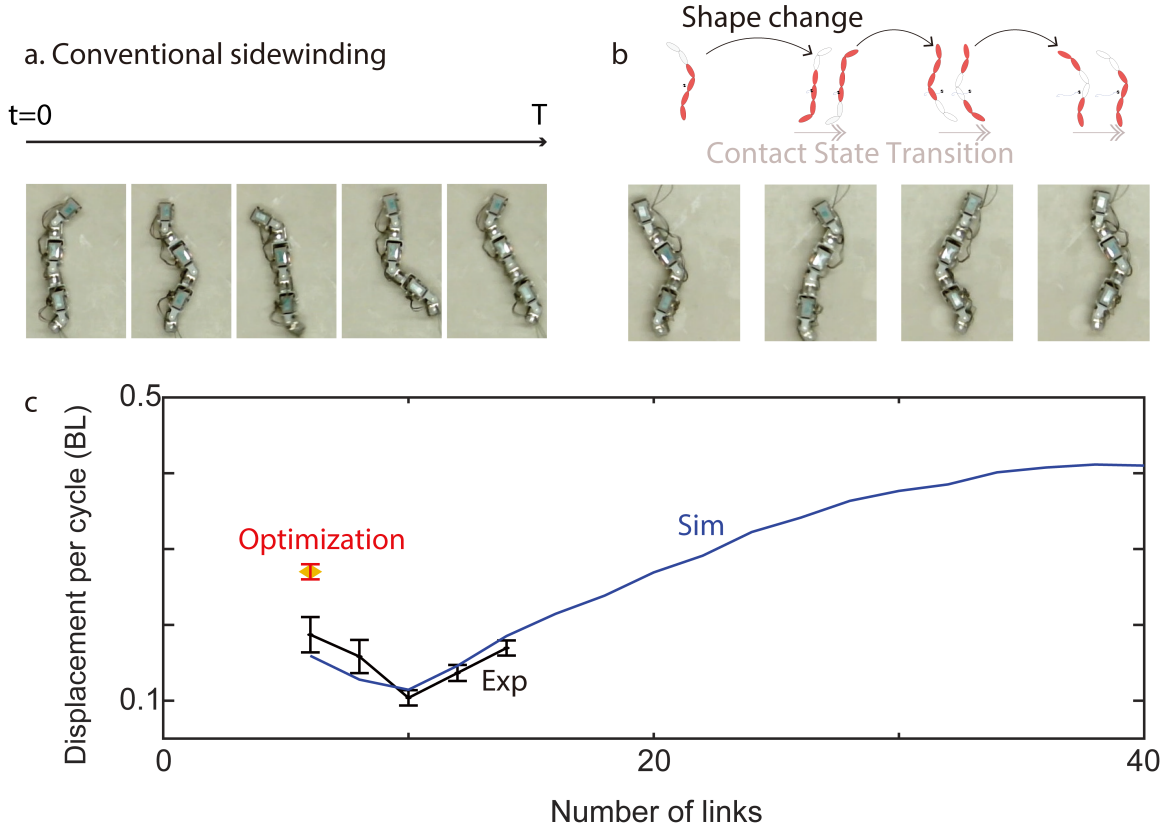


Figure 2.33: **Sidewinding with fewer number of links.** (a) Snapshots of a 6-link robot implementing the sidewinding gait with the sinusoidal templates ((Equation 2.33), (Equation 2.33)). (b) Snapshots of a 6-link robot implementing the sidewinding gait with our optimization method. (c) The sidewinding speed (in unit BL per cycle) as a function of link numbers (sidewinding gait is prescribed using the sine wave template). The blue solid line represents simulation and the black line with error bars is robophysical experimental data. The speed decreases as the link number decreases until $N = 10$. For $N < 10$, the configuration is unstable and turning emerged. The speed of the gait with our optimization method is highlighted as a diamond marker.

transitional points that maximized the displacement in forward direction, $Q^x = \{q_\alpha^x, q_\beta^x, q_\gamma^x\}$.

We observed that the transitional points Q^y can only lead to pure translation (i.e., zero in forward and rotational directions). Further, the transitional points determined by Q^x can lead to effective displacement in both forward and lateral directions, and thus establish a finite angle. In this way, we propose to modulate the angle of motion by a convex combination of Q^y and Q^x :

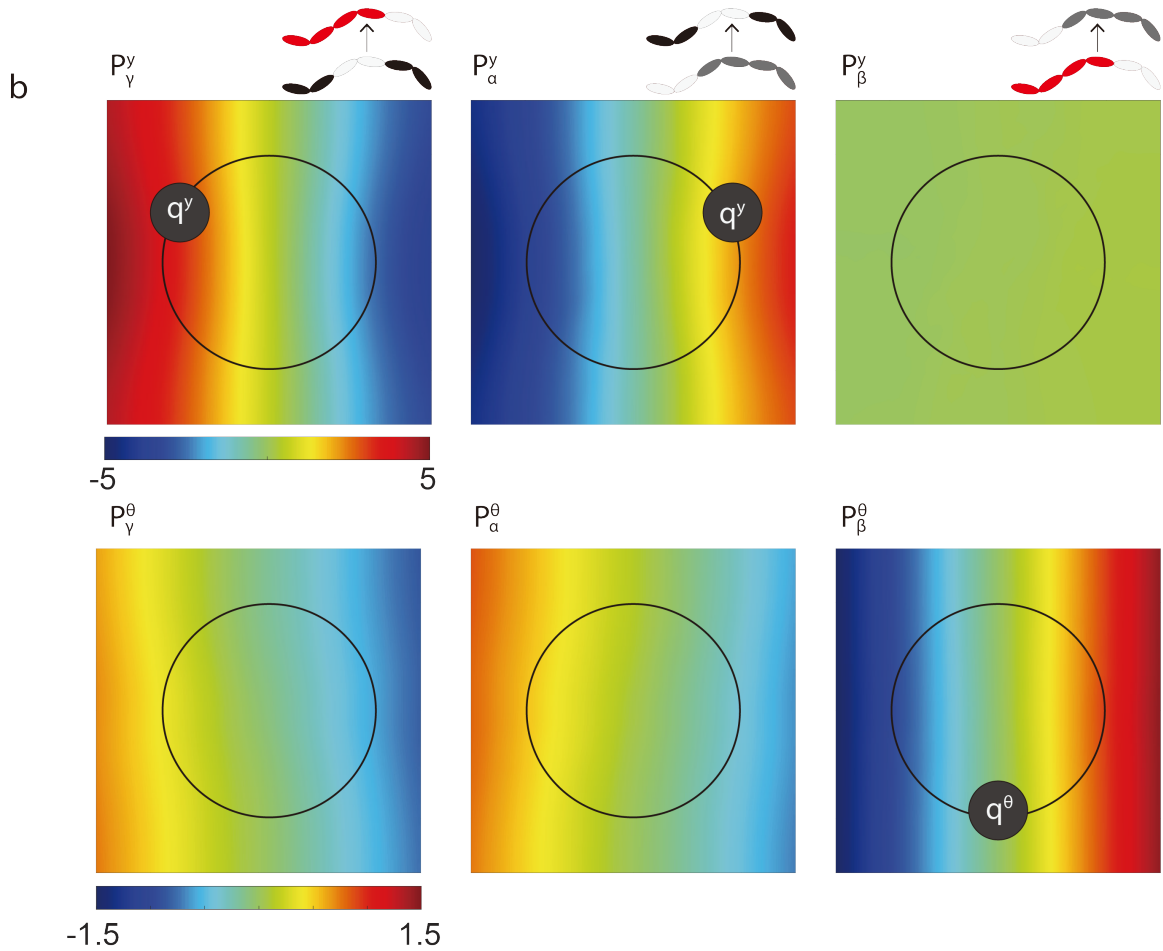


Figure 2.34: **Designing sidewinding gaits for a 6-link robot.** (a) Three stable contact patterns and their corresponding vector fields.

$$Q(\epsilon) = \epsilon Q^x + (1 - \epsilon)Q^y, \quad (2.48)$$

where $\epsilon \in [0, 1]$ is the coefficient of the convex combination, and $Q(\epsilon)$ are the transition points determined by the convex coefficient ϵ .

In this way, using (Equation 2.48), we formulated an equation to modulate the angle of motion. As shown in Fig Figure 2.31b, data from robophysical experiments agreed with our predictions, verifying the validity of our theoretical approach. As such, we have shown that our method is effective in modulating the angle of motion for limbless sidewinding robots in isotropic environments.

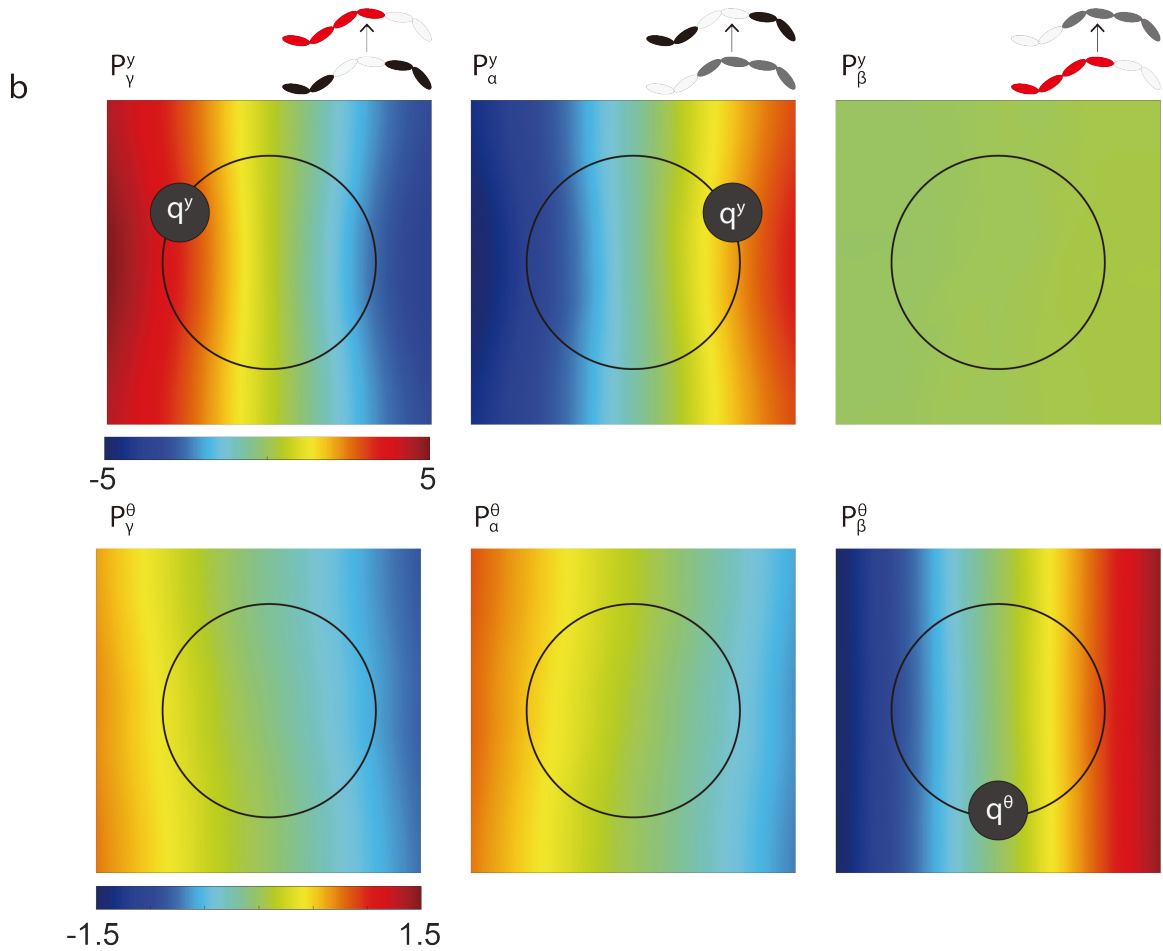


Figure 2.34: **Designing sidewinding gaits for a 6-link robot (continued).** (b) The PFD of lateral and rotational directions. The color bars of PFD are identical in three illustrations. The black circle indicates the robot's joint angle limit: $\|[r_1, r_2]\|_2 \leq \pi/3$.

2.6.6 Sidewinding of a 6-link Robot

While limbless robots have advantages in confined spaces, one of their major restrictions is longitudinal length. In other words, in certain applications such as search and rescue in obstacle-rich environments, it could be desirable to have robots with short body length but high locomotive performance in sidewinding. However, there is often a trade-off between the body length and the locomotive performance for limbless robots: if the size of the motor is fixed, it is only possible to reduce the size of the robot by decreasing the number of motors, i.e., decreasing the degrees of freedom. The disadvantage of fewer motors can be slower locomotion speed. As shown in [153], even when executing the same gait, robots

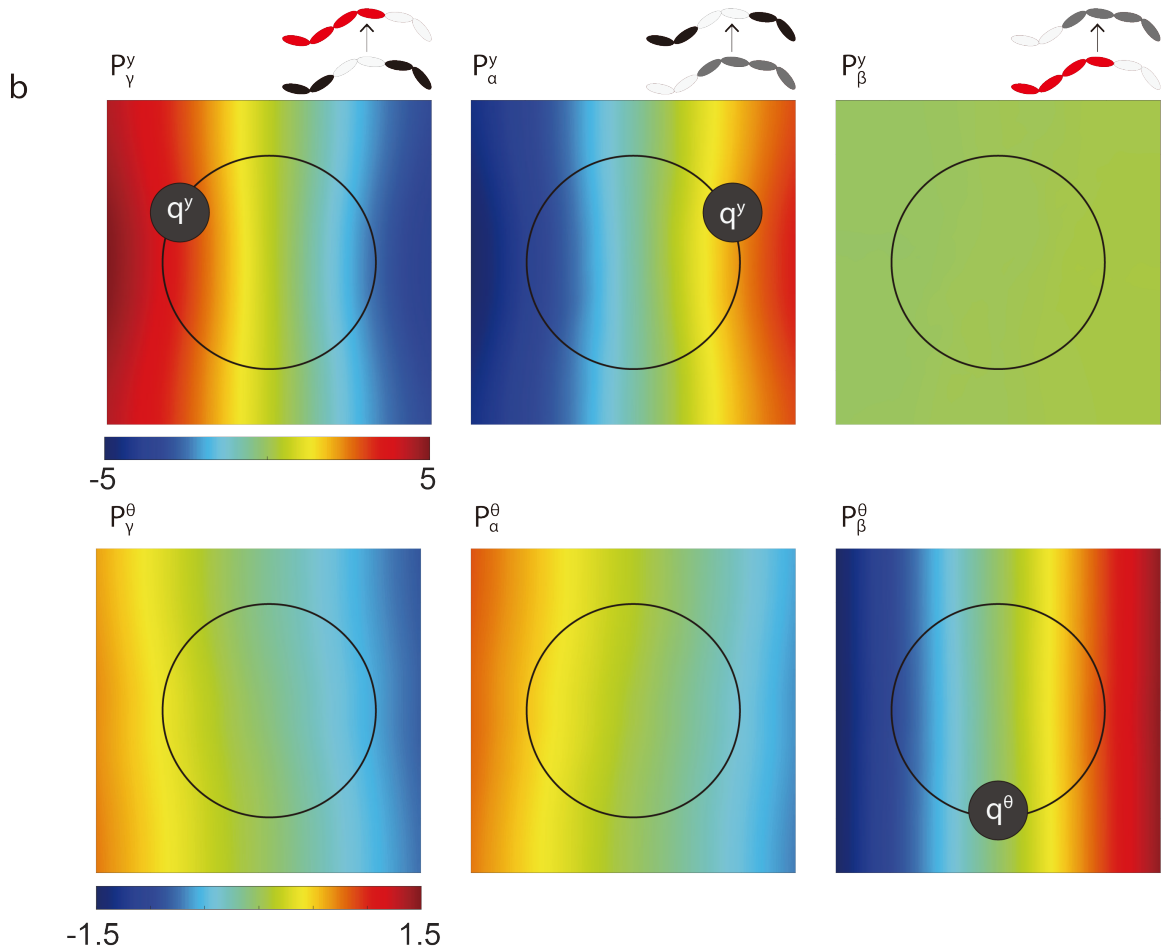


Figure 2.34: **Designing sidewinding gaits for a 6-link robot (continued).** (c) The boundary of each contact state, the vector field, and the height function with the optimal contact pattern, determined from the obtained transitional points. The units of color bar in height function are BL/π^2 .

with few motors have lower speed than those with more motors.

We conducted a series of experiments using the same motion equations but different numbers of motors. Specifically, we fixed the parameters $A_l = \pi/3$, $A_v = \pi/9$, $K = 1.5$, and $f = 0.1$ and evaluated the relationship between the speed and the number of motors, N . The experimental results are shown in Figure 2.33. As expected, the displacement decreased as the number of motors decreased until $N = 10$. Turning behavior emerged at $N < 10$, which can be caused by the unstable configurations in the gaits. These unstable turning behaviors led to high variability in speed, which we attribute to instability. An example of the unstable turning behavior for $N = 6$ can be found in the supplementary video.

We then used our method to design effective sidewinding gaits for the 6-link robot. We first identified three stable contact patterns for this 6-link robot such that the center of mass is enclosed by the supporting polygon. Using the methods introduced in Sec. II, we obtained the potential function difference in lateral directions (P_γ^y , P_α^y , and P_β^y) and rotational directions (P_γ^θ , P_α^θ , and P_β^θ). Interestingly, we noticed that the magnitude of P_β^y is significantly lower than those in P_γ^y and P_α^y . Therefore, the lateral speed is almost independent of the choice q_β ; and given q_γ and q_α , we are free to choose q_β such that the net rotation is zero.

Given the transitional points, we interpreted the boundary of these contact states as the half line connecting origin and chosen transitional points. We then computed the corresponding vector field and height function.

We implemented our designed gaits in robot experiments. The experimental data shows quantitative agreement with the theoretical predictions. Interestingly, we noticed that with proper design of the contact pattern, the speed of the 6-link robot can even out-perform those with 12 links (Figure 2.33.c).

2.7 Design gaits for obstacle aided locomotion

The content in this subsection is adapted from a collaborative project with Tianyu Wang, who performed robophysical experiments. My contribution in this project includes (1) designing the experiments, (2) conducting the numerical analysis, (3) writing the manuscript.

Limbless locomotors have the potential to move through tightly cluttered environments that conventional robots cannot. In cluttered environments, it is inevitable that such robots will interact with their environment to locomote. Despite recent advances in obstacle-aided locomotion (OAL), gait design in obstacle-rich environments remains difficult. In earlier sections, we showed that geometric mechanics is a powerful tool for designing gaits for limbless locomotion. However, the use of geometric mechanics has thus far been limited to homogeneous environments. In this section, we expand the scope of geometric mechanics

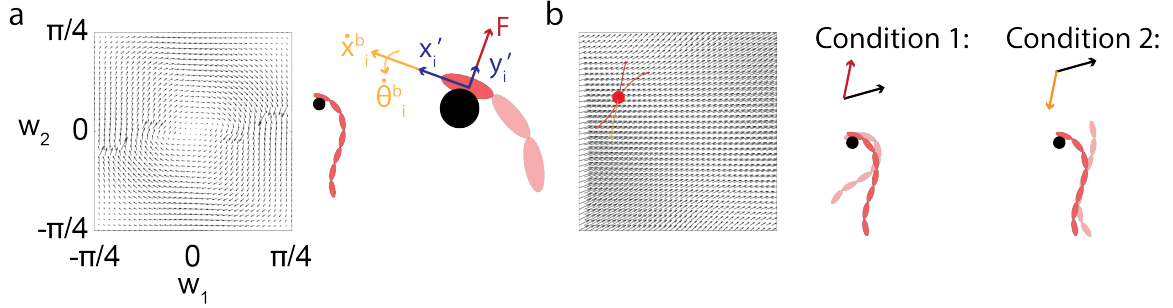


Figure 2.35: **Modeling interactions between robot and obstacles** (a) (Left) The vector field V_1 assuming the obstacle has interactions with the head link ($i_o = 1$). (Right) Force relationship illustrations for interactions between robot and obstacle. (b) (Left) The vector field V_2 assuming the obstacle has interactions with the head link ($i_o = 1$). (Right) The two conditions (Sec.subsubsection 2.7.1 and Sec.subsubsection 2.7.1)

to design gaits in heterogeneous environments.

2.7.1 Modeling Interaction with Obstacles

In the previous section, we introduced a derivation of the local connection vector field in homogeneous environments. In heterogeneous environments, the interactions with obstacles can often lead to changes in force and torque balance, and thus changes in the connection vector field. In this section, we establish a new method to numerically calculate the connection vector field, respecting the interactions between the robot and obstacles in its environment.

For simplicity, we only consider one obstacle in contact with the robot. Index i_o denotes the link of contact. We assume that i_o does not change in each obstacle-interaction instance. Our assumptions can later be justified in robot experiments, which reveal that transient contact with an obstacle typically involves a single link of contact.

For simplicity, our analysis below assumes that the obstacle resides on the left hand side (LHS) of link i_o . The analysis for the right hand side (RHS) obstacle will be symmetric to our analysis below. Existence of the obstacle will restrict the lateral body velocity $\xi_y \geq 0$. In this way, there are two mutually exclusive conditions for the lateral body velocity:

$$\dot{y}_1^b > 0$$

In this case, the robot will leave the obstacle. In this way, original force and torque balance are still valid to determine the local connection vector field (adapted from Equation 2.14 and Equation 2.18):

$$\mathbf{F} = \sum_{i \in I} \left[\mathbf{F}_{\parallel}^i \left(\begin{bmatrix} \dot{x}_1^b \\ \dot{y}_1^b \\ \dot{\theta}_1^b \end{bmatrix}, \mathbf{w}, \dot{\mathbf{w}} \right) + \mathbf{F}_{\perp}^i \left(\begin{bmatrix} \dot{x}_1^b \\ \dot{y}_1^b \\ \dot{\theta}_1^b \end{bmatrix}, \mathbf{w}, \dot{\mathbf{w}} \right) \right] = 0. \quad (2.49)$$

$$\dot{y}_1^b = 0$$

In this case, the robot will remain in contact with the obstacle. If we assume that the friction between the robot and the obstacle is negligible, then the net force from obstacle to robot (F) will align with the lateral direction (y'_i) of the body frame in link i_0 . In the body frame of link i_0 , the interaction between the obstacle and the robot only contributes in the lateral direction. In other words, the force and torque balance in forward and rotational directions are independent from the interactions with obstacles. In this way, we can rewrite Equation 2.49 into:

$$\mathbf{F} = \sum_{i \in I} \left(\mathbf{F}_{\parallel}^i \left(\begin{bmatrix} \xi_x \\ 0 \\ \xi_{\theta} \end{bmatrix}, \mathbf{w}, \dot{\mathbf{w}} \right) + \mathbf{F}_{\perp}^i \left(\begin{bmatrix} \xi_x \\ 0 \\ \xi_{\theta} \end{bmatrix}, \mathbf{w}, \dot{\mathbf{w}} \right) \right) = \begin{bmatrix} 0 \\ F \\ 0 \end{bmatrix}. \quad (2.50)$$

In Equation 2.50, there are two variables and two equality constraints, allowing us to numerically determine the local connection vector field.

2.7.2 Direction of \dot{y}_1^b

We determine the direction of \dot{y}_1^b by checking solving Equation 2.49. Specifically, we can numerically find \dot{y}_1^b from Equation 2.49. If the obtained \dot{y}_1^b is positive, then we confirm that condition subsection 2.7.1 is active. Otherwise, condition subsection 2.7.1 is self-

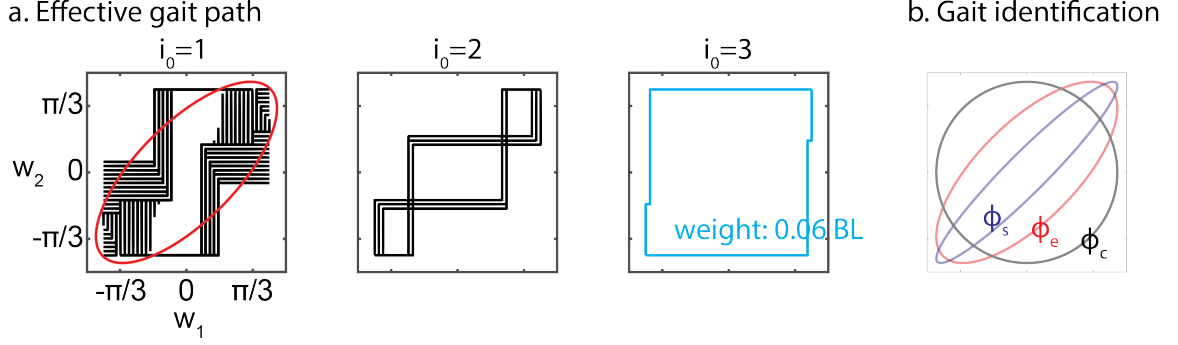


Figure 2.36: **Identification of gaits** (a) Numerically computed effective gait paths for $i_0 = \{1, 2, 3\}$. In (left) and (mid) panels, we showed the effective gait paths with weight higher than 0.1 body length. In (right) panel, we showed the gait path with the highest weight (0.06 body length). (b) Comparison between circular-wave (ϕ_c), elliptical-wave (ϕ_e), and standing-wave (ϕ_s) gaits.

contradictory, which leads to condition subsection 2.7.1 being active. Further, from Equation 2.19, the lateral velocity \dot{y}_1^b can be approximated by:

$$\dot{y}_1^b = \mathbf{A}_y(\mathbf{w})\dot{\mathbf{w}},$$

where $\mathbf{A}_y(\mathbf{w})$ is the second row of the local connection matrix $\mathbf{A}(\mathbf{w})$. If $\mathbf{A}_y(\mathbf{w})\dot{\mathbf{w}} > 0$, then condition subsection 2.7.1 is active, If $\mathbf{A}_y(\mathbf{w})\dot{\mathbf{w}} \leq 0$, then condition subsection 2.7.1 is not active, indicating condition subsection 2.7.1 is active (condition subsection 2.7.1 and subsection 2.7.1 are mutually exclusive).

2.7.3 Gait Design

With the above model, we can now design gaits for limbless robots in obstacle-rich environments. With the optimal gait, the robot should take the best advantage of each obstacle-interaction and leave the obstacle only when necessary. Consider the joint angle limit being θ_m ($w_1, w_2 \in [-\theta_m, \theta_m]$). Let $\Phi = \{\phi : [0, T] \rightarrow [-\theta, \theta] \times [-\theta, \theta]\}$ be the collection of all paths in the shape space; let V_1 be the local connection vector field generated from condition subsection 2.7.1 (Equation 2.50); and $V_2 = \mathbf{A}_y(\mathbf{w})$. The gait optimization problem becomes:

Problem 3. Find the path $\phi \in \Phi$, subject to: $\frac{d\phi(t)}{dt} \cdot V_2(\phi(t)) > 0 \forall t \in [0, T]$, such that $\int_0^T \frac{d\phi(t)}{dt} \cdot V_1(\phi(t)) dt$ is maximized.

Assuming $i_0 = 1$, we showed an example of V_1 and V_2 in Figure 2.35.

a. Half-cycle displacement

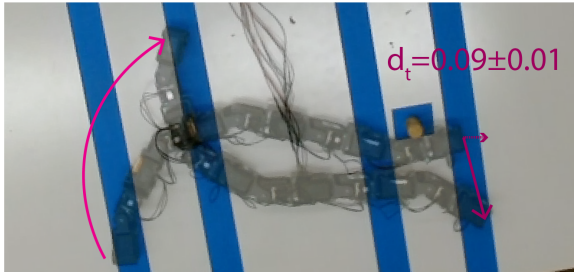
Standing wave



Elliptical wave



Traveling wave



b. Range of beneficial obstacle

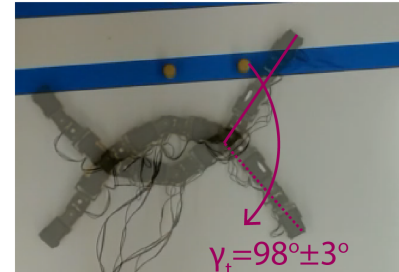
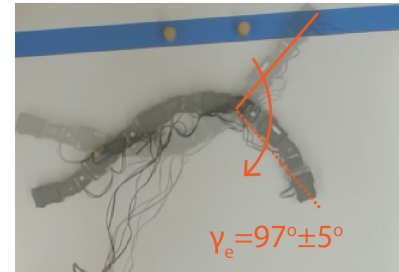
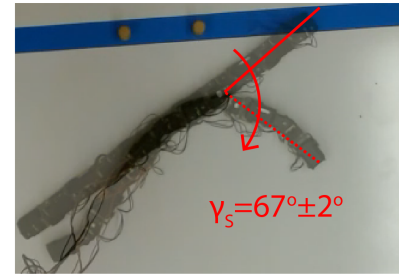


Figure 2.37: **Single post experiments** (a) The half-cycle displacements for different gaits are measured. We illustrated configurations before and after interaction with the obstacle. The net forward displacement d (net displacement along the direction of motion) is labelled with a dashed arrow. The net displacement (forward and lateral) is labeled with a solid arrow. BL denotes body length. The purple arrows indicate the direction of motion over the half gait cycle. (b) The ranges of beneficial obstacles are measured. We illustrated the starting and ending configuration where the interaction with the obstacle is beneficial. γ is measured to quantify the ranges of beneficial obstacles.

2.7.4 Numerical Optimization

In practice, we discretize the shape space into a $(n + 1) \times (n + 1)$ lattice grid, where n is a suitable positive integer. The values of V_1 and V_2 are then numerically calculated at the grid points: $V_i(x, y) = \left[V_{i,1}(x, y), V_{i,2}(x, y) \right]$ where $i = 1, 2$ and (x, y) is a discretized element in the shape space. We optimize ϕ among lattice paths with horizontal and vertical line segments. V_2 is one part of the vector fields for locomotion in isotropic environment; thus it is reasonable to assume that V_2 is a conservative vector field [154, 155, 148]. Then we can compute a potential function $P(x, y)$ defined on the shape space such that V_2 is the gradient of $P(x, y)$.

We consider a weighted directed graph $G = (U, A)$, where the set of vertices U consists of the $(n + 1) \times (n + 1)$ lattice points⁹. In this way, at each vertex $u = (x, y) \in U$, there are 4 adjacent vertices: $\{(x \pm 1, y), (x, y \pm 1)\}$. The arcs are constructed in the following way:

- (i) If $P(x + 1, y) > P(x, y)$, then we add an arc from (x, y) to $(x + 1, y)$ with weight $V_{1,1}(x, y)$ to A ;
- (ii) If $P(x - 1, y) > P(x, y)$, then we add an arc from (x, y) to $(x - 1, y)$ with weight $V_{1,1}(x, y)$ to A ;
- (iii) If $P(x, y + 1) > P(x, y)$, then we add an arc from (x, y) to $(x, y + 1)$ with weight $V_{1,2}(x, y)$ to A ;
- (iv) If $P(x, y - 1) > P(x, y)$, then we add an arc from (x, y) to $(x, y - 1)$ with weight $V_{1,2}(x, y)$ to A ;

Thus, the existence of an arc $a_{ij} \in A$ (from vertex u_i to u_j , $u_i, u_j \in U$) indicates that the move from u_i to u_j has positive dot product in V_2 . The weight of a_{ij} denotes the line integral from u_i to u_j along V_1 .

⁹We chose the symbol U (instead of V) to represent the collections of vertex to avoid notation confusion with $V_{1,2}$ as vector fields

Lemma 4. *G is a directed acyclic graph (DAG).*

Proof of Lemma 4. Let C be a directed cycle in G . From our previous assumptions, every arc in C has positive dot products in V_2 . Thus, the sum of all dot products of arcs in C and V_2 must be strictly positive. This indicates that there exists a path in a conservative vector field (V_2) with positive strictly line integral, which violates our assumption. Therefore, there is no directed cycle in G . \square

With the aforementioned notation, a discretized version of Problem 3 becomes

Problem 5. *Find a simple directed path in $G = (U, A)$ with maximal weight.*

It is well-known that Problem 5 in a DAG has a linear-time algorithm if the starting point is fixed [156, p. 661]. So we can run this algorithm once for each vertex in U to solve Problem 5. Since $|U| = (n + 1)^2$, our algorithm has time complexity $O(n^4)$.

2.7.5 Gait Identification

From the algorithms introduced earlier, we solved Problem 3 and identified the optimal gait path ϕ_{LHS}^* . Specifically, we sampled (over the discretized shape space) the initial and end points, and saved the effective gait paths (with the weights greater than 0.1 body length). In Figure 2.36, we showed the collection of all effective gait paths. We noticed that the most effective gaits emerged when $i_0 = 1$: the head link being the link of contact. Both the weights and the number of effective gait paths decrease dramatically as the link of contact advances from the head link to mid-body links. Specifically, the maximum weight for $i_0 = 3$ is approximately 0.06 body length, much less effective than the maximum weight for $i_0 = 1$ (0.15 body length). Thus, we hypothesized that it is beneficial to use the head link to make interactions with obstacles for effective OAL.

To seek a simple differentiable path, we fit the effective gait paths with an oriented ellipse. An ellipse with flatness (defined as the ratio of short-axis and long-axis) around 0.5 can reasonably fit the numerically optimized gait path.

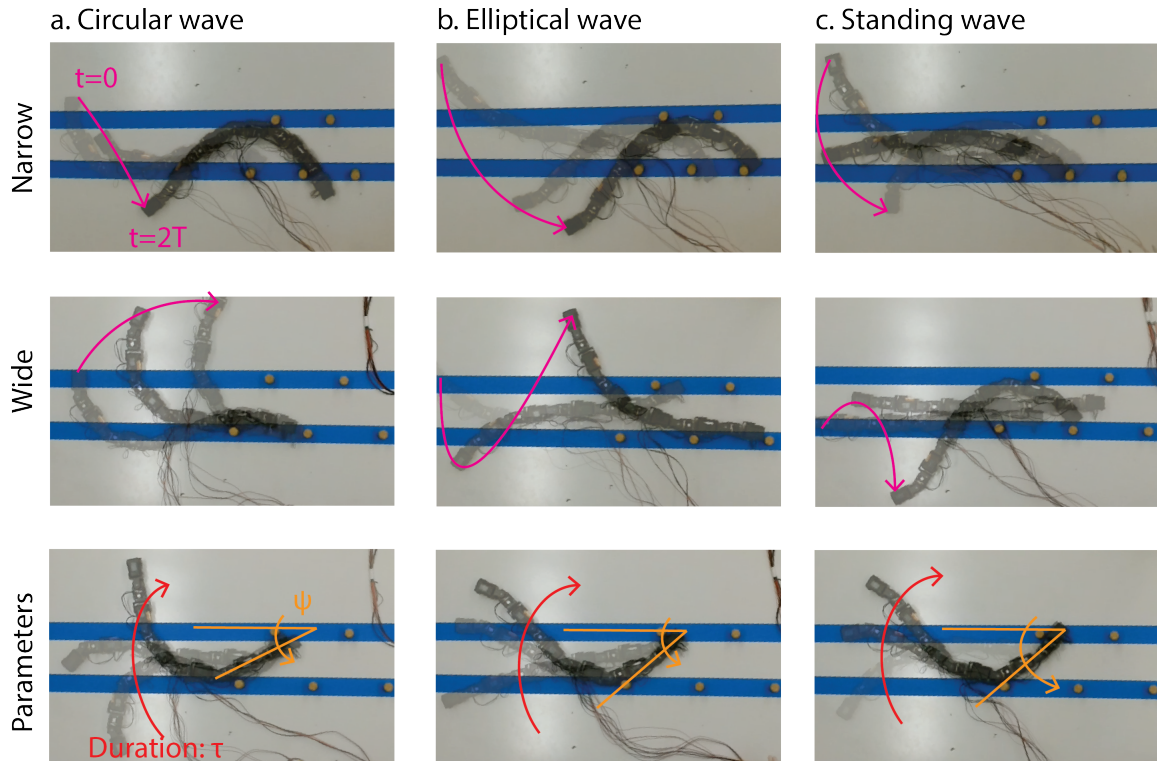


Figure 2.38: **Multiple posts experiments** We illustrated snapshots of robots implementing (a) circular, (b) elliptical, and (c) standing wave gaits on wide-distributed posts (0.3 BL) and narrow-distributed posts (0.2 BL). Elliptical-wave gait outperformed standing-wave and circular-wave gaits in both posts. Purple arrows indicate the direction of motion over two gait cycles. On the right panel, we illustrated the definition of attack angle ψ and contact duration τ .

We used this elliptical gait for experiments, implemented in later sections. We compared our predicted elliptical gait with two empirical gaits widely used in literature: a circular-wave (serpenoid-wave) and a standing-wave. A circular-wave gait arises from a circular path in the shape space where the amplitude of the wave is constant throughout the gait (phase modulation). A standing-wave gait arises from a flat ellipse in the shape space where the phase of the wave is constant throughout the gait (amplitude modulation).

2.7.6 Single Post Experiments

To systematically test the effectiveness of our predicted gaits, we conducted single post (rigid, $h = 1.5$ cm, $d = 3$ mm) experiments. Specifically, we placed our robot with its

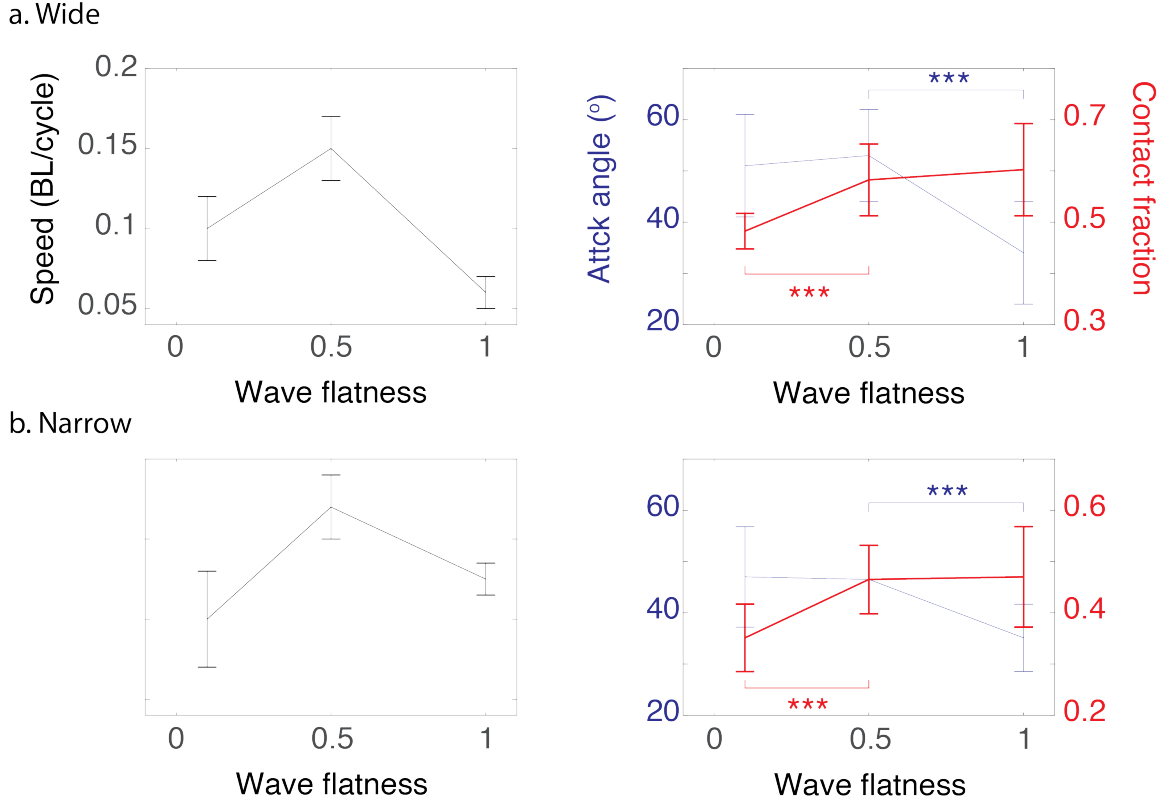


Figure 2.39: **Experiment data for multiple post experiments** (Left panel) The speeds of standing-wave ($\sigma = 0.1$), elliptical-wave ($\sigma = 0.5$), and circular-wave ($\sigma = 1$) gaits are compared in (a) wide-distributed posts and (b) narrow-distributed posts. (Right panel) The attack angle and contact duration for all cases are measured and compared. ** denotes $p < 0.01$

head hitting the obstacle. We then ran the gait for half of a cycle¹⁰ and measured the displacement of the head link along the direction of motion, d . Snapshots of the experiments can be found in Figure 2.37a. We compared the displacement for circular, elliptical, and standing wave gaits. Interestingly, we observed that the standing-wave gait has the highest half-cycle forward displacement, indicating highest line integral along the vector field V_1 (per unit length of duration). The elliptical-wave gait has slightly less half-cycle forward displacement whereas the circular-wave gait has the lowest half-cycle forward displacement.

However, other than half-cycle forward displacement, it is also important to have a wide

¹⁰We chose half of a cycle because it is often the duration of interaction with one obstacle



Figure 2.40: **Unevenly distributed post experiments** A sequence of video frames of the robot executing the elliptical-wave gait in an unevenly arranged planar peg board over two gait cycles.

area where the presence of an obstacle can be beneficial (range of beneficial obstacles). In other words, we also aim to maintain high contact duration with beneficial obstacles. Mathematically, we aim to design a gait path that has a positive dot product with V_2 . We measured the angular range of beneficial obstacle γ (Figure 2.37b), such that within γ the presence of obstacle is beneficial. Interestingly, we observed that the standing-wave gait has the least angular range of beneficial obstacles (Figure 2.37). On the other hand, elliptical-wave and circular-wave gaits have similar angular range of beneficial obstacles.

In summary, we observed that elliptical-wave gaits leverage the benefits of both standing-wave and circular-wave gaits: (1) it can take advantage of each obstacle and (2) has high probability to interact with a “beneficial” obstacle. Thus, we hypothesize that the elliptical-wave gait can be the best candidate gait during obstacle aided locomotion.

2.7.7 Multiple Post Experiments

We tested the effectiveness of all gaits in a lattice with regular spacing. We used two different lattices: one with wide-distributed posts, post spacing ≈ 0.3 BL (body length), and one with narrow-distributed post spacing ≈ 0.2 BL. Snapshots of experiments can be found in Figure 2.38. We measured the speed of robots by body length per cycle (

Figure 2.39). In both multiple post experiments, the elliptical-wave gait outperforms the other two candidates.

To further test our hypothesis, we measured the duration of obstacle-contact in these experiments. Here, we defined the duration of contact by the average fraction that the robot is interacting with obstacles τ/T , where τ is empirically measured average contact duration (Figure 2.38) and T is the gait period. In both environments, the contact duration in the standing-wave gait is significantly lower than the elliptical-wave and circular-wave gaits, indicating that the standing-wave gait has the lowest duration of beneficial contact between robot and obstacle. We also measured the attack angle between the robot and the obstacle. It is defined as the angle between the head link and the obstacle at the end of the robot-obstacle interaction. As posited by [157], larger attack angle indicates better push from the obstacle to robot. As shown in Figure 2.39, the attack angles in the circular-wave gait are significantly lower than the elliptical and standing wave gaits, indicating that the traveling wave gait can take the least advantage of the obstacle.

2.7.8 Unevenly Distributed Posts Experiments

To test the effectiveness of different gaits within confined environments, we performed the elliptical-wave, the circular-wave, and the standing-wave gaits in a two-dimensional artificial indoor obstacle-rich environment: an unevenly arranged peg board.

The elliptical-wave gait exhibits effective OAL behaviors in the planar peg board. An example of a successful elliptical-wave motion on the peg board is shown in Figure 2.40. The robot was able to generate 0.12 ± 0.05 BL/cycle on average over six trials. Note that the motion performance is highly dependent on the initial configuration, therefore the standard deviation is relatively large. The circular-wave and the standing-wave gaits performed poorly, generating far less forward motion within the pegs, 0.06 ± 0.04 and 0.06 ± 0.05 BL/cycle, respectively. A comparison video of the three gaits in the same environment can be found in the supplementary video. These preliminary tests show that the elliptical-wave

is the most promising of the tested gaits.

2.8 Appendix

2.8.1 Numerical solution: minimal perturbation coordinate

Problem 1 is similar to the Helmholtz-Hodge decomposition [138, (B5)]. Nonetheless, the torus cannot be embedded into \mathbb{R}^2 , and it is a manifold without boundary, so the standard Helmholtz-Hodge decomposition does not apply. As a result, we cannot directly apply the decomposition, and our approach to Problem 1 would be an analogue of the Helmholtz-Hodge decomposition on the torus.

In practice, we cannot hope to have analytic formulas for f_1, f_2 . So we need to look for numerical solutions. Since we only know the values of f_1, f_2 at a finite number of points in T^2 . As a result, we have to discretize the problem and solve for a discrete approximation of $P(r_1, r_2)$.

For suitable $n \in \mathbb{N}$, we can decompose $[0, 2\pi) \times [0, 2\pi)$ into a mesh of n^2 squares, and we focus on the lattice points $(\frac{2\pi i}{n}, \frac{2\pi j}{n}), 0 \leq i, j \leq n-1$. For sufficiently large n , the mesh is dense enough, and we try to find the values of a solution $P(r_1, r_2)$ at all those lattice points. For convenience, we denote the side length of squares in the mesh by $u = \frac{2\pi}{n}$.

Now we apply the *finite-element method* as in [118]. We define a family of basis functions $\phi_{i,j}$ such that $\phi_{i,j}$ takes value 1 at $(\frac{2\pi i}{n}, \frac{2\pi j}{n})$ and 0 at all other lattice points.

The motivation of introducing $\phi_{i,j}$'s is Lemma 6.

Lemma 6. *Suppose $P(r_1, r_2)$ takes value $c_{i,j}$ at $(\frac{2\pi i}{n}, \frac{2\pi j}{n})$. Then at all lattice points*

$$P(r_1, r_2) = \sum_{0 \leq i, j \leq n-1} c_{i,j} \cdot \phi_{i,j}(r_1, r_2). \quad (2.51)$$

The choice of the basis functions is the following: given integers $0 \leq i, j \leq n-1$, for all r_1, r_2 such that $\frac{2\pi(i-1)}{n} \leq r_1 < \frac{2\pi(i+n-1)}{n}, \frac{2\pi(j-1)}{n} \leq r_2 < \frac{2\pi(j+n-1)}{n}$, we define

$$\begin{aligned} \phi_{i,j}(r_1, r_2) &= \max\left(1 - \frac{|r_1 - \frac{2\pi i}{n}|}{u}, 0\right) \\ &\cdot \max\left(1 - \frac{|r_2 - \frac{2\pi j}{n}|}{u}, 0\right). \end{aligned} \quad (2.52)$$

Then $\phi_{i,j}$ is well-defined on T^2 , only takes value 1 at the lattice point $(\frac{2\pi i}{n}, \frac{2\pi j}{n})$ and takes value 0 at all other lattice points. In addition, $\phi_{i,j}$ is bilinear within each of the 4 quadrants around $(\frac{2\pi i}{n}, \frac{2\pi j}{n})$.

Proof of Lemma 6. For any lattice point $(\frac{2\pi i_0}{n}, \frac{2\pi j_0}{n})$, we have $\phi_{i,j}(\frac{2\pi i_0}{n}, \frac{2\pi j_0}{n}) = 1$ if $i = i_0$ and $j = j_0$, and $\phi_{i,j} = 0$ for all other choices of $0 \leq i, j \leq n-1$. So the right hand side of (Equation 2.51) equals $c_{i_0, j_0} \cdot 1 = c_{i_0, j_0} = P(\frac{2\pi i_0}{n}, \frac{2\pi j_0}{n})$. \square

For convenience, for any two vector fields G, H defined on T^2 , let their inner product be

$$\langle G, H \rangle = \int_{T^2} [G_1(r_1, r_2)H_1(r_1, r_2) + G_2(r_1, r_2)H_2(r_1, r_2)] dr_1 dr_2.$$

Then $D = \langle \mathbf{A}_\theta - \nabla P, \mathbf{A}_\theta - \nabla P \rangle$. Now suppose a solution $P(r_1, r_2)$ is expressed as in (Equation 2.51). By the linearity of ∇ operator,

$$\nabla P = \sum_{0 \leq i, j \leq n-1} c_{i,j} \cdot \nabla \phi_{i,j}. \quad (2.53)$$

Since P is a solution, the choice of each $c_{i,j}$ must be optimal. Then for any $0 \leq i_0, j_0 \leq n-1$, we have

$$\begin{aligned}
0 &= \frac{\partial D}{\partial c_{i_0, j_0}} = \frac{\partial \langle \mathbf{A}_\theta - \nabla P, \mathbf{A}_\theta - \nabla P \rangle}{\partial c_{i_0, j_0}} \\
&= \frac{\partial \langle \mathbf{A}_\theta, \mathbf{A}_\theta \rangle}{\partial c_{i_0, j_0}} + \frac{\partial \langle \nabla P, \nabla P \rangle}{\partial c_{i_0, j_0}} - 2 \frac{\partial \langle \mathbf{A}_\theta, \nabla P \rangle}{\partial c_{i_0, j_0}} \\
&= 0 + \sum_{0 \leq i, j, k, l \leq n-1} \frac{\partial \langle \nabla \phi_{i, j}, \nabla \phi_{k, l} \rangle c_{i, j} c_{k, l}}{\partial c_{i_0, j_0}} \\
&\quad + \sum_{0 \leq i, j \leq n-1} \frac{\partial \langle \mathbf{A}_\theta, \nabla \phi_{i, j} \rangle c_{i, j}}{\partial c_{i_0, j_0}} \\
&= 2 \sum_{0 \leq i, j \leq n-1} \langle \nabla \phi_{i, j}, \nabla \phi_{i_0, j_0} \rangle c_{i, j} - 2 \langle \mathbf{A}_\theta, \nabla \phi_{i_0, j_0} \rangle.
\end{aligned}$$

Therefore we get n^2 linear equations (for all pairs of $0 \leq i_0, j_0 \leq n-1$):

$$\sum_{0 \leq i, j \leq n-1} \langle \nabla \phi_{i, j}, \nabla \phi_{i_0, j_0} \rangle c_{i, j} - \langle \mathbf{A}_\theta, \nabla \phi_{i_0, j_0} \rangle = 0. \quad (2.54)$$

Now we analyze the linear system (Equation 2.54). The coefficient matrix is $n^2 \times n^2$ and sparse.

Lemma 7. *Let $0 \leq i, j, k, l \leq n-1$ be integers*

1. $\langle \nabla \phi_{i, j}, \nabla \phi_{i, j} \rangle = \frac{8u^2}{3}$;
2. if (i, j) and (k, l) are distinct pairs such that both i, k and j, l differ by at most 1 modulo n , then $\langle \nabla \phi_{i, j}, \nabla \phi_{k, l} \rangle = -\frac{u^2}{3}$;
3. for all other (i, j) and (k, l) , $\langle \nabla \phi_{i, j}, \nabla \phi_{k, l} \rangle = 0$.

Lemma 7 follows from direct computations based on (Equation 2.52).

Proposition 8. *The square matrix*

$$A = \{ \langle \nabla \phi_{i, j}, \nabla \phi_{k, l} \rangle \}_{0 \leq i, j, k, l \leq n-1}$$

has rank $n^2 - 1$.

Proof. By Lemma 7, the sum of the column vectors in A is the zero vector. So the all-one vector $\mathbf{1}$ belongs to the null space of A . In addition, by the symmetry and sparsity of A , there is no other linear dependence among the column vectors in A , so the rank of A is the size of A minus the dimension of the null space of A , which is $n^2 - 1$. \square

By Proposition 8, the solution space of (Equation 2.54) has dimension 1. While it is easy to verify that $\sum_{0 \leq i, j \leq n-1} \phi_{i,j}(r_1, r_2) \equiv 1$ for all $(r_1, r_2) \in T^2$. Hence any scaling to a solution of $c_{i,j}$'s would result in another solution, and at the level of $P(r_1, r_2)$ it only differs a constant from the previous one. So (Equation 2.54) gives a unique solution of $P(r_1, r_2)$ up to a constant scaling.

The values of $\langle \nabla \phi_{i,j}, \nabla \phi_{k,l} \rangle$ could be computed from (Equation 2.52), and the values of $\langle \mathbf{A}_\theta, \nabla \phi_{i_0, j_0} \rangle$ can be approximately computed using the values of \mathbf{A}_θ at lattice points near $\left(\frac{2\pi i_0}{n}, \frac{2\pi j_0}{n}\right)$.

Note that we applied a similar approach to determine the Optimal choice of reference position [118], corresponds to finding the potential function of the first two rows of the local form of the connection matrix $\mathbf{A}(\mathbf{r})$.

CHAPTER 3

COORDINATION OF LATERAL BODY BENDING AND LEG MOVEMENTS FOR SPRAWLED POSTURE QUADRUPEDAL LOCOMOTION

Part of this chapter is adapted from a journal article “Coordination of lateral body bending and leg movements for sprawled posture quadrupedal locomotion.” *The International Journal of Robotics Research* 40.4-5 (2021): 747-763. My contribution in this project includes (1) designing the experiments, (2) conducting the numerical analysis, (3) writing the manuscript. Robophysical experiments presented in this chapter are conducted by Yasemin Ozkan-Aydin.

Animals, and increasingly robots, can use limbs to propel themselves to maneuver across a variety of terrains ([18, 19, 22, 23, 4]). In addition to these appendages, undulatory body motions can also contribute to locomotor propulsion, even when not directly in contact with the environment. For example, salamanders ([84, 66, 85, 86]), lizards ([87]), and some mammals ([88]) use lateral body undulation in coordination with their legs for effective locomotion. While previous studies have elucidated the benefits of using lateral body undulation in conjunction with quadrupedal limb motion for individual tasks such as walking, running or turning ([66, 85, 35, 88]), no general framework yet exists to systematically explore coordination and performance in quadrupedal systems that employ body undulatory motion, or more specifically back bending. To building this framework, it requires not only coordinating many degrees of freedom (DoF), but also coordinating different types of DoF (i.e., body bending and the leg movements) in distinct types of behaviors (i.e., forward, turning and sideways motion)

As discussed in earlier chapters, geometric mechanics offers qualitative and quantitative insight into how animal and robots can generate optimal high level control ([83, 15]) to affect desired behaviors, such as forward, sideways, turning locomotion. Here we expand

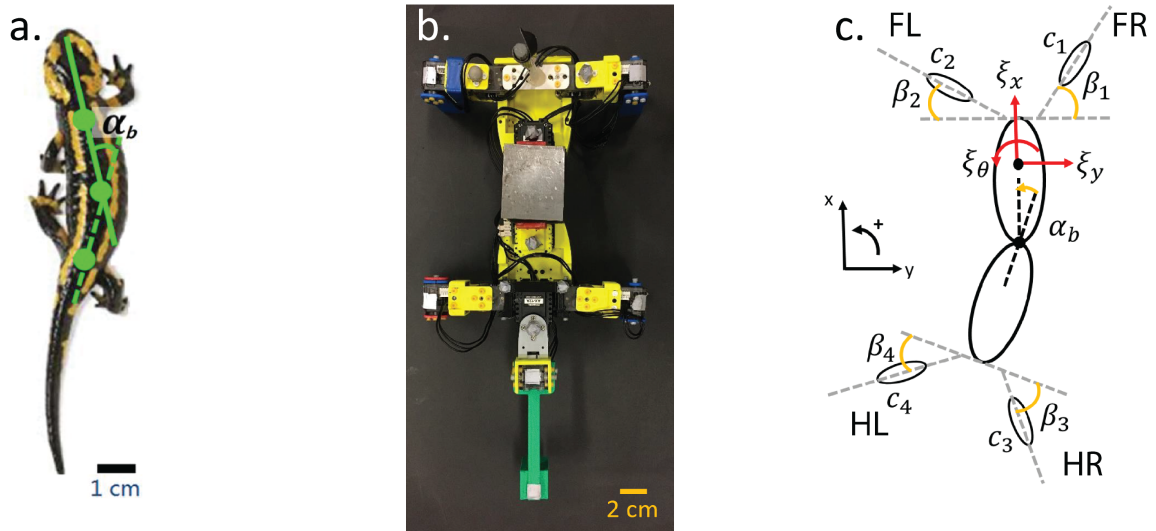


Figure 3.1: **The animal, robot and theoretical models studied in the chapter.** (a) top view of a Fire salamander. The body angle, α_b , is defined as an angle between the center lines that are parallel to the front and the back part of the body. (b) top view of the robo-physical model. It has two body parts connected with a servo, four 2 DoF legs, and a tail. The metal part at the center is used to pick up the robot with an electromagnetic gripper. All legs and tail have the same foot geometry (24X24 mm cube shape). (c) the theoretical model with shape variables and body velocities labeled.

the scope of geometric mechanics to four-legged body-bending systems. The challenges of extending geometric mechanics to quadrupedal systems lie in the fact that these systems periodically make and break contact with the environment. Here, we prescribe the leg contact states by their phase; this phase, together with the body-bending angle, forms the shape space, in which we can apply geometric mechanics tools. We demonstrate that proper body undulation, obtained from optimization in the new shape space, can improve the locomotion performance of our quadrupedal robots in forward, rotational and lateral directions. Furthermore, experimental data collected from Fire salamanders (*Salamandra salamandra*) (Figure 3.1a) reveal that our geometric-based approach closely predicts motion observed in a biological system.

3.1 Related work on turning

Turning motions in quadrupedal robots have been less studied. In addition, existing turning policies of quadrupedal robots heavily rely on leg placement: previous work has shown that careful foot placement planning can enable quadrupedal turning motions ([158]). [159] introduced the footfall planning objective function, where speed, stability, translation direction, and turning were all included. [160] designed a turning fuzzy controller by placing the fore legs to the outside of the turn and the hind legs to the inside. In addition to the control algorithms in foot placement, biologists indicate that body bending also plays an important role during turning motion. For example, [88] showed the body shape changed from *S*-shape to *C*-shape during the turning motion of ferrets.

Legs movements and body undulations can both lead to quadrupedal turning motions. In this chapter, we investigate how leg movement modulation can coordinate with body undulation to enable different turning behaviors in quadrupedal locomotion from in-place turning to steering.

3.2 Geometric mechanics

3.2.1 Periodic Ground Contacts

Here, we apply geometric mechanics to study the body-leg coordination in quadrupedal locomotion. First, we seek to identify the shape variables. In our simplified model, the shape variable $\mathbf{r} \in \mathbb{R}^5$ includes the body bending joint angle (α_b , see Figure 3.1.c) and the leg “shoulder” (shoulder for fore-legs and hip for hind legs) joint angle (β_i , $i \in \{1, 2, 3, 4\}$, see Figure 3.1.c).

In legged systems, robots and animals repeatedly make and break contact with the environment. We introduce a binary *contact state variable*, \mathbf{C} , that describes the contact states: 0 (no contact, and therefore no contact forces) or 1 (full contact). Thus, the equation of motion (adapted from Equation 2.7) becomes a function of both shape variables and

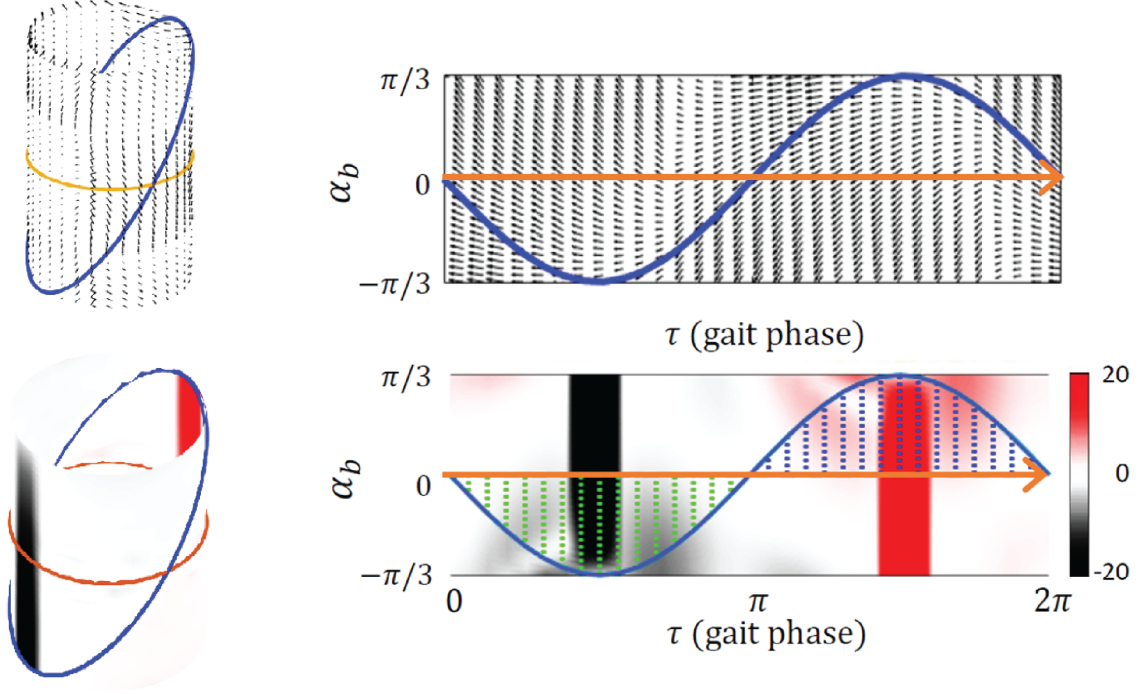


Figure 3.2: **The connection vector field and the height functions in the cylindrical shape space.** The connection vector field (top) and the height function (bottom) in a cylindrical shape space corresponding to the forward motion of a quadruped robot moving with a four-beat walking gait on the surface of ~ 1 mm poppy seeds. We show the vector field and height function on a cylindrical space and on the Euclidean parameterization of a cylindrical space. The blue curve represents a sample gait in the corresponding cylindrical shape space. Orange lines represent the assistive lines to form closed loops with the gait path in the unfolded cylindrical shape space. The area in the blue shading represents the area where the gait path and the assistive line form a clockwise loop; the area in the green shading represents the area where the gait path and the assistive line form a counterclockwise loop. Red, white, and black colors indicate positive, zero and negative values in the height function respectively.

contact states, i.e.,

$$\xi = A(r, C)\dot{r}, \quad (3.1)$$

where $\xi = [\xi_x \ \xi_y \ \xi_\theta]^T$ denotes the body velocity in forward, lateral and rotational directions respectively. Note that in this chapter, we use ξ to represent the body velocity to simplify the notation. We assume that the contact variable C and the shape variable β_i can all be written as a function of leg phase τ , i.e.,

$$c_i = F_i(\tau), \quad \beta_i = f_i(\tau), \quad i = 1, 2, 3, 4 \quad (3.2)$$

We prescribe the contact patterns, c_i , from existing knowledge of the footfall sequence (see Figure 3.3). Then, we use the contact state to prescribe the shoulder angle β_i . Specifically, we enforce the β_i to be a piece-wise sinusoidal function, partially because it permits the differentiability at transition. The specific shape of the sinusoid is chosen to respect the contact state of the foot, as depicted in Fig. Figure 3.3. The leg shoulder angle β_i is prescribed as a piece-wise sinusoidal function over either contact state or non-contact state with smooth connection. The generic examples of functions F_i and f_i are shown in Figure 3.3.

With leg movements prescribed by f_i and F_i , we can form a new shape space that consists of two variables α_b and τ , the body bending angle and the leg phase. This reduced shape space is parameterized by $\mathbf{\Omega} = [\alpha_b, \tau]^T$. Note that according to the chain rule, we have:

$$\dot{\mathbf{r}} = \frac{d\mathbf{r}}{d\mathbf{\Omega}} \frac{d\mathbf{\Omega}}{dt} = \begin{bmatrix} 1 & 0 \\ 0 & \frac{df_1(\tau)}{d\tau} \\ 0 & \frac{df_2(\tau)}{d\tau} \\ 0 & \frac{df_3(\tau)}{d\tau} \\ 0 & \frac{df_4(\tau)}{d\tau} \end{bmatrix} \dot{\mathbf{\Omega}} \quad (3.3)$$

Therefore, we can rewrite Equation 3.1 as:

$$\xi = A(\mathbf{r}, C)\dot{\mathbf{r}} = A(\mathbf{\Omega})\frac{d\mathbf{r}}{d\mathbf{\Omega}}\dot{\mathbf{\Omega}} = A'(\mathbf{\Omega})\dot{\mathbf{\Omega}}, \quad (3.4)$$

where $A'(\mathbf{\Omega})$ is the new local connection relating the reduced shape velocity $\dot{\mathbf{\Omega}}$ to body ve-

locity ξ . Since one of the shape variables, τ is periodic, the shape space is now cylindrical.

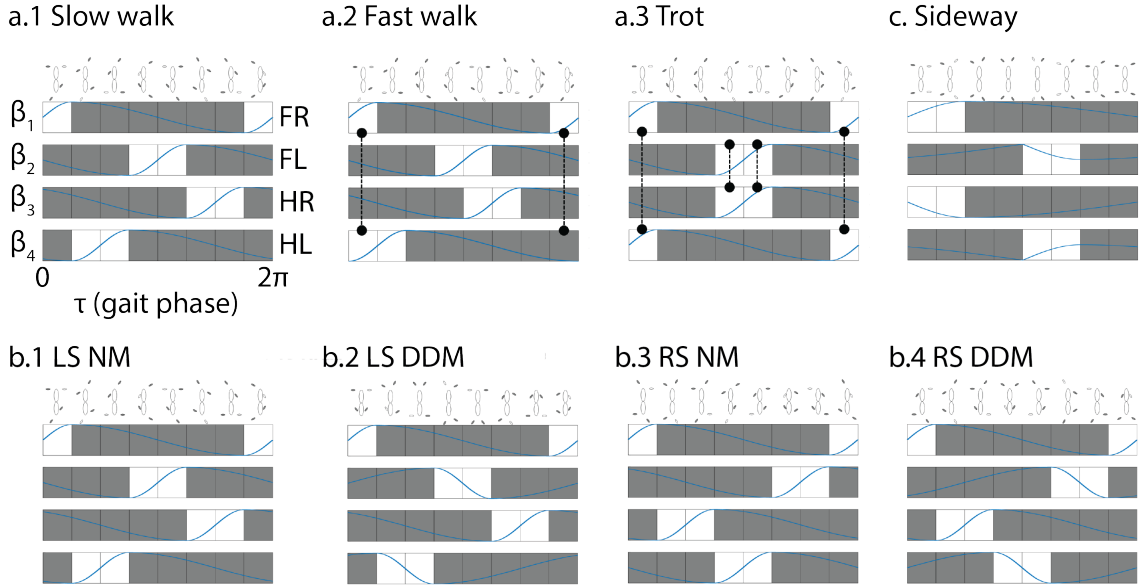


Figure 3.3: The leg contact variables c_i and joint angles β_i prescribed by gait phase τ for (a.1) (forward) slow walk, (a.2) (forward) fast walk, (a.3) (forward) trot (b.1) (rotational) lateral sequence with no modulation (**LS NM**), (b.2) (rotational) lateral sequence with differential drive modulation (**LS DDM**), (b.3) (rotational) rotary sequence with no modulation (**RS NM**), (b.4) (rotational) rotary sequence with differential drive modulation (**RS DDM**), and (c) (lateral) sideways leg movements. The “cartoon sequence” shows the leg joint angles and contact states (solid means contact; open in air) at different gait phases. A row of eight boxes indicates the contact state of a leg at eight different phases of the gait, where filled gray color represents contact and open white color represents non contact state. The blue curves indicate the joint angles of the leg “shoulders” (shoulder for fore-legs and hip for hind legs). The initials F, H, L, R represent front, hind, left and right leg, respectively. All the panels have the same ordinate range (from $-\frac{\pi}{3}$ to $\frac{\pi}{3}$) as in (a.1). The dashed lines in (a.2) and (a.3) indicate two legs are simultaneously in the air, which could only occur for diagonal leg pairs.

3.2.2 Cylindrical shape space

To form an enclosed area in the Euclidean parameterization of the periodic shape space, we introduce the notion of an assistive line ([142]). The assistive line is defined to be a path in shape space where only one shape variable changes and is used to form a closed loop with the gait path in the shape space. Note that, in principle, the choice of assistive line is arbitrary with respect to the same winding number. In practice, we often choose an

assistive line with a physical meaning. In this example, we choose the assistive line to be $\partial\phi_0 : \alpha_b = 0$ (orange line in Figure 3.2b), such that the assistive line represents the gaits with straight fixed body.

The net displacement can be approximated by the path integral along the assistive line $\partial\phi_0$ plus the surface integral of the area enclosed by the gait path $\partial\phi$ and the assistive line ([142]):

$$\int_{\partial\phi} \mathbf{A}(\mathbf{r})d\mathbf{r} = \int_{\partial\phi_0} \mathbf{A}(\mathbf{r})d\mathbf{r} + \iint_{\phi-\phi_0} \nabla \times \mathbf{A}(\mathbf{r})d\alpha_b d\tau, \quad (3.5)$$

where $\phi-\phi_0$ is the area enclosed by the assistive line $\partial\phi_0$ and gait path $\partial\phi$. Note that when the gait path and the assistive line enclose disjointed areas in the shape space, the handedness (the direction of the curl) of these enclosed areas can be different. For example, as shown in our example in Figure 3.2.b, the assistive line (orange curve) and our gait path (blue curve) form two disjoint areas: the area where $\partial\phi_0$ is above (blue shading area) and below (green shading area) $\partial\phi$. Thus, taking the handedness of the enclosed area into consideration, the second term in Equation 3.5 is computed as the surface integral of area where $\partial\phi$ is above $\partial\phi_0$ subtracted from the surface integral of area where $\partial\phi$ is below $\partial\phi_0$.

The physical meaning of the first term in Equation 3.5 is the displacement resulting from leg movements while keeping the back fixed, i.e., the contribution solely from leg movements. It is independent from any gait path we design and can be pre-computed. The second term in Equation 3.5 is the additional displacement resulting from coordinating body bending with leg movement. We can thus design the body bending according to our motion objectives.

3.2.3 Granular Resistive Force Theory

Similar to prior work, we numerically derive \mathbf{A}' using resistive force theory (RFT) ([121, 11, 122]) to model the granular media on which our system moves. Depending on the substrate, we can choose the corresponding RFT functions to approximate the ground reaction

forces. In our experiments, robots moved on poppy seeds, a model granular media ([11]); therefore we used the following previously suggested empirical functions to approximate F_{\perp} and F_{\parallel} :

$$f_{\perp} = C \sin(\gamma)$$

$$f_{\parallel} = A \cos(\gamma) + B(1 - \sin(\gamma)) + F_0$$

where $C = 0.66$, $A = 0.27$, $B = -0.32$, $F_0 = 0.09$ is the empirically fitted function to characterize the granular media resistant force.

Salamander animals moved on $300 \mu\text{m}$ glass particles, so we used the following previously suggested empirical functions to approximate F_{\perp} and F_{\parallel} ([63]):

$$f_{\perp} = a_0 + \sum_{i=1}^2 a_i \cos(iw\gamma) + b_i \cos(iw\gamma)$$

$$f_{\parallel} = A_0 + \sum_{i=1}^3 A_i \cos(iW\gamma) + B_i \sin(iW\gamma)$$

where $a_0 = 0.004041$, $a_1 = 0.0002925$, $b_1 = 0.002832$, $a_2 = -0.001038$, $a_2 = -0.0007345$, $w = 2$; $A_0 = -0.4833$, $A_1 = 0.3498$, $B_1 = 0.7504$, $A_2 = 0.2046$, $B_2 = -0.297$, $A_3 = -0.07208$, $B_3 = -0.009435$, $W = 1.333$.

The attack angles χ of each segment can be calculated from the body velocity ξ , body shape Ω , and shape velocity $\dot{\Omega}$. By assuming that the motions of quadrupeds in granular material are quasi-static ([82]), we consider the total net force applied to the system is zero:

$$F = \int (dF_{\parallel}(\xi, \Omega, \dot{\Omega}) + dF_{\perp}(\xi, \Omega, \dot{\Omega})) = \mathbf{0}. \quad (3.6)$$

At a given body shape Ω , (Equation 3.6) connects the shape velocity $\dot{\Omega}$ to the body velocity ξ . Therefore, by linearizing (Equation 3.6), we can numerically derive the local

connection matrix $A'(\mathbf{\Omega})$. In our implementation, we compute the root of (Equation 3.6) using the MATLAB function *fsolve*.

With the above assumptions, the local connection of a quadrupedal robot moving in granular media can be approximated by numerically calculating displacements in the body frame.

3.2.4 Gait Design

Note that 2-D cylindrical shape space is a simple representation that includes both body bending and leg movements. Compared with higher dimensional systems, the 2D shape space has the advantage of allowing visual gait analysis, as we can design gaits by looking at the height functions. To achieve such simple representation, we made many assumptions (e.g., using one degree-of-freedom body joint to represent the body bending in sprawled posture quadrupedal locomotion) to perform dimensionality reduction.

With the height function, one can design gaits by drawing a path through the shape space. The periodic gait path is assumed to be described by Fourier series. To limit the number of parameters to be optimized while maintaining the flexibility of the gait design ([161]), we keep the first two orders of the Fourier series in our prescription, i.e.,

$$\partial\phi_{a_i, b_i} = \{[\alpha_b, \tau] : \alpha_b = \sum_{n=1}^{n=2} a_n \cos(n\tau + b_n).\} \quad (3.7)$$

We denote $\partial\phi_{a_i, b_i}$ as $\partial\phi_{a_1, a_2, b_1, b_2}$ to simplify notation. Finally, we maximize the area enclosed by gait path and the assistive line by optimizing over the parameters a_i 's and b_i 's:

$$\begin{array}{ll} \text{argmax} & \iint_{\phi_{a_i, b_i} - \phi_0} \mathbf{H} d\alpha_b d\tau, \\ \text{subject to} & \max_{\phi_{a_i, b_i}} \alpha_b < \Gamma_\alpha \end{array}$$

where $\mathbf{H} = \mathbf{H}_x, \mathbf{H}_y$ or \mathbf{H}_θ depending on the direction of gait that we wish to design motion; Γ_α is the body bending joint angle limit.

Figure 3.5 shows several examples of gaits on height functions for a variety of maneuvers. In summary, our approach uses the following steps:

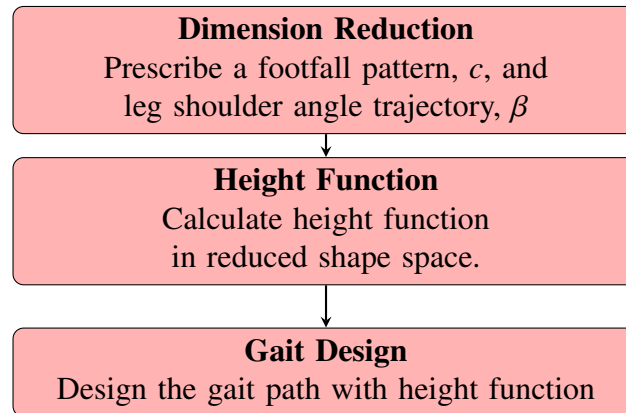


Figure 3.4: The flow chart of our gait design process

3.2.5 Forward Height Functions

We studied how body bending, coordinated with leg movements, improved the forward displacement per gait cycle. We first prescribed three typical types of leg movements, taken from prior work ([17]), that will result in forward displacement.

The three types of leg movements prescribed in this section are slow walk, fast walk and trot. Inspired by Hildebrand’s analyses, ([17]), we classified these gaits with two parameters: lateral leg phase shift (the fraction of the step cycle that hind limbs lead the fore limbs on the same side) and duty factor (the fraction of the step cycle where the foot is on the ground). The duty factors for the three gaits are all 0.75, and the lateral leg phase shifts are: 0.25, 0.375, and 0.5 respectively. Each of these parameter choices lead to a specific footfall pattern which can be seen in Figure 3.3a. The leg “shoulder” joint angles are prescribed as piece-wise sinusoidal functions which move from cranial end to caudal end when the leg makes contact with the ground, and move from caudal end to cranial end

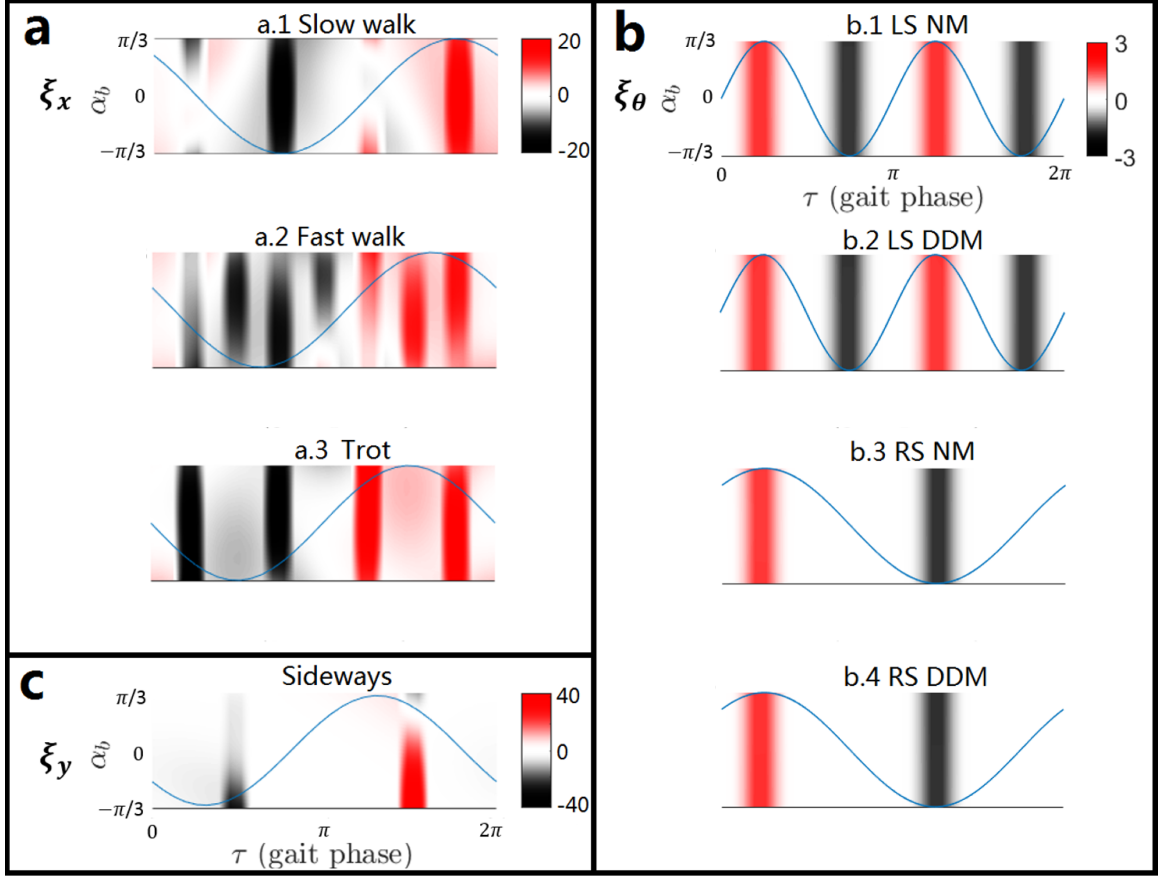


Figure 3.5: **Height functions** (a) Forward height functions associated with trot (a.1), fast walk (a.2) and slow walk (a.3) leg movements. The units of the colorbars are cm per step, i.e., $cm/4\pi^2$. (b) Rotational height functions associated with lateral sequence no modulation (**LS NM**) (b.1), lateral sequence differential drive modulation (**LS DDM**) (b.2), rotary sequence no modulation (**RS NM**) (b.3) and rotary sequence differential drive modulation (**RS DDM**) (b.4) leg movements. The units of the colorbars are rad per step, i.e., $rad/4\pi^2$. (c) Lateral height function associated with sideways leg movements. The blue curves are the identified “optimal” gait paths. Red, white and black indicate positive, zero and negative values respectively. The ordinate range is the same for all panels. The units of the colorbars are cm per step, i.e., $cm/4\pi^2$.

when the leg is in the air (Figure 3.3a). We set the body bending joint angle limit $\Gamma_\alpha = \frac{\pi}{3}$ in this section unless otherwise noted.

The **slow walk** (lateral leg phase shift = 0.25) is a four-beat¹ gait with evenly spaced leg lifting following the sequence fore right, hind left, fore left, hind right (defined as lateral sequence (**LS**)) ([17]). The **fast walk** (lateral leg phase shift = 0.375) is another four-beat

¹Imagine each leg placement is like beating a drum. For the slow walk gait, one would hear four separate beats of the drum as the leg makes contact with the ground. A trot gait is a two-beat gait

gait following the lateral sequence. Unlike the slow walk gait, there is an overlap of the aerial phase between fore right and hind left legs (as well as fore left and hind right). The **trot gait** (lateral leg phase shift = 0.5) is a two-beat gait with diagonally paired leg movement. The fore right leg is always in phase with the hind left leg; while the fore left leg is always in phase with the hind right leg. The detailed descriptions of these gaits are presented in Figure 3.3a. Note that the overlaps in diagonal-leg (the FR-HL pair or FL-HR pair) non-contact state increase from slow walk to fast walk to trot, which leads to higher speeds.

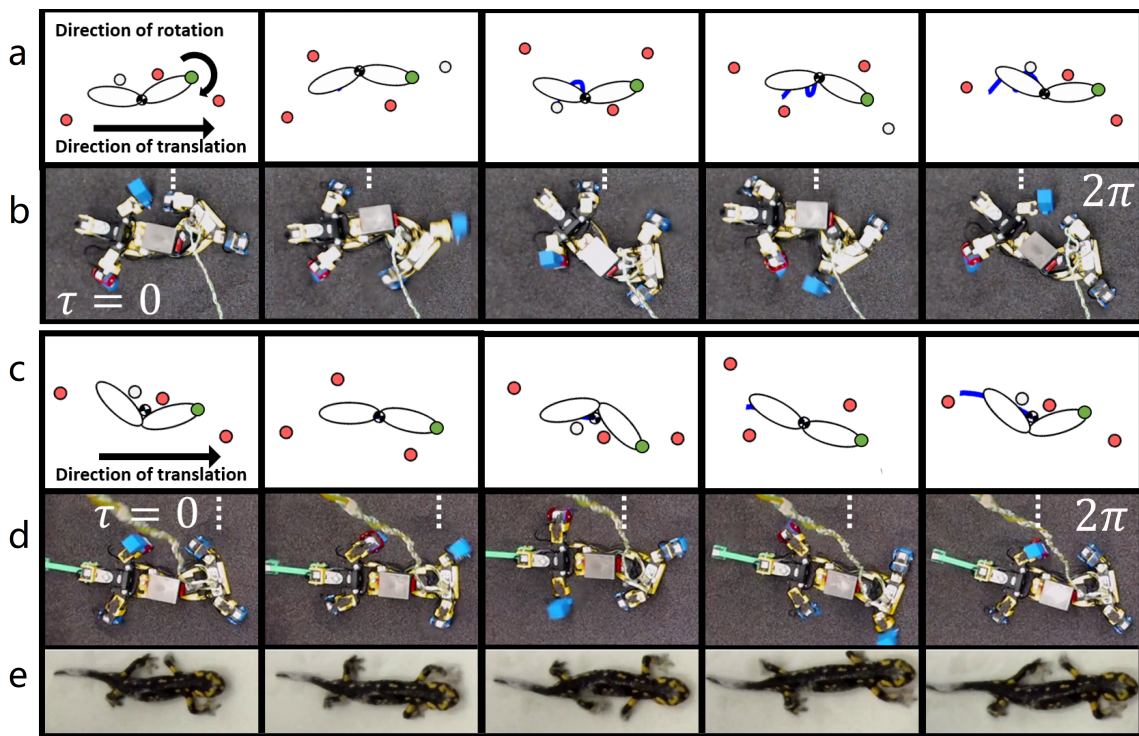


Figure 3.6: Snapshots of robot experiment (b and d), RFT simulation (a and c) and animal experiments (e). Body bending coordinated with leg movements (a-b) changes the orientation of the body or increases forward displacement. In (a) and (c), the green dots identify the head and the solid blue line represents the trajectory of center of mass. In (b) and (d), the module connected to hanging tail (not making contact with the ground) indicates the hind body module. We compared our designed forward gaits (c and d) with the forward locomotion observed in animal experiments (e)

We can coordinate body bending to improve forward displacements per gait cycle by investigating the forward height functions. The forward height functions for these leg move-

ments are shown in (Figure 3.5a). The gait paths with the maximum surface integral in the forward height functions (“optimal” gaits) are predicted to be the gaits with the largest forward displacement per gait cycle. We also identified the worst body bending coordination with the minimal surface integrals (“worst” gaits). We tested the “neutral” gaits with fixed straight back ($\alpha_b = 0$) for reference.

We observed that body bending that optimizes the forward displacement per gait cycle is dominated by the first term of the Fourier series, in which case a_1 tends to Γ_a and a_2 tends to 0. However, the optimized b_1 s vary for fast walk, slow walk, and trot leg movements.

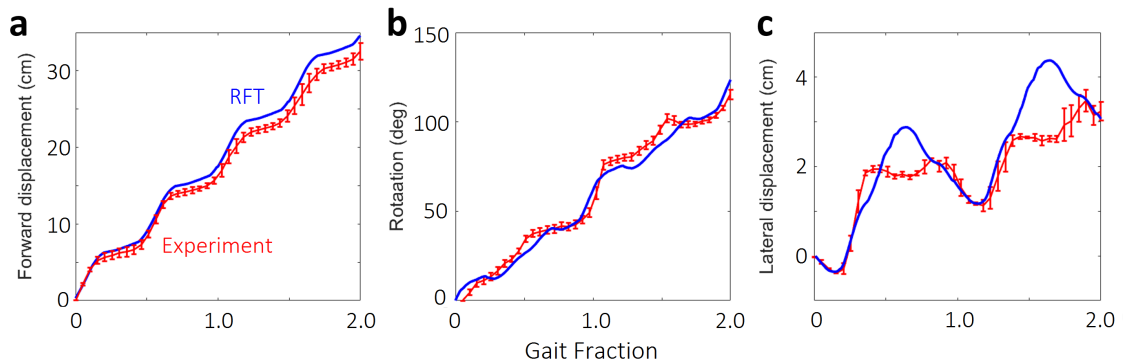


Figure 3.7: Sample trajectories of robot experiments and RFT simulations implementing (a) fast walk gait, (b) rotary sequence no modulation gait, and (c) sideways gait, showing close agreement between RFT simulations and robot experiments. In these gaits, body undulations are properly designed to improve (a) forward, (b) rotational, and (c) lateral displacements.

3.2.6 Rotational Height Functions

Next, we studied the role of body bending in rotational motions. Four types of leg movements were prescribed: the lateral footfall sequence with no modulation (Figure 3.3b.1), the lateral footfall sequence with differential drive modulation (Figure 3.3b.2), the rotary footfall sequence with no modulation (Figure 3.3b.3), and the rotary footfall sequence with differential drive modulation (Figure 3.3b.4).

Lateral sequence and rotary sequence.

While the lateral sequence (FR-HL-FL-HR) (**LS**) footfall pattern is widely used in forward walking; we show that by properly coordinating body bending, the **LS** footfall pattern can also give rise to rotational motion (e.g., turning). As expected, other sequences favor motions in other directions. [162] introduced *rotary sequence footfall pattern* (FR-HR-HL-FL) (**RS**) that favors counterclockwise turning. In this section, we prescribed both **LS** and **RS** to produce rotational motions. The leg movements prescribed in Figure 3.3b.3 and Figure 3.3b.4 followed the (**RS**) footfall pattern.

Differential drive modulation and no modulation.

In this section, we introduce the notion of modulation of the joint amplitudes to cause rotational motion as well. To distinguish modulated motion from unmodulated motion, we use the abbreviation **NM** to mean no modulation. In no modulation (**NM**) leg movements, the leg “shoulder” joint angles are prescribed as piece-wise sinusoidal functions as mentioned in Section 4.2.1 (move from cranial end to caudal end when the leg makes contact with ground, and move from caudal end to cranial end when the leg is in the air) (see Figure 3.3b.1 and Figure 3.3b.3). Leg movements previously prescribed in **NM** will lead to pure forward translation and no rotation. However, rotation can be introduced by coordinating body undulation.

Now we define differential drive modulation (**DDM**) leg movements. The leg “shoulder” angles are also prescribed as piece-wise sinusoidal functions. However, the right (FR and HR) limb joint angles move from cranial end to caudal end when the leg makes contact with ground, and move from caudal end to cranial end when the leg is in the air; while the left (FL and HL) limb joint angles move from caudal end to cranial end when the leg makes contact with ground, and move from cranial end to caudal end when the leg is in the air (see Figure 3.3b.2 and Figure 3.3b.4). In this way, the differential on lateral limb amplitude is modulated to introduce rotational motion ([163]). We call counterclockwise

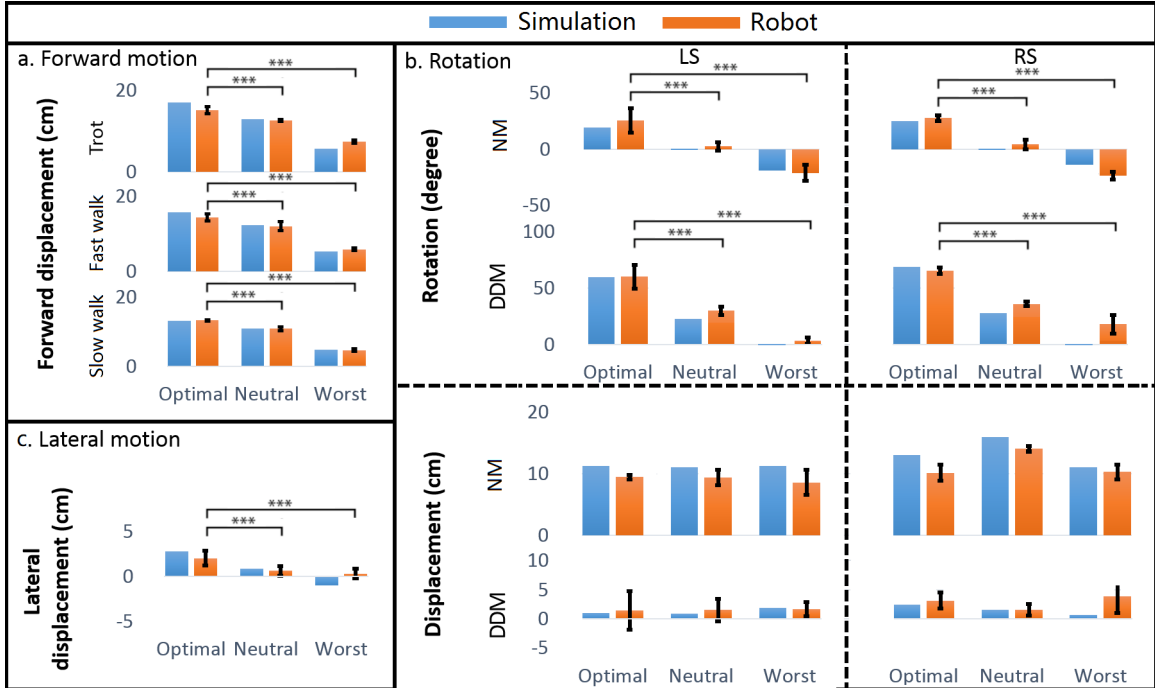


Figure 3.8: Comparison of displacement in RFT simulations (blue bars) and robot experiments (orange bars with error bar, representing 1 standard deviation) results of (a) forward, (b) rotational and (c) lateral gaits, showing close agreement between RFT simulations and robot experiments. Each gait is tested for ~ 3 experiment trials; each trials containing at least ~ 3 gait periods. The “optimal”, “neutral” and “worst” respectively represent the optimal body bending, no body bending (fixed straight back) and the worst body bending. We indicate statistically significant improvement comparing the ‘optimal’-‘neutral’, as well as ‘optimal’-‘worst’ gaits. The gait comparison with a horizontal bracket with *** represents statistically significant improvement ($p < .001$); the gait comparison without a horizontal bracket represents no statistically significant improvement ($p > .05$). For rotational gaits in (b), we show both transitional and rotational displacement values for completeness only: body bending is optimized with respect to rotation only, and displacement changes are not optimized.

(CCW) rotation as the positive direction. The differential drive modulated leg movements can lead to pure CCW rotation without translation. Properly coordinating body undulation will further increase the rotation per gait cycle.

Note that in Section 4.1, we prescribe the leg movement without modulating the leg amplitude. Therefore, they are in the category of no modulation. Also, prescribed leg movements of the slow walk gait in Section 4.1 (Figure 3.3a.1) are identical to the prescribed LS leg movements with NM (LS NM) in this subsection (Figure 3.3b.1). We

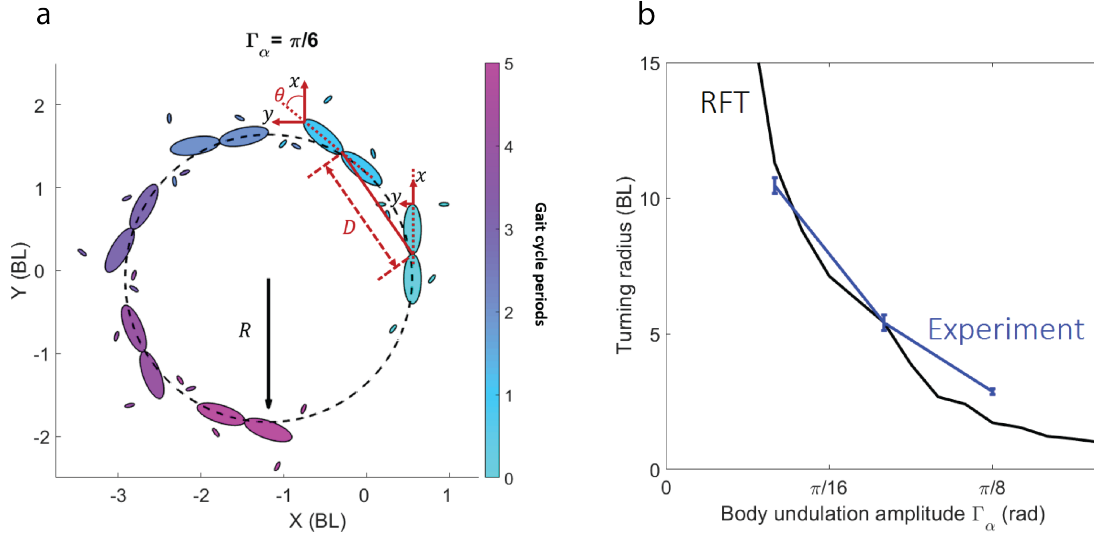


Figure 3.9: (a) Snapshots of robot simulation following a circle. Rotation with forward motion will lead to an arc in center of mass trajectory. R is the curvature radius of the center of mass trajectory; θ is the stride rotation and D is the stride displacement. (b) Body undulation amplitude vs. robot turning radii (the curvature radius of the center of mass motion trajectory). We hypothesize that by modulating the body undulation amplitude, we can control the turning radius of the robot. Robot experimental data (blue) and RFT simulation data (black) validate our hypothesis.

will show that body undulation can lead to either additional rotation or additional forward displacement to the original leg movements (see Figure 3.6).

Body undulation during rotation

In addition to modulating the amplitudes, we can also design the turning motions by investigating the rotational height functions. The rotational height functions are presented in Figure 3.5b. The gait paths that enclose the maximum surface integral in the rotational height functions are predicted to be the gaits with the maximum **CCW** rotation per gait cycle (“optimal” gait). Similarly, the gait paths that enclose the minimum surface integral in the rotational height functions are predicted to be the gaits with the minimum **CCW** (i.e., the maximum **CW**) rotation (“worst” gait). Interestingly, the body bending in coordination with **LS** that optimizes rotation is dominated by the second term of Fourier series, while the body bending in coordination with **RS** that optimizes rotation is dominated by the first

term of Fourier series.

Steering.

In Section 4.2.2, we showed that with the help of body bending, quadrupedal systems can simultaneously go forward and rotate; we call this type of motion steering because it is reminiscent of a car driving down the street. In this section, we will show that properly coordinated body bending can control the steering angle of quadrupedal systems. The leg movements in this section are prescribed by slow walk (NMLS).

One of the most important parameters in steering is the turning radius. As illustrated in (Figure 3.9.), the quadrupeds that walks and turns simultaneously will essentially follow a circle. The turning radius, R , is given by:

$$R = \frac{D \cdot \sin(\frac{\pi-\theta}{2})}{\sin(\theta)}, \quad (3.8)$$

where D is the stride displacement (displacement per gait cycle) and θ is the stride rotation (body rotation per gait cycle).

Next, we aim to control the turning radius by modulating the body bending. From the rotational height function in Figure 3.5b.1, we observe that the surface integral enclosed by the assistive line and the gait path will increase with body joint angle amplitude. However, that path in Figure 3.5b.1 will enclose no additional area in its corresponding forward height function Figure 3.5a.1. Thus by increasing the body bending joint angle amplitude, Γ_α , greater stride rotation, θ , is expected while stride displacement D remains constant. In this way, we show that we can control the turning radius by modulating the body bending amplitude.

3.2.7 Lateral Height Function

Finally, we studied how properly coordinated body bending can improve lateral displacement per gait cycle. [162] introduced the footfall patterns that produce slight lateral motion,

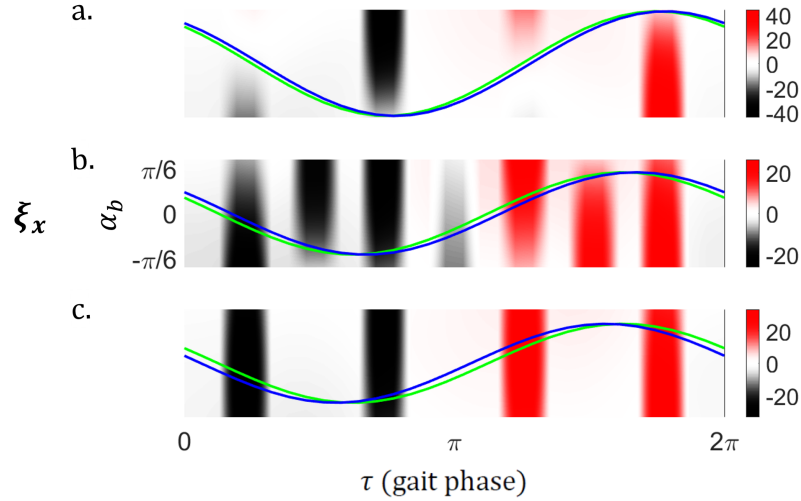


Figure 3.10: Height functions for salamanders, namely experimentally-measured gaits for (a) slow walk, (b) fast walk and (c) trot, with salamander gait in blue curves and geometric mechanics predicted gait in green curves overlaid. All the panels have the same body angle range as in the middle panel.

in which the fore right leg is in phase with the hind right leg, and the fore left leg is in phase with the hind left leg. The detailed description of leg movements is shown in Figure 3.3c. We then calculate lateral height functions (Figure 3.5c).

The gait path with maximum surface integral in the height function (“optimal” gait) is predicted to be the gait with the largest lateral displacement per gait cycle. We also identified the body bending that corresponds to the minimal surface integral (“worst” gait). We tested the “neutral” gait with fixed straight back ($\alpha_b = 0$).

Quadrupeds have limited ability to move sideways ([164]). However, body bending will greatly enhance the ability of a quadrupedal robot to move laterally. In the next section, we will show the lateral displacement for optimal, neutral and worst body bending in coordination with leg movements across granular media.

3.3 Experimental Results

To verify and explore our theoretical model predictions, we developed a robophysical model ([149]). Specifically, we built a quadrupedal robot (Figure 3.1a) and tested its

performance on granular media. This open-loop, servo-driven, 3D-printed robot (450 g, ~40 cm long) has four legs and an actuated back. Each leg has two servo motors (XL-320) to control its vertical position and its lateral position. A joint in the middle of the body (AX-12 servo) controls lateral body bending.

Using a fully-automated setup ([165]), we experimentally and systematically tested the role of body bending during quadrupedal locomotion on a bed filled with ~ 1 mm diameter poppy seeds. We performed three trials for each gait, with each trial consisting of at least three complete gait periods. The robot executed a programmed set of movements to move on the loosely-packed poppy seeds. Throughout the experiment, four Optitrack Flex13 cameras recorded the positions of infrared-reflective markers on the robot (at 120 frame per second). At the end of each experiment, the robot's final position was identified. A 3-axis motor system moved to the robot, picked it up and sent it back to the starting position. Before each experiment, an air-fluidized bed erased the footprints and allowed the seeds to be reset into a loosely-packed state ([166]).

We provide snapshots of the robot executing gaits predicted by geometric mechanics in Figure 3.6. We compared the trajectories of quadrupedal robot experiments and RFT simulations in Figure 3.7, and show that they are in good agreement (Figure 3.8). Note that in Figure 3.7c, there is deviation between the robot experiments and RFT simulation. We believe that the relatively shorter displacement in a robot experiment is due to the poppy seed accumulation that is not modeled in RFT simulation.

3.3.1 Robot Experiment Verification of Forward Height Function Prediction

In Section 4.1, we identified the 'optimal', 'neutral' and 'worst' body bending from forward height functions to improve forward displacement per gait cycle. We verified the predictions from forward height functions by RFT simulations and robot experiments across granular materials. Both RFT simulations and robot experiments suggest that the 'optimal'

body-leg coordination can improve the forward displacement, while the ‘worst’ phasing can lead to ineffective forward gait. Simulation and experiment data are presented in Figure 3.8a.

3.3.2 Robot Experiment Verification of Rotational Motions

Lateral sequence and rotary sequence

In Section 4.2, we identified the ‘optimal’, ‘neutral’ and ‘worst’ body bending from rotational height functions in coordination with **LS** and **RS**. We verified predictions from rotational height functions by RFT simulations and robot experiments across granular materials. The data are presented in Figure 3.8b. Both RFT simulations and robot experiments suggested that proper body-leg coordination can improve the **CCW** rotation.

Differential drive modulation and no modulation.

From Figure 3.8b, we observed that when the body is maintained fixed straight (i.e., the ‘neutral’ body bending), the **DDM** leg movements lead to pure rotation without translation while **NM** leg movements lead to pure translation without rotation.

In leg movements prescribed in **DDM**, the ‘optimal’ body bending coordination can improve the body orientation rotation per gait cycle (good in place turn) whereas ‘worst’ body bending can decrease the body orientation rotation per gait cycle (bad in place turn).

In leg movements prescribed in **NM**, the ‘optimal’ body bending coordination will introduce counterclockwise rotation to forward motion (counterclockwise steering) whereas the ‘worst’ body bending will introduce clockwise rotation to forward motion (clockwise steering).

Steering

We further verified our steering radius control hypothesis with robot experiments and RFT simulation. We plotted the body bending amplitude Γ_α against the turning radii in Fig-

ure 3.9. Both robot experiments and simulations suggested that by modulating the body bending joint angle amplitude, we can control the turning radius. Note that the simulation-experiments discrepancy increases at larger amplitude. Since our robot experiments were performed on granular media, there can be granular material accumulation on the side when robots exhibit large turns. The accumulated granular material can have greater effect on the locomotion performance when the robots implement multiple gait cycles. Therefore, we suspect that it is the granular material accumulation that leads to underperformance of steering experiments in Figure 3.9.

3.3.3 Robot Experiment Verification of Lateral Height Function Prediction

Finally, we identified the ‘optimal’, ‘neutral’ and ‘worst’ body bending from lateral height functions to improve lateral displacement per gait cycle. We verified predictions from lateral height functions using RFT simulations and robot experiments across granular materials. Both RFT simulations and robot experiments suggest that the ‘optimal’ body-leg coordination can improve the lateral displacement, while the ‘worst’ phasing can lead to an ineffective lateral gait. Simulation and experiment data are presented in Figure 3.8c.

3.3.4 Animal Experiment Verification of Forward Height Function Prediction

To extend our study to biological quadrupedal systems, we collected data and performed analysis on fire salamanders (*Salamandra salamandra*) to investigate if the animal uses body kinematics to optimize the forward motion.

In these experiments, individual animals walked along a straight trackway filled with 300- μm glass particles. Three cameras (GoPro Hero3+, 720 pixel resolution) were positioned around the trackway and recorded synchronized videos at 120 FPS. All experiments were approved by the Royal Veterinary College’s Clinical Research Ethical Review Board, approval number 2015 1336. No animals were harmed for the experiments, and animals had rest periods in between data collection trials. Experiments were conducted in a humidity-

controlled laboratory at the University of Oviedo, Spain. The temperature ($\sim 18^\circ\text{C}$) and light cycle (12hr dark, 12hr light) were maintained at constant levels.

At least three gait periods were recorded in each experiment. Limb positions, body angles, and footfall timing were manually extracted from each recording. According to the limb positions and footfall timing, we selected three representative salamander motion videos (each contains at least three gait periods of animal motion), which correspond to “trot” (duty factor 0.75 ± 0.03 , lateral leg phase shift 0.25 ± 0.05), “fast walk” (duty factor 0.76 ± 0.04 , lateral leg phase shift 0.36 ± 0.02) and “slow walk” gaits (duty factor 0.73 ± 0.1 , lateral leg phase shift 0.50 ± 0.02). We fitted the animal body angles with the first two terms of Fourier Series as in Equation 3.7. We plotted the obtained animal body bending angles as a function of the leg movement phase (blue curves in in Figure 3.10).

To predict the proper body bending coordination with “trot”, ”slow walk”, and “fast walk” salamander leg movements, we calculated the corresponding forward height functions. In the forward height function, we then can design and predict the body bending gait paths to maximize forward displacements. The green curves in Figure 3.10 are the predicted body bending gait paths with body-bending amplitudes Γ_α extracted experimental data. We show that the body-leg coordination gait paths in salamander locomotion are in close agreement with our theoretical prediction to maximize forward displacement.

CHAPTER 4
COORDINATING TINY LIMBS AND LONG BODIES: GEOMETRIC
MECHANICS OF LIZARD TERRESTRIAL SWIMMING

Part of this chapter is adapted from a journal article “Coordinating tiny limbs and long bodies: Geometric mechanics of lizard terrestrial swimming.” *Proceedings of the National Academy of Sciences* 119.27 (2022): e2118456119. My contribution in this project includes (1) designing the experiments, (2) conducting the numerical analysis, (3) writing the manuscript. Robophysical experiments presented in this chapter are conducted by Tianyu Wang.

Recent studies have demonstrated that body elongation and limb reduction has convergently evolved in most major lineages, including not but limited to fishes [167], amphibians [168], reptiles [169], and even mammals [170]. Of particular interest, in Squamate reptiles (lizards and snakes) snake-like body shapes have independently evolved at least 25 times [101, 171]. While the exact selective pressures for this evolutionary transition remain a mystery, prior studies revealed possible advantages of certain body plans in navigating their corresponding environments [172, 101, 68, 106]. One of the best supported hypotheses is that limbless and/or short-limb forms have evolved as adaptations for fossoriality (underground environments) or cluttered environments [99, 100, 101, 99].

Transitions in body morphology are just one of many aspects of evolutionary adaptations for cluttered or fossorial habitats. Another crucial but less studied aspect in such adaptation is how animals can use these diverse morphologies during locomotion. For example, stereotyped snakes and lizards have distinct body movement patterns: snakes primarily use traveling wave body undulations to generate thrust [60, 61, 62, 63]. Lizards use a standing wave to assist limb retraction [64, 65]; and employ traveling waves of axial body undulation at high speed [66, 67, 65], believed to help the limbs in transmitting forces

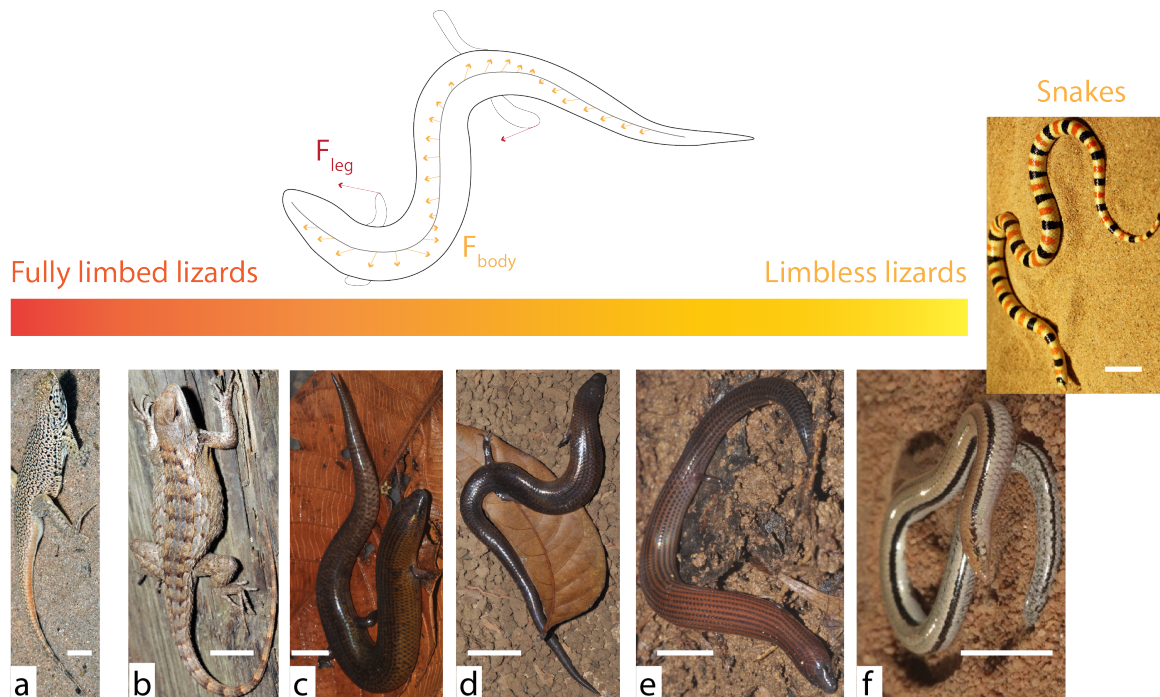


Figure 4.1: **Target and model systems for understanding the role of body undulation in the lizard body elongation and limb reduction continuum** (Left) (from top to bottom) fully limbed lizards (*U. scoparia* and *S. olivaceus*) in comparison with extant short limbed, elongate lizards (*B. kadwa*, *B. taylori*, and *B. muntingkamay*) and limbless/almost limbless species (*L. praepedita* and *C. occipitalis*). Scale bars indicate 2 cm. (Right) An illustrative diagram of the thrust generation in short limbed, elongate lizards: the thrust generated by limb retraction is labeled in red arrows, the thrust generated by body undulation is labeled in yellow arrows.

along the axis of progression [65].

In lizards with short limbs and elongate bodies, because of the proximity to the substrate, both the body and limbs directly contribute to generate thrust and overcome drag [65]. This regime, which because of its similarities to sand-swimming in lizards [72] and snakes [122, 63, 73] we refer to as *terrestrial swimming* is less studied than inertial running in large limbed lizards [66, 67, 65]. Since the short limbs of elongate lizards typically cannot support the animal's body weight, the two propulsive mechanisms (limb retraction and body undulation) can coexist, requiring proper coordination. Further, the support of body weight must be properly distributed between the ventral surface of the body and the limbs to facilitate effective thrust-generation mechanics. Thus a challenge of studying terrestrial

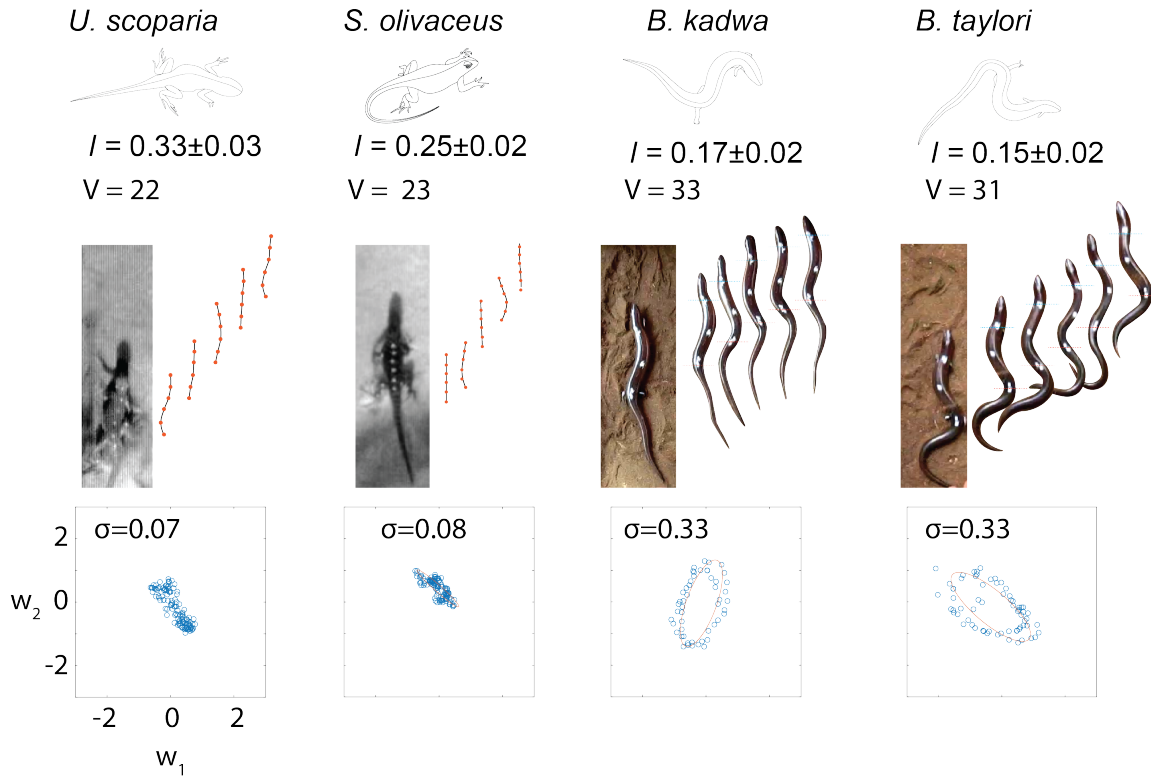


Figure 4.2: **The diversity of body waves in the body elongation and limb reduction continuum.** (top) Photos of species and the snapshots of their body motion during one period (at a scale of seconds) of locomotion. Seven species were studied (from left to right): *U. scoparia*, *S. olivaceus*, *B. kadwa*, *B. taylora*, *B. muntingkamay*, *L. praepedita*, and *C. occipitalis*. The relative limb size (l : the hind limb length normalized by SVL) and number of presacral vertebrae (V) for each species are labeled [173, 105]. (bottom) The projections of body curvature into the reduced shape space and the estimation of σ for each animal. Units of axes are identical to the left panel.

swimming lies in discerning the coordination between body undulation and limb retraction while generating effective body weight distribution.

To address these questions, we take a comparative biological, robophysical, and theoretical modeling approach. We compile a collection of high-speed videos of a spectrum of lizard body forms collected in both field and laboratory settings. Through the use of neural network markerless tracking [174], we analyze the data and reveal a striking diversity in body undulation dynamics. Specifically, we find that body undulation in lizards with short limbs is a linear combination of a standing wave and a traveling wave; and that the ratio of the amplitudes of these two components is inversely related to the degree of

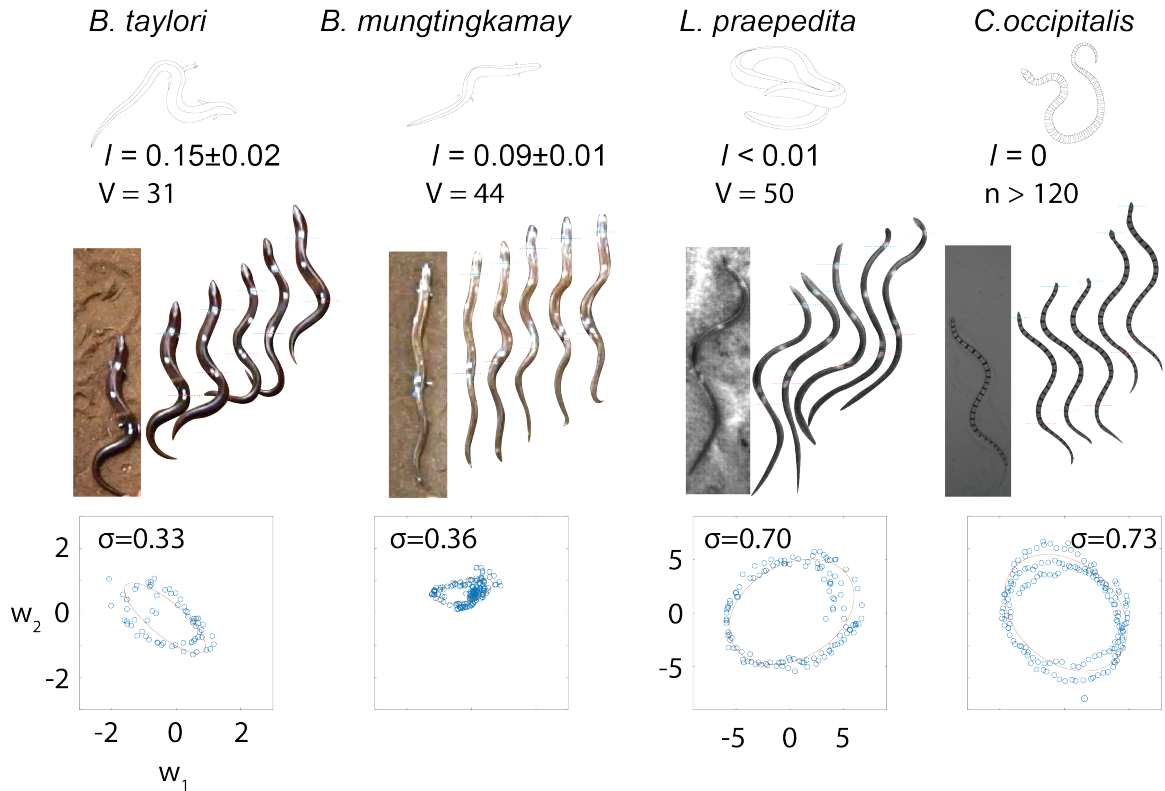


Figure 4.2: **The diversity of body waves in the body elongation and limb reduction continuum.** (top) Photos of species and the snapshots of their body motion during one period (at a scale of seconds) of locomotion. Seven species were studied (from left to right): *U. scoparia*, *S. olivaceus*, *B. kadwa*, *B. taylori*, *B. muntingkamay*, *L. praepedita*, and *C. occipitalis*. The relative limb size (l : the hind limb length normalized by SVL) and number of presacral vertebrae (V) for each species are labeled [173, 105]. (bottom) The projections of body curvature into the reduced shape space and the estimation of σ for each animal. Units of axes are identical to the left panel.

limb reduction and body elongation. The fact that our animals move in highly damped environments, where frictional forces dominate over inertial forces, allows the use of the geometric mechanics framework [81, 118] to explain wave dynamics and body-limb coordination. This geometric mechanics theory, which replaces laborious calculation with diagrammatic analysis, rationalizes the advantage of using traveling waves in short limbed elongate lizards, and predicts that such advantages emerge when the primary thrust generation source shifts from the limbs to the body. We test our hypothesis with biological and robophysical experiments by manipulating the substrate on which fully limbed lizards move, and with robophysical experiments by controlling the body and limb thrust mecha-

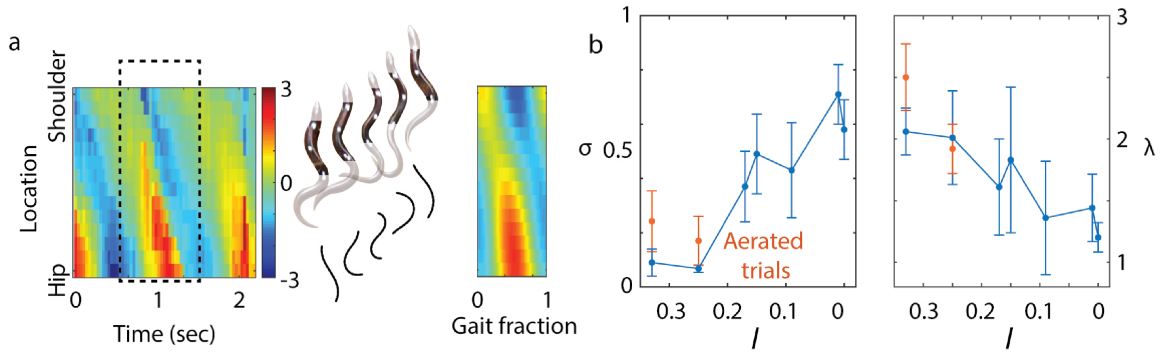


Figure 4.3: **From standing wave to traveling wave** (a) Comparison between the original body curvature profile of *B. taylori* and the reconstructed body curvature profile over a gait cycle from the estimated wavelength λ and flatness σ . The units of the colorbar are SVL^{-1} . (b) The relationship between the locomotion parameters (σ and λ) and morphology parameter (the relative hind limb length l). Red points with error bars correspond to the locomotion parameters of *U. scoparia* and *S. olivaceus* on an aerated granular medium to reduced the resistive force of the media. Note that we use $l = 0.01$ for *L. praepedita* on the plot and that the abscissa is reversed (descending left to right) to correspond to Fig. 2.

nism. Answering these questions will not only establish a relationship between what they have (the body morphology) and how they move (the body-limb coordination) [32, 102, 103, 104], but also facilitate our understanding of the locomotor implications of the evolution of snake-like forms [105, 106].

4.1 Results

4.1.1 Diversity in lizard body movements

We investigated three short limbed, elongate species with similarly developed fore and hind limbs [175, 105] (*Brachymeles kadwa*, *Brachymeles taylori*, and *Brachymeles muntingkamay*) and compared them with fully limbed lizards (*Uma scoparia* and *Sceloporus olivaceus*) and limbless species (the almost limbless lizard *Lerista praepedita* and the shovel-nosed snake *Chionactis occipitalis*). These species were chosen because they form a spectrum of limb reduction and body elongation (Figure 4.1). The relative limb size is defined as the hind limb length normalized by SVL (snout vent length). The number of presacral

vertebrae is a measure of elongation [105] (Figure 4.2). We recorded field videos of these species moving on granular media (consisting of soil and poppy seeds), and compared the kinematics of their body movements. The snapshots of their body postures during locomotion are compared in Figure 4.2 (middle panel). Qualitatively, we observed the node¹ of body bending is almost stable in fully limbed lizards (at the shoulder and hip), and propagates from snout to cloaca in shovel-nosed snakes. Interestingly, in short limbed, elongate species, one of the nodes is almost stable near the snout, and the other node propagates from the mid-body to tail.

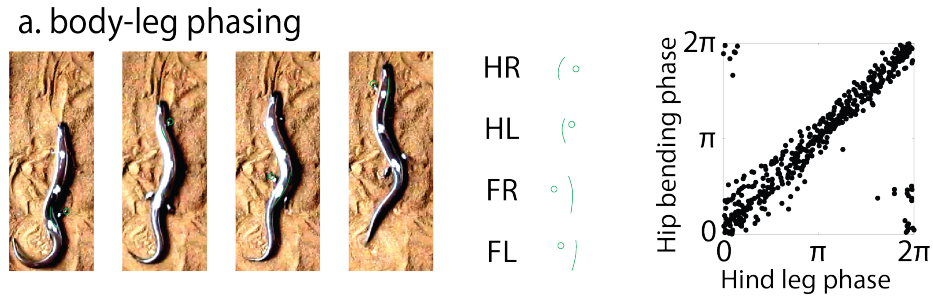


Figure 4.4: **Geometric mechanics analysis of the body-limb coordination in short limbed, elongate lizards** (a) The limb movement in short limbed, elongate lizards follows the lateral couplet sequence (FR-HL-FL-HR). The phase relationship of hip bending and hind limb movements are plotted in the right side panels.

We considered locomotion as a properly coordinated sequence of “self-deformations” (internal shape changes) that generate thrust to overcome drag forces (self-propulsion²) via interactions with substrates. Prior work [124, 176, 75, 82, 83] suggested that despite possessing high dimensionality, the essence of self-deformation can be described by a linear combination of shape basis functions. Consider the body curvature³ $\kappa(s, t)$ at time t and location s ($s = 0$ denotes the snout in snakes (or the shoulder in lizards) and $s = 1$ denotes the cloaca in snakes (or the hip in lizards)). Thus, the body curvature profile can be approximated by:

¹The point in the body which has zero body curvature

²We will explain further the terminology of self-propulsion and self-deformation when we discuss geometric mechanics

³Body curvature is the inverse of radius of curvature

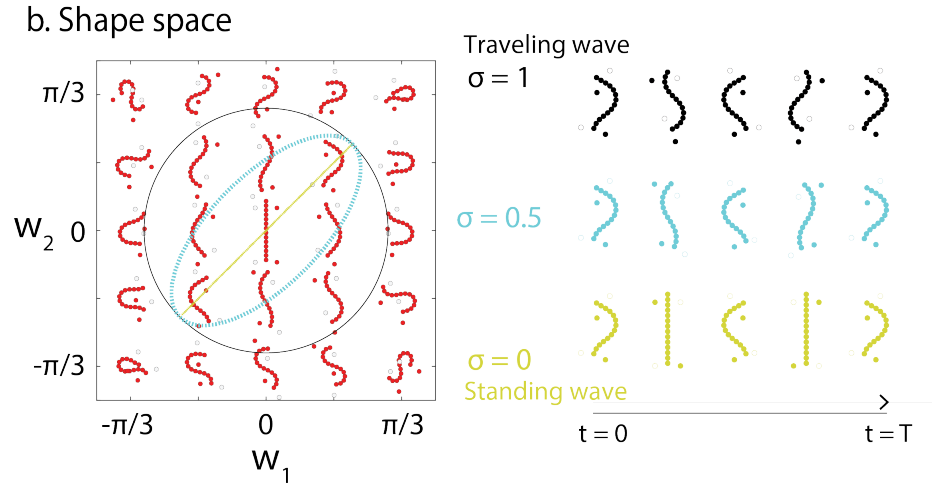


Figure 4.4: **Geometric mechanics analysis of the body-limb coordination in short limbed, elongate lizards** (b) The shape space for short limbed, elongate lizards. The body movements are prescribed by the reduced shape variable w_1 and w_2 , and the limb contact states are inferred from the body movements. Gaits can be represented by closed-loop paths in the shape space. A standing wave gait path, a traveling wave gait path, and an intermediate wave gait path are compared.

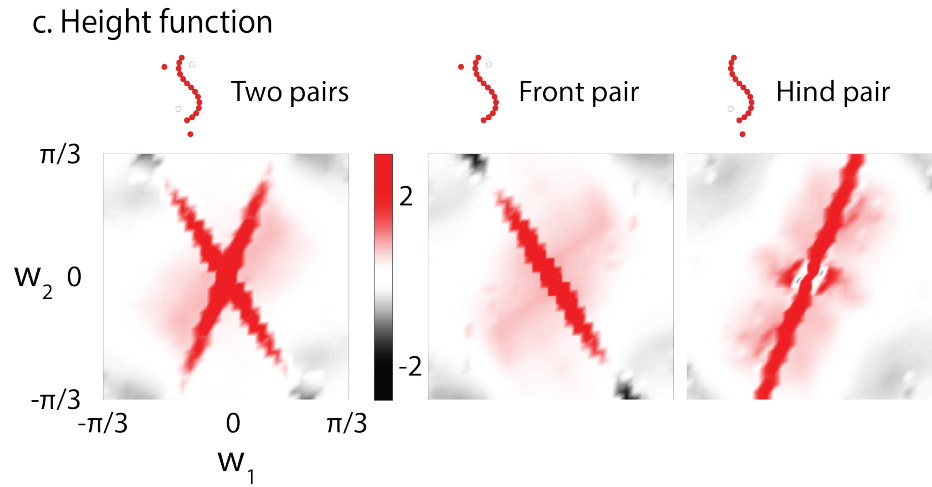


Figure 4.4: **Geometric mechanics analysis of the body-limb coordination in short limbed, elongate lizards** (c) Height functions to investigate the body undulation in lizards with intermediate limbs. (left) Two strips emerged in the height function for short limbed, elongate lizards, such that a circular gait path can enclose significantly more surface than a flattened elliptic gait path. To further understand the two stripes, we calculated the height function for hypothetical lizards with one pair of limbs near the head (middle panel) and near the tail (right panel). Each stripe is associated with a pair of limbs, in which case a flattened elliptic gait path can enclose sufficient surface in the height function. The units of the colorbar are $(10^{-3} \times \text{SVL}^{-1} / \text{rad}^2)$.

$$\kappa(s, t) = w_1(t) \sin(2\pi\xi s) + w_2(t) \cos(2\pi\xi s), \quad (4.1)$$

where ξ is the spatial frequency of body undulation obtained from direct fitting ($1/\xi$ denotes the wavelength, λ , in the unit of SVL); $w_1(t)$ and $w_2(t)$ are the reduced shape variables describing the instantaneous shape of the locomotor at time t . In this way, we can map the original high-dimensional body curvature profile $\kappa(s, t)$ into a space spanned by w_1 and w_2 . In pure standing waves, the body curvature trajectory in the reduced shape space can be described as a flattened ellipse (with eccentricity $e \rightarrow 1$). In pure traveling waves, the body curvature trajectory in the reduced shape space can be described as a circle (with eccentricity $e \rightarrow 0$). In this way, an elliptical trajectory can be considered a linear combination of the flattened ellipse path and the circular path, the ratio of which can be quantified by the flatness ($\sigma = \sqrt{1 - e^2}$), where $\sigma = 0$ denotes a pure standing wave and $\sigma = 1$ denotes a pure traveling wave. We compared the gait trajectory for species ranging from fully limbed to limbless animals in Figure 4.2 (bottom panel), where we observed a transition from a flattened ellipse in stereotyped lizards to a circle in snakes.

To quantitatively measure the flatness of the gait trajectories in the reduced shape space, we fit these trajectories with oriented ellipses. To test the accuracy of the fitting, we compared the original body undulation profile (collected from tracking in field videos, left panel) and the fitted body undulation profile (from a reconstruction of the ellipses in reduced shape spaces, right panel) in Figure 4.3a. Interestingly, we observed that σ increased and λ decreased, indicating a transition from standing wave to traveling wave, as the limb size decreased (and number of presacral vertebrae increased) (Fig. Figure 4.3b).

4.1.2 Wave dynamics are key to body-limb coordination

We further analyzed the limb movement in the short limbed, elongate species (*B. kadwa* and *B. taylori*). Snapshots showing the body posture during the touchdown of each foot are illustrated in Figure 4.4a (left panel). The limb movements in short limbed, elongate

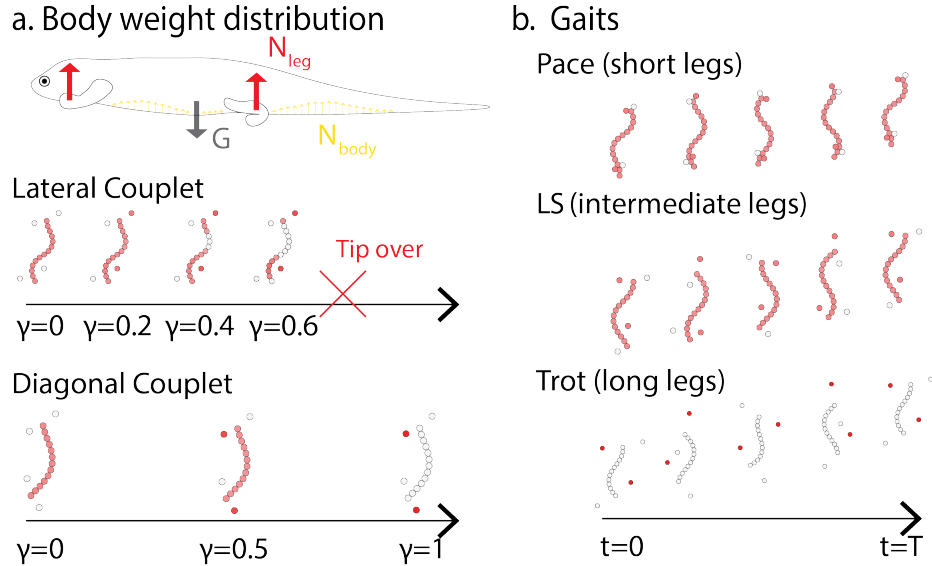


Figure 4.5: **The weight distribution role of limbs in lizard locomotion** (a) The body weight can be supported by the limbs and the body; γ indicates the fraction of body weight supported by limbs. (b) Three typical gaits: the pace gait (duty factor = 0.5, leg phase shift = 0) implemented by lizards with short limbs, the LS (lateral sequence: duty factor = 0.5, leg phase shift = 0.25) gait implemented by lizards with intermediate limbs, and the trot gait (duty factor = 0.5, leg phase shift = 0.5) implemented by lizards with long limbs.

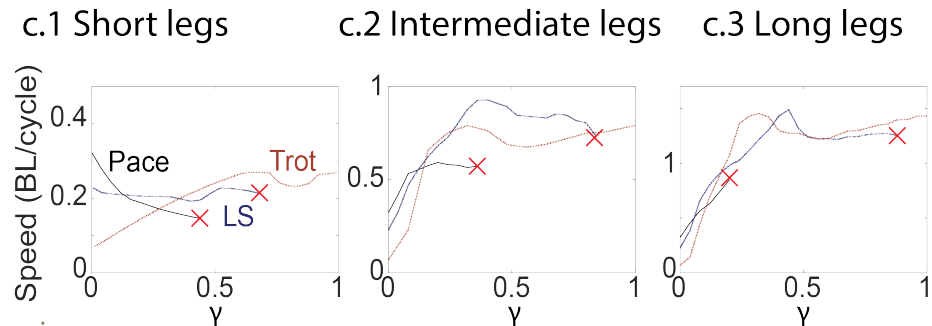


Figure 4.5: **The weight distribution role of limbs in lizard locomotion** (c) The relationship between γ and speed for (solid black curves) pace, (dashed blue curves) LS, and (dashed red curves) trot gaits on lizards with (c.1) short, (c.2) intermediate, and (c.3) long limbs. Potential tip-overs are indicated by a red cross.

species follow the sequence: FR-HL-FL-HR (F, H, R, and L represent fore, hind, right, and left respectively). Specifically, the hind leg leads the fore leg on the same side by 0.38 ± 0.07 of a period, which is a lateral couplet sequence [17]. Further, for each leg, the ground-contact (stance phase) duration is approximately the same as the off-ground (swing phase) duration, indicating the duty factor (the fraction of a period that each limb is on the

ground) is approximately 0.5.

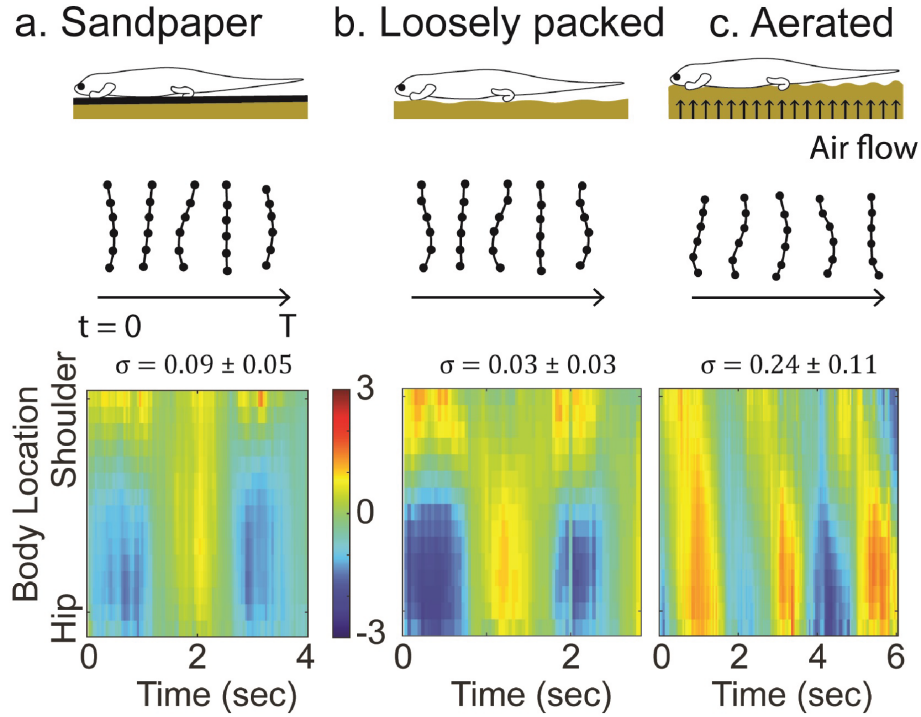


Figure 4.6: **Traveling wave in fully limbed lizards induced by substrate variation** Comparison of the body wave dynamics of *Uma scoparia* (a) on sandpaper and (b) on a loosely packed granular medium, and (c) on an aerated granular medium. An almost perfect standing wave is observed for *Uma scoparia* on sandpaper and on the loosely packed granular medium, while features of a traveling wave emerge for *Uma scoparia* on the aerated granular medium. Resulting σ and λ are shown in Fig. Figure 4.3b. The units of the colorbar are SVL^{-1} for all panels.

We also noticed that during a foot touchdown, the local body element develops maximal curvature (in the convex direction towards the leg) to increase its reach (Figure 4.4a, middle panel), which is consistent with observations of other quadrupedal locomotors [177, 176]. This observation indicates that the fore (hind) limb movement should be in phase with shoulder (hip) bending. We quantify this observation by showing the phase relationship between the hind limb movement and hip bending in Figure 4.4a (right panel). The relationship between the fore limb movement and shoulder bending was shown in Fig. S1. We observed a stronger in-phase relationship between the hind limb and hip bending. We suspected that this is a consequence of the low visibility of the fore limbs in the field-recorded

videos, and the low magnitude of the shoulder bending compared to hip bending.

The observations of the phase relationship between limb movements and body bending allow us to reduce the shape variables of short limbed, elongate lizard locomotion into two-dimensions. As discussed earlier, the body undulation profile $\kappa(s, t)$ can be approximated by a linear combination of $\sin(2\pi\xi s)$ and $\cos(2\pi\xi s)$ (under coefficients w_1 and w_2). We took $\xi = 0.65$ from our previous analysis ($\lambda \approx 1.5$ for *B. taylori* and *B. kadwa* Figure 4.3b). We can then infer the limb contact states from the choice of reduced shape variables w_1 and w_2 such that the shoulder (hip) bending is in phase with the fore (hind) limb movement. The explicit shape space can be found in Figure 4.4b (left panel).

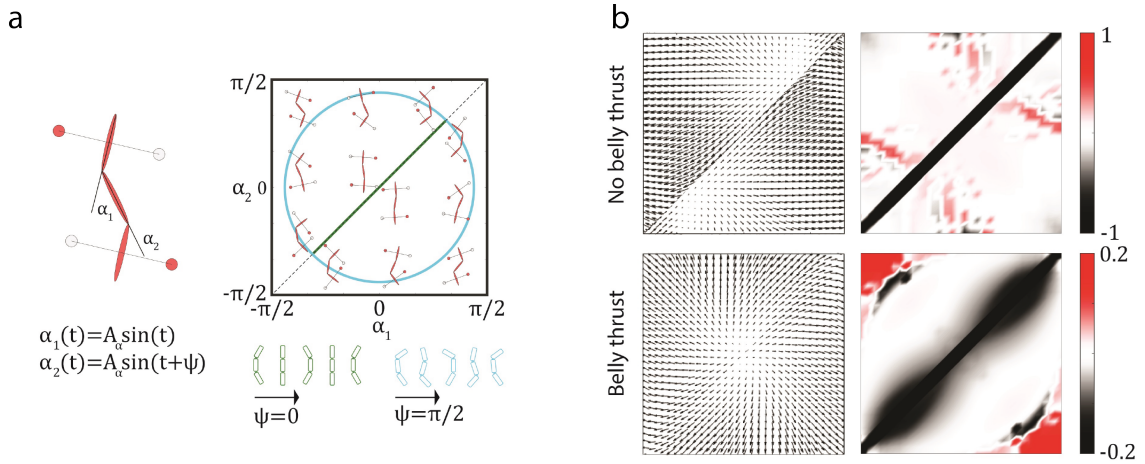


Figure 4.7: **Geometric mechanics modeling for the robophysical experiments** (a) The definition of α_1 and α_2 and the body-limb coordination in the 3-link swimmer and 4 leg contacts. ψ is the phase lag between the upper back and lower back actuators. Right panel demonstrates how leg contact patterns are coupled to the shape variables (α_1 and α_2). On the lower right half of the shape space, the contact patterns are counter-diagonal; on the upper left half of the shape space, the contact patterns are diagonal. Examples of the standing wave ($\psi = 0$) and the traveling wave ($\psi = \pi/2$) are compared in the shape space. (b) Vector field and height functions for modelling the robophysical experiments on poppy seeds. The displacement can be approximated by the surface integral enclosed by the gait path over the height function (right panels). The units of the colorbar are $(10^{-3} \times \text{SVL}^{-1} / \text{rad}^2)$. Units of axes in (b) are identical to the shape space in (a).

Hypothesizing that terrestrial swimming is dissipation dominated (ground resistive forces dominate body or substrate inertial forces), we next used the geometric mechanics framework [178, 81, 83] to compare the effectiveness of standing and traveling waves in these

short limbed, elongate lizards. Geometric mechanics was originally developed to study locomotion via self deformation at low Reynolds numbers [76, 81]. Since the thrust is generated from properly coordinated self-deformation to counter the drag forces, we refer to such thrust generation as self-propulsion. Recent work has shown that geometric mechanics replaces laborious calculation with a diagrammatic scheme and offers novel insights into the self deformation patterns in various types of biological locomotion, such as slithering and sidewinding in snakes and body-leg coordination in salamanders [83, 176].

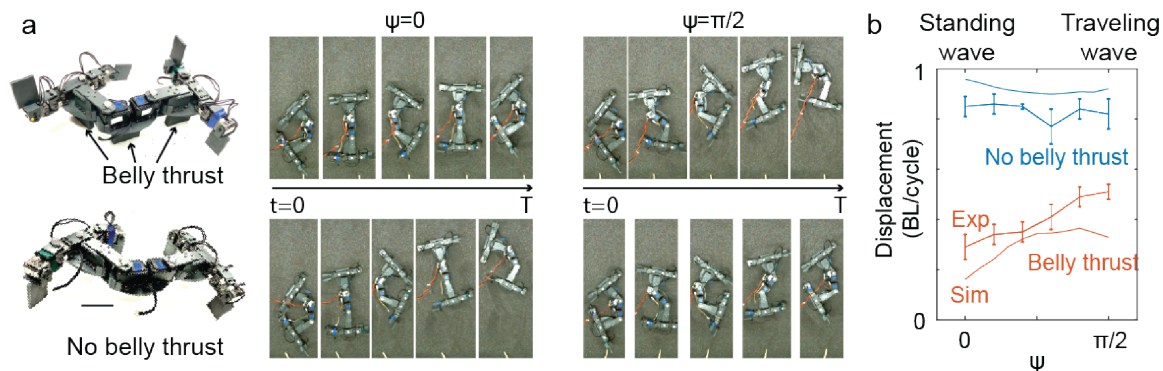


Figure 4.8: **Robophysical experiments** (a) Snapshots of robots (top panel: belly thrust; bottom panel: no belly thrust) implementing standing wave ($\psi = 0$) and traveling wave ($\psi = \pi/2$) gaits. (b) The effect of ψ on locomotion performance for robot with no belly thrust (blue curve) and robot with belly thrust (orange curve).

In the geometric mechanics framework, we seek to calculate performance (measured by body lengths moved per cycle) from the sequences of self-deformation. The space spanning the self-deformations (in our case, internal shapes of lizards) is then called shape space (Figure 4.4b). For simplicity, we only analyze the over-damped regime⁴ of lizard locomotion, where there is zero acceleration on the center of mass (CoM) in lizards. In this way, the velocities in shape space (shape velocity) and body velocities are then connected by a matrix called the *connection vector field* (e.g., S3) [75]. A gait, a periodic sequence of shape changes, can be represented as a closed-loop path in the shape space. In Figure 4.4b (right panel), we compared the standing and traveling wave body movements and their

⁴Over-damped motion then implies that inertial forces are negligible compared to the ground reaction forces.

corresponding limb contact sequences. The net displacement of a gait can be approximated by a line integral of the vector field along the gait path [118]. From Stokes' theorem, the line integral of a closed-loop path over a vector field can be visualized by a surface integral over the curl of the vector field (the height function, or often referred to as a constraint curvature function, CCF [75, 83]). The height function for the short limbed, elongate lizards was computed in Figure 4.4c (left panel). In summary, with geometric mechanics framework, we can investigate the seemingly complicated and diverse lizard wave dynamics with the help of a pre-computed diagram, and analyze locomotion performance by evaluating the surface integral.

The actual force models of environmental interactions generated by these lizards in the field are unknown. We chose to approximate them using a model granular medium (poppy seeds) to numerically calculate the connection vector field [11, 176] (Figure 4.4c). To bound the uncertainty in ground reaction forces, we used different force models (rate independent Coulomb friction and rate dependent viscous fluid, S2) and achieved similar conclusions as in Figure 4.4c. Further, in the derivation of the local connection vector field, we assumed that the magnitude of limb retraction is 0.17 of the total thrust (body undulation and limb retraction), a value similar to the relative limb size.

Two stripes emerged in the height function with an oblique intersection, which we interpreted as corresponding to the coordination for limb movements. To better understand the meaning of the height function, we recomputed the height function for two hypothetical lizards: lizards with only fore limbs (Figure 4.4c: middle panel) and lizards with only hind limbs (Figure 4.4c: right panel). One of these stripes emerged in each height function for the hypothetical lizards, supporting our hypothesis that each stripe corresponds with the coordination of one pair of limbs. From the structure of the height function, we inferred that an elliptical gait path with $\sigma \approx 0.5$ can lead to the greatest displacement, which was qualitatively the range of σ measured from animal experiments (Figure 4.3b).

4.1.3 Body weight distribution

From the above analysis, we noticed that the presence of limbs significantly affects the dynamics of body movements. In fully limbed lizards, almost the entire body weight is supported by the limbs, whereas in limbless lizards the ventral surface supports the entire body weight. But for short limbed, elongate lizards, how should the body weight be distributed between the limbs and the ventral body surface for effective locomotion? We used geometric mechanics modeling to predict the optimal body weight distribution for short limbed, elongate lizards.

Quadrupedal locomotors typically utilize two types of limb contact patterns: the diagonal couplet and the lateral couplet [17]. In the diagonal couplet, the limbs in the ground-contact phase are distributed in pairs along the diagonal (FR/HL) or counterdiagonal (FL/HR), where the body weight can be stably supported by the limbs (Figure 4.5a). In the lateral couplet, the limbs in the ground-contact phase are on the same side, which cannot stably support the entire body weight (Figure 4.5a). Thus, some ventral surface support is essential for the lateral couplet. We quantified the fraction of body weight supported by the limbs as γ . There is a limit on the force that the limbs can support without the animals tipping over (the torque between lateral couplets is greater than the torque from gravity) in the lateral couplet (Figure 4.5a). The detailed derivation to compute the body weight distribution can be found in Chapter 4.

We compared three typical limb contact patterns: the pace, the lateral sequence (LS), and the trot, where leg phase shifts (fraction of a period that the hind limb leads the ipsilateral fore limb) were 0, 0.25, and 0.5 respectively (Figure 4.5b). In the pace, the contact patterns were entirely lateral couplets; in the trot, the contact patterns were entirely diagonal couplets; in the LS, there was a mix of lateral and diagonal couplets. Assuming the duty factor to be 0.5, the fraction of the lateral couplet in the pace, the LS, and the trot were 1, 0.5, and 0 respectively. Further, the body bending spatial frequency ξ was 1, 0.75, and 0.5 for the pace, LS, and trot, respectively, to enforce the in-phase relationship between the

fore (hind) limb movements and shoulder (hip) bending.

We conducted numerical simulations to predict the relationship between γ and forward speed. We studied lizards with short limbs (a hypothetical locomotor with $l = 0.05$, shorter limbs than *B. muntingkamay*), lizards with intermediate limbs (a hypothetical locomotor with $l = 0.17$, similar to *B. kadwa* and *B. taylori*), and lizards with long limbs (a hypothetical locomotor with $l = 0.30$, similar to *U. scoparia*). We observed that for short limbed lizards, it was optimal to use only body undulation to generate thrust ($\gamma = 0$, the pace, Figure 4.5c.1) while intermediate limbed lizards optimally used a hybrid thrust generation mechanism using both body undulation and limb retraction ($\gamma = 0.4$, the LS, Figure 4.5c.2). Finally, one available optimum for long limbed lizards was to solely use limbs to generate thrust ($\gamma = 0$, the trot, Figure 4.5c.3).

Thus, we showed that limbs are crucial to locomotion by short limbed, elongate lizards because they contribute to thrust as well as share some body weight with the ventral surface of the body, which can modulate lifting forces and thus thrust. Depending on the limb size, our model suggests that lizards should properly distribute their body weight between the limbs and the ventral surface to generate effective locomotion. Therefore, we predicted that a traveling wave enhances locomotor performance as the body weight distribution (and thus thrust generation mechanism) shifts from the limbs to the body.

4.1.4 Terrestrial swimming

In fully limbed lizards, nearly the entire body weight is supported by the limbs. It is thus commonly believed that at low speeds, lizards use standing wave body bending to coordinate with their limb movements [87, 35, 176]. Our geometric mechanics modeling predicts that the body weight distribution will affect how much a traveling wave contributes to thrust. We tested this hypothesis by manipulating the substrate on which fully limbed lizards moved and investigated whether we could stimulate terrestrial swimming in fully limbed lizards.

To modulate the body weight distribution, we used an upward air flow through a granular medium to control the ground penetration resistance⁵ [179], maintaining airflow below the onset of fluidization⁶ as in [180]. This technique proved useful in previous biological and robotics studies to evaluate locomotors' performance on flowable ground of various penetration resistance [180]. In doing so, the lifting forces at the limbs no longer fully supported the body weight and therefore some finite resistance lifting force acted on the ventral surface. When the fully limbed lizards (*U. scoparia* and *S. olivaceus*) ran across the region with reduced ground penetration force, they exhibited features of a traveling wave, indicated by the propagation of nodes (Figure 4.6). We compared the wave flatness (σ) and wavelength λ of the body undulations (Figure 4.3b) for lizards on the aerated granular medium, the loosely packed granular medium, and sandpaper. We found no difference in σ between sandpaper and the loosely packed medium, but noted a significantly higher σ on the aerated medium than the loosely packed medium for both species (*U. scoparia*: $t = 2.94$, $df = 11$, $p = 0.013$; *S. olivaceus*: $t = 2.43$, $df = 9$, $p = 0.038$), indicating a higher degree of traveling wave.

4.1.5 Robophysical experiments

In the previous sections, we showed that although thrust generation in lizards results from a complex coordination of limb and body movements, we could modulate the degree to which traveling wave undulations were used by modulating the ground penetration resistance. We further explored the relative advantages of traveling waves and standing waves using a robophysical model where we could precisely control the thrust generation mechanism. Our robophysical model has four actuated limbs and two actuated body bending joints. The body shape of the robot can be uniquely described by the body joint angles: upper back α_1 and lower back α_2 (Figure 4.7a, left panel). Two actuated body joints in our robot are the minimum degrees of freedom needed to enable a traveling wave [114]. We

⁵Ground penetration resistance is defined as the vertical ground resistance force per depth during intrusion

⁶Fluidization of granular media characterized by ground penetration resistance dropping to zero

designed removable belly intrusion plates to control the belly thrust generation mechanics. We compare the robot with belly thrust (top panel) and the robot without belly thrust (bottom panel) in Figure 4.8a. The shoulder joints control the contact patterns of each limb. For simplicity, we only considered two combinations of contact patterns: diagonal contact and the counter-diagonal contact.

As with the geometric mechanics models presented earlier, the gait of the robot could also be represented by a closed path in its shape space (Figure 4.7a). For simplicity, we considered the upper back and lower back as oscillating sinusoidal waves: $\alpha_1(t) = A_\alpha \sin(t)$, $\alpha_2(t) = A_\alpha \sin(t + \psi)$, where A_α is the amplitude, ψ is the phase lag between the upper back and the lower back. A typical traveling wave can be described such that the upper back and lower back are $\pi/2$ out of phase [75]: $\psi = \pi/2$, which leads to a circular path in the shape space (blue curve in Figure 4.7a). A typical standing wave can be described such that the upper back and lower back are in phase: $\psi = 0$, which leads to a flattened ellipse (with eccentricity = 1) in the shape space (green curve in Fig. Figure 4.7a).

We used contact pattern design algorithms to determine the coordination between the contact pattern and the body movements [155]. The optimal coordination is shown in Figure 4.7a’s right panel, in agreement with our data on body-limb coordination in the biological experiments. We then tested the effect of ψ on the robot⁷. Snapshots of the robot implementing standing and traveling waves are shown in Figure 4.8a. All experiments were conducted with at least 5 trials. The experimental results are shown in Figure 4.8b. We found that traveling waves only increase speed (measured by distance moved per cycle) in the robot with belly thrust (Pearson’s $\rho = 0.883$, $p = 0.001$), whereas there are no significant differences between standing and traveling waves when robot lacks belly thrust (Pearson’s $\rho = -0.147$, $p = 0.438$).

Geometric mechanics derived height functions helped explain our observations (Fig-

⁷Note that some regions of shape space contain shapes where parts of the robot collide with other parts (e.g., upper right corner and lower right corner). The amplitude A_α was chosen such that the gait path does not pass through the self-collision region

ure 4.7b, right panel). As in the above analysis of lizard terrestrial swimming, the displacement can be approximated by the surface integral over the gait path in the shape space. Further, the magnitude of the height function for locomotors without belly thrust (top panel in Figure 4.7b) is much higher than that with belly thrust (bottom panel in Figure 4.7b), indicating that a robot without belly thrust should have higher speed than one with belly thrust. The trends in the theoretical predictions and experimental data agreed, but we posit that the discrepancy in magnitude (Figure 4.8b) was due to the accumulation of granular media in front of the robot as it moves, impeding progress [104] as the robot implemented its gait.

From the structure of the height function, we observed that most of the negative volumes (indicated by black color) are distributed along the narrow diagonal line, which can be sufficiently bounded by a flattened ellipse. It therefore predicts that the standing wave body bending can be as good as those of traveling wave body undulations. On the other hand, the traveling wave body undulation can better coordinate the robot with belly thrust because the negative volumes are distributed widely around the diagonal line. In the latter case, a higher surface integral can be achieved for ellipses with increasing ψ (and thus increasing σ). We interpreted our observations on traveling and standing waves by analyzing the connection vector field in Figure 4.7b (left panel) [181]. The connection vector field in locomotors with no belly thrust is almost curl-free (S3), which indicates that the contribution of body bending postures is almost path independent. In other words, the trajectories of body posture changes (e.g., traveling waves or standing waves) will not matter. On the other hand, the connection vector field in locomotors with belly thrust has non-negligible curls (S3), which indicates that the trajectory of body bending will affect the locomotor performance.

4.2 Discussion and Conclusion

Lizards have evolved a diversity of body forms from fully limbed and short-bodied to limbless and elongate. We showed that this diversity in morphology coincides with a similar diversity in locomotion patterns, ranging from standing wave to traveling wave body undulation. We observed that the degree of body elongation and limb reduction were closely related to how the body and limb movements were coordinated, indicating an interconnected morphological and locomotor continuum. Using biological experiments, a geometric theory of locomotion, and robophysical experiments, we showed that the body weight distribution between the limbs and the body (and therefore, the primary thrust generation mechanism) plays a crucial role in the locomotor transition from fully limbed to limbless. Specifically, we found that fully limbed lizards adopted a traveling wave to undergo terrestrial swimming when the penetration resistance of the substrate was reduced and the belly contracted the medium. Further, our robophysical experiments revealed that a traveling wave enhanced locomotor performance only when some thrust was generated by the body.

One of the contributions presented in this chapter was to use geometric mechanics as a tool to analyze seemingly complicated lizard locomotion. Specifically, we formulated different body wave dynamics as different paths in the shape space. The diagrammatic analysis by geometric mechanics then allowed us to visually and intuitively compare different wave dynamics. In this sense, our analysis simplified the laborious calculations, which would otherwise be required to study the diversity in lizard body wave dynamics. In addition, the geometric mechanics served as a bridge connecting the biological experiments and robophysical experiments, allowing us to systematically test gaits and conditions that are less commonly seen in biological systems.

Limb reduction and body elongation result in a shift in body weight distribution from the limbs to the body [182]. We showed a traveling wave of body undulation enhanced locomotor performance during this transition. However, traveling wave body undulation

requires larger local body curvatures, more complex neuromechanical control (to propagate the node in undulation) [35], and more degrees-of-freedom (at least two DoF) than standing wave undulation (one DoF). That a fully limbed lizard adopted terrestrial swimming when crossing a medium with low penetration resistance suggests that the degrees-of-freedom and neuromechanical control necessary for traveling waves may be widespread among lizards. Our work is the first to show that the coordination between body undulation and the limbs is a key feature of locomotion within the morphological transition between fully limbed, short bodied and limbless, elongate forms.

We used *Brachymeles* as morphologically intermediate species because they have similar levels of development of their fore and hind limbs [175, 105]. However, the limbed species of this genus are secondarily limbed, having re-evolved their limbs from a limbless ancestor [68]. Therefore, our results should not be interpreted as representing an evolutionary transition in locomotion. Despite this, the geometric mechanics and robophysical approaches we used are naïve to evolutionary history, and our observations on *Brachymeles* and the other, unrelated species that we used, coincide closely with these approaches, suggesting that biomechanics may dictate locomotor patterns in many of these convergent evolutions of snake-like forms. The role of how the evolutionary history affects locomotion of these forms could be further tested in a clade like *Lerista*, which has evolved snake-like forms from limbed, short bodied ancestors [183, 106]. We also expect that our work on body and limb dynamics in these lizards will inform control of robots that need to traverse complex terrain.

CHAPTER 5

A GENERAL LOCOMOTION CONTROL FRAMEWORK FOR MULTI-LEGGED LOCOMOTORS

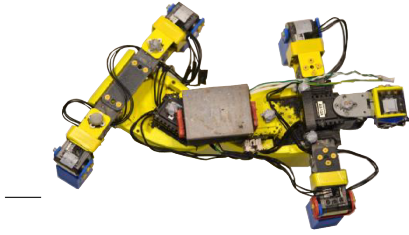
Part of this chapter is adapted from a journal article “A general locomotion control framework for multi-legged locomotors.” *Bioinspiration & Biomimetics* 17.4 (2022): 046015. My contribution in this project includes (1) designing the experiments, (2) conducting the numerical analysis, (3) writing the manuscript. Robophysical experiments presented in this chapter are conducted by Yasemin Ozkan-Aydin.

For multi-segment locomotors, their performance characteristics can depend on the number of limbs. Quadrupeds are known for their agility [30], whereas hexapods and myriapods for their stability [184, 4], and limbless robots for their ability to fit into confined spaces [185]. But multi-segment locomotors with increasing complexity and numbers of degrees-of-freedom (DoF) present challenges in motion coordination, which if not addressed, may render them unusable. Furthermore, the diversity of shape and form makes it challenging to transfer control insights gained from one platform onto another. We are left with limited intuition and physical understanding of how to coordinate the many DoF in diverse and complex robots to generate effective locomotion.

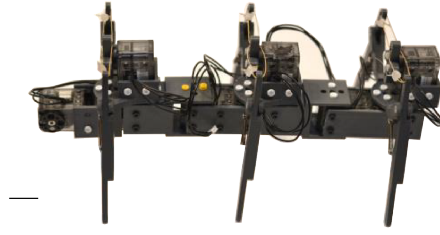
To address the growing need to analyze multi-segment locomotors with different shapes, modular control¹ strikes a balance between encompassing a variety of shapes while still being able to precisely control them [187, 188]. Modular control has been successfully used in serially connected limbless robots where a single control principle can be applied in robots with different sizes [189]. In contrast, the study of modular control in general multi-segment locomotors has been limited. The challenge in serially multi-segment locomotors

¹A robot control framework where the policy structure is conditioned on the hardware arrangement, and use just one training process to create a policy that controls a wide variety of designs [186].

a. Quadruped



b. Hexapod



c. Myriapod



d. Sidewinder



Figure 5.1: **Legged and limbless robotic models studied in the paper.** a. Quadrupedal robot [176] b. Hexapod robot c. Myriapod robot with eight pairs of legs d. Sidewinder robot [134]. All scale bars are 5 cm.

lies not only in designing the stepping patterns of legs, but also in the coordination between the body and legs. For example, in multi-segment locomotors that combine limbs and body undulation, if stepping patterns and body undulations are not properly coordinated, limbs can interfere with each other, resulting in reduced locomotor performance, instability, or even failure [190, 191].

We would like to develop control schemes to generate effective periodic “self-deformation patterns”² for the general class of serially connected legged and limbless robots. Over the past decades, many techniques (e.g., gait generation [192, 193], central pattern generators [35, 194], nearest limb synchronization [195], and learning methods [30, 12]) have been developed, each of which can control some specific robot type [4, 196, 75, 45, 35]. In this chapter, we take inspiration from gaits of living systems: organisms with diverse numbers of appendages and body plans exhibit effective locomotion on almost all terrestrial environments [87, 197, 45] by making/breaking the ground contact with limbs (e.g., salamanders)

²We consider self-deformation patterns to be the relative movement of body and limb elements.

and bodies (e.g., sidewinders) in conjunction with waves of undulation.

One method used over the last century to understand legged locomotion is a gait classification scheme called “Hildebrand diagrams”. In 1965, Hildebrand [17] developed schemes to study symmetric gaits³ observed in quadrupedal animals (e.g., horses). These gaits have two key variables: *duty factor*, the fraction of a period that each leg is on the ground over a full gait cycle, and *lateral phase lag*, the fraction of a period that the hind leg leads the foreleg on the same side. Both key variables are modulated in response to speed changes in biological systems [89, 90, 91]. Using these gait principles as a reference, a multitude of algorithms have been developed for quadrupedal robot locomotion, or to explain why living quadrupeds choose certain gaits [92, 25, 39, 93, 94, 95]. But thus far, these gait principles have not been applied to robots with more than four appendages. For multi-legged robots, there is a lack of a systematic gait description framework that allows us to modulate the balance between locomotion metrics such as speed and stability.

In animals and increasingly in robots, appendages that make direct contact with substrates are not the sole contributor to locomotion. Undulatory body motions play an important role in generating propulsive forces in many systems [88, 87, 84, 43]. For undulatory locomotors, the geometric mechanics community [178, 79, 198, 108, 199, 16, 176, 142] has developed a gait design framework to prescribe self-deformations of systems immersed on continuous media, such as 3-link robots, lizards, and snakes [83, 199, 75]; and in discontinuous settings, including sidewinders [126, 150]. While mathematically elegant, geometric mechanics has limitations. In particular, it is not directly applicable to systems with a large number of appendages. Furthermore, despite some recent efforts [83, 107], application of geometric mechanics in frictional environments (e.g., rate-independent Coulomb dry friction) has not been systematically studied. Therefore, we must develop dimensionality reduction and physical modelling methods before we can use geometric mechanics to design gaits for serially connected multi-legged robots.

³In symmetric gaits, the contralateral (left and right pair) of legs are 180° out of phase.

In this chapter, we integrate dimensionality reduction techniques with tools from geometric mechanics to develop locomotion control schemes for serially connected robots. We first extend the Hildebrand gait classification scheme to prescribe a wide range of contact patterns (the sequence of making/breaking contacts with environments) using the classical Hildebrand parameters (duty factor and lateral phase lag). We use the extended Hildebrand scheme to reduce dimensionality and prescribe body undulation as a traveling wave. In doing so, we can apply geometric mechanics to coordinate the lateral body undulation and limb contact patterns. We evaluate gait performance based on speed and static stability, and investigate the relationship between these metrics and the Hildebrand parameters. We demonstrate our motion control framework on robots with four (quadrupedal), six (hexapod), 16 (myriapod-like), and even zero (snake-like) limbs (Figure 5.1). Our analysis reveals empirical rules to balance the trade-off between speed and static stability, and the potential benefit of body undulation in multi-legged robot locomotion.

Moreover, by properly coordinating lateral body undulation and leg movement, our framework provides additional insights to both legged and limbless robots. Specifically, our framework facilitates centralized control of serially connected multi-legged robots by introducing waves in both limb contact and lateral body undulation. With properly coordinated lifting and landing body segments, our framework can also improve the mobility of limbless robots by giving insights into coordination and trade-offs of stability and speed in serially connected multi-legged robots. In this way, our framework offers the potential to modulate gaits for different tasks by switching between fast gaits and stable gaits. Further, we show that our scheme can generate control hypotheses for diverse living systems including salamanders and centipedes, thereby offering new insights on the functional role of body-leg coordination from a biomechanical and robophysical perspective.

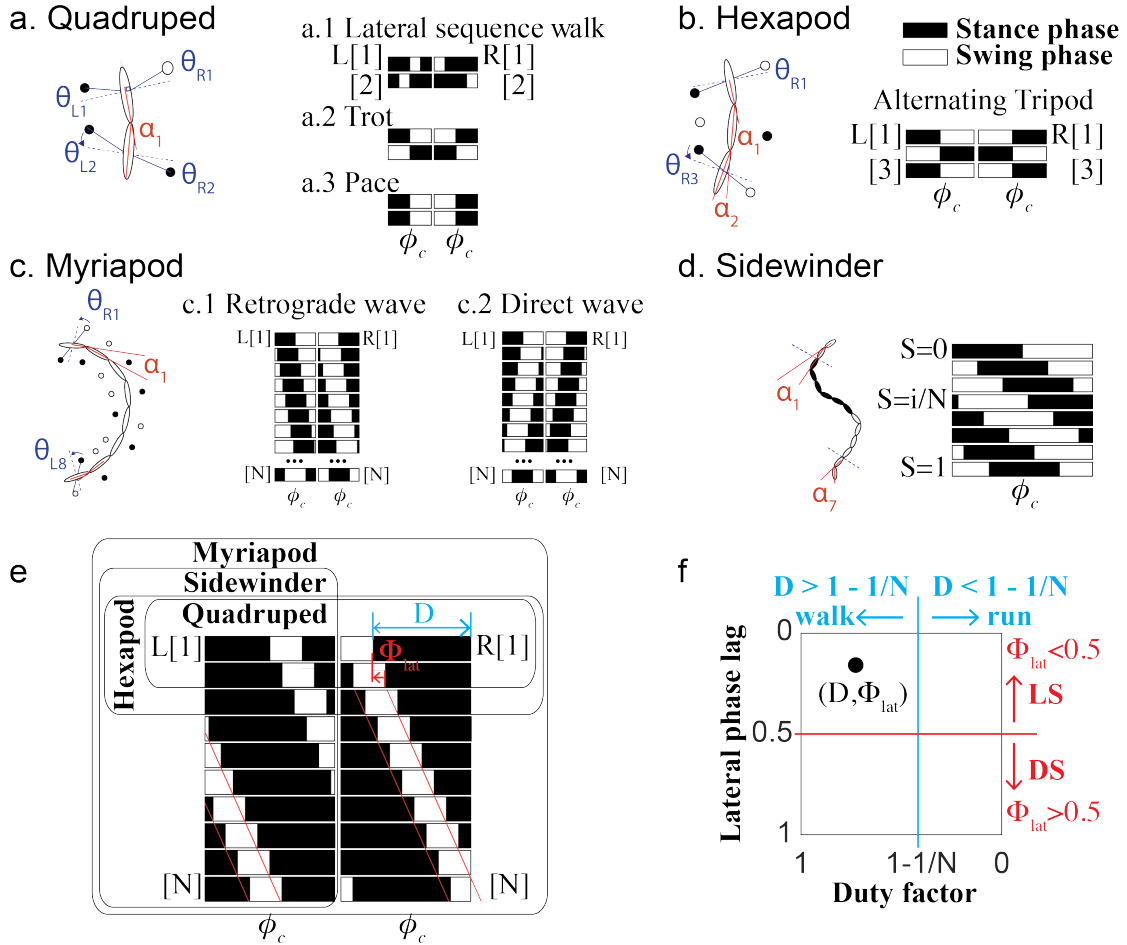


Figure 5.2: **Modelling multi-legged systems and sidewinders.** The contact patterns of some well-known gaits: (a.1) lateral sequence walking, (a.2) trotting, and (a.3) pacing in quadrupeds; (b) alternating tripod in hexapods, (c.1) retrograde-wave and (cc.2) direct-wave gaits in myriapods, and (d) sidewinding in snake-like limbless robots,. For each system, these diagrams show the variables included in the model, such as leg joint angles θ_N , and body joint angles $\alpha_{(N-1)}$, where N is the number of leg pairs for legged systems or joint sets in the sidewinder. In the contact sequence diagrams, filled blocks represent stance phase, and open blocks represent swing phase. (e) A general contact pattern table. The blue arrow represents the duty factor D . The red arrow represents the lateral phase lag, Φ_{lat} . τ denote gait phase. (f) Hildebrand plots with two parameters D and Φ_{lat} to characterize the motions in the vertical plane. We labeled the region associated with walking, running, lateral sequence (LS) and diagonal sequence (DS) gaits.

5.1 Hildebrand Gait Prescription

5.1.1 Related work

In the Hildebrand gait formulation [17], symmetric quadrupedal gaits are categorized by two parameters: The duty factor represents the fraction over a gait period that each leg is on the ground, and the lateral phase lag represents the fraction over a gait period that the hind leg leads the foreleg on the same side. There are three major assumptions in the Hildebrand symmetric gait family: (1) the duty factor of each leg is the same, (2) the pairs of contralateral legs are 180° out of phase, and (3) the lateral phase lag is the same for left and right legs.

We use a binary variable c to represent the contact state of a leg, where $c = 1$ represents the stance phase and $c = 0$ represents the swing phase. The contact pattern of symmetric quadrupedal gaits can be written as

$$\begin{aligned}
 c_{FL}(\phi_c) &= \begin{cases} 1, & \text{if } \text{mod}(\phi_c, 2\pi) < 2\pi D \\ 0, & \text{otherwise} \end{cases} \\
 c_{FR}(\phi_c) &= c_{FL}(\phi_c + \pi) \\
 c_{HL}(\phi_c) &= c_{FL}(\phi_c + 2\pi\Phi_{lat}) \\
 c_{HR}(\phi_c) &= c_{FL}(\phi_c + 2\pi\Phi_{lat} + \pi)
 \end{aligned} \tag{5.1}$$

where Φ_{lat} denotes the lateral phase lag, D the duty factor, $c_{FL}(\phi_c)$, $c_{FR}(\phi_c)$, $c_{HL}(\phi_c)$, and $c_{HR}(\phi_c)$ the contact state of the fore-right (FR), fore-left (FL), hind-left (HL), and hind-right (HR) limbs at the gait phase ϕ_c (defined in radians with a period of 2π), respectively. Note that in contrast to ϕ_c , the lateral phase lag Φ_{lat} represents the fraction of a cycle, so Φ_{lat} has a period of 1. Many common quadrupedal gaits can be described using the Hildebrand formula. For example, the lateral sequence walking gait (Figure 5.2) can be described by $D = 0.75$, $\Phi_{lat} = 0.25$. Plotting a diagram of the stance/swing phases of the feet from

just these two parameters shows that in this gait, each leg is lifted for a quarter of a cycle, only one leg is lifted at any given instant, and the leg lifting sequence follows FR, HR, FL, and HR. The trot gait (Figure 5.2) can be described by $D = 0.5$, $\Phi_{lat} = 0.5$, where the FR and HL are coupled in phase, as are the FL and HR pair. Another quadrupedal gait, the pace gait (Figure 5.2), can be described by $D = 0.5$, $\Phi_{lat} = 0$, where the FR and HR are coupled in phase, as are the FL and HL pair. Note that asymmetric quadrupedal gaits, such as bounding and galloping, exist but cannot be prescribed by the same gait classification methods [97].

5.1.2 Prescription of Contact Patterns for Arbitrary Robots

The first two assumptions of the Hildebrand symmetric gait family generally can hold for non-quadrupedal systems with discrete contacts. To expand the third assumption to a broader range of locomotors, we can generalize the definition of the lateral phase lag to be the phase lag between two consecutive legs (instead of only the fore and hind legs) on the same side. Then, the contact function of a multi-legged system can be written as:

$$\begin{aligned}
 c_l(\phi_c, 1) &= \begin{cases} 1, & \text{if } \text{mod}(\phi_c, 2\pi) < 2\pi D \\ 0, & \text{otherwise} \end{cases} \\
 c_l(\phi_c, i) &= c_l(\phi_c + 2\pi(i-1)\Phi_{lat}, 1) \\
 c_r(\phi_c, i) &= c_l(\phi_c + \pi, i),
 \end{aligned} \tag{5.2}$$

where $c_l(\phi_c, i)$ (and $c_r(\phi_c, i)$) denotes the contact state of i -th leg on the left (and the right) at gait phase ϕ_c , $i \in \{1, \dots, N\}$ for $2N$ -legged systems.

Many common multi-legged gaits can also be described by this extended Hildebrand formulation. For example, many hexapod robots and animals use the alternating tripod gait (Figure 5.2), which couples FL, MR (middle-right), and HL in phase, and couples the FR, ML, and HR similarly. The alternating tripod gait for a hexapod ($N = 3$) can be described

by $D = 0.5$ and $\Phi_{lat} = 0.5$.

Myriapod gaits can be classified into direct waves and retrograde waves of limb contact [200] (Figure 5.2). Typically, for gaits with $\Phi_{lat} < 0.5$, the phase of the hind leg is ahead of the phase of its immediate fore leg. In other words, the legs move in a wave propagating from tail to head, which we call a diagonal sequence gait, and which corresponds to direct waves in myriapods. On the other hand, when $\Phi_{lat} > 0.5$, the phase of the hind leg is behind the phase of its immediate fore leg. Therefore, the leg wave propagates from head to tail, which we call a lateral sequence gait, and which corresponds to retrograde waves in myriapods. Interestingly, on level ground, animals with four legs (e.g., lizards and salamanders) more commonly use lateral sequence gaits [17, 96, 89, 201], and animals with more legs (e.g., centipedes) use both diagonal sequence and lateral sequence gaits [43, 202]. As we will discuss later, we hypothesize that this difference in gait choice is a result of a balance between speed and stability.

Our proposed gait formulation can also include systems without legs, e.g., sidewinding limbless robots. The seemingly complex mode of limbless locomotion, sidewinding, can be prescribed as the superposition of two waves: lateral and vertical body waves [16]. Similar to legged systems, sidewinders can regulate their contacts by modulating the vertical traveling wave [16]. The typical contact pattern of a sidewinder is shown in Figure 5.2. Note that the contact pattern during sidewinding locomotion is the same as one side (either left or right) of the contact pattern of a legged system. As such, we prescribe the contact state of the i -th link of the sidewinding system as $c(\phi_c, i) = c_l(\phi_c, i)$, where $c_l(\phi_c, i)$ is defined in Equation 5.2

5.1.3 Prescription of Leg Shoulder Movement

Legs generate self-propulsion by protracting during the stance phase to make contact with the environment, and retracting during the swing phase to break contact. That is, the leg moves from the anterior to the posterior end during the stance phase and moves from the

posterior to anterior end during the swing phase. With this in mind, we use a piece-wise sinusoidal function to prescribe the anterior/posterior excursion angles (θ , Figure 5.2) for a given contact phase (ϕ_c) defined earlier,

$$\theta_l(\phi_c, 1) = \begin{cases} A_\theta \cos\left(\frac{\phi_c}{2D}\right), & \text{if } \text{mod}(\phi_c, 2\pi) < 2\pi D \\ -A_\theta \cos\left(\frac{\phi_c - 2\pi D}{2(1-D)}\right), & \text{otherwise,} \end{cases}$$

$$\theta_l(\phi_c, i) = \theta_l(\phi_c + 2\pi(i-1)\Phi_{lat}, 1)$$

$$\theta_r(\phi_c, i) = \theta_l(\phi_c + \pi, i) \tag{5.3}$$

where A_θ is the shoulder angle amplitude, $\theta_l(\phi_c, i)$ and $\theta_r(\phi_c, i)$ denote the leg shoulder angle of i -th left and right leg at contact phase ϕ_c , respectively. Note that the shoulder angle is maximum ($\theta = A_\theta$) at the transition from swing to stance phase, and is minimum ($\theta = -A_\theta$) at the transition from stance to swing phase. Figure 5.3 shows an example of a hexapod gait under this equation.

5.1.4 Numerical Prediction on Speed and Stability

We numerically calculated the speed of various gaits over a range of duty factors and lateral phase lags for quadrupedal, hexapod, myriapod, and sidewinder systems ([199] and Materials and Methods). Figure 5.3 and Figure 5.4 graphically depict the process, and the Materials and Methods section provides details. To explicitly show the effect of limb-substrate contact on speed, we fixed the swing angle A_θ when comparing the displacements of different gait parameters. Note that in this section, there is no body undulation in any of the gaits.

The numerical predictions of body speed, measured in units of body length per cycle (BLC), are plotted in Figure 5.5 (middle column). We observe that modulating the lateral phase lag does not significantly affect body speed. This observation becomes more apparent

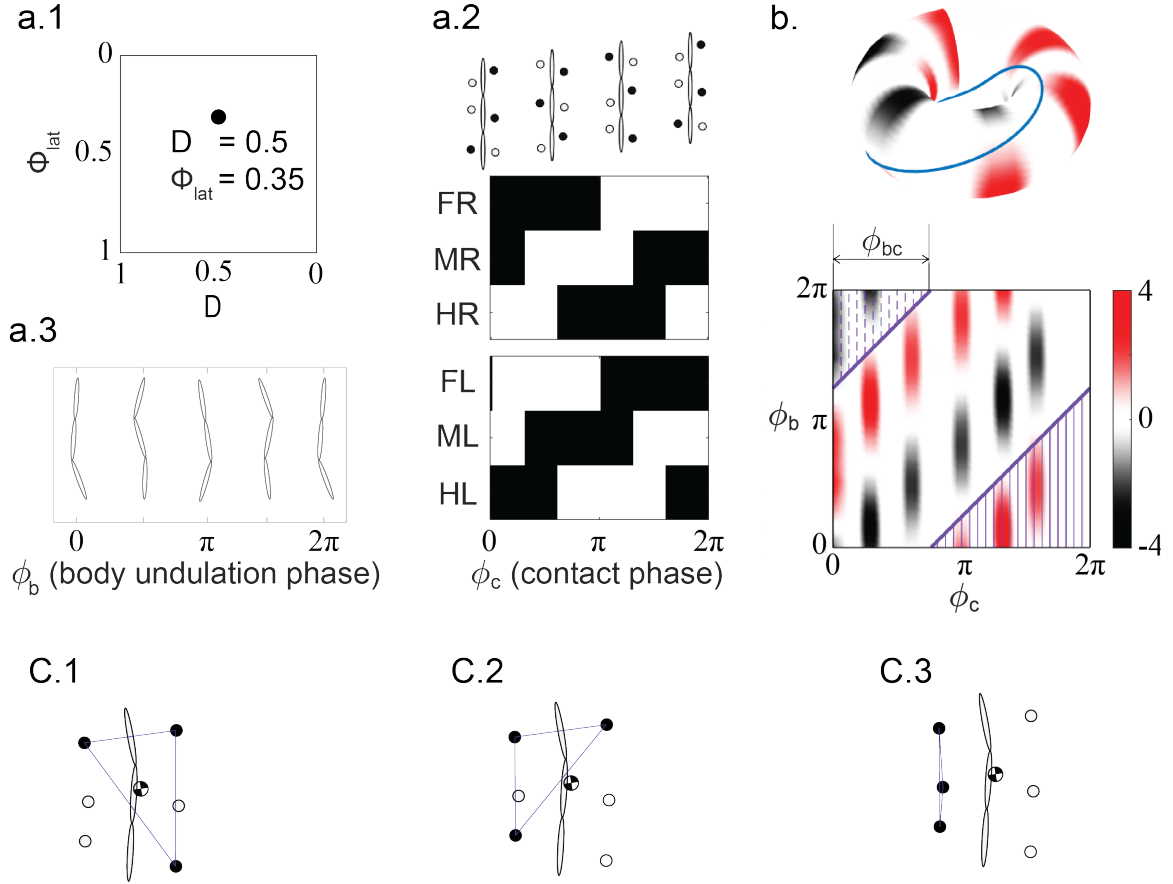


Figure 5.3: An example of gait design for a hexapod using Hildebrand gait principles and geometric mechanics. From the parameter space (a.1), we select the duty factor D and lateral phase lag Φ_{lat} . We prescribe the contact by its phase ϕ_c (a.2), and the lateral body undulation by its phase ϕ_b (a.3). (b) The gait parameters determine the equations of motion, which in turn are used to derive a height function, and design a gait. The gait path (the purple curve) shown maximizes the volume enclosed in the lower right corner (in solid shadow) minus the volume enclosed in the upper left corner (in dashed shadow). The left panel is the toroidal visualization of the height function, the right panel is the Euclidean visualization of the height function. (c) Typical configurations in which the robot is statically stable (c.1), statically unstable (c.2) and unstable (c.3)

for systems with more legs. In the myriapod system, the step displacement⁴, characterized by displacement traveled per cycle, is almost independent of the lateral phase lag and is uniquely determined by the duty factor.

In addition to measuring body speed, we utilize other metrics to quantify gait stability. For instance, the contact pattern of quasi-static gaits (e.g., quadrupedal walking gaits) needs

⁴The absolute speed v is related to the step displacement d by $v = fd$, where f is the step frequency.

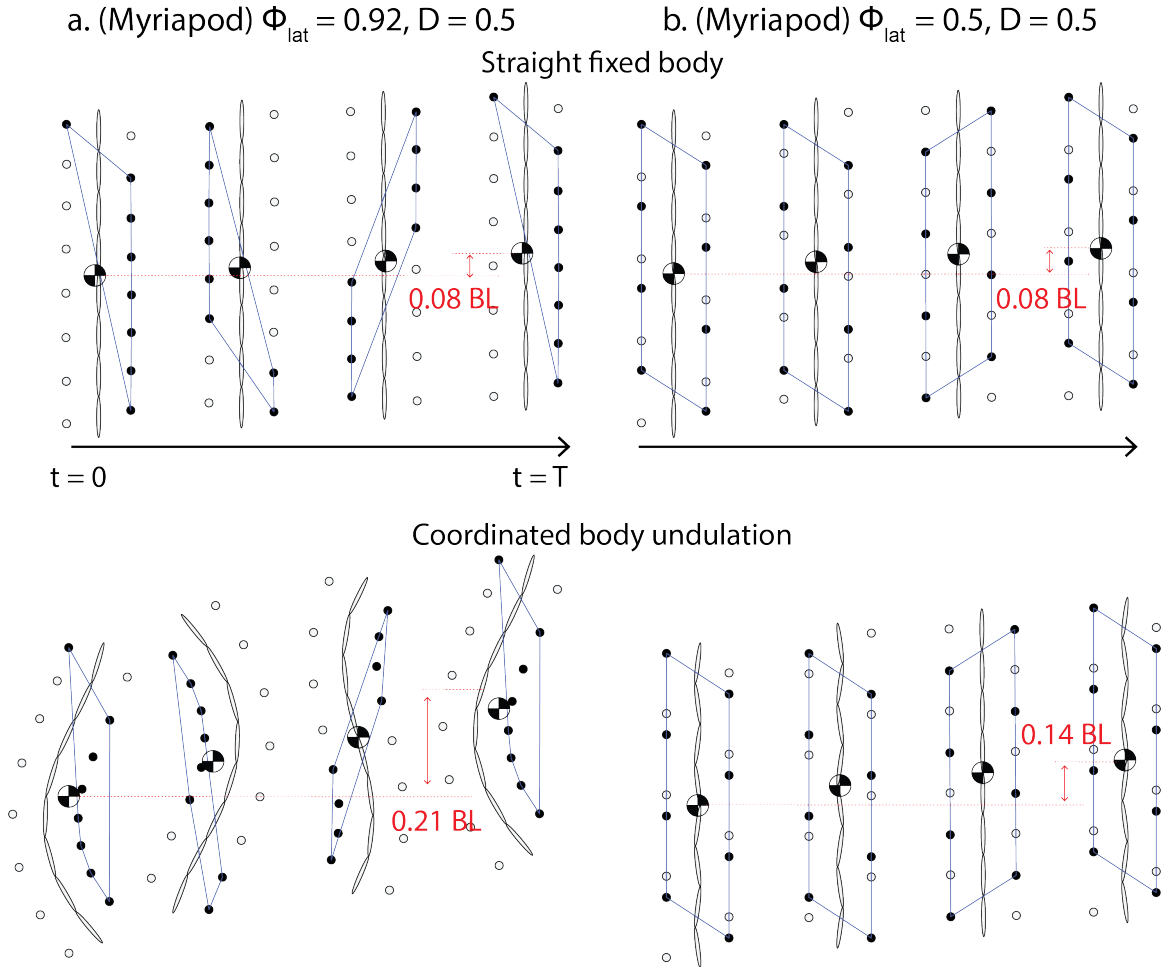


Figure 5.4: **Snapshots of the numerical simulation showing examples of two prescribed myriapod gaits.** (a) statically unstable, $\Phi_{lat} = 0.92$, $D = 0.5$ and (b) statically stable $\Phi_{lat} = 0.5$, $D = 0.5$. We compared the gait with straight fixed body (top) and gaits with coordinated body undulation (bottom). The displacement, in body length (BL) per cycle, are labeled with a red arrow. The black/white circles show the stance/swing phase of the feet.

significantly fewer sensors and less feedback control efforts to be stably implemented on robots than the contact pattern of dynamically stable gaits (e.g., bouncing gaits) [92]. In this paper, we separate robots' configurations into three groups (1) statically stable, (2) statically unstable, and (3) unstable. In the statically stable configurations, the center of mass is bounded within the supporting polygon (Figure 5.3c.1). In the statically unstable configurations, often produced by unstable diagonal-couplet gaits [96], the center of mass is outside the supporting polygon but there is at least one leg in stance phase on the left

and the right side (Figure 5.3c.2). Despite not being statically stable, the statically unstable configurations can be made dynamically stable when the speed increases [89] or when combined with a low-level controller [93, 196, 94]. In the unstable configurations, also known as unstable lateral-couplet gaits [96], either the left or the right side of the legs are all in swing phase (Figure 5.3c.3), which makes such gaits more difficult to stabilize⁵. We define a static stability metric as the fraction of the gait cycle spent in statically stable configurations. Note that this measure only applies to the gaits with statically stable and statically unstable configurations; the appearance of unstable configurations will contradict our assumptions. Therefore, we define the measure of static stability to be 0 if there exists unstable configurations in the gait.

We numerically calculated the static stability for the quadrupedal, hexapod, and myriapod systems in Figure 5.5. As expected, when comparing the same gait parameters (duty factor D and phase lag Φ_{lat}) among different systems, the static stability increases with increasing number of legs. Similarly, an increase in duty factor results in an increase in static stability. Moreover, we observe that the diagonal sequence ($\Phi_{lat} > 0.5$) is in general less stable than the lateral sequence ($\Phi_{lat} < 0.5$). Thus, most diagonal sequence gaits are stable only for systems with many legs, such as myriapods.

Surprisingly, modulating the lateral phase lag only affects the static stability, while body speed is not correlated with the lateral phase lag. On the other hand, animals including myriapods [43] and quadrupedal lizards [87, 203, 204] have been observed to modulate the lateral phase lag as speed increases. In other words, in biological systems, the loss of static stability is compensated by a gain in speed while our findings indicate that speed is independent of lateral phase lag modulation. We hypothesize that this discrepancy is due to differences in body-limb coordination, which we consider in later sections.

⁵in the case of limbless sidewinding, unstable configurations are defined as those with no contact, see S4

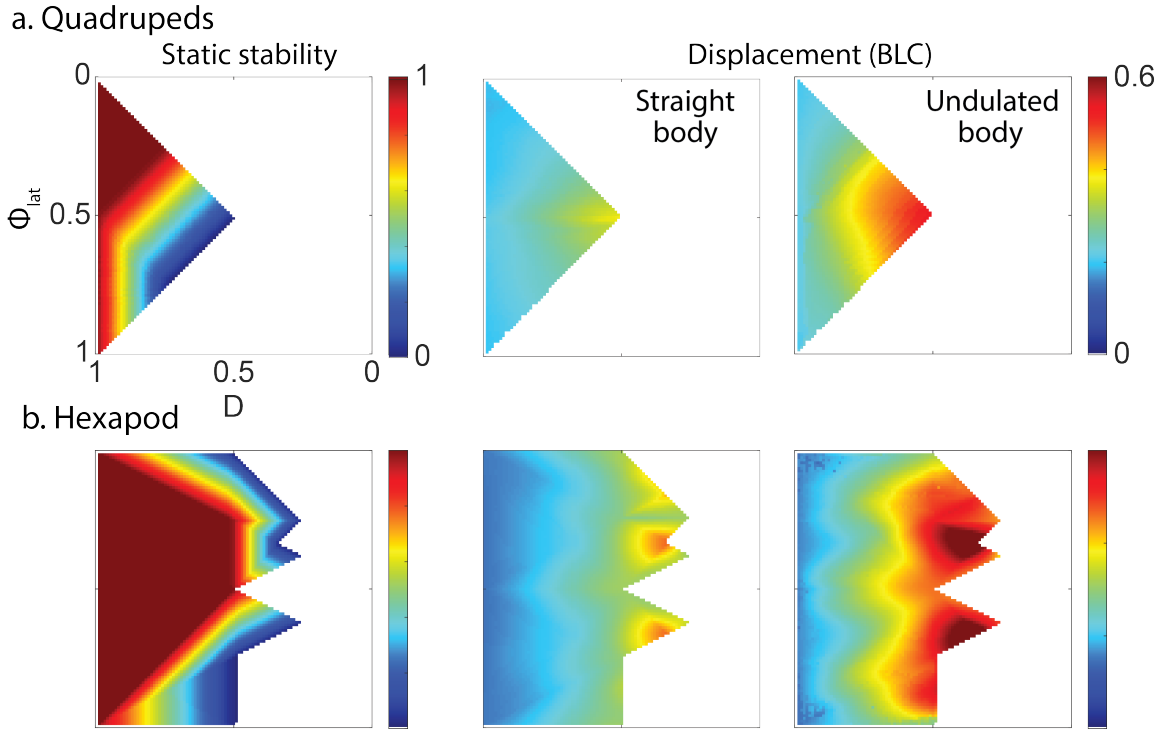
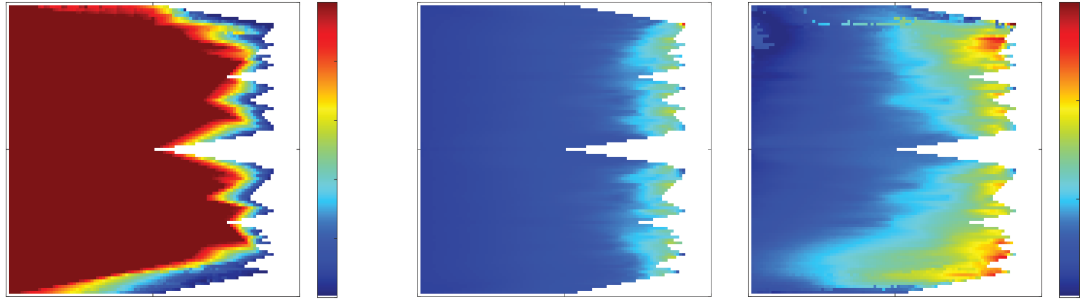


Figure 5.5: **Trade-off between speed and static stability in quadruped, hexapod, myriapod, and sidewinding systems.** Theoretically predicted static stability (left column), displacement in body lengths per cycle (BLC) with fixed straight back (middle column), and displacement with coordinated lateral body undulation (right column) over the space of Hildebrand parameters D and Φ_{lat} , for the quadruped (a), hexapod (b), myriapod (c) and sidewinder (d). White space in all panels represents the regions where unstable configurations exist (Figure 5.3c.3); we defined static stability to be zero in those regions. Note that static stability of the quadruped, hexapod and myriapod is numerically calculated for configurations with a straight backbone. The static stability of the sidewinder is numerically calculated for gaits with coordinated lateral body undulation. Note that we only consider gaits where unstable configurations (Figure 5.3c.3) do not occur. Axes in each sub-figure are identical. The color-maps in each column are identical.

5.1.5 Testing speed and stability predictions in experiments

Using robophysical models, we tested the locomotor performance of gaits with a range of lateral phase lags for quadruped, hexapod, myriapod, and sidewinder systems (Figure 5.6). Hexapod, myriapod, and sidewinder experiments were performed on hard ground. Since the quadrupedal systems in general are less statically stable, we posited that we would predominantly observe the effect of stability rather than the kinematics of gaits. Thus, for quadrupeds we tested performance on a granular medium (here, poppy seeds) since

c. Myriapod



d. Sidewinder

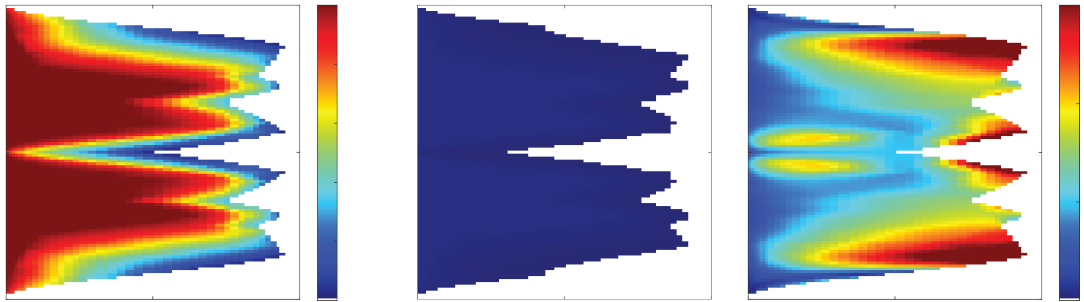


Figure 5.5: **Trade-off between speed and static stability in quadruped, hexapod, myriapod, and sidewinding systems.** Theoretically predicted static stability (left column), displacement in body lengths per cycle (BLC) with fixed straight back (middle column), and displacement with coordinated lateral body undulation (right column) over the space of Hildebrand parameters D and Φ_{lat} , for the myriapod (c) and sidewinder (d).

the body is in contact with the substrate, ensuring static stability. The duty factor for the hexapod, myriapod and the sidewinder systems were fixed to $D = 0.5$, and the duty factor for the quadrupedal system was set to $D = 0.75$ for reference (see the Materials and Methods for additional experiment details). Note that in this section, there is no body undulation in any of the gaits.

We measured gait speed via the number of body lengths traveled per gait cycle. Interestingly, we observe for statically stable gaits, there is good agreement between the theory and experiments. Since our predictions are based on 2D calculations, they cannot capture 3D unstable behaviors, such as tipping over and falling to the ground. Therefore, we hypothesize that the discrepancy between our hexapod theory and experiments is caused by static instability. Note that our experiments on quadrupeds were performed on poppy seeds, where the ventral surface often was in contact with the environment. In our myriapod ex-

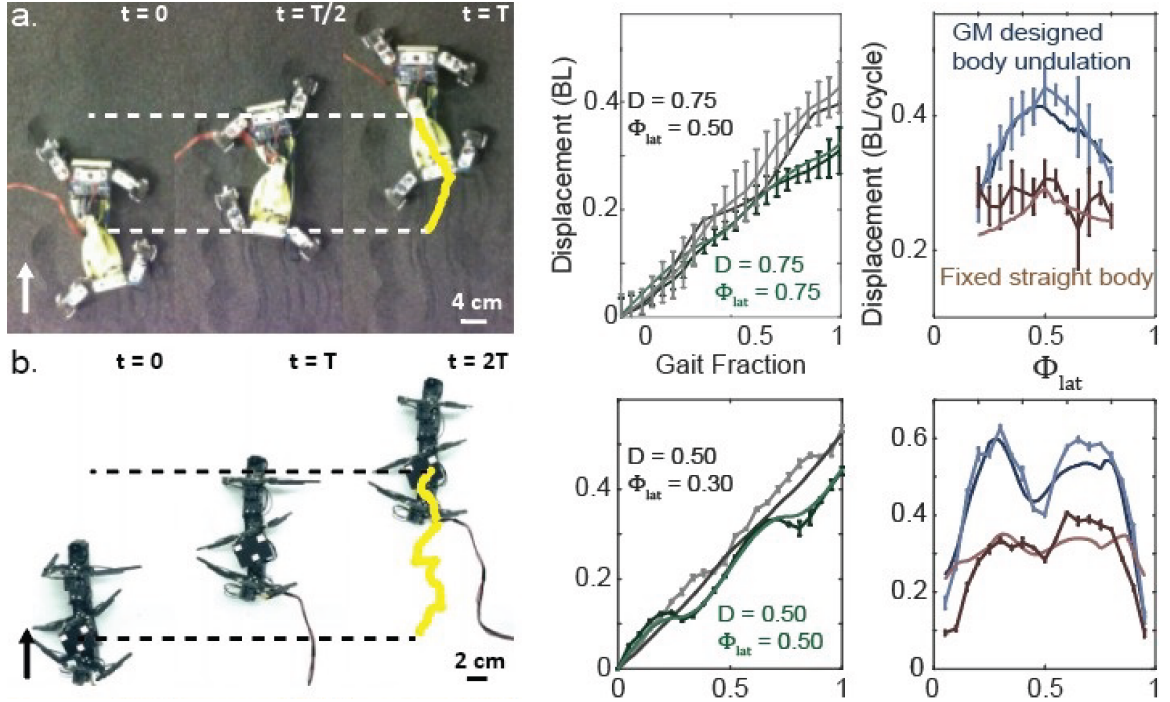


Figure 5.6: **Verification of the theoretically generated gaits in the robotic models** (left column) Gait cycle of each robot (a: quadruped, $D = 0.75$ and $\Phi_{lat} = 0.5$; b: hexapod, $D = 0.5$ and $\Phi_{lat} = 0.3$). The arrows show the direction of locomotion and T is one gait cycle. The center of mass trajectories (yellow) are given in the last snapshots. (Middle column) The comparison of simulations (solid curves) and experimental data (curves with error bar) of displacement over time for each system. Two gaits with body undulation coordinated with geometric mechanics (GM) are illustrated for each system. (Right column) The relationship between the lateral phase lag, Φ_{lat} , and the displacement for the same system either with fixed straight backbone (red) or with coordinated lateral body undulation (blue). The color scheme and axes in (b, c, d) are the same as in (a).

periments, configurations tend to be mostly statically stable given their large number of legs. Therefore, the effect of static stability was only critical in our hexapod experiments.

To test our hypothesis that static stability is the source of the theory-experiment discrepancy, we characterized unstable behaviors by the roll and pitch of the robots. We recorded the body pitch and roll during the course of the robophysical hexapod gaits. The experimental data for these experiments over three gait settings ($D = 0.5$ $\Phi_{lat} = 0.15$, $D = 0.5$ $\Phi_{lat} = 0.45$, $D = 0.5$ $\Phi_{lat} = 0.65$) is compared in Figure 5.7a. We observed that only the statically stable hexapod gait ($\Phi_{lat} = 0.45$) has both low pitch and low roll. The unstable hexapod gaits have either high roll angle ($\Phi_{lat} = 0.15$) or high pitch angle

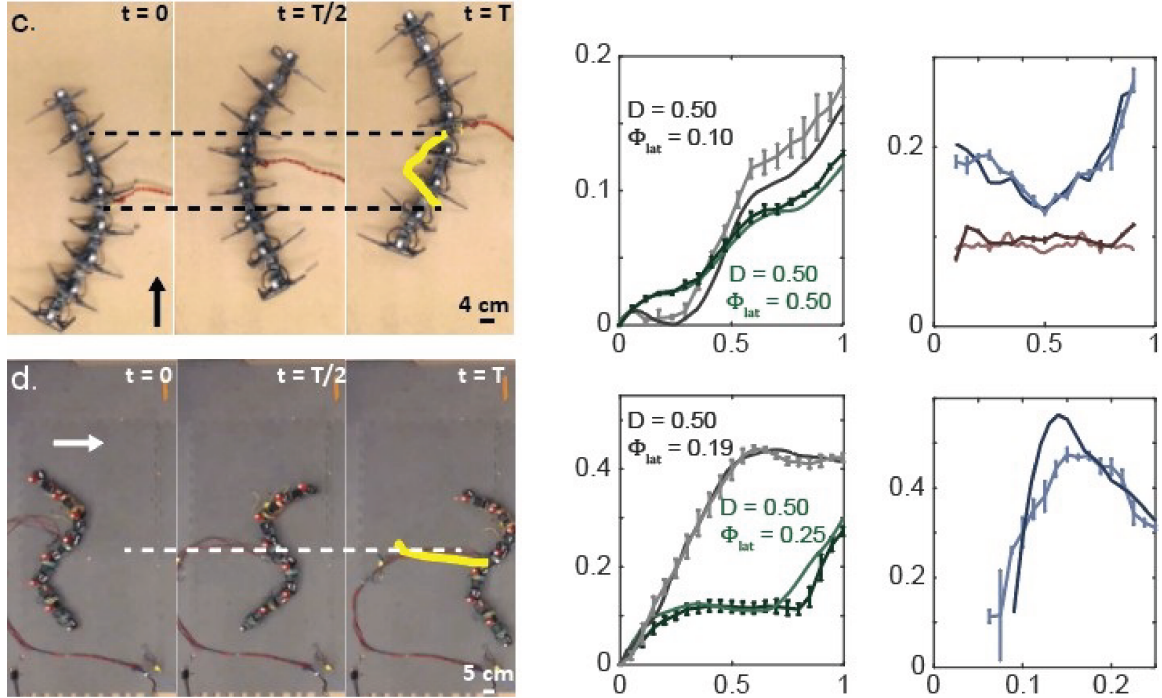


Figure 5.6: **Verification of the theoretically generated gaits in the robotic models** (left column) Gait cycle of each robot (c: myriapod, $D = 0.5$, $\Phi_{lat} = 0.1$; d: sidewinder). The color scheme and axes in (b, c, d) are the same as in (a).

($\Phi_{lat} = 0.65$). We calculated the average pitch and roll for each gait, and compared them with the numerical predictions of static stability. We observe that the range of low average pitch and roll overlaps with the range of statically stable gaits. When the hexapod body is in configurations with low roll and low pitch, the experimental data agrees with the theoretical predictions.

5.2 Body-leg Coordination in Hildebrand Gait Formulation

5.2.1 Geometric Mechanics to Coordinate Lateral Body Undulation

As discussed in the previous sections, speed is not correlated with the lateral phase lag when there is no body undulation. However, previous experimental gait studies with lizards and myriapods [43, 87] have found that modulation of lateral phase lag is associated with changes in the lateral body undulation. For example, lizards increase the amplitude of their lateral body undulation during transitions from lateral sequence walking to trotting or even

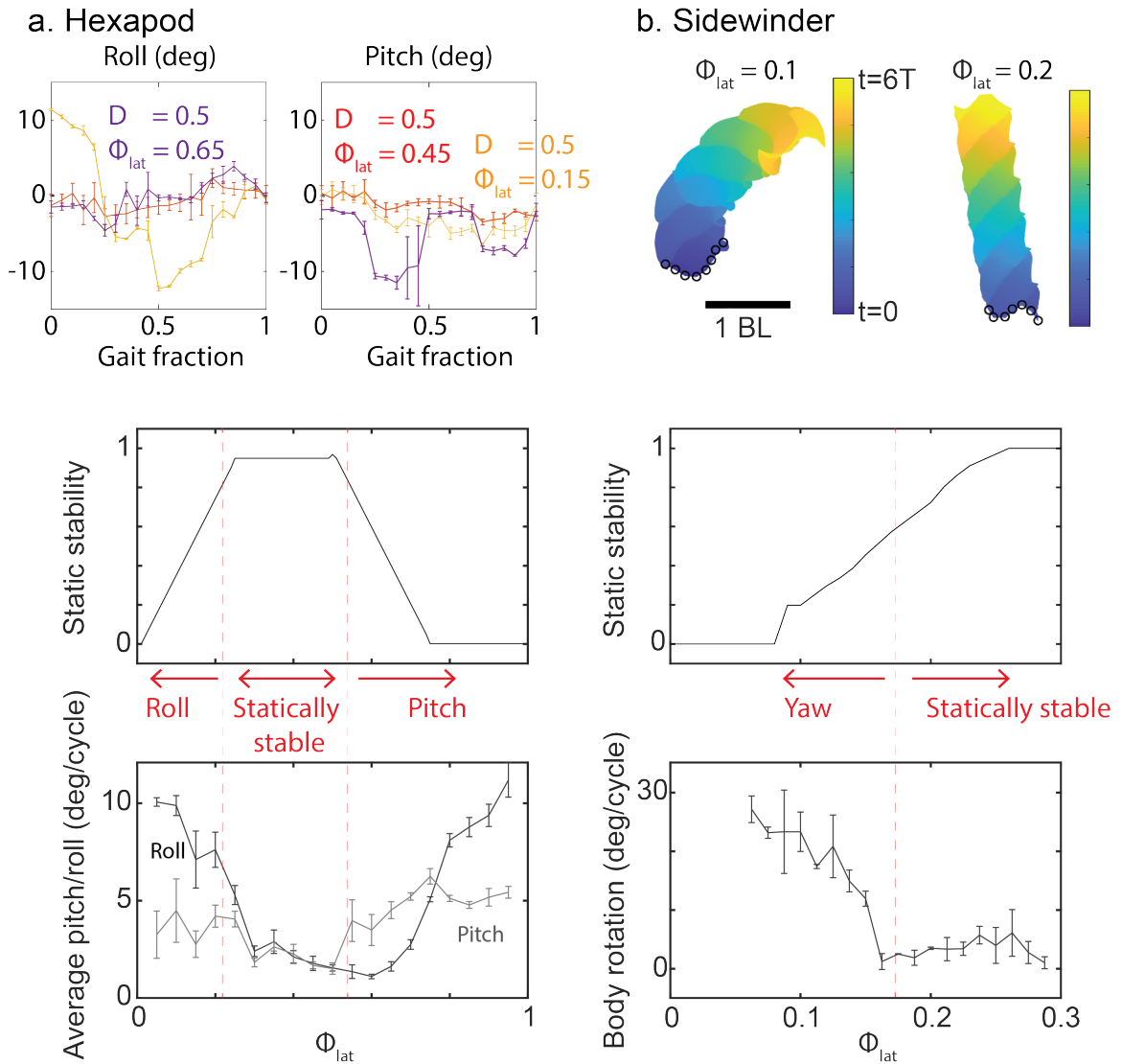


Figure 5.7: **The effect of static stability on locomotion performance.** In the left column (a.), the body roll and pitch over the course of the hexapod experiments are recorded as a function of gait fraction. Three gaits ($D = 0.5$, $\Phi_{lat} = 0.65$ in purple; $D = 0.5$, $\Phi_{lat} = 0.45$ in red; and $D = 0.5$, $\Phi_{lat} = 0.15$ in yellow) in Hildebrand gait space are compared. In the middle row, we show the theoretical prediction of static stability as a function of lateral phase lag. In the bottom row, we show the average \pm SD experimental body roll and pitch as a function of the lateral phase lag. In the right column, (b.), a similar analysis is performed for the sidewinder experiments. The top-right shows the trajectory of body motion over six gait cycles, where the color scale represents the evolution of time. We marked the initial position of the robot in the black circles. In the middle row, we showed the theoretical prediction of static stability as a function of lateral phase lag. In the bottom panel of Fig 7b, The body yaw angle is recorded as a function of lateral phase lag.

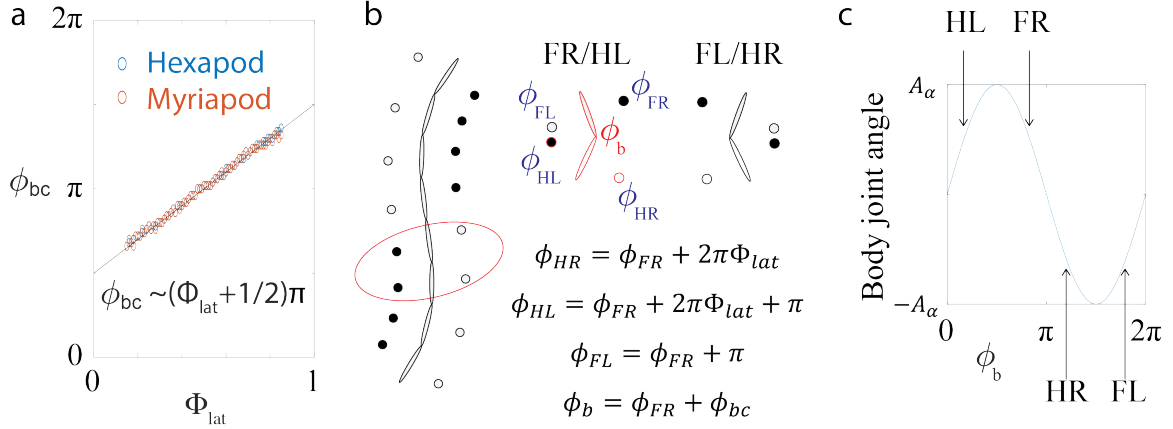


Figure 5.8: Physical intuition in body-leg coordination (a) The relationship between Φ_{lat} , lateral phase lag, and ϕ_{bc} , the optimal phasing between body and leg. ϕ_{bc} is numerically calculated from a height function (Figure 5.3). The empirical data for the hexapod (blue circle) and myriapod (red circle) are compared. (b) Consider a quadrupedal “sub-unit” consisting of two pairs of legs and one body-joint. The Hildebrand prescription allows us to write the phase relation of each leg and the body bending with respect to the fore right leg (FR). (c) To maximize locomotive performance with body-bending, at FL (fore left) and HR (hind right) touchdown, the body is bent clockwise; and at FR (fore right) and HL (hind left) touchdown, the body is bent counterclockwise [176]. Given this empirical relation $\phi_{bc} \sim (\Phi_{lat} + 1/2)\pi$, the HL/FR and HR/FL touchdown phases are symmetrically distributed around the peaks of the bending trajectory, which we use to coordinate body-bending with foot contacts.

diagonal sequence gaits [87, 201, 203, 204, 91, 90]. Similarly, myriapods change their leg wave pattern (lateral phase lag) at high speeds while simultaneously increasing lateral body undulation amplitude [43]. Accordingly, we hypothesize that modulating the lateral phase lag can regulate the balance between speed and stability if properly coordinated with lateral body undulation.

To account for these observations, we introduce the lateral body undulation by propagating a wave along the backbone from head to tail [205]. Note that we only consider the format of traveling wave body undulation here; relative advantages of standing and traveling waves are discussed in [206]; and for quadrupeds, the number of body undulation DoF drops to 1, where the format of traveling wave body undulation essentially reduces to a

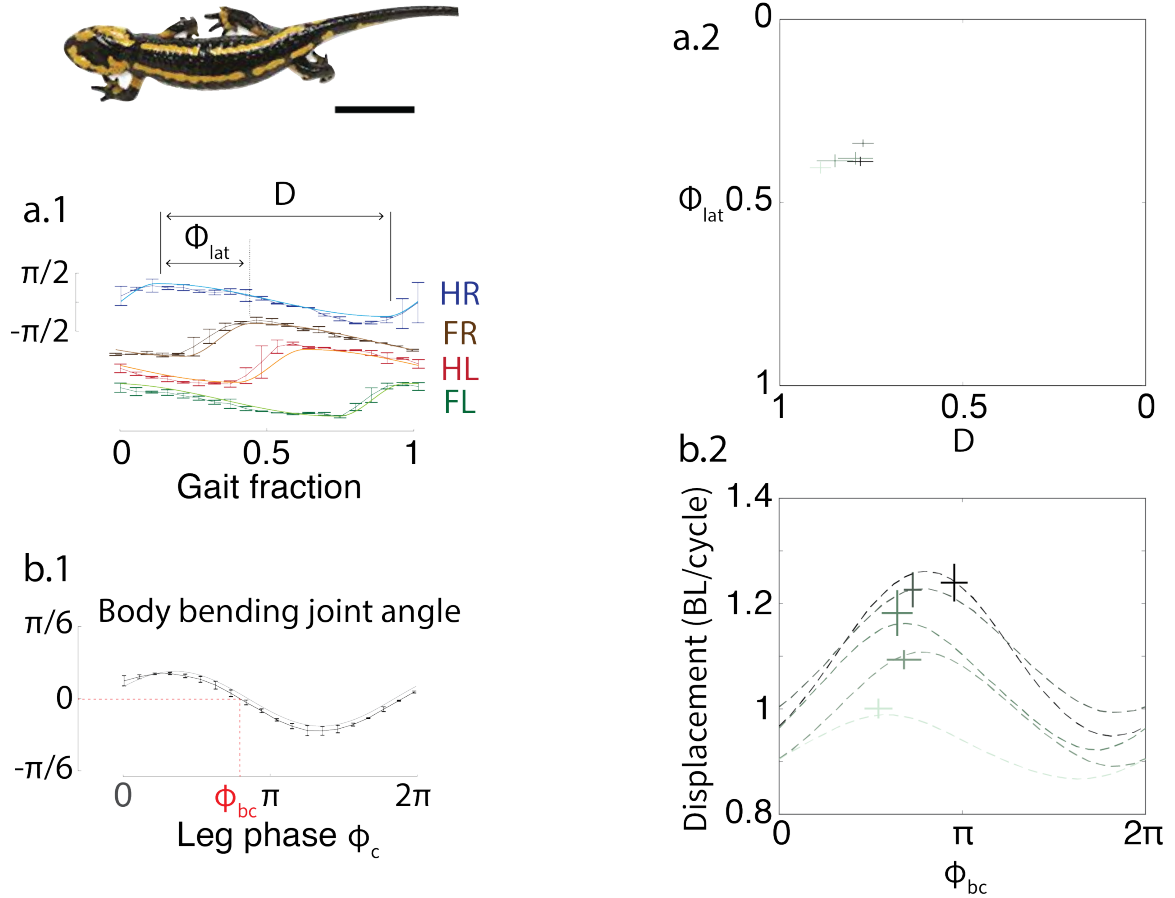


Figure 5.9: **Analysis of salamander (*Salamanca salamandra*) locomotion using the Hildebrand framework and geometric mechanics** (a.1) Estimation of the duty factor, D , and lateral phase lag, Φ_{lat} from animal joint angle trajectories. Curves with error bars are the average leg shoulder (hip) angle over three cycles. The lighter-color solid curves are piece-wise linear sinusoidal functions (defined in Equation 5.3) fit to the tracked data. (a.2) Estimated D and Φ_{lat} for animal locomotion under different speeds. (b.1) Estimating ϕ_{bc} from body bending angle trajectories. (b.2) Relationship between ϕ_{bc} and speed, measured in body lengths (BL) per cycle. The prediction made with geometric mechanics is shown as dashed curves. The measured salamander data are shown as crosses in the same color as their corresponding prediction curves, where the length and height of the crosses denote the standard deviation of the measured animal data. The scale bar near the salamander photo indicates 30 mm.

standing wave. The body undulation wave is

$$\alpha(\phi_b, i) = A_\alpha \cos(\phi_b - 2\pi(i-1)\Phi_{lat}^b), \quad (5.4)$$

where $\alpha(\phi_b, i)$ is the angle of i -th body joint at phase ϕ_b , $2\pi\Phi_{lat}^b$ is the phase lag between

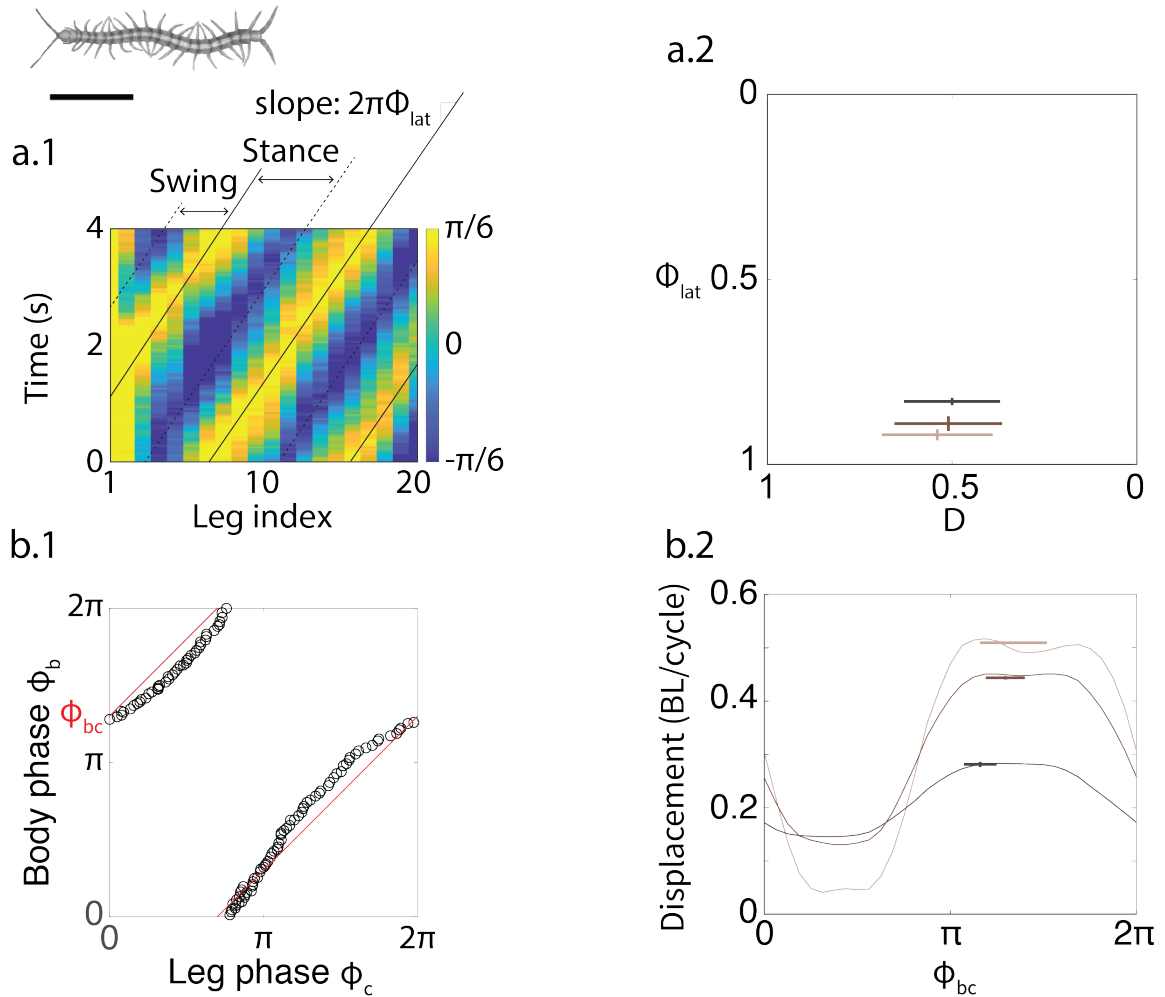


Figure 5.10: **Analysis of centipede (*Scolopendra polymorpha*) locomotion using the Hildebrand framework and geometric mechanics** (a.1) Estimation of the duty factor, D , and lateral phase lag, Φ_{lat} from animal joint trajectories. The colorbar here denotes the shoulder joint angle for each leg on right-hand side. (a.2) Estimated gait parameters D and Φ_{lat} for the centipede's locomotion. (b.1) Estimating ϕ_{bc} from body phase and leg phase. (b.2) Relationship between ϕ_{bc} and the speed, measured in body lengths per cycle. The prediction made with geometric mechanics is shown as solid curves. The measured centipede data is presented by crosses in the same color as their corresponding prediction curves, where the length and height of the crosses denote the standard deviation of the measured animal data. The scale bar near the centipede photo indicates 30mm.

consecutive joints. For simplicity, we assume that the spatial frequency of the body undulation wave and the contact pattern wave are the same⁶, i.e. $\Phi_{lat}^b = \Phi_{lat}$. In this way, gaits of

⁶In most biological and robotics systems, the body undulation and the contact waves in general share the same frequency. In some cases, such as Sinus Lifting in snakes [146], the body undulation and the contact waves differ.

multi-legged locomotors by superposition of a body wave and a leg wave can be described as the phase of contact, ϕ_c , and the phase of lateral body undulation ϕ_b . These two independent phase variables represent a reduced shape space (see Materials and Methods) on a two-dimensional torus on which we can apply geometric mechanics gait design techniques to optimize body-limb coordination (Materials and Methods).

The geometric mechanics gait design framework [199, 142, 207] separates the configuration space of a system into two spaces: the position space and the shape space. The position space represents the location (position and orientation) of a system relative to the world frame, while the shape space represents the internal shape (joint angles) of the system. The geometric mechanics framework then establishes a functional relationship to map velocities in the shape space into velocities in the position space; this functional relationship is often called a *local connection*. The curl of the local connection, which we call a “height function” can then be used to design, analyze, and optimize gaits.

Using geometric mechanics tools, we derived height functions and designed gaits (Materials and Methods). Figure 5.3 and Figure 5.4 show examples of coordination between the lateral body undulation and contact phase derived with geometric mechanics. We also provided an example of coordinating the body undulation and contact pattern for sidewinding in S4. Once we design a coordination pattern $\phi_c \rightarrow \phi_b$ in the reduced shape space, we can convert that pattern into both a contact pattern and body undulation.

We quantified the body-leg coordination by its phase lag: $\phi_{bc} : \phi_c - \phi_b$. Interestingly, we observed that the empirically calculated ϕ_{bc} has a linear relationship with Φ_{lat} (Figure 5.8). We next seek the physical intuition behind this relationship. We first decomposed the body-leg coordination to a single “sub-unit,” which we define as two pairs of legs and one body joint. Our Hildebrand-based approach then allows us to prescribe the phase of each foot and the body bending. Previous work [176] found that at the optimal body-leg coordination, the body is bent clockwise (respectively, counterclockwise) when the HL/FR (respectively, HR/FL) feet land. Deviation from this coordination can lead to a loss in speed. We can

encode this relation by $\phi_{bc} \sim (\Phi_{lat} + 1/2)\pi$. Then, the FR and HL foot touch-down are symmetrically distributed around the peak of the clockwise body bending angle, and the touch-down of FL and HR feet are symmetrically distributed around the peak of counter-clockwise body bending angle. Via this relationship, we posit that despite the seemingly complicated whole-body motion, the optimal body-leg coordination is achieved by locally coordinating each sub-unit of two legs and a body joint.

5.2.2 Numerical Prediction of Speed and Stability

We used a numerical simulation to predict the gait speed and stability at a range of lateral phase lags and duty factors for the quadrupedal, hexapod, myriapod and sidewinder systems. We observed that modulating the lateral phase lag can regulate the balance between speed and stability if properly coordinated with lateral body undulation. The loss of static stability is compensated by a gain in speed only when the body and limb phases are properly coordinated. These observations were derived by plotting gait speed and stability against the extended Hildebrand gait parameters, shown in Figure 5.5. The addition of body undulation slightly changes the static stability, as depicted in S1.

5.2.3 Testing predictions for body-leg coordination in experiments

We tested the locomotion performance of systems with discrete contact and coordinated lateral body undulation using robophysical models (Materials and Methods for details). We recorded the displacement over time for two gaits in each system (Figure 5.6). Our numerical predictions quantitatively agree with experiments not only in the average displacement per gait cycle, but also in the time evolution of the displacement.

The only notable theory-experiment discrepancies occur in the hexapod and the sidewinder systems. As discussed earlier, static instability can lead to theory-experiment discrepancy for hexapods and sidewinders due to the planar assumptions made in our theoretical model. To investigate this discrepancy further, we studied the effect of static instability

on sidewinders and observed that some gaits result in significant yaw (Figure 5.7b), such that the robot's path deviates from the desired straight-line course. Comparing the net yaw change per gait cycle with the numerical predictions of static stability reveals that significant yaw only occurred in gaits with low static stability. As static stability increases (for sidewinding, stability increases with the lateral phase lag), the unmodelled turning vanished.

5.3 Body-leg Coordination in Biological Locomotors

Symmetric gaits in quadrupedal animals can be categorized using Hildebrand analysis [17, 96]. Recent work revealed that a geometric mechanics framework predicted optimal body-leg coordination for fire salamanders (*Salamandra salamandra*) [208, 176]. However, the means by which salamanders modify their leg movements and body-leg coordination in response to speed changes was previously unstudied. In this work, we recorded fire salamanders moving on sand. Five individuals were recorded, and their foot placement and backbone positions tracked. For simplicity, we only consider the body movement between the shoulder and the hip, for which salamanders exhibit a standing wave [209]. From the tracking data we measured gait parameters such as duty factor, lateral phase lag, amplitude of body bending, and amplitude of leg movements. We then used geometric mechanics to predict the optimal body-leg coordination for salamanders walking at various speeds. We observed quantitative agreement between the geometric mechanics prediction and the biological measurements (Figure 5.9).

Beyond quadrupedal animals, our methods can also be applied to study animals with various numbers of legs and backbone segments. Centipedes are known to be fast-moving locomotors: certain centipedes are the fastest-running terrestrial arthropods [43, 202]. Given their high speeds, past works have often used dynamic models to analyze their locomotion [210, 211]. We hypothesized that despite their high speeds, centipede locomotion could be analyzed with our quasi-static geometric model because of the high damping from

many leg contacts. To test this hypothesis, we recorded videos of centipedes (*Scolopendra polymorpha*) moving at different speeds. Three individuals were recorded, their leg and body positions tracked, and their gait parameters estimated. We then used geometric mechanics to predict the optimal body-leg coordination. We once again observed quantitative agreement between geometric mechanics predictions and the biological measurements (Figure 5.10).

5.4 Discussion and Conclusion

5.4.1 Principles of gait modulation

In this paper, we developed a general gait design framework for a broad class of locomotors: multi-legged robots (with an arbitrary number of pairs of legs) with an articulated backbone, including limbless sidewinding. Specifically, we extended the Hildebrand gait formulation [17, 96], originally used to categorize symmetric quadrupedal gaits, and combined it with modern geometric mechanics tools to investigate optimal leg-body coordination. We showed that the symmetry in Hildebrand quadrupedal gaits is conserved for other locomotors. The framework is not only simple enough to enable physical interpretation of the gait parameters; but also covers a range of potentially interesting gaits, offering a scheme to modulate gaits in a diversity of robot shapes. These properties enable our framework to link well-studied locomoting systems like quadrupeds and hexapods with less-studied systems like myriapods, generating new opportunities to transfer insights among and compare between different locomoting morphologies. Given a new robot with arbitrary pairs of legs or without legs, our framework can immediately provide effective open-loop gaits, which can serve as the basis for closed-loop adaptive or data-driven/learning-based control algorithms.

Our gait identification and dimensionality reduction principles reveal insights into proper contact scheduling. These principles could serve as a starting point for additional layers within in a robot’s control architecture or even for mechanical design iterations. [212]

found that while direct application of gait design tools can prove ineffective in rough terrain, adding passive leg compliance can greatly improve performance in this environment. Our proposed framework can not only simplify the gait design and modulation process for robots with different morphologies in various homogeneous environments, but can also be used to test hypotheses and therefore give novel insights into the control principles behind gaits in biological systems.

Finally, our framework facilitated testing hypotheses about the role of body undulation in multi-legged systems. These observations can act as guidelines in the control of a variety of legged robots. For example, in RHex [4], a hexapod with flexible legs attached to a rigid body, the duty factor is the only tuning parameter that can regulate the balance between speed and stability. In other cases, such as in [213], a segmented robot with a flexible backbone and contralateral legs mechanically coupled to have opposite contact states (and therefore, to have a fixed duty factor $D = 0.5$), the lateral phase lag acts as the salient parameter to balance between speed and stability when properly coordinated with lateral body undulation. Additionally, body undulation also plays an important role in turning motions. Although not explicitly studied in this work, our framework can also be used to investigate the coordination between body movement and contact patterns during turning motions in both legged [176] and limbless [107] systems.

5.4.2 Insights from robotics to biological systems

We also demonstrated that once two gait parameters (duty factor and lateral phase lag) are specified, the gait can be prescribed and can then be analyzed with geometric tools. To explore gait tuning principles for locomoting systems, we quantitatively investigated the effect of modulating gait parameters on locomotor performance. As shown in Figure 5.6, we found that in robots with a fixed straight backbone, the displacement per gait cycle is nearly invariant to the changes in the lateral phase lag, Φ_{lat} . On the other hand, in gaits where body undulation is properly coordinated with leg motions, Φ_{lat} affects the displace-

ment. This seemingly counter-intuitive observation can help us develop hypotheses about gait modulation principles.

In addition to these robotics applications, our proposed control principles can also offer explanatory power to some hypotheses about biological locomotion. For example, biological myriapods (*Chilopoda*) can be categorized into direct-wave myriapods [43] and retrograde-wave myriapods [43]). Direct-wave myriapods propagate their leg contact wave from tail to head (corresponding to $\Phi_{lat} < 0.5$ in our modified Hildebrand formulation) while retrograde-wave myriapods propagate their wave from head to tail ($\Phi_{lat} > 0.5$) [200]. Interestingly, Manton [43] showed that there is no significant lateral body undulation in direct-wave myriapods regardless of their speed; instead, the only significant gait modulation at high speed is a decrease in duty factor. On the other hand, gait modulation in retrograde-wave myriapods is much more complicated: they not only decrease the duty factor, but also increase the lateral phase lag. More importantly, they exhibit characteristic lateral body undulation at high speeds [43, 202]. This observation is consistent with the principles discovered via our gait analysis methods, where we found that tuning the lateral phase lag can only improve the speed if accompanied with properly coordinated lateral body undulation.

5.5 Appendix

5.5.1 Numerical Derivation of Local Connection Matrix

Force and torque balance in the vertical plane

In Equation 5.2, we prescribed the contact pattern by its phase, ϕ_1 . However, the supporting force (against gravity) is not uniformly distributed among all the legs in stance phase, especially when the robot locomotes on the flat hard ground. In order to precisely model the friction, we need to calculate the supporting force distribution among legs.

As shown in Figure 5.11, we labeled the legs in stance phase with numbers. The lo-

cation of each leg is represented as $[x_i \ y_i]$ with respect to a pre-chosen coordinate. The supporting force on each leg is N_i . Assuming that all the legs are elastic bodies, the supporting force on each leg can be calculated as:

$$N_i = \begin{cases} KL\epsilon_i, & \text{if } K\epsilon_i \leq 0 \\ 0, & \text{otherwise} \end{cases} \quad (5.5)$$

where ϵ_i is the strain at leg i in stance phase; K is the spring constant and L is the leg length. As suggested in [214], it is reasonable to assume that the robot is a toppling table. In other words, we assume that only the legs are deformable bodies whereas the deformation in the ground substrate and in the main robot body is negligible. In this way, the distance of the body plane and the ground plane at location $[x_i \ y_i]$ in a fixed reference coordinate can be expressed as:

$$L_i = [x_i \ y_i \ 1] \begin{bmatrix} e_1 \\ e_2 \\ d \end{bmatrix} \quad (5.6)$$

where e_1 and e_2 are the tilt angle in the x and y directions and d is the constant offset. Note that the distance of body plane and the ground plane can relate to the strain as:

$$\epsilon_i = (L_i - L)/L = [x_i \ y_i \ 1] \begin{bmatrix} e_1/L \\ e_2/L \\ (d - L)/L \end{bmatrix} = [x_i \ y_i \ 1] \begin{bmatrix} e'_1 \\ e'_2 \\ d' \end{bmatrix}. \quad (5.7)$$

Therefore, the collection of the supporting forces of all legs is:

$$\boldsymbol{\epsilon} = \begin{bmatrix} \epsilon_1 \\ \epsilon_2 \\ \dots \\ \epsilon_n \end{bmatrix} = \begin{bmatrix} x_1 & y_1 & 1 \\ x_2 & y_2 & 1 \\ \dots & \dots & \dots \\ x_n & y_n & 1 \end{bmatrix} \begin{bmatrix} e'_1 \\ e'_2 \\ d' \end{bmatrix}, \quad (5.8)$$

for simplicity of notation, we define:

$$S = \begin{bmatrix} x_1 & y_1 & 1 \\ x_2 & y_2 & 1 \\ \dots & \dots & \dots \\ x_n & y_n & 1 \end{bmatrix}, \epsilon = S \begin{bmatrix} e'_1 \\ e'_2 \\ d' \end{bmatrix}.$$

Next, the force and torque balance in the vertical plane can be written as:

$$\begin{bmatrix} x_c \\ y_c \\ 1 \end{bmatrix} mg = \begin{bmatrix} x_1 & x_2 & \dots & x_n \\ y_1 & y_2 & \dots & y_n \\ 1 & 1 & \dots & 1 \end{bmatrix} \begin{bmatrix} N_1 \\ N_2 \\ \dots \\ N_n \end{bmatrix}, \quad (5.9)$$

where $[x_c \ y_c]$ is the coordinate of the center of mass. With Equation 5.5-Equation 5.8, we can numerically calculate the supporting force distribution on legs in stance phase N . Note that in the simple linear case,

$$N = -S(S^T S)^{-1} \begin{bmatrix} x_c \\ y_c \\ 1 \end{bmatrix} mg, \quad (5.10)$$

is the solution to (Equation 5.5-Equation 5.8), if the obtained $N < 0$ (element-wise).

Force and torque balance in the lateral plane

In this section, we will briefly describe the steps to numerically calculate the local connection matrix. We refer readers to [75, 208] for detailed derivation.

The ground reaction force (GRF) experienced by the robot is the sum of the GRF experienced by each body segment in stance phase, as show in example in Figure 5.11. In each body segment in contact with substrate ($c_i = 1$), the GRF, f_i , is directed related to its body velocity (ξ_i) (see Figure 5.11). In the isotropic environments, the direction of f_i is solely determined by the direction of ξ_i . For example, in the isotropic Coulomb friction model,

the GRF can be related to the body velocity by:

$$f_i = \mu N_i \frac{\xi_i}{|\xi_i|} \quad (5.11)$$

where μ is the friction coefficient and N_i is its supporting force.

In the anisotropic environments, the direction of GRF is also related to the orientation of the limb. Specifically, we choose the x axis to be along the direction parallel to the limb orientation, and the y axis to be perpendicular to the direction of the limb orientation. We then decompose f_i and ξ_i into x and y directions as:

$$f_i = \begin{bmatrix} f_x^i & 0 \\ 0 & f_y^i \end{bmatrix} \begin{bmatrix} \hat{x} \\ \hat{y} \end{bmatrix}, \xi_i = \begin{bmatrix} \xi_x^i & 0 \\ 0 & \xi_y^i \end{bmatrix} \begin{bmatrix} \hat{x} \\ \hat{y} \end{bmatrix}. \quad (5.12)$$

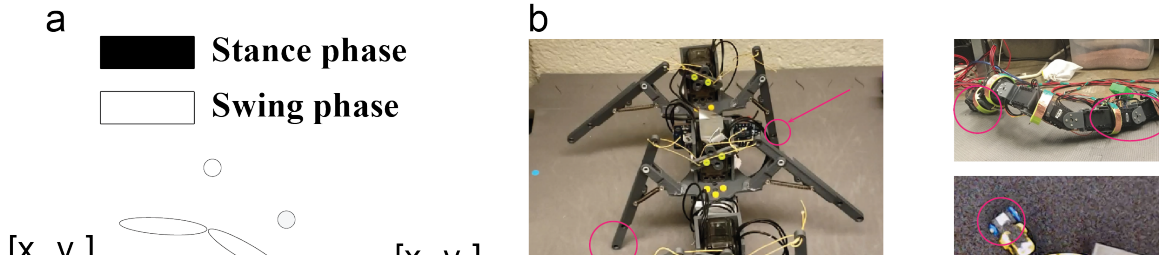


Figure 5.11: **Supporting force distribution** (a) An example of the myriapod model. In this example, the robot is supported by eight legs. For a leg i , it provides supporting force N_i . Its location is labeled as $[x_i \ y_i]$. The location of center of mass is labeled $[x_c \ y_c]$. (b) The robots with hybrid contact with environments. The body segments in stance phase are labelled by red circle. (c) The illustration of the force-velocity relationship. (Left) The vector of body velocity (ξ) and GRF f on the body segment in contact with environments (red cube). (Right) The decomposition of body velocity and GRF in the direction of body orientation.

We showed examples of such decomposition in Figure 5.11. In the anisotropic Coulomb friction model [215, 216], the x, y component of the GRF and the body velocity can be related as:

$$\begin{bmatrix} f_x^i \\ f_y^i \end{bmatrix} = \frac{N_i}{|\xi_i|} \begin{bmatrix} \mu_x & 0 \\ 0 & \mu_y \end{bmatrix} \begin{bmatrix} \xi_x^i \\ \xi_y^i \end{bmatrix} \quad (5.13)$$

We estimated $\mu_x/\mu_y \sim 0.7$ from experiments on the robophysical model. In the poppy seed RFT model [104], the x, y component of the GRF and the body velocity can be related as:

$$f_y = C \sin(\gamma) \quad (5.14)$$

$$f_x = A \cos(\gamma) + B(1 - \sin(\gamma)) + F_0 \quad (5.15)$$

where $\gamma = \arctan(\xi_y/\xi_x)$; $C = 0.66$, $A = 0.27$, $B = -0.32$, $F_0 = 0.09$ is the empirical fitted function to characterize the granular media resistant force.

Note that in each configuration, the body velocity of the body segment i , ξ_i , can be related to the body velocity of the locomotor (in our case, we choose head frame as the body frame of the locomotor) ξ_0 , by [82, 217]:

$$\xi_i = \text{Ad}_{g_{0i}^{-1}} \xi_0 + J_i(\Phi) \dot{\Phi} \quad (5.16)$$

where $J_i(\Phi) \in \mathbb{R}^{3 \times 3}$ is the body Jacobian matrix, a linear differential map from shape velocity $\dot{\Phi}$ to the body velocity of body segment i with respect to the head frame; Ad_g denotes the adjoint operator, which maps body velocity between different frames; g_{0i} denotes the configuration of the body frame of body segment i with respect to the head frame. Note that $\text{Ad}_{g_{0i}^{-1}}$ and $J_i(\Phi)$ are uniquely determined by the shape variable Φ .

Finally, the force and torque balance in the lateral plane can be written as:

$$\sum_{i=1}^n f_i^0 = \sum_{i=1}^n \text{Ad}_{g_{0i}^{-1}}^T \begin{bmatrix} f_x^i \\ f_y^i \\ 0 \end{bmatrix} = 0 \quad (5.17)$$

where f_i^0 denoted the force applied to body segment i with respect to the head frame; $\text{Ad}_{g_{0i}^{-1}}^T$ transforms the force in the body frame to the head frame.

With (Equation 5.11-Equation 5.18), we established a relationship between the body velocity in the head frame ξ_0 and the shape velocity $\dot{\Phi}$ and shape velocity Φ . We then linearize the equations and obtain:

$$\xi_0 = A(\Phi)\dot{\Phi}. \quad (5.18)$$

CHAPTER 6

SELF PROPULSION VIA SLIPPING: FRICTIONAL RESISTIVE FORCE THEORY FOR MULTI-LEGGED LOCOMOTORS

Part of this chapter is adapted from a journal article under review “Self propulsion via slipping: frictional resistive force theory for multi-legged locomotors.” *Proceedings of the National Academy of Sciences*. My contribution in this project includes (1) designing the experiments, (2) conducting the numerical analysis, (3) writing the manuscript. Robophysical experiments presented in this chapter are conducted by Juntao He.

Locomotion by body undulation is often observed in locomotors continuously immersed in an environment (such as fluid or granular media) [218, 132, 219, 220, 221, 222, 223]. During such self-propulsion, body elements continuously experience forces set by the physics of the medium and the instantaneous orientations and velocities of body elements. An approach to analyze this form of locomotion, which integrates thrust and drag forces over the body, was introduced in the early to mid 20th century and goes by Resistive Force Theory (RFT). This method has successfully modeled organisms in highly damped environments, like microorganisms and sand-swimmers etc [72, 63, 73]. RFT works at its core because of a so-called “drag anisotropy” in continuous element flow. For example, long thin systems like spermatozoa can be thought of as a superposition of slender rods, which differ in reaction forces in the perpendicular and parallel directions [224, 225, 78, 226, 227].

In contrast, on hard ground where frictional force is typically assumed rate-independent isotropic Coulomb friction, a key feature of the locomotion dynamics is that the anatomical elements (like limbs or body segments) are no longer in constant contact with the environment. Rather, elements can make and break contact [146, 228]. In such situations, control algorithms [20, 229] are developed to minimize slip (the sliding between

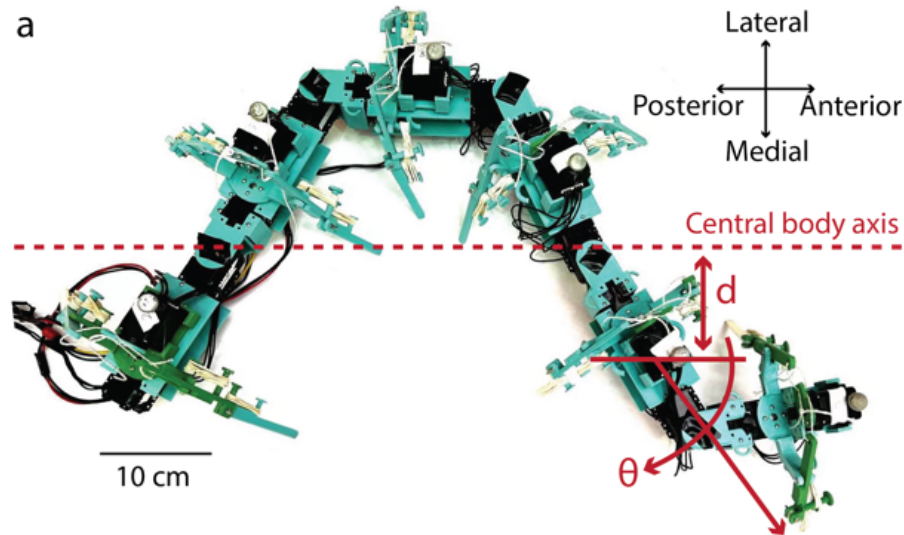


Figure 6.1: **Swimming in terrestrial environments** (a) Top view of a robophysical device swimming on frictional ground.

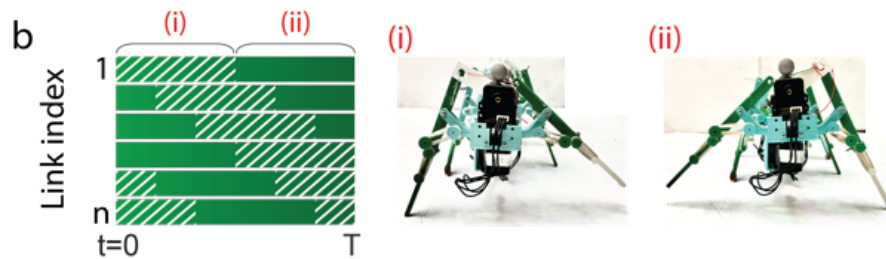


Figure 6.1: **Swimming in terrestrial environments** (b) The patterns of lifting and landing of contralateral feet. Each row represents the contact states of i -th link. Shadow region represents right foot in stance phase, open region presents left foot in stance phase. (right) Front view of the robophysical device lifting (i) left and (ii) right feet of the first module

the foot and the substrate); similarly, active slip avoidance is also observed in biological systems [230, 231]. Slipping is assumed minimal partially because Coulomb friction introduces a step-function between the velocity reaction force relationship, which can cause unstable oscillations [232]. Furthermore, if not properly controlled, slipping can cause a loss in energetic efficiency.

While the bulk of prior work on terrestrial locomotors [69] have 2 and 4 limbs, many biological and increasingly robotic systems possess 6, 20, 40 limbs. In contrast to the few limbed systems in which an assumption of no-slip contact is often feasible [70], for sys-

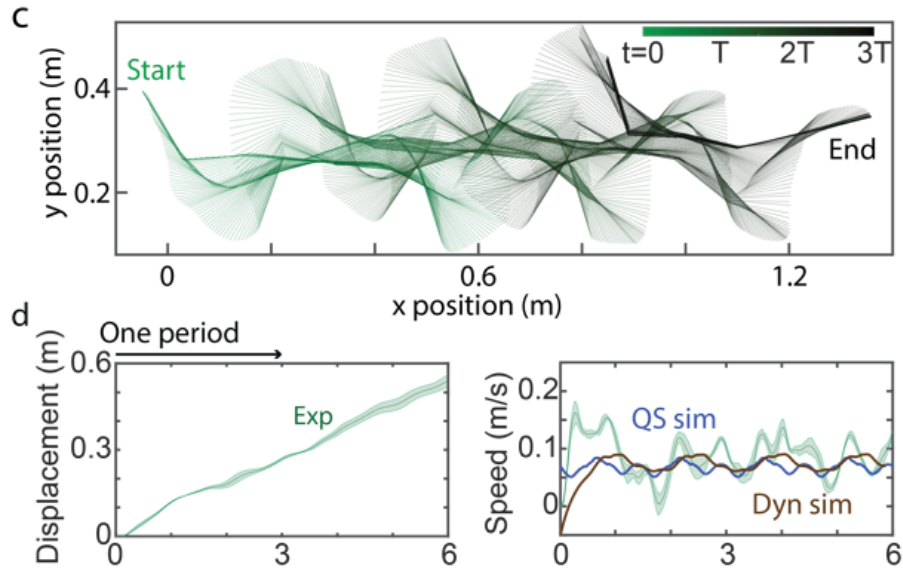


Figure 6.1: **Swimming in terrestrial environments** (c) Trajectory of backbone during terrestrial swimming ($\Theta_{body} = \pi/3$, $\Theta_{leg} = 0$, $n = 6$) colored by time. (d) (*left*) Displacement and (*Right*) velocity profile of terrestrial swimming. We compared the experimental data with dynamical simulation (brown curve) and quasi-static simulation (blue curve) for body-dominated terrestrial swimming. After the transient development, both experiments dynamical simulation converge to a limit cycle similar to quasi-static simulation.

tems with more than 4 legs, there is a high possibility that some slip has to occur during locomotion [71] because of kinematic constraint violations, (e.g., the BigAnt [71]). We hypothesized that instead of avoiding slipping, we can actively analyze slipping using a method similar to RFT on continuous media, and establish a unifying model for both terrestrial and continuous locomotion. The challenges lie on the nonlinearity and the isotropy of Coulomb friction in terrestrial environments in contrast to linear, anisotropic viscous friction.

Here, we investigated a new regime of multi-legged terrestrial locomotion enabled by properly sequenced feet-substrate sliding. Specifically, both body undulation and leg retraction contribute to slipping and therefore self-propulsion. Using a centipede-like robo-physical model, we showed that the steady-state terrestrial locomotion has a property of geometric locomotion (the effect of inertia is negligible) even when operated at high frequency on a low-friction substrate. We used RFT to study slipping in multi-legged systems

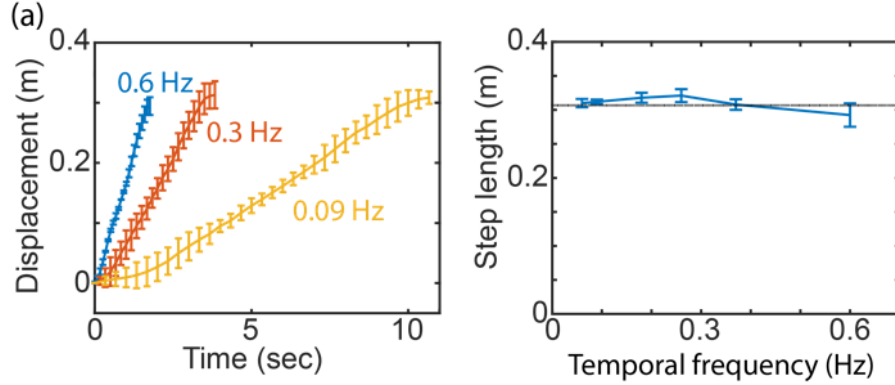


Figure 6.2: **The geometric nature of terrestrial swimming** (a) Robot ($n = 6$) implementing the same gait ($\Theta_{body} = \pi/3$, $\Theta_{leg} = 0$) under different temporal frequencies. (*Left*) The development of displacement as a function of time under different temporal frequencies. (*Right*) The step length is stable over a range of temporal frequencies. Dashed lines represent prediction from quasi-static simulation.

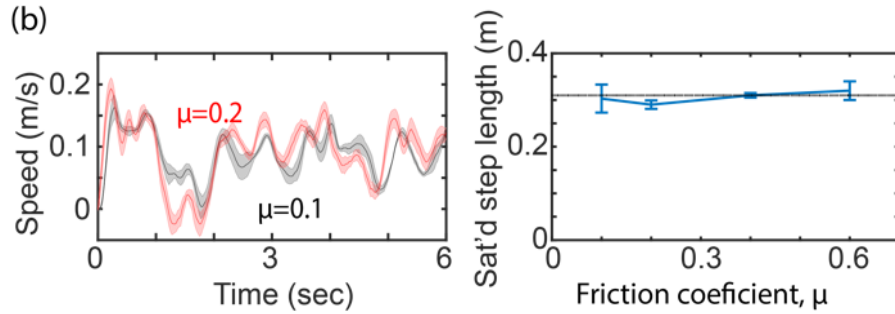


Figure 6.2: **The geometric nature of terrestrial swimming** (b) Robot implementing the same gait under different substrate (different friction coefficients, μ). (*Left*) The development of velocity as a function of time. Despite the initial high-magnitude oscillation, robots on low-friction surfaces converged to quasi-static velocity profiles after one gait cycle. (*Right*) The saturated step length is stable over a range of friction coefficient.

and proposed a new principle of acquired drag anisotropy. Specifically, by periodic lifting and landing of body appendages, the nonlinear and isotropic Coulomb friction experienced on each limb can be simplified into a velocity-dependent whole-body drag, similar to that of organisms at low Reynolds number, which we refer to as terrestrial swimming. In an effort to unify our proposed slip-driven and the conventional minimal-slipping mechanism, we establish a performance space of terrestrial swimming, and discuss the relative advantage (i.e., higher speed and less sensitivity to obstacle-rich environments) of body-dominated (slip-driven) over leg-dominated (minimal slipping) terrestrial swimming by

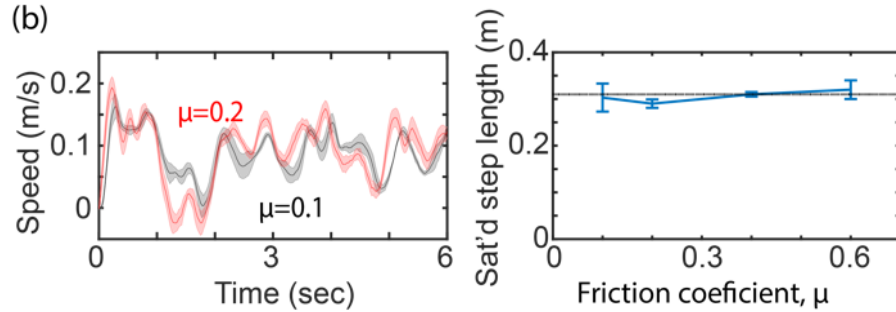


Figure 6.2: **The geometric nature of terrestrial swimming** (c) Experimental verification of force-velocity relationship ($\Theta_{body} = \pi/3$, $\Theta_{leg} = 0$, $n = 8$). We test the relationship between the whole body drag force and the velocity by measuring the speed of robots on slopes. We compared two spatial frequencies, $\xi = 1$ and $\xi = 1.3$. In both experiments, we observed that there exists an linear relationship between force and velocity near equilibrium.

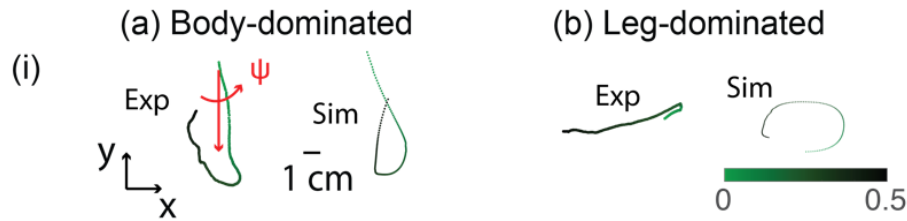


Figure 6.3: **Direction of limb slipping** (i) Typical trajectories of foot tips of robo-physical device ($n = 6$) during stance phase for (a) body-dominated ($\Theta_{body} = \pi/3$, $\Theta_{leg} = 0$) and (b) leg-dominated ($\Theta_{body} = 0$, $\Theta_{leg} = \pi/6$) terrestrial swimming. x -axis is the direction of motion. We quantify the slipping of a foot by its direction (Ψ unit: rad) and magnitude (unit: BL/cycle).

robo-physical experiments. Finally, we used our scheme to analyze the locomotion of a biological multi-legged system and reveal slip-driven terrestrial swimming in centipedes. Similar to our predictions on robo-physical experiments, we also observe a smooth gait transition from leg-dominated to body-dominated locomotion as speed increases.

Body undulation

We adapted a robo-physical modeling approach [233] to systematically study terrestrial locomotion. Specifically, we constructed a multi-legged robot consisting of repeated modules. Each module contains one pair of legs and one body connection. All combined, each module has three degrees of freedom (DoF): the shoulder lifting joint that controls

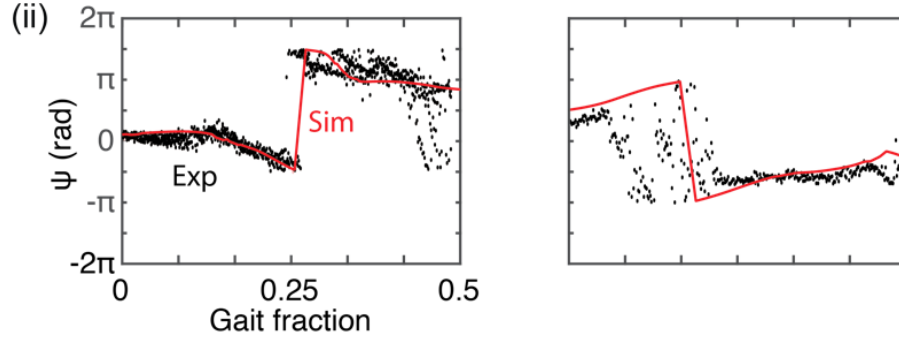


Figure 6.3: **Direction of limb slipping** (ii) The simulation prediction (red curves) and experimental measured (black dots) time series of slipping angles.

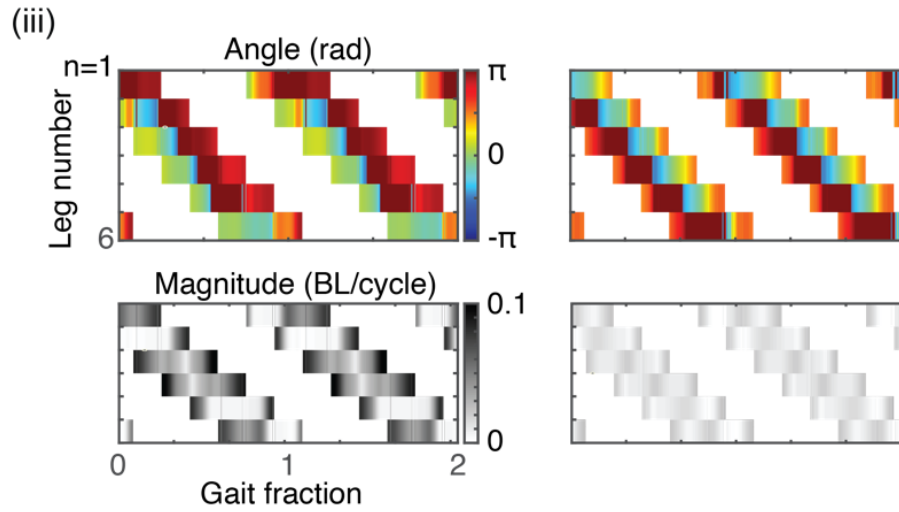


Figure 6.3: **Direction of limb slipping** (iii) The slipping profiles from simulation. We illustrate (*top*) the slipping direction profile and (*bottom*) the slipping magnitude profile.

the contact states of contralateral legs, the shoulder retraction joint that controls the for/aft positions of limb movements, and the body bending joint that controls the lateral body undulation. The synchronization of these three DoF is coupled using the extended Hildebrand framework, which prescribe a leg stepping wave and a body undulation wave, both propagating from head to tail. The amplitude of body undulation, Θ_{body} , the amplitude of leg movement, Θ_{leg} , and the spatial wave number ξ , can then uniquely prescribe the gait of the multi-legged robot. Note that unless otherwise mentioned, we set $\xi = 1$ throughout paper.

As discussed in prior work, body undulation can play an important role in multi-legged systems [234, 176]. In Figure 6.1c, we show the midline trajectory during undulatory

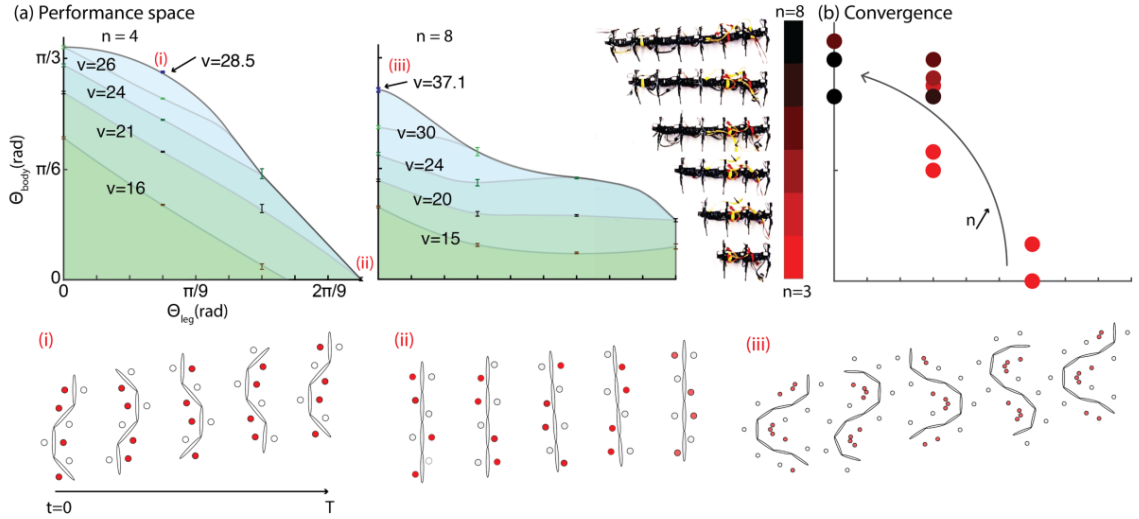


Figure 6.4: Performance space of multi-legged terrestrial locomotion. We characterize the terrestrial locomotion using a performance space consisting of the amplitudes of body undulation and leg movement. (a) The heat map of velocity (v , unit: cm/cycle) over the performance space for robophysical model with (left) 4, (right) 8 pairs of limbs. n is the number of limb pairs. Note that optimal terrestrial locomotion (the highest velocity) occurs at “hybrid” region when $N = 4$ and at body-dominated when $N = 8$. (bottom) We showed the snapshots of body configurations over a cycles for (i) $N = 4$, $\Theta_{body} = 60^\circ$, $\Theta_{leg} = 15^\circ$, (ii) $N = 4$, $\Theta_{body} = 0^\circ$, $\Theta_{leg} = 45^\circ$, and (iii) $N = 8$, $\Theta_{body} = 60^\circ$, $\Theta_{leg} = 0^\circ$. (b) The transition of optimal terrestrial locomotion from leg-dominated to body-dominated as the number of leg pairs increases.

locomotion of the multi-legged robot ($\Theta_{body} = \pi/3$, $\Theta_{leg} = 0$, $n = 6$, n is the number of modules). We refer to gaits with high Θ_{body} and low Θ_{leg} as body-dominated, and gaits with low Θ_{body} and high Θ_{leg} as leg-dominated. While the body parts were lifted off the ground, the undulatory body trajectory was similar to slithering motion (commonly observed in snakes and nematodes locomoting on continuous media such as sand [126] and viscous fluid [116]).

To quantitatively investigate terrestrial swimming, we tracked the trajectory of the CoG (center of geometry) of the robophysical model. In Figure 6.1d left panel, we illustrated the displacement and speed profile. Interestingly, we observed that after the transient response ($t < 2s$) upon the initiation of gait, the trajectory of velocity converged to a stable oscillation. To better understand the initial transient response and the stable oscillation,

we established a dynamic model (see [235]) and a quasi-static model [234] (Figure 6.1d). While the dynamic model under-predicted¹ the magnitude of the transient response upon the initiation of gait, the predicted velocity from dynamical model also converged to a stable oscillation. The average of the stable oscillation is almost identical in experiments, dynamical model prediction and quasi-static model prediction, indicating that the effect of inertia is not significant in the dynamic system in terrestrial swimming.

To quantify the effect of inertia, we tested the locomotion performance of the multi-legged system ($\Theta_{body} = \pi/3$, $\Theta_{leg} = 0$, $m = 6$) under different temporal frequencies (Figure 6.2a). We showed that despite the changes in absolute speed (ranging from ≈ 15 cm/s to 1.5 cm/s), the step length is almost constant. Furthermore, we tested the locomotion performance of the multi-legged systems ($\Theta_{body} = \pi/3$, $\Theta_{leg} = 0$, $m = 6$) on different surfaces ranging from coarsely fabricated wood ($\mu \sim 0.6$) to coated smooth surfaces ($\mu \sim 0.1$). In all surfaces, swimming motion converged to the steady-state equilibrium velocity within in one gait cycle. (Figure 6.2b).

We posited that such convergence to steady-state equilibrium velocity can be a result of an emergent friction-velocity negative feedback. To explore this force-velocity relationship, we tested the locomotion performance on slopes. Specifically, by varying the slope tilting angle α , we can measure the relationship between the external force $\tan \alpha$ (normalized by nominal friction μN) and the step length (body length traveled per cycle). We tested two undulatory gaits with different spatial wave numbers ($\Theta_{body} = \pi/3$, $\Theta_{leg} = 0$, $m = 6$, $\xi = \{1, 1.3\}$). In both cases, we observed a locally negative linear relationship (Fig. Figure 6.2c) between external force and the step length. The emergence of such negative linear relationship not only explains the convergence, but also raises an intuiting concept: effective viscous friction emerged from terrestrial swimming with Coulomb friction. In the next sections, we will further analyze and model such emergent negative linearity.

¹We posited that it is the static friction that leads to the discrepancy between the empirically measured and model predicted transient response

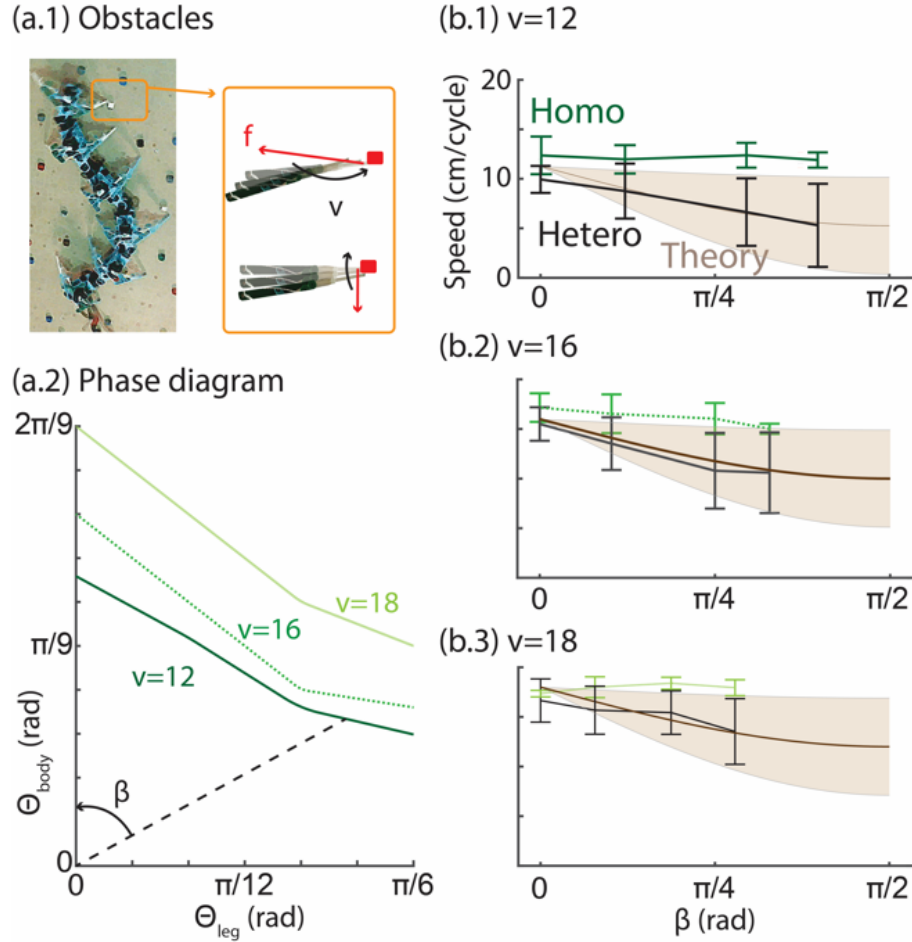


Figure 6.5: **Advantage of body-dominated terrestrial swimming in obstacle-rich environments** (a.1) A snapshot of robot ($n = 6$) moving on obstacle-rich environments ($\rho = 0.06$). Cartoon illustration of interaction between robot and obstacles subject to different slipping directions (*top*: typical body-dominated; *bottom*: typical leg-dominated). Red blocks represents obstacles, legs from darker color to lighter color represents progression of time. (a.2) We choose three isoheight lines on the velocity heat-map over the performance space: $v = 12$ cm/cycle, $v = 16$ cm/cycle, and $v = 18$ cm/cycle. We quantify the degree of body and leg use by $\beta = \tan^{-1}(\Theta_{leg}/\Theta_{body})$. (b) Comparison of locomotion performance in homogeneous (curves with error bar in green colors), heterogeneous environments (curves with error bar in black color), and theoretical predictions from Equation 6.6 (curves and areas in light brown color). From top to bottom the flat line descended from isoheight lines with $v = 18$ cm/cycle, $v = 18$ cm/cycle, and $v = 18$ cm/cycle.

Effective viscous friction

Slipping analysis

Similar to locomotion at low Reynolds number, we consider terrestrial swimming as a body undulatory system with assistance from the periodic leg lifting and landing. As documented

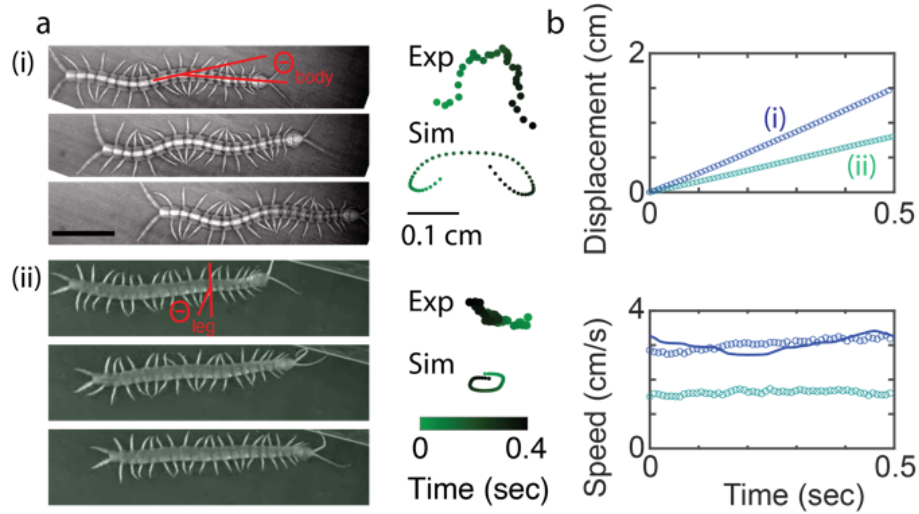


Figure 6.6: **Analysis of centipede locomotion** (a) (*left*) Snapshots of a trial of (i) body-dominated and (ii) leg-dominated centipede locomotion. (*right*) The trajectory of foot slipping colored by time. The stance phase spans 0.4 seconds. Trajectory of centipede body during terrestrial swimming colored by time. (b) The (*top*) displacement and (*bottom*) velocity profiles. Measured animal data is presented in cycles and the predictions from quasi-static model is presented in blue curve.

in prior work on locomotion at low Reynolds number [115, 228], the drag anisotropy of slender rods (higher reaction forces in the perpendicular than in the parallel direction) is the critical physical property enabling swimming in viscous flows. In terrestrial environments where the drag force is typically assumed isotropic Coulomb friction, the direct implementation of undulatory motion would be ineffective [148].

In Coulomb friction, the direction of ground reaction forces should be opposite to the direction of slipping. Therefore, it is crucial to investigate the direction of slipping. Unlike other legged systems with fewer legs, there is significant slipping during undulatory locomotion of the multi-legged robot. We predicted from the quasi-static model that in body-dominated gaits, the direction of slipping is predominantly in the lateral direction. We verified this prediction by tracking the trajectory of the tip of a foot (second foot from the left) and empirically measuring the direction of the slipping ($\Theta_{body} = \pi/3$, $\Theta_{leg} = 0$, $n = 6$). Both simulation and experiment suggested that slipping in lateral/medial direction (perpendicular to the direction of motion, Figure 6.1) dominates over the slipping in ante-

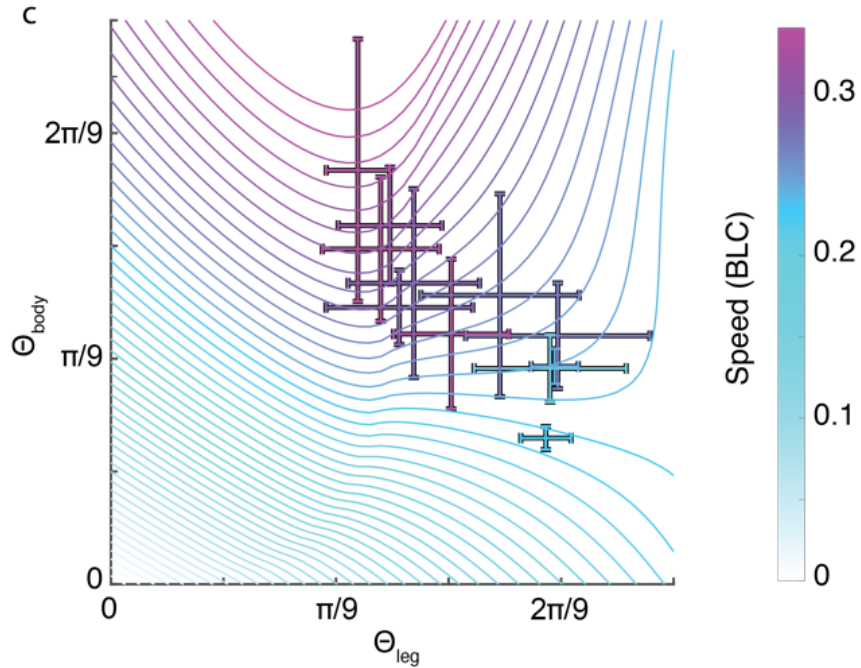


Figure 6.6: **Analysis of centipede locomotion** (c) The transition from leg-dominated gaits to swimming dominated gaits as speed increases. In each centipede locomotion trial, we extract amplitude of body undulation and leg retraction, and represented it as a cross (colored by its speed) on performance space.

rior/posterior (parallel to the direction of motion) direction (Figure 6.3). We quantified the direction of slipping by measuring the slipping angle Ψ , defined as the angle between the direction of slipping and the medial direction. We compared the experimentally measured and simulation predicted time series of slipping angle in Figure 6.3a.ii, and both suggest that the direction of foot slipping is almost always perpendicular to the direction of motion ($\Psi = 0$ or π). Finally, we showed the slipping angle profile from numerical simulation in Figure 6.3a.iii. We noticed that for almost all feet, the slipping angle is distributed around either 0 or π , both suggesting lateral/medial slipping.

Kinematic model

With the knowledge of lateral/medial dominated slipping, we developed a theoretical model to illustrate how periodic leg lifting and landing can acquire drag anisotropy similar to locomotors in viscous flow.

As documented in prior work on undulatory locomotion, each body segment experiences oscillation in the lateral and rotational directions with an offset of $\pi/2$ [123, 83]. Specifically, d , the distance from the body to the central body axis can be expressed as: $d(\tau) = d_m \sin \tau$, where d_m is the magnitude of lateral oscillation and $\tau \in [0, 2\pi)$ is the gait phase; θ , the angle between the body orientation and the direction of motion can be expressed as $\theta(\tau) = \theta_m \cos \tau$, where θ_m is the magnitude of rotational oscillation (Figure 6.1a). θ_m and d_m are determined by the amplitudes, (Θ_{leg} and Θ_{body}) and the spatial wave number (ξ) of body undulation. From geometry, we know that $d_m = n\Theta_{body}/(2\pi\xi)^2$, and $\theta_m = \Theta_{leg} + \tan^{-1}(n\Theta_{body}/(2\pi\xi))$.

To simplify our analysis, we assume that the center of geometry (CoG) of the robot has a constant forward velocity, v . The velocity of a foot (for simplicity, we only discussed the right feet. The analysis of left feet will be symmetric to our analysis) can then be expressed as a joint effect of CoG movement and the lateral/rotational oscillation:

$$\begin{aligned} v_x(\tau) &= \dot{d}(\tau) + l\dot{\theta}(\tau) \sin(\theta(\tau)) \\ v_y(\tau, v) &= v + l\dot{\theta}(\tau) \cos(\theta(\tau)) \end{aligned} \quad (6.1)$$

where v_x and v_y are velocity components in the lateral and anterior directions respectively; l is the leg length. Friction should have the opposite direction to the direction of foot slipping. Thus, the projection of the instantaneous frictional force to the anterior direction is:

$$f_y(\tau, v) = -\mu N \sin\left(\tan^{-1}\left(\frac{v_y(\tau, v)}{v_x(\tau)}\right)\right) \quad (6.2)$$

where μN is the magnitude of friction determined by normal force N and friction coefficient μ . Assuming that each of contralateral foot is in contact with the substrate for half of a

period (e.g., $s_1 < \tau < s_1 + \pi$), we can calculate the average friction over the stance phase:

$$\bar{f}(v) = \int_{s_1}^{s_1+\pi} -\mu N \sin\left(\tan^{-1}\left(\frac{v_y(\tau, v)}{v_x(\tau)}\right)\right) d\tau \quad (6.3)$$

We can calculate the steady-state CoG velocity, v_{ss} , by assuming the force in equilibrium ($\bar{f}(v_{ss}) = 0$). By the force balance ($\bar{f}(v_{ss}) = 0$), we established an implicit function $v_{ss} = v_{ss}(s_1)$. Furthermore, we took a variational approach to find the optimal stance period $[s_1, s_1 + \pi]$ to maximize v_{ss} (i.e., $dv_{ss}/ds_1 = 0$). The sufficient condition for s_1 (to optimize v) is then:

$$\sin\left(\tan^{-1}\left(\frac{v_y(s_1 + \pi)}{v_x(s_1 + \pi)}\right)\right) = \sin\left(\tan^{-1}\left(\frac{v_y(s_1)}{v_x(s_1)}\right)\right), \quad (6.4)$$

Solving Equation 6.4 yields two optima: $s_1 = 0$, $s_1 = \pi$. They correspond to maximal v_{ss} (highest forward speed) and minimal v (highest backward speed) respectively. In other words, by properly controlling the sequence of lifting and landing, we can effectively acquire drag anisotropy in either direction and therefore enable swimming along (direct wave [43]) and against (retrograde wave [43]) the direction of wave propagation. Interestingly, $s_1 = 0$ also optimizes body-leg coordination as reported in [234] where the body undulation is considered to assist leg retraction. In this paper, we only considered the retrograde-wave terrestrial swimming. Thus we set $s_1 = 0$ unless otherwise discussed.

Since slipping is primarily in the lateral direction, we assume $v_x \gg v_y$. We can therefore calculate the changes in friction in response to disturbance to steady state velocity ($v = v_{ss} + \delta_v$):

$$\begin{aligned}
f_y(\tau, v_{ss} + \delta_v) &= -\mu N \sin\left(\tan^{-1}\left(\frac{\delta_v + v_y(\tau, v_{ss})}{v_x(\tau)}\right)\right) \\
[\because v_x \gg v_y] \quad &\approx f_y(\tau, v_{ss}) - \mu N \sin\left(\tan^{-1}\left(\frac{v_{ss}}{v_x(\tau)}\right)\right) \frac{\delta_v}{v_{ss}},
\end{aligned}$$

Integrating over the stance period, we can obtain the changes of the average friction:

$$\begin{aligned}
\underbrace{\bar{f}(v_{ss} + \delta_v)}_{\bar{f}_d(\delta_v)} &= \underbrace{\bar{f}(0)}_0 - \delta_v \underbrace{\int_0^\pi \frac{\mu N}{v_{ss}} \sin\left(\tan^{-1}\left(\frac{v_{ss}}{v_x(\tau)}\right)\right) d\tau}_{\gamma_0} \\
\bar{f}_d(\delta_v) &= -\gamma_0 \delta_v
\end{aligned} \tag{6.5}$$

The effective linear force-velocity relationship allows us to analyze the terrestrial swimming similar to that in viscous fluid. Despite being counter-intuitive with Coulomb friction, Equation 6.5 predicts that this equilibrium is asymptotically stable. Note that our analysis is invariant to the choice of foot. Equation 6.3 and Equation 6.5 can thus be generalized to the overall multi-legged system by a scaling factor of n (the number of leg pairs).

To verify our analysis, we compared predictions from Equation 6.5 and the experimental measurement in Figure 6.2c, and we observed good agreement between theory and experiments, especially locally near equilibrium.

Performance space

As discussed earlier, both body undulation and leg retraction can contribute to generate thrust in multi-legged systems. To systematically explore the coordination and balance of body and leg, we introduced a performance space (Figure 6.4) where the axes are Θ_{leg} , the amplitude of leg retraction, and Θ_{body} , the amplitude of body undulation. Depending on the relative magnitude of Θ_{body} and Θ_{leg} , we soft classify the performance space into (1) body-dominated ($\Theta_{body} \gg \Theta_{leg}$), (2) hybrid ($\Theta_{body} \sim \Theta_{leg}$), and (3) leg-dominated ($\Theta_{body} \ll \Theta_{leg}$).

Note that competition exists between high Θ_{body} and high Θ_{leg} since it will lead to self-collision among legs which can break the robot. In previous discussions, we focused on body-dominated terrestrial swimming regime of the performance space. The conventional leg-dominated counter-part experiments ($\Theta_{body} = \pi/3$, $\Theta_{leg} = 0$, $n = 6$) are provided in Figure 6.3b. Note that the slipping in conventional leg-dominated gaits is significantly lower than those in body-dominated terrestrial swimming.

To systematically explore the competition and coordination between body undulation and limb reduction, we experimentally tested the locomotion performance of different points on the performance space. Figure 6.4a shows a heat-map of speed over performance space for robots with 4 (Figure 6.4a. *left*) and 8 (Figure 6.4a. *right*) pairs of legs. Immediately, we noticed that for systems with different leg pairs, the optima reside in different regimes. For robots with 4 pairs of legs, a hybrid mode of body undulation and leg retraction can lead to the highest speed. On the other hand, for robots with 8 pairs of legs, pure body-dominated terrestrial swimming ($\Theta_{leg} = 0$) can lead to the highest speed. This is also evidenced by the gradient of iso-height contours. To further quantify the transition, we identified the optima $[\Theta_{leg}, \Theta_{body}]$ for robots with 3, 4, 5, 7, and 8 pairs of legs. Note that we numerically determine the optima as over 90 percentile of the step length among all gaits. We then colored the optima $[\Theta_{leg}, \Theta_{body}]$ by the number of leg pair n . From Figure 6.4b, we observe that the optima transition from leg-dominated to body-dominated as the number of leg pairs increases.

Interaction with obstacles

In this section, we further explored the relative advantage of body-dominated and leg-dominated gaits in obstacle-rich environments. We posited that the slipping direction plays an important role in the interaction with obstacles; and that the body-dominated gaits (with lateral/medial slipping) are more robust over the presence of obstacles as compared to the leg-dominated gaits (with anterior/posterior slipping).

In Figure 6.3. we compared the direction of slipping for leg-dominated and body-dominated gaits. Specifically, slipping in leg-dominated gaits almost always occurs first in the anterior direction (the direction of motion) then follows in the posterior direction. This chronological order of slipping can affect the interaction with terrain heterogeneity (obstacles). In other words, the interaction between a leg and an obstacle is more likely to occur during the preceding slipping than the succeeding slipping. The interactions between obstacles and the preceding anterior slipping feet are in the posterior direction, which can be detrimental to locomotion. Thus, qualitatively, we predict that the terrain heterogeneity will reduce the locomotion performance of conventional leg-dominated gaits. On the other hand, in body-dominated gaits, feet slip in lateral/medial directions, which reactions from interactions with obstacles are also in medial/lateral direction and will not affect the locomotion performance in the direction of motion.

To verify this prediction, we constructed a heterogeneous environment (low-height obstacles randomly distributed on a flat terrain, see [235]) and tested the locomotion performance of different gaits in the multi-legged system ($n = 6$). We identified three iso-height lines on the performance space such that all points on an iso-height line have the same step length on homogeneous environment. We chose the iso-height lines with $v = 12$, $v = 16$, and $v = 18$ (unit cm/cycle). We quantified the degree of body and leg use by the angle $\beta = \tan^{-1}(\frac{\Theta_{leg}}{\Theta_{body}})$. Interestingly, we noticed that gaits with low β had almost the same step length in heterogeneous environments as in homogeneous environments. However, gaits with high β had significantly reduced step length in heterogeneous environments.

To better understand the robustness of gaits in heterogeneous environments, we established a simple statistical model. To simplify the analysis, we approximated the slipping angle Ψ (Figure 6.3) by β such that $\Psi = 0$ during body-dominated terrestrial swimming ($\beta = 0$) and $\Psi = \pi/2$ during conventional leg-dominated terrestrial swimming ($\beta = \pi/2$). Assume that the reaction force from terrain heterogeneity is a constant, F . Then the projection of reaction force in fore-aft direction can be approximated by $F \sin(\beta)$.

Consider an obstacle-rich environment with obstacle density ρ and a robot with n pairs of legs, then the distribution function of at least one leg interacts with an obstacle is $h(y) = \{1 \text{ if } y < n\rho; 0 \text{ if } y \geq n\rho\}$, where $y \sim U(0, 1)$, U is the uniform distribution. Thus the distribution function of the projection of reaction force in fore-aft direction is $Fh(y) \sin\beta$. From Equation 6.5, the distribution function of step length is:

$$\begin{aligned} v &\sim v_{ss} - \gamma_0^{-1} F \sin(\beta) h(y) \\ \bar{v} &= v_{ss} - \gamma_0^{-1} F (1 - n\rho) \sin(\beta) \\ \text{std}(v) &= \gamma_0^{-1} F \sqrt{n\rho(1 - n\rho)} \sin(\beta), \end{aligned} \tag{6.6}$$

where γ_0 is the effective drag coefficient from Equation 6.5. We observe quantitative agreement between the theoretical prediction and the experiments (Figure 6.5).

Biological centipedes

Biological centipedes can properly coordinate their body and leg movement and rapidly traverse different terrestrial environments [43, 202, 195, 236]. However, there have been limited biomechanical analysis on centipede locomotion. In many existing works, it is often assumed that there is no foot slipping [237, 211, 184]. Here, we use our framework to study the slipping in the rapid-moving biological centipedes.

We predict from our drag anisotropy analysis (solving Equation 6.3) that body-dominated gaits should be a faster mode of locomotion as compared to leg-dominated (Figure 6.6 the underlying heatmap). The model predicts that at high Θ_{body} , low Θ_{leg} , centipedes could maintain high-speed steady-state motion by having feet slipping laterally/medially. However, if Θ_{leg} is increased, it will introduce unwanted anterior/posterior slipping, which can break the symmetry in the steady-state swimming motion and therefore is detrimental to locomotion.

To verify such prediction, we studied the locomotion performance of a biological cen-

tipede (*Scolopendra polymorpha*, 5 individual, in total 11 trials) and quantitatively characterized the leg dynamics under different speeds. Specifically, we collected high speed video recordings of centipedes moving on white board. We extracted the amplitude of body undulation (A_{body}) and leg movements (Θ_{leg}), and the speed (in the unit of body length per cycle) from each trial (presented by colored cross in Figure 6.6c). We noticed that the emergence of body undulation is accompanied by the decrease in Θ_{leg} . This indicates that in response to high speeds, the behavior of these centipedes is beyond just the emergence of body undulations. Instead, there is a transition of leg-dominated gaits (high Θ_{leg} , low Θ_{body}) to body-dominated gaits (low Θ_{leg} , high Θ_{body}), in quantitative agreement with our prediction.

Further, we use our model to study the kinematics behind centipede locomotion. Similar to our analysis on the robot, we compared a body-dominated gait (Figure 6.6a.i) and a leg-dominated gait (Figure 6.6a.ii) in biological centipedes. We then investigated the direction of foot slipping for both cases. Interestingly, we observed that the slipping is extensive and mostly in lateral (medial) direction for the body-dominated gait; and the slipping is reduced and in anterior/posterior direction for leg-dominated gait. Finally, we showed the displacement and velocity profile for both body-dominated and leg-dominated gaits in Figure 6.6b and that our quasi-static model can give a quantitative predictions of the velocity profile for the relatively high-speed (~ 0.5 BL per second) centipede terrestrial swimming. In this way, we showed that our terrestrial swimming analysis can be applied to rapid-moving systems, providing alternative solutions to the potential agile robots.

Conclusions

Locomotors on solid substrates typically rely on leg retraction to generate thrust, whereas locomotors on continuous media typically use body undulation for propulsion. Often, these are considered two distinct locomotive behaviors. One of key differences lies in the interaction with substrates. In continuous media, each body segment experiences continuous

reaction forces, which allows us to analyze reaction forces and therefore locomotion dynamics using RFT. It not only analyzes the biological systems, but also provides guidelines to robot controls. However, because of the discontinuous and nonlinear reaction force, the application of RFT to terrestrial locomotion is limited.

The discontinuous and nonlinear reaction force is often caused by the no-slipping condition. Slipping during terrestrial locomotion has been considered detrimental to locomotion because it can be energetically inefficient and cause unstable oscillation [20, 229, 230]. Therefore, in both biological and artificial locomotors, slipping is often actively avoided [20, 229, 230, 231]. For these systems, complicated feedback control is often required to maintain the no-slip condition [230, 231]. However, many biological locomotors, for example cockroaches [238] and centipedes, can acquire high-speed stable locomotion with the presence of extensive foot-slipping. Despite the interesting slip-driven locomotion, the mechanism of such locomotion is less studied.

Here, we studied slipping in terrestrial locomotion using an RFT framework. Specifically, we studied slipping in terrestrial swimming, and established a framework to analyze the causal relationship between slipping and locomotion performance. Furthermore, our framework connected the studies of locomotion in continuous media to terrestrial environments. Specifically, we showed that by properly controlling the lifting and landing of contralateral feet (and thus the slipping direction), terrestrial locomotors can acquire drag anisotropy and effective viscous friction in the environments dominated by isotropic, rate-independent Coulomb friction.

Finally, we systematically compared the performance of slip-driven (body-dominated) locomotion and the reduced slipping (conventional leg-dominated) locomotion. We noticed that the advantage of body-dominated swimming in continuous media (the capability to benefit from terrain heterogeneity to aid locomotion [239, 150, 240, 241]) preserved in terrestrial environments. Specifically, we established a performance space of terrestrial swimming, and compared its performance in homogeneous and heterogeneous environments by

robophysical experiments. Further, we used our framework to discover and rationalize the relationship between the slipping and behavior in biological multi-legged locomotors. In doing so, we discovered a new regime of effective locomotion in terrestrial environments revealing its advantage in high-speed regime and in obstacle-rich environments.

CHAPTER 7

A SHANNON-INSPIRED FRAMEWORK FOR MULTI-LEGGED MATTER TRANSPORT

Part of this chapter is adapted from a journal article under review “A Shannon-inspired framework for multi-legged matter transport.” *Science*. My contribution in this project includes (1) designing the experiments, (2) conducting the numerical analysis, (3) writing the manuscript. Robophysical experiments presented in this chapter are conducted by Juntao He.

The transmission of information over distance has played an increasingly important role in human history [242]. Early on, information was often transmitted with physical matter (e.g., carrier pigeons) as the medium. With the emergence of analog or digital signal transmission channels (e.g., drum beat patterns, electrical transmission lines, and space-based links) information transmission was decoupled from matter transportation. Over a noiseless channel, a continuous analog signal is in principle sufficient for effective information transmission [243]. Despite its efficiency, the establishment of such error-free channels can be expensive. To counter channel noise inherent in all communication modalities, Shannon [112] constructed a digitized encoding scheme, in which a core concept is to “buffer” and correct the transmission error via redundancy (Fig. Figure 7.1a). Specifically, a signal is first encoded into redundant digital *bits* to transmit through a noisy channel, then these channel-noise contaminated bits are decoded to recover the original signal. Note that such signal transmission strategy of *error correction coding* (correction via redundancy) is an alternative to *error detection coding*, where in the latter, the presence of a reverse channel can facilitate the re-transmission of signals, thereby improving signal transmission accuracy [112, 242].

The transport of physical matter is another important aspect in human society, biologi-

cal systems, and increasingly in physics in the form of “active matter” [244]. Locomotion as a means of matter transport has been thoroughly studied in various forms [1, 2, 3, 4], where a core concept is to actively generate thrust against drag to develop “self-propulsion”. Thrust is typically generated from interactions between locomotors and surrounding substrates, and heterogeneous substrate structures can cause interference. On land, to counter substrate heterogeneity and its effect on locomotion, humans have built costly platforms (such as tracks and roads) where continuous thrust can be reliably generated from continuous substrate-contact. In particular, the conveyance arising from wheels on tracks or roads is believed to be one of the most efficient terrestrial matter transportation schemes [5]. Similar to analog signal transmission, matter transportation with continuous thrust relies heavily on the homogeneity of the established platforms (Fig. Figure 7.1b) and thus general principles governing more complex terrestrial environments are lacking [14, 13].

In environments where construction of low-noise “channels” is inconvenient, researchers have either increased the size of the wheels [14] or have developed appendage based self-propulsion (e.g., legged locomotion). A properly-coordinated leg lifting and landing scheme offers the potential to simplify self-propulsion from the complexity of natural “terradynamic” [74] interactions. However, it is generally believed that environmental awareness is necessary to exploit such potential [70, 245]. State-of-the-art robots with legs are mostly bipedal and quadrupedal systems, and their increasingly agile locomotive performance relies heavily on accurate sensors [3, 111]. Specifically, sensor-based closed-loop controls enable environmental awareness which facilitates appropriate selection of feasible substrate-contact points to counter the uncertainty from the substrate [3, 111, 70, 245]. Note that a sensor-based framework in locomotion shares a mechanism similar to error detection coding in information theory where the framework relies on an accurate re-transmission channel.

To locomote effectively on legs with minimal sensing and environmental awareness (effective open-loop locomotion), increasing the number of legs can be beneficial. That is,

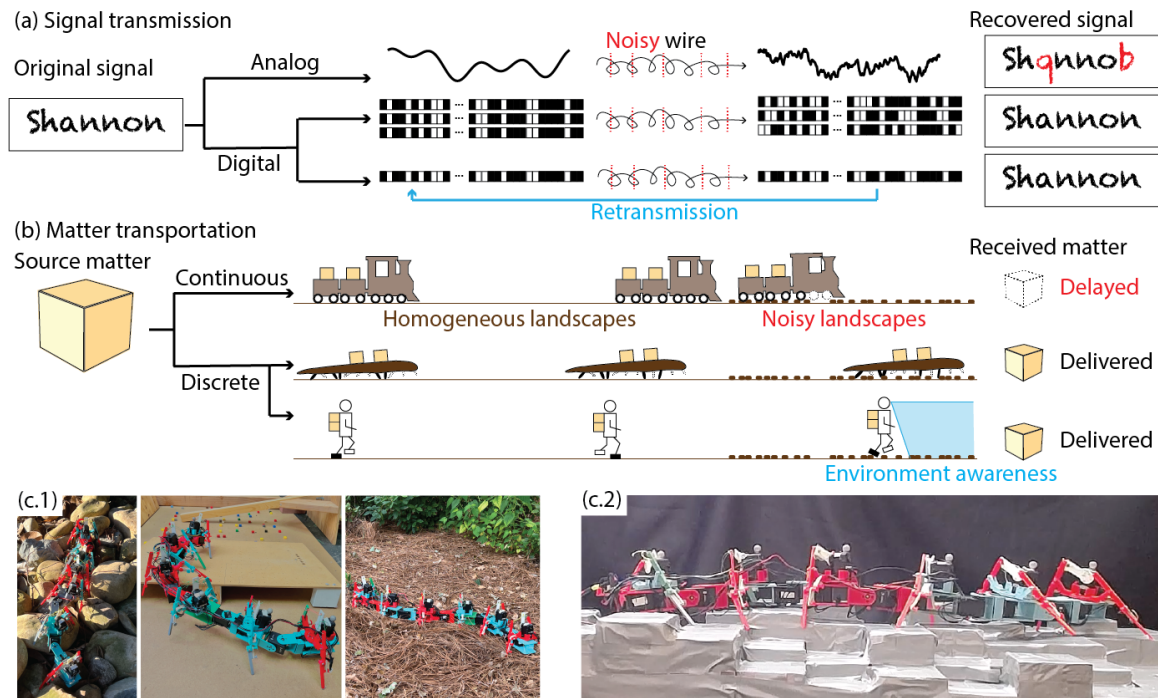


Figure 7.1: **An analogy between signal transmission and matter transportation.** (a) The flowchart of signal transmission. We compare analog and digital signal transmission through noisy wires. Digital redundant signal allows reliable transmission through a noisy wire via either redundancy or a re-transmission channel. (b) Matter transportation with both continuous and discrete active contacts can be effective on perfect tracks. Discrete redundant contacts enable robust matter transportation over rugose tracks via redundancy or environmental awareness. (c) Multi-legged robophysical locomotors traverse noisy landscapes: (c.1.*left*) pebbles, (c.1.*middle*) stairs and slopes, (c.1.*right*) entangled granular media, and (c.2) a laboratory model of rugose terrain.

in recent years hexapods have become an intriguing alternative to bipedal and quadrupedal robots over noisy landscapes [4]. If properly coordinated, the additional legs in hexapods provide additional ground supports to avoid catastrophic failures (e.g., loss of stability). However, terrain heterogeneity can still cause thrust deficiency which significantly reduces the locomotion performance [246, 247]. Therefore, although to a lesser extent than in bipedal or quadrupedal systems, sensors in hexapods are also believed to be essential [248, 249]. Our recent work on design, construction [212] and control [235] of myriapod robots with up to 16 legs has demonstrated remarkable progress towards robust open-loop operations in diverse environments [250]. However, it remains unclear what mechanism drives such robustness and, more importantly, whether redundancy in leg numbers can be gener-

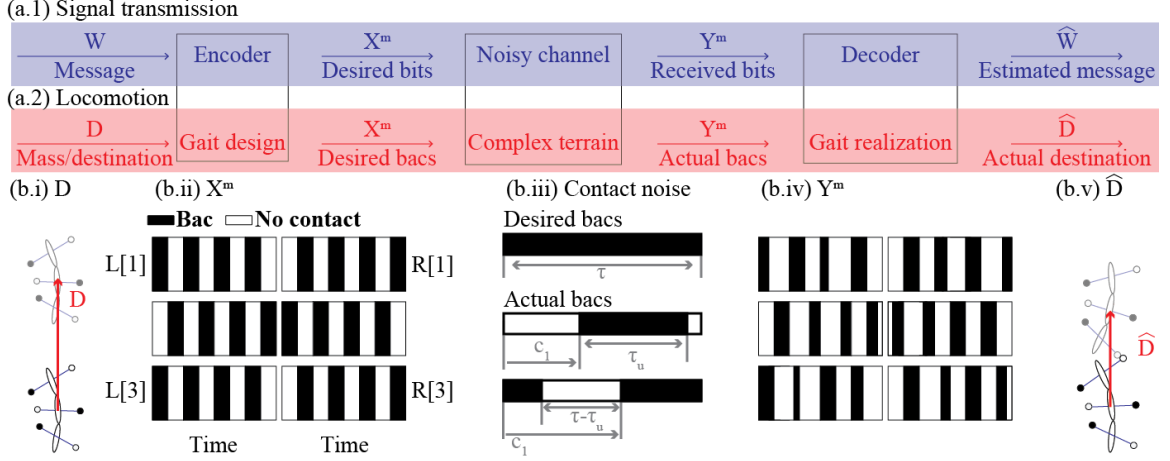


Figure 7.2: **Encoding and decoding of signal transmission and matter transportation.**

(a) The analogy of (a.1) signal transmission (adapted from [112]) and (a.2) locomotion (matter transportation). (b.i) The matter to be transported to a destination D . (b.ii) The desired bac sequence to reach the locomotion destination. (b.iii) Noisy landscapes can introduce contact errors such as delaying bacs and shortening the duration of bacs. We labeled the desired bac (spans the duration of τ) and two terrain-contaminated bacs (starts at c_1 with duration τ_u). (b.vi) The actual bac sequence (contaminated by contact errors). (b.v) The actual locomotion destination \hat{D} .

ally sufficient to counter the terrain noise for self-propulsion or some environmental awareness would be necessary.

Inspired by the principles which facilitate signal transmission on noisy channels, we hypothesize there exist general principles of matter transportation by which, for a complex terradynamic task, we can “guarantee” that multi-legged robots can self-transport over distance with error rate (e.g., loss of stability or thrust deficiency) arbitrarily close to zero, even without environmental awareness. To explore such principles, we develop a general framework of locomotion, analogous to that of signal transmission [112]. Our analogy proceeds as the following (Fig. Figure 7.2): consider a matter transportation task to deliver some payload to a specific destination D . To enable robust matter transportation, thrust generation is digitized into what we will refer to as basic active contacts (*bacs*, our analogy to bits), discrete units of active environmental interaction, such as legs [15] and vertical waves of contact in limbless robots [16]. We quantify the temporal and spatial distribution of bacs as a sequence X^m . As the locomotor implements the desired bac sequence in

a noisy landscape (the analogue of a noisy channel), the terrain uncertainty can introduce contact noise to the actual bac sequence, Y^m . Such contact noise can therefore lead to a discrepancy between the actual destination \hat{D} and the desired destination, D . This chapter aims to bound the uncertainty in such discrepancy by the redundancy in bacs.

A terrestrial terrain can have different types of heterogeneities with different terradynamic bac interactions [74]. Consider a terrain given by a height map, $h(x, y)$. Depending on the scale of the gradient, $[\partial h/\partial x, \partial h/\partial y]$, the terrain heterogeneity can interfere with the locomotion in the form of slopes, walls, or obstacles (Fig 1c), which directly affect the thrust-generation process in the plane parallel to the terrestrial surface. As discussed in prior work [250], parallel thrust disturbances could be minimized by proper design of mechanical structures or passively compliant mechanisms. Here, we focus a class of noisy landscapes (rugose terrains) where the height distribution, $h(x, y)$, can affect the supporting force distribution (e.g., missing steps) in directions perpendicular to the terrestrial plane: $Y^m = X^m + X_u^m$, where X_u^m is the contact noise emerging from interaction between carriers and rugose terrains.

We first consider an abstract characterization of thrust generation with one pair of legs. We quantify the instantaneous thrust over a bac, $f(t)$, as the instantaneous external force required to keep the locomotor in place at time $t \in [0, \tau)$, where τ is the duration of the bac. The nominal average thrust in open space is: $f_n = \frac{1}{\tau} \int_0^\tau f(t) dt$.

Next we introduce a function which encapsulates the uncertainty in the bac, $c(t)$. The terrain-disturbed thrust can be formulated by $\tilde{f} = \frac{1}{\tau} \int_0^\tau c(t) f(t) dt$. We assume $c(t)$ has the property $\frac{1}{\tau} \int_0^\tau c(t) dt = 1$, so that the supporting force balances gravity. Further, we assume that the initiation of a bac is delayed by time c_1 , and the duration of a bac is shortened to τ_u : $\{c(t) = 0, t \notin [c_1, c_1 + \tau_u]\}$. Specifically, c_1 is assumed to be a random variable from a uniform distribution: $c_1 \sim U(0, \tau)$; and the duration of the bac, τ_u , is assumed to be a random variable determined by the terrain uncertainty. Here we sample τ_u from the cumulative distribution function given by $G(\tau_u) = (1 - b)\tau_u/\tau + b$, $\tau_u \in [0, \tau]$ so that

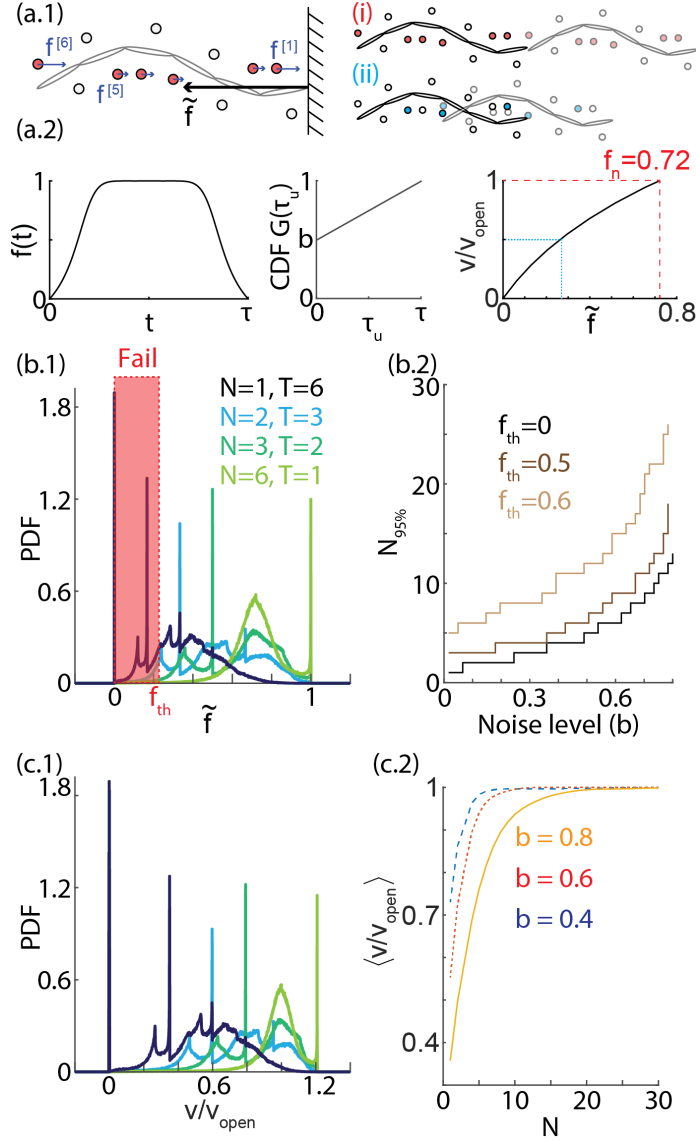


Figure 7.3: **Numerical verification of the sufficiency to bound contact errors via redundancy.** (a.1) (*Left*) An illustration of thrust generation from backs. (*Right*) Illustrations of the relationship between thrust and velocity. Self-propulsion with (i) nominal contact and (ii) contact errors are compared. (a.2) (*Left*) The instantaneous thrust $f(t)$ as a function of time, derived from [235]. (*mid*) The cumulative distribution function of τ_u . (*Right*) The thrust-velocity (normalized by nominal velocity) relationship. (b.1) The numerical histogram of terrain-disturbed thrust for robots with different combinations of temporal (T) and spatial (N) redundancy. (b.2) Numerically calculated $N_{95\%}$, the minimal number of leg pairs to facilitate successful locomotion with 95% confidence interval (CI), plotted against noise level (b). (c.1) The numerical distribution of velocity for robots with different spatial and temporal redundancy. The color schemes are identical to (b.1). (c.2) The numerically calculated expected average velocity plotted as a function of the number of leg pairs.

there is a finite probability of complete bac loss: $p(\tau_u = 0) = b$, and $b < 1$ characterizes the contact noise level. As we will discuss later, the contact noise level can give us an approximation to the rugosity of the terrain. Note that in case where $c_1 + \tau_u > \tau$, we extend the excessive contact duration ($c_1 + \tau_u - \tau$) over into the next bac (Fig. Figure 7.2.b.iii and SI section IV). For simplicity, we assume that $c(t)$ is otherwise uniformly distributed during the bac: $\{c(t) = \tau_u^{-1}\tau, t \in [c_1, c_1 + \tau_u]\}$. In this way, the terrain-disturbed thrust reduces to: $\tilde{f} = \text{sign}(\tau_u)\tau_u^{-1}f_u$, where $f_u = \int_{c_1}^{c_1+\tau_u} f(t)dt$ is the thrust disturbance. The sign function $\text{sign}(\tau_u)$ indicates that no thrust will be generated ($\tilde{f} = 0$) with complete bac loss ($\tau_u = 0$).

Taking the analogy from information theory in which redundant bits can bound the uncertainty from channel noise, we hypothesize that locomotors with redundant bacs can offer robustness over terrain uncertainty. The direct practice would be the simple repetition over multiple periods (temporal redundancy):

$$\tilde{f}_T^{[1]} = \frac{1}{T} \sum_{i=1}^T \text{sign}(\tau_u^i) \frac{f_u^i}{\tau_u^i}, \quad (7.1)$$

where $\tilde{f}_T^{[1]}$ is the average generated thrust over T periods, τ_u^i and f_u^i are the contact and thrust disturbance respectively over the i -th period. T here represents the order of temporal redundancy. We expect the variance of the generated thrust, $\sigma^2(\tilde{f}_T^{[1]})$, to decrease as T increases. Further, $\tilde{f}_T^{[1]}$ converges to a Dirac delta function as T approaches infinity (proof given in the SI, section VII). Moreover the expected average generated thrust, $\langle \tilde{f}_T^{[1]} \rangle$, remains constant (Central Limit Theorem). Such direct repetition could be inefficient because of its low code rate ¹, as per the information theory paradigm [242]. In analogy to Shannon’s encoding scheme, we now develop a framework to remove inefficient redundancy and compensate it with “redundancy of the right sort” [242, p. 164] for more effective locomotion.

Subtly different from the signal transmission over a noisy channel, redundancy in locomotion can also exist in the spatial domain. The spatial-domain redundancy is important because it can facilitate the simultaneous “communication” among bacs in response to con-

¹The ratio between useful information symbols and actual transmitted symbols [242]

tact noise. Specifically, with proper coordination, the effect of contact noise will be shared by all bacs instead of acting on an individual bac. Effectively, the spatial-domain redundancy can serve as a moving average filter over the contact noise. To develop a specific scenario for legged systems, we consider spatial redundancy in the form of repeating serially connected modules, where a module is defined as a pair of legs. For simplicity, we consider a simple module coordination that the instantaneous thrust $f(t)$ on each module is identical and invariant to the number of modules. The average thrust generated from N serially connected modules over T periods is:

$$\tilde{f}_T^{[M]} = \frac{1}{T} \sum_{i=1}^T \left(\text{sign} \left(\sum_{j=1}^N \tau_u^{ij} \right) \frac{\sum_{j=1}^N f_u^{ij}}{\sum_{j=1}^N \tau_u^{ij}} \right), \quad (7.2)$$

where τ_u^{ij} and f_u^{ij} are disturbances on j -th module over i -th temporal repetition. Intuitively, in the case where there are M complete bac losses in i -th temporal repetition, $M = |\{j, \tau_u^{ij} = 0\}|$, the locomotor with N modules will essentially reduce to the that with $N - M$ modules. In other words, locomotors with N spatial redundancy can afford up to $N - 1$ complete bac losses without significant thrust deficiency, indicating that spatial redundancy can also serve to bound the uncertainty in thrust generation. We show that with arbitrary $T \geq 1$, $\tilde{f}_T^{[N]}$ will also converge to a Dirac delta function as spatial redundancy N approaches infinity (proof in SI, section VII). Further, the expected average thrust generated, $\langle \tilde{f}_T^{[M]} \rangle$, can be approximated by $(1 - b^N)C_s$ where C_s is a constant determined by $f(t)$ and b (proof in SI, section VII). Therefore, greater spatial redundancy not only reduces variance but also improves the expected average generated thrust, a feature otherwise not feasible with only temporal redundancy.

To illustrate our prediction, we choose a module coordination pattern simplified from observations in biological centipedes [235] such that the instantaneous thrust $f(t)$ is independent of our choice of spatial redundancy (proof in SI section IV). We illustrate $f(t)$ in Fig. Figure 7.3.a.2 with nominal thrust $f_n = 0.72$. Assuming $b = 0.5$, we compare the

distribution of \tilde{f} for different combinations of temporal and spatial redundancy in Fig. Figure 7.3.b.1. Note that in this example, $C_s = f_n$, indicates that the terrain-disturbed thrust will converge to nominal thrust given sufficient spatial redundancy.

Considering drag in terrestrial locomotive systems, effective self-transportation often requires a minimal threshold thrust, f_{th} . The source of threshold thrust can be frictional drag which is a first approximation for terradynamic interactions. We define locomotion failure as thrust generated below f_{th} . The probability of locomotion failure can be non-negligible with insufficient or ill-designed redundancy. Our theory predicts that when $f_{th} < C_s$ the probability of locomotion failure can be arbitrarily close to zero if provided with sufficient spatial redundancy. To illustrate our prediction, we calculate the order of spatial redundancy $N_{95\%}$ required to facilitate successful locomotion with 95% confidence interval (CI) as a function of contact noise level for different f_{th} values in Fig. Figure 7.3.b.2. Note that we set $T = 1$ and approximate contact noise level by b .

As suggested in previous studies of multi-legged locomotion on relatively flat surfaces [235, 251], robot locomotion velocity is correlated with the generated thrust (\tilde{f}). Assuming $f_{th} = 0$, we show an example of thrust-velocity curve in Fig. Figure 7.3.a.2. In Fig. Figure 7.3.a.2, we normalize velocity by the velocity in undisturbed systems, v_{open} . This thrust-velocity relationship facilitates mapping from the abstract thrust generation to the observable robot velocity subject to different combinations of temporal and spatial redundancy (Fig. 3.c.1). As discussed earlier, increasing spatial redundancy can improve the expected average generated thrust, and therefore the expected average velocity. To illustrate this prediction, in Fig. Figure 7.3.c.2, we numerically calculate the expected average velocity as a function of spatial redundancy subject to different contact noise levels. Notably, we observe that the marginal benefit of having more legs decreases as the spatial redundancy increases, and the expected average velocity converges to v_{open} .

We next test the theoretical framework and its predictions in a laboratory robophysical model, focusing on the efficacy of open-loop multi-legged robots with different leg num-

bers and terrain complexity. To facilitate comparison across different spatial redundancy N , our chosen substrate-contact sequence has the property such that all robots share the same thrust function $f(t)$, the same performance on flat terrain, and the same thrust-velocity relationship (see SI, section IV).

To develop an approximation of contact errors, we construct laboratory models of rugose terrains defined as terrains composed of blocks with variation in heights [252] (Fig. Figure 7.4a). The block ($10 \times 10 \text{ cm}^2$) heights, $h(x, y)$, are randomly distributed (see SI, section I). Such rugose terrains were previously used as a testing terrain in field robotics [212] ensuring that limbs will experience thrust deficiency from stochastic contact ². We define the terrain rugosity, R_g , as the standard deviation of heights normalized by block size. We test the performance of 6-16 legged/segmented robophysical models on rugose terrains and record the bac duration (τ_u) on each leg. The distributions of τ_u (measured from 225 and 309 bacs for terrain with rugosity 0.17 and 0.32 respectively) are shown in SI section II.E, where the empirical distributions justify our assumptions on bac duration distribution.

To illustrate that the thrust deficiency from contact error is the primary driving force to cause variations in velocity, we record the locomotion velocity (v/v_{open} , normalized by nominal velocity) and the bac duration (τ_u/τ , normalized by nominal bac duration) of a 12-legged robot on rugose terrains (30 trials on each terrain). In Fig. Figure 7.4.b, we observe a clear correlation between the bac duration and the locomotion velocity. In matter transportation, the “estimated time of arrival” is an important metric to evaluate transportation performance. Therefore, we estimate the robot performance via number of periods, $T_{[D=60]}$, required for a robot to transport 60 cm over rugose terrains with $R_g = \{0, 0.17, 0.32\}$ (10 trials in each condition). We notice that a hexapod can eventually self-transport over 60 cm but there is a large variation in $T_{[D=60]}$. In contrast, systems with high spatial redundancy (e.g., $N \geq 5$) can finish the self-transport task with short average estimated time of

²Note that the contact error can also come from robot motor noise.

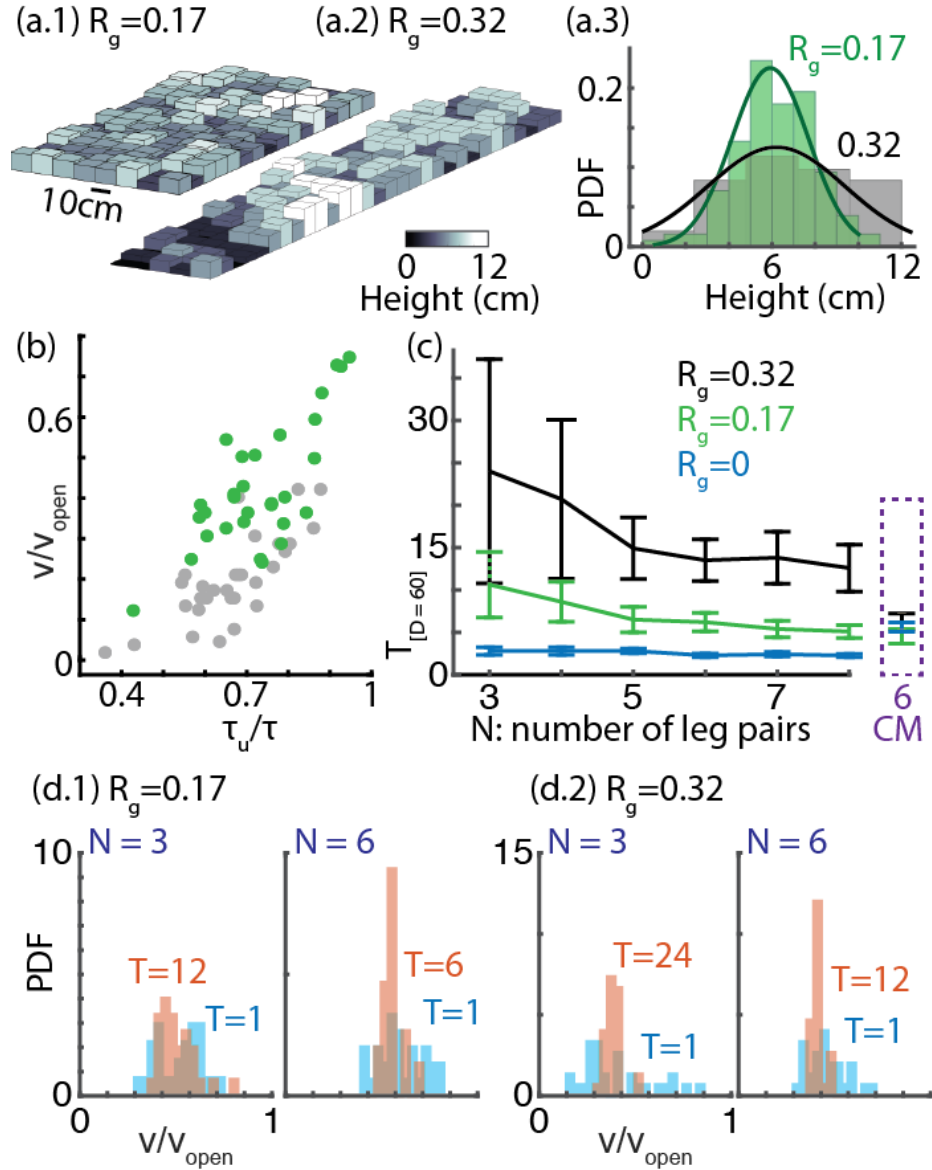


Figure 7.4: **Experimental verification of the sufficiency to bound contact errors via redundancy.** (a) Rugose terrains with rugosity (a.1) $R_g = 0.17$ and (a.2) $R_g = 0.32$. The block height distribution is shown on the right panel. (b) The correlation between bac duration and locomotion velocity of a 12-legged robots on rugose terrains. Color schemes are identical to (a). (c) For robot with different number of leg pairs N , we recorded $T_{[D=60]}$, the number of periods required to transport $D = 60\text{cm}$ on terrains with (blue) $R_g = 0$, (green) $R_g = 0.17$, and (black) $R_g = 0.32$. The error bar was calculated from at least 10 trials. $T_{[D=60]}$ for contact modulated gaits are illustrated in the purple rectangle. (d) The empirical distribution of velocity on terrains with (d.1) $R_g = 0.17$ and (d.2) $R_g = 0.32$. Effect of temporal redundancy on (Top) the 6-legged robot and (Bottom) the 12-legged robot. Non-negligible locomotion failure is observed when there is not sufficient redundancy. The empirical distributions were obtained from 30 trials.

arrival and small variation. Further, $T_{[D=60]}$ converges as we increase the number of legs, in agreement with our prediction of marginal benefit of spatial redundancy (Fig. Figure 7.4c). Our robophysical experiments indicate that with only temporal redundancy, carriers can self-transport reliably to the destination but with unpredictable estimated time of arrival. The value of spatial redundancy thus lies in not only reliable self-transport, but reliable self-transport on time.

From the Shannon scheme for signal transmission, it is reasonable to anticipate improved performance with more elaborate coding schemes, which we redefine as designing the kinematic property of bacs (e.g., instantaneous thrust function $f(t)$ and thrust-velocity relationship). Unfortunately, we cannot directly engineer the kinematic property of bacs. Instead, the kinematic property of bacs can be modulated via gait designs (the temporal and spatial distribution of bacs and the associated body postures), such as amplitude modulation [235] or frequency modulation [107]. In practice, however, effective gait modulation can be challenging because of the high dimensionality associated with the many bacs. In SI section IV, we provide a subset of parameterized gait modulation and their effects on bac kinematic property based on our prior work on myriapod locomotion [253, 235].

Here, we illustrate one example of coding which takes the form of temporal modulation of bacs. Specifically, we impose a vertical wave along the body such that the duration of bacs (τ) is actively and systematically shortened (see SI section V). We test the performance of contact-modulated (CM) myriapods over rugose terrain and observe improved locomotion robustness over terrain rugosity with some sacrifice of nominal velocity v_{open} (Fig. Figure 7.4 in purple rectangle box). Further, using the framework as well as contact modulation our myriapod robot is capable of traversing diverse laboratory (obstacles, slopes and walls) experiments (Fig. 1.c.1 and in SI movie) and field-like environments (granular media, pebbles, and rock piles) with completely open loop operations.

These experiments reveal that a value of our framework lies in its robustness over contact errors, in contrast to contact error prevention as in the conventional sensor-based

closed-loop controls which take advantage of visual, tactile, or joint torque information from the environment to effect a change in dynamics of the robot [3, 111]. Similar to error correction codes in signal transmission, redundancy in matter transportation is sufficient to bound the uncertainty from (contact) noise, which explains the robust performance of our myriapod robots. In this way, the complexity of matter transport can be transferred from the real-time feedback-based control (e.g., dealing with the flow of sensor information) to premeditated gait design. Despite the challenges in gait design with high dimensionality, our framework simplifies matter transport tasks such as search-and-rescue [254], extraterrestrial exploration [255] or even micro-robotics [256], where robot deployments are often preferred yet challenging due to unpredictable terradynamic interactions and unreliable sensors.

In addition to the importance of self-transport in artificial locomotors, we posit that our matter transport framework can give insights into aspects of neuromechanical and morphological evolution [206] from a living systems physics perspective. That is, animals ranging from those which generate propulsion via a single bac pair (i.e., bipeds) [257, 258] to those which utilize many bacs (i.e., myriapods) [259] are capable of traversing complex natural terrains. Interestingly, the importance of environmental awareness and whole body coordination is hypothesized to diminish as the number of bacs (redundancy) increases [260, 261]. Thus, in biological terrestrial locomotors there appears to be a shift towards either advanced neuromechanical control with reduced body appendages, or redundant body appendages with simplified neuromechanical control. Integration of our framework with advances in biological experimentation [2, 262] could yield insights into benefits and trade-off of diverse control architectures [1].

Supplement Information

Terrain construction

To systematically emulate rugose terrains, we used stepfields in accordance with NIST standards for assessing search-and-rescue robot capabilities [252]. Each block is a 10 by 10 cm square with a height between 0 and 12 cm in 1 and 2.5 cm increments for the terrains with rugosity $R_g = 0.17$ and $R_g = 0.32$, respectively. The number of blocks associated with each height was determined from a normal distribution generated in MATLAB with a mean (μ) and standard deviation (σ) of 6.0 and 2.0 cm for the $R_g = 0.17$ terrain and 6.25 and 4 cm for the $R_g = 0.32$ terrain. We truncate these distributions between 0 and 12 cm using MATLAB's `truncate()` command such that we avoided negative heights in our model and extreme heights when physically constructing these terrains. We formed these blocks out of foam (FOAMULAR Insulating Sheathing (IS) XPS Insulation) and laid them spatially across a 2D grid of size W, H where $(W, H) = (80, 160)$ cm for the $R_g = 0.17$ terrain and $(50, 300)$ cm for the $R_g = 0.32$ terrain.

We placed the blocks such that we would avoid extreme height differences (≥ 8 cm) as that would require active lifting across the body and would thus classify these terrains as a different form of noise than we wish to test. The procedure we followed is detailed below. The original code can be found in ³.

We denote the starting height distribution of blocks as H_0 , the total number of blocks as N , and the distribution after some number M of blocks have been placed as H_M . We begin the act of populating the grid by placing a block of 0 height at location $(1, 1)$. That forms our base case that allows to implement the more general process of determining arbitrary block height after M blocks have been placed. To determine what height the $M + 1$ block should be at a location (x, y) , we look to each neighboring block of that position according to a Manhattan distance metric. These block heights are denoted as h_1, h_2, h_3 , and h_4 . Note that

³<https://doi.org/10.5281/zenodo.7121219>

along the edges of the grid when $x, y = 0$ or W, H respectively, there will be less neighbors according to how many edges this (x, y) location touches and we denote the total number of neighbors as n . We then generate n distributions of height differences by subtracting these neighboring block heights from the remaining height distribution and denote these new distributions as Δ_i where $\Delta_i = H_M - h_i = \delta_1, \delta_2, \dots, \delta_M$. From these sets, we discard all $|\delta_i| \geq \delta_{lim}$ where δ_{lim} is our chosen height difference limit of 8 cm. These new sets are denoted as $\Delta_{i,s}$. We then add the corresponding neighboring block height to each of these sets ($H_{i,s} = \Delta_{i,s} + h_i$) and generate a final set of heights $H_{M,f}$ made up of heights that appear within each $H_{i,s}$ ($H_{M,f} = H_{1,s} \ \& \ H_{2,s} \ \& \ H_{3,s} \ \& \ H_{4,s}$). From $H_{M,f}$, we uniformly randomly choose a height and place that at location (x, y) . We repeat this process until the grid is populated, iterating along x until W is met after which y is incremented by 1 and x is reset to 0.

Robophysical experiments

Modular design

To verify our theoretical predictions with robophysical experiments, we build a multi-legged robotic system. The robot was 3D-printed by Taz Workhorse and the printing material is PolyLite PLA. AX-12A and 2XL430-W250 motors control body undulation, and limb retraction/protraction. The overall robot is composed of multiple repeating modules (Fig. Figure 7.5a). Each module has three degrees of freedom (DoF): the shoulder lifting joint that controls the contact states of contralateral legs, the shoulder retraction joint that controls the fore/aft positions of leg movements, and the body bending joint that controls the lateral body undulation. Specifically, a leg up/down servo motor and a leg swing motor control the limb stepping and are connected by a hip connector (Fig. Figure 7.5b). Those limb motors are connected with a body undulation motor with a undulation connector. The limb lifting connector which contains fishing lines (yellow lines in Fig. Figure 7.5a) connecting the up/down motor to the legs. Each leg is hinged to the hip connector using a

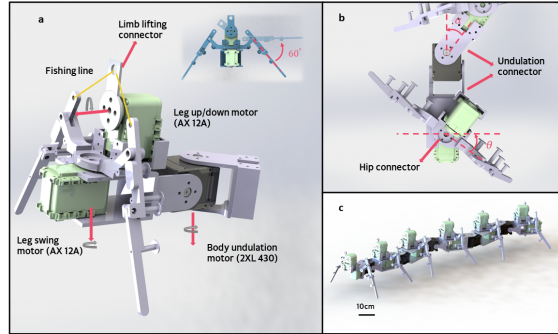


Figure 7.5: **Robophysical model.** (a) CAD of one module of the robot. The legs are out-of-phase and their up/down and fore/aft positions are controlled by two AX 12A motors. The body motor (2XL 430) controls the lateral undulation of the body. Body angle and legs are coupled to each other with a hip and a undulation connector. Inset shows the max lifting angle (60°) of the leg. (c) Overall sketch of a 12-legged robot.

rigid DoF revolute joint whose rotation axis is parallel to the fore/aft direction. The legs can lift up to 60° from their neutral position which corresponds to a maximum lift of about 7cm above the ground (see the inset of the Fig. Figure 7.5a). The leg lifting angles can be modulated by controlling the up/down motor. The leg swing angle, θ , and the lateral body angle, α , are actively controlled by a leg swing motor and a body undulation motor (Fig. Figure 7.5b). The final design of a module (length = 15 cm) with three servos is given in Fig. Figure 7.5. This modular design allows us to readily change the number of the modules (and legs) of the robot. We perform experimental verification of our prediction model by changing modules of the robophysical model (3 to 8 modules corresponding to 6 to 16-legged robotics system).

Leg compliance design

Inspired by real centipede animals, we leverage rubber bands (1/4 LB) to design two types of leg compliance to minimize the parallel force disturbance. The first intelligent design is an inward leg compliance (Fig. Figure 7.6a). Rubber bands connect legs and hip joint connector, and support the body weight of each robot module by drag forces. The contralateral legs from the same module are 180° out of phase with each other. Instead of independently actuating two legs, this inward compliance can couple two legs with only one motor.

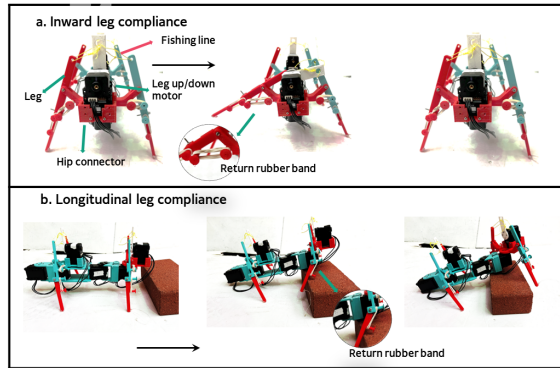


Figure 7.6: **Leg compliance design.**(a) Working principle of inward compliance. Return rubber bands connect legs and the hip connector. Drag forces from rubber bands support the weight of each module of the robot. Rubber bands also recover the lifted leg to its neutral position when the leg up/down motor stops lifting. (b)Working principle of the directional flexible (bends from head to tail) leg with a return rubber band. The leg approaches the obstacle, pivots around the tip, and bends. After it passes the obstacle, the rubber band returns the leg to its neutral position. Black arrow indicates the moving direction of the robot.

Fig. Figure 7.6a shows an example of how this design works. The up/down motor rotates and fastens fishing line to lift the right leg. Then the motor return to its neutral position whereas the return rubber band drags the right leg down to its neutral position.

The second compliance design is the longitudinal leg compliance. This design enables the leg to passively bend when hitting obstacles and subsequently slide on obstacles to pass (Fig. Figure 7.6b). The return rubber band together with a rotation pivot connect the upper part and lower part of a leg. The lower part bends passively when hitting an obstacle, then the leg can slide on the obstacle and finally pass it. After passing, return rubber band recovers the lower part to its neutral position.

Programming and control

We use the Dynamixel SDK library to develop control code for our robophysical model and finish programming in MATLAB. The PC input control signals to the robot via Robotis U2D2 while a DC power supply HY3050E provides power for the motors (Fig Figure 7.7). The voltage of the power supply is set as 11.1 V which is the recommended input voltage

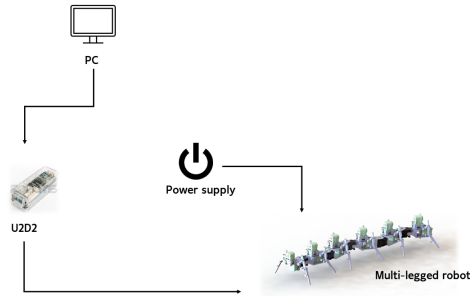


Figure 7.7: **Robot connection.** The PC input control signals to the robot via a Robotis U2D2 USB communication converter. A DC power supply HY3050E provides power for the motors.

of AX 12A and 2XL430-W250 motors.

Robophysical experiment tracking

We use 4 OptiTrack prime 13w cameras to track the movement of the robot, collect, and analyze experimental results. Four cameras are mounted on tripods and are placed at each corner of the robot testing arena (Fig. Figure 7.8). The tracking system is calibrated by a CW-500 Calibration Wand Kit and a CS-400 Calibration Square. Markers are mounted on the top of each leg’s up/down motor for capturing. We use Motive as motion capture software to collect tracking data.

Contact duration

We manually measure contact duration from the side-view recording of the robot experiments on rugose terrains. We identify the duration of any “missing steps” of all legs on the same side and then approximate the contact duration. In Fig. Figure 7.9, we illustrate a snapshot of a side-view video and label the missing steps using blue arrows. The cumulative distribution functions of empirically measured contact duration are illustrated in the bottom panel of Fig. Figure 7.9.

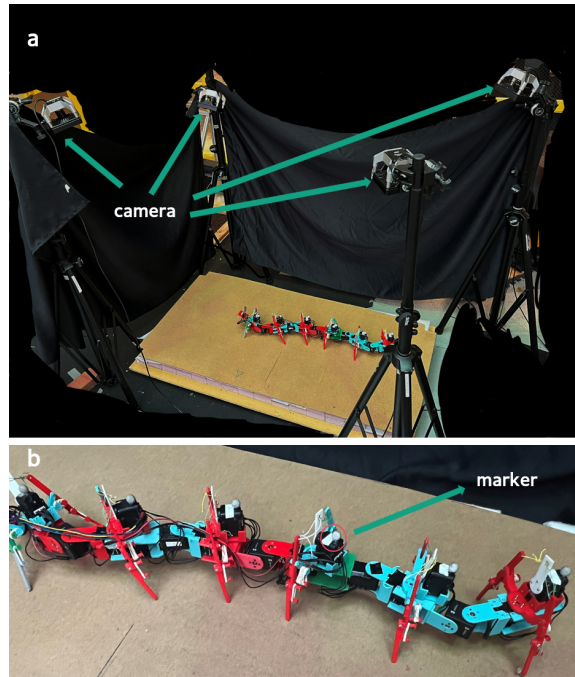


Figure 7.8: **Tracking system setup.** (a). Four 4 OptiTrack prime 13w cameras are fixed on tripods and placed at each corner of the testing arena for tracking. (b). A 12-legged robot mounted with markers.

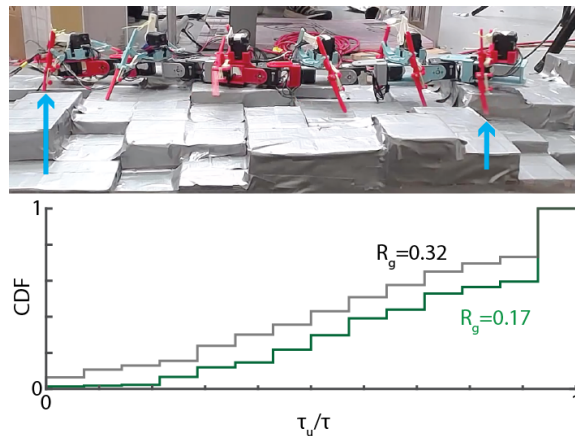


Figure 7.9: **Contact error.** (Top) Side view of robot on rugose terrain. Missing steps are identified in blue arrows. (Bottom) Cumulative distribution functions of empirically measured contact duration for (green) lower rugose terrain with $R_g = 0.17$ and (black) higher rugose terrain with $R_g = 0.32$

Contact planning

We use a binary variable c to represent the contact state of a leg, where $c = 1$ represents the stance phase and $c = 0$ represents the swing phase. Following [253], the contact pattern of robophysical model with N pairs of legs can be written as

$$\begin{aligned}
 c_l(\tau_c, 1) &= \begin{cases} 1, & \text{if } \text{mod}(\tau_c, 2\pi) < 2\pi D \\ 0, & \text{otherwise} \end{cases} \\
 c_l(\tau_c, i) &= c_l(\tau_c - 2\pi \frac{\xi}{N}(i-1), 1) \\
 c_r(\tau_c, i) &= c_l(\tau_c + \pi, i),
 \end{aligned} \tag{7.3}$$

where ξ denotes the number of spatial waves on legs, D the duty factor, $c_l(\tau_c, i)$ (and $c_r(\tau_c, i)$) denotes the contact state of i -th leg on the left (and the right) at gait phase τ_c , $i \in \{1, \dots, N\}$ for $2n$ -legged system.

Legs generate self-propulsion by protracting during the stance phase to make contact with the environment, and retracting during the swing phase to break contact. That is, the leg moves from the anterior to the posterior end during the stance phase and moves from the posterior to anterior end during the swing phase. With this in mind, we use a piecewise sinusoidal function to prescribe the anterior/posterior excursion angles (θ) for a given contact phase (τ_c) defined earlier,

$$\begin{aligned}
 \theta_l(\tau_c, 1) &= \begin{cases} \Theta_{leg} \cos\left(\frac{\tau_c}{2D}\right), & \text{if } \text{mod}(\tau_c, 2\pi) < 2\pi D \\ -\Theta_{leg} \cos\left(\frac{\tau_c - 2\pi D}{2(1-D)}\right), & \text{otherwise,} \end{cases} \\
 \theta_l(\tau_c, i) &= \theta_l(\tau_c - 2\pi \frac{\xi}{N}(i-1), 1) \\
 \theta_r(\tau_c, i) &= \theta_l(\tau_c + \pi, i)
 \end{aligned} \tag{7.4}$$

where Θ_{leg} is the shoulder angle amplitude, $\theta_l(\tau_c, i)$ and $\theta_r(\tau_c, i)$ denote the leg shoulder angle of i -th left and right leg at contact phase τ_c , respectively. Note that the shoulder angle is maximum ($\theta = \Theta_{leg}$) at the transition from swing to stance phase, and is minimum ($\theta = -\Theta_{leg}$) at the transition from stance to swing phase. Note that we chose $D = 0.5$ unless otherwise mentioned.

We then introduce lateral body undulation by propagating a wave along the backbone from head to tail, The body undulation wave is

$$\alpha(\tau_b, i) = \Theta_{body} \cos(\tau_b - 2\pi \frac{\xi^b}{N} (i - 1)), \quad (7.5)$$

where $\alpha(\tau_b, i)$ is the angle of i -th body joint at phase τ_b , ξ^b denotes the number of spatial waves on body. For simplicity, we assume that the spatial frequency of the body undulation wave and the contact pattern wave are the same, i.e. $\xi^b = \xi$.

In this way, gaits of multi-legged locomotors by superposition of a body wave and a leg wave can be described as the phase of contact, ϕ_c , and the phase of lateral body undulation τ_b . As discussed in [253], the optimal body-leg coordination (optimal phasing of body undulation to assist leg retraction) is $\phi_c = \tau_b - (\xi/N + 1/2)\pi$. In this paper, we took $\Theta_{leg} = \pi/6$, $\Theta_{body} = \pi/6$, $\xi = N/6$ for all experiments.

Gait design and bac kinematics

We consider the myriapod gaits following the prescriptions above. The instantaneous thrust is given by [235]:

$$f(t) = \sin \left(\tan^{-1} \frac{v_y(t)}{v_x(t)} \right) \text{ if } t \in (0, \tau)$$

where

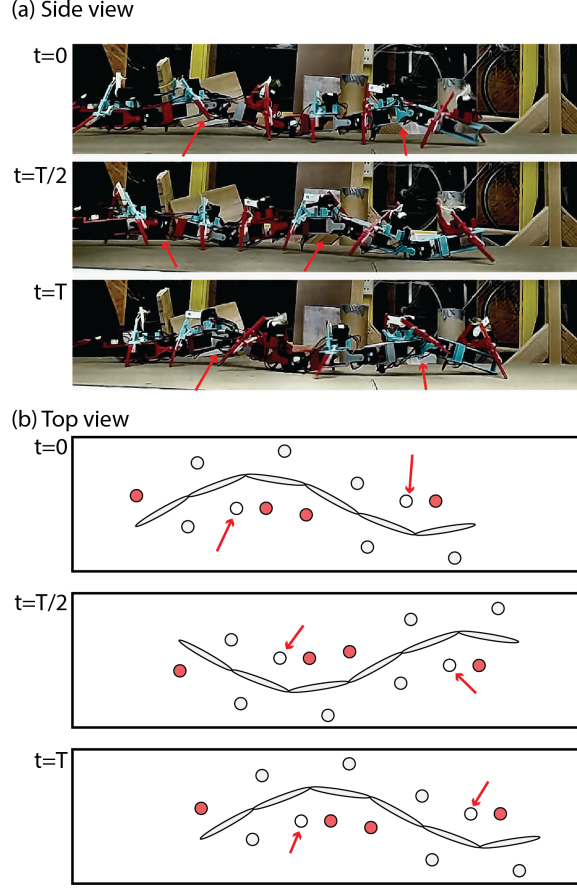


Figure 7.10: **Contact modulation.** Snapshots of (a) top view and (b) side view of contact modulated gaits. Note that for modules in the concave part of the vertical wave (labelled in red arrow), both legs are not in contact with substrate because of contact modulation. We also label the modules in concave part of vertical wave in the top view.

$$v_x(t) = x_m \cos(2\pi \frac{t}{2\tau}) - l\gamma_m \sin(2\pi \frac{t}{2\tau}) \sin(\gamma_m \cos(2\pi \frac{t}{2\tau}))$$

$$v_y(t) = l\gamma_m \sin(2\pi \frac{t}{2\tau}) \cos(\gamma_m \cos(2\pi \frac{t}{2\tau}))$$

$$\gamma_m = \tan^{-1}(2\pi\xi x_m) + \Theta_{leg}$$

$$x_m = N\Theta_{body}/(4\pi^2\xi^2)$$

Note that l is the ratio between leg length and body length. For modules with fixed leg length, we have $l = \frac{l_{leg}}{Nl_{body}}$, where l_{leg} is the length length and l_{body} is the module length.

In our framework, we consider the case where $t > \tau$ (e.g., $\tau_u + c_1 > \tau$). In those cases, we define the actual bac to have two segments: $[0, c_1 + \tau_u - \tau] \cup [c_1, \tau_u]$. In this way, we define $f(t)$ to be periodic: $f(t) = f(t + k\tau)$, $k \in \mathbb{Z}$.

Proposition: $f(t)$ is invariant of N .

Proof. By re-arranging the definition of x_m , we find

$$\gamma_m = \tan^{-1}(6\Theta_{body}/(\pi)) + \Theta_{leg},$$

which is invariant of N .

Also from algebra, we have:

$$\begin{aligned} v_x(t) &= x_m \cos(2\pi \frac{t}{2\tau}) - l\gamma_m \sin(2\pi \frac{t}{2\tau}) \sin(\gamma_m \cos(2\pi \frac{t}{2\tau})) \\ &= \frac{9\Theta_{body}}{\pi^2 N} \cos(\frac{\pi t}{\tau}) - \frac{\gamma_m l_{leg}}{N l_{body}} \sin(\frac{\pi t}{\tau}) \sin(\gamma_m \cos(\frac{\pi t}{\tau})) \\ &= \frac{1}{N} g_x(t), \end{aligned}$$

where $g_x(t)$ is a function that does not depend on N .

Similarly, we have:

$$\begin{aligned} v_y(t) &= l\gamma_m \sin(2\pi \frac{t}{2\tau}) \cos(\gamma_m \cos(2\pi \frac{t}{2\tau})) \\ &= \frac{l_{leg}}{N l_{body}} \gamma_m \sin(2\pi \frac{t}{2\tau}) \cos(\gamma_m \cos(2\pi \frac{t}{2\tau})) \\ &= \frac{1}{N} g_y(t), \end{aligned}$$

where $g_y(t)$ is a function that does not depend on N .

In all, we find that $\frac{v_y(t)}{v_x(t)}$ is invariant of N , which implies that $f(t)$ is invariant of N .

□

The nominal velocity, v_{open} has the following property:

$$\int_0^\tau \sin\left(\tan^{-1} \frac{v_y(t) - v_{open}}{v_x(t)}\right) dt = 0.$$

Proposition: The absolute velocity is invariant of N .

Proof. Note that v_{open} has units of body lengths per cycle. The body length is given by Nl_{body} . Therefore the absolute velocity is given by $v_{abs} = v_{open} \times Nl_{body}$.

In this way, we have:

$$\begin{aligned} & \int_0^\tau \sin\left(\tan^{-1} \frac{v_y(t) - v_{open}}{v_x(t)}\right) dt \\ &= \int_0^\tau \sin\left(\frac{\frac{1}{N}g_y(t) - \frac{1}{N} \frac{v_{abs}}{l_{body}}}{\frac{1}{N}g_x(t)}\right) dt \\ &= \int_0^\tau \sin\left(\frac{g_y(t) - \frac{v_{abs}}{l_{body}}}{g_x(t)}\right) dt = 0. \end{aligned}$$

since both $g_x(t)$ and $g_y(t)$ are invariant of N , we know that v_{abs} is also invariant to N . \square

The thrust-velocity relationship is given by:

$$\tilde{f} - f_n = \frac{1}{\tau} \int_0^\tau \sin\left(\tan^{-1} \frac{v_y(t) - v}{v_x(t)}\right) dt,$$

where $f_n = \frac{1}{\tau} \int_0^\tau \sin\left(\tan^{-1} \frac{v_y(t)}{v_x(t)}\right) dt$ is the nominal thrust.

Contact modulation

We modulate the contact duration by imposing an vertical wave. The vertical wave is implemented by vertical joints $\alpha_v(i)$. The vertical wave and lateral wave are coupled as the following:

$$\alpha_v(\tau_b, i) = \Theta_v \cos\left(2\tau_b - 4\pi \frac{\xi^b}{N}(i - 1)\right), \quad (7.6)$$

such that the vertical wave has spatial frequency twice that of the lateral wave. The modules in the concave part of the vertical wave are lifted off the ground (Fig. S6) such that both legs are not in contact with substrate. The contact modulation follows similar coordination as the sinus lifting as discovered in snakes [146]. Snapshots of contact modulation is illustrated in Fig. Figure 7.10.

Convergence proof

The sign function $\text{sign}(x)$ is defined as the following:

$$\text{sign}(x) = \begin{cases} 1, & \text{if } x > 0 \\ 0, & \text{if } x = 0 \\ -1, & \text{if } x < 0 \end{cases}$$

Proposition: $\tilde{f} = \text{sign}(\tau_u)\tau_u^{-1}f_u$, as defined in Eq. 1, is sampled from a probability density function, and

$\tilde{f}_T^{[1]} = \frac{1}{T} \sum_{i=1}^T \tilde{f}$ tends to a Dirac delta function as T tends to infinity.

Proof. This follows from the central limit theorem [263]. $\tilde{f}_T^{[1]}$ represents a sum of T identical random variables, each having finite variance independent of T . Say that $\text{Var}(\tilde{f}) = \sigma^2$. Then $\tilde{f}_T^{[1]}$ has variance given by $\text{Var}(X^T) = \sigma^2/T$. This variance limits to 0 as T approaches infinity, which implies that X^T is a constant random variable with probability 1. \square

Proposition: Consider $\tilde{f}_T^{[M]}$, as defined in Eq. 2. Define $\tilde{f}_1^{[M]} = \tilde{f}_T^{[M]}$. As N tends to infinity, $\tilde{f}_1^{[M]}$ tends to a Dirac delta function. $\langle \tilde{f}_1^{[M]} \rangle$ can be approximated by $(1 - b^N)C$ when N is large, where C is a constant determined by $f(t)$ and b .

Proof. Now we consider the complete missing step in Eq. 2. The probability of complete missing step ($\sum_{j=1}^N \tau_u^j = 0$) is then b^N . Recall that $p(\tau_u \leq 0)$ is given by $G(0)$, and the definition of G precedes Eq. 1 in the text. Thus, $\langle \tilde{f}_1^{[M]} \rangle$ can be expressed by:

$$\langle \tilde{f}^{[N]} \rangle = b^N \times 0 + (1 - b^N) \left\langle \frac{\sum_{j=1}^N f_u^j}{\sum_{j=1}^N \tau_u^j} \right\rangle \quad (7.7)$$

We can then simplify Eq. S5 into:

$$\begin{aligned} \langle \tilde{f}^{[N]} \rangle &= (1 - b^N) \left\langle \frac{1}{N} \sum_{j=1}^N f_u^j \right\rangle \left\langle \frac{N}{\sum_{j=1}^N \tau_u^j} \right\rangle \\ &= (1 - b^N) \langle f_u \rangle \left\langle \frac{N}{\sum_{j=1}^N \tau_u^j} \right\rangle \end{aligned} \quad (7.8)$$

In the cases where N is large, the following approximation exists [264]:

$$\left\langle \frac{N}{\sum_{j=1}^N \tau_u^j} \right\rangle \approx 1 / \langle \tau_u \rangle. \quad (7.9)$$

From the distribution of τ_u , we have: $\langle \tau_u \rangle = \frac{1-b}{2} \tau$. With the approximation in Eq. S7, we have:

$$\langle \tilde{f}^{[N]} \rangle \approx (1 - b^N) \underbrace{\frac{2 \langle f_u \rangle}{(1 - b) \tau}}_c \quad (7.10)$$

Now we consider the variance. We define a random variable Z as follows:

$$\begin{aligned} Z &= \frac{\sum_{j=1}^N f_u^j}{\sum_{j=1}^N \tau_u^j} \\ &= \frac{\frac{1}{N} \sum_{j=1}^N f_u^j}{\frac{1}{N} \sum_{j=1}^N \tau_u^j}. \end{aligned} \quad (7.11)$$

We notice that as N approaches infinity, both the numerator and the denominator con-

verge to a normal distribution, by the weak law of large numbers.

$$\begin{aligned}
 Z &\rightarrow \frac{\langle f_u \rangle + x_f}{\langle \tau_u \rangle + x_\tau} \\
 x_f &\sim \mathcal{N}\left(0, \frac{\sigma(f_u)}{\sqrt{N}}\right) \\
 x_\tau &\sim \mathcal{N}\left(0, \frac{\sigma(\tau_u)}{\sqrt{N}}\right)
 \end{aligned} \tag{7.12}$$

As N approaches infinity, we have $\langle f_u \rangle \gg x_f$ and $\langle \tau_u \rangle \gg x_\tau$, therefore Eq. S10 reduces to:

$$Z \rightarrow \frac{\langle f_u \rangle}{\langle \tau_u \rangle} + \frac{x_f}{\langle f_u \rangle} - \frac{x_\tau}{\langle \tau_u \rangle}, \tag{7.13}$$

which will approach a Dirac delta function centered at $\frac{\langle f_u \rangle}{\langle \tau_u \rangle}$. The random variable Z is related to $\tilde{f}^{[N]}$ in that:

$$\begin{aligned}
 p(\tilde{f}^{[N]} = 0) &= b^N \\
 p(\tilde{f}^{[N]} = Z) &= 1 - b^N.
 \end{aligned} \tag{7.14}$$

Note that $b^N \rightarrow 0$ as $N \rightarrow \infty$, because $b < 1$. Hence $\tilde{f}^{[N]}$ also converges to a Dirac delta function centered at $C_s = \frac{\langle f_u \rangle}{\langle \tau_u \rangle}$ as N approaches infinity. \square

CHAPTER 8

CONCLUSION

8.1 Summary

This thesis advanced the geometric mechanics theory and applied it to various locomotors across scales. Surprisingly, many seeming complicated biological and robotic systems (e.g., undulatory snakes and fast-walking centipedes) can be described by geometric mechanics framework, where the inertial effect is assumed to be negligible. Despite the relatively high speed (e.g., ~ 0.5 body length/second in centipedes), we show that the geometric theory can still capture the essence of locomotion, especially at steady-state equilibrium.

We used geometric mechanics analysis to connect the biological observations and the robot controls. On the one hand, with the illustrative diagram (height function), geometric mechanics can rationalize the seeming complicated animal behaviors (e.g., differential turns in sidewinder snakes) with simple parameterization. On the other hand, using the geometric mechanics as a model, we can systematically investigate the relationship between the morphological details (what they have) and locomotion strategy (how they move). With insights from geometric mechanics, we can use robot experiments to test behaviors which are less commonly observed in biological systems (e.g., traveling wave and standing wave in intermediate lizards), thereby verifying the hypothesis of animal locomotion behaviors.

In Chapter 2, we used geometric mechanics to study the optimal amplitude for undulatory limbless locomotion across scales, from nematodes in microscopic scale to snakes in macroscopic scale. The predictions from geometric mechanics are in quantitative agreement with the measurement in biological experiments. Further, with the introduction of contact function, we not only predicted the optimal lateral wave amplitude in sidewinders, but also revealed a turning modulation scheme for steering during differential turn.

In Chapter 3, we advanced geometric mechanics to legged systems. We first studied quadruped with a single body bending DoF. We showed that properly coordinated body bending can improve locomotion performance in forward, sideways, and rotational motions. Our geometric mechanics prediction is also in quantitative agreement with measurement in fire salamanders.

In Chapter 4, we further studied the body-leg coordination in short-limb elongate lizards. Lizards have evolved a diversity of body forms from fully limbed and short-bodied to limbless and elongate. We showed that this diversity in morphology coincides with a similar diversity in locomotion patterns, ranging from standing wave to traveling wave body undulation. We observed that the degree of body elongation and limb reduction were closely related to how the body and limb movements were coordinated, indicating an interconnected morphological and locomotor continuum. Using biological experiments, a geometric theory of locomotion, and robophysical experiments, we showed that the body weight distribution between the limbs and the body (and therefore, the primary thrust generation mechanism) plays a crucial role in the locomotor transition from fully limbed to limbless. Specifically, we found that fully limbed lizards adopted a traveling wave to undergo terrestrial swimming when the penetration resistance of the substrate was reduced and the belly contracted the medium. Further, our robophysical experiments revealed that a traveling wave enhanced locomotor performance only when some thrust was generated by the body.

In Chapter 5, we developed a general gait design framework for a broad class of locomotors: multi-legged robots (with an arbitrary number of pairs of legs) with an articulated backbone, including limbless sidewinding. Specifically, we extended the Hildebrand gait formulation [17, 96], originally used to categorize symmetric quadrupedal gaits, and combined it with modern geometric mechanics tools to investigate optimal leg-body coordination. We showed that the symmetry in Hildebrand quadrupedal gaits is conserved for other locomotors. The framework is not only simple enough to enable physical interpretation of the gait parameters; but also covers a range of potentially interesting gaits, offering

a scheme to modulate gaits in a diversity of robot shapes. Furthermore, our framework facilitated testing hypotheses about the role of body undulation in multi-legged systems. Specifically, we found that in robots with a fixed straight backbone, the displacement per gait cycle is nearly invariant to the changes in the lateral phase lag, Φ_{lat} . On the other hand, in gaits where body undulation is properly coordinated with leg motions, Φ_{lat} affects the displacement. This seemingly counter-intuitive observation can help us develop hypotheses about gait modulation principles. Finally, our proposed control principles can also offer explanatory power to some hypotheses about body-leg coordination in biological locomotion (*Salamandra salamandra* and *Scolopendra polymorpha*).

In chapter 6, we studied slipping in terrestrial locomotion using an RFT framework. Specifically, we studied slipping in centipede terrestrial swimming, and established a framework to analyze the causal relationship between slipping and locomotion performance. Furthermore, our framework connected the studies of locomotion in continuous media to terrestrial environments. Specifically, we showed that by properly controlling the lifting and landing of contralateral feet (and thus the slipping direction), terrestrial locomotors can acquire drag anisotropy and effective viscous friction in the environments dominated by isotropic, rate-independent Coulomb friction. Finally, we systematically compared the performance of slip-driven (body-dominated) locomotion and the reduced slipping (conventional leg-dominated) locomotion. We noticed that the advantage of body-dominated swimming in continuous media (the capability to benefit from terrain heterogeneity to aid locomotion [239, 150, 240, 241]) preserved in terrestrial environments. Specifically, we established a performance space of terrestrial swimming, and compared its performance in homogeneous and heterogeneous environments by robophysical experiments. Further, we used our framework to discover and rationalize the relationship between the slipping and behavior in biological multi-legged locomotors. In doing so, we discovered a new regime of effective locomotion in terrestrial environments revealing its advantage in high-speed regime and in obstacle-rich environments.

In Chapter 7, we illustrated that the redundancy in legs can be sufficient to counter the terrain roughness without environmental awareness. The value of our framework lies in its robustness over contact errors, in contrast to contact error prevention as in the conventional sensor-based closed-loop controls which take advantage of visual, tactile, or joint torque information from the environment to effect a change in dynamics of the robot [3, 111]. Similar to error correction codes in signal transmission, redundancy in matter transportation is sufficient to bound the uncertainty from (contact) noise, which explains the robust performance of our myriapod robots. In this way, the complexity of matter transport can be transferred from the real-time feedback-based control (e.g., dealing with the flow of sensor information) to premeditated gait design. Despite the challenges in gait design with high dimensionality, our framework simplified matter transport tasks such as search-and-rescue [254], extraterrestrial exploration [255] or even micro-robotics [256], where robot deployments are often preferred yet challenging due to unpredictable terradynamic interactions and unreliable sensors.

8.2 Future work

8.2.1 Connection morphology to locomotion

There is generally believed that the morphology of a locomotor (what they have) can affect their locomotion strategy (how they move) [15, 32, 206]. Below are a few possible directions to be pursued in future study.

Small surface features in biological systems can have significant and diverse functional consequences [265]. For example, the structurally anisotropic texture in snake skins can provide drag anisotropy which benefits the undulatory motion [103]. Note that such drag anisotropy in snakes has the property with lower resistive force to slide longitudinally than to slide laterally. To quantify such anisotropy, we define d_a as the ratio between resistive force in lateral direction and the longitudinal directions. Apparently, d_a in snakes is greater than 1. However, in legged systems, it is commonly believed that the skin structures should

have higher resistive force in longitudinal direction to avoid slipping [266]. That is, d_a in legged systems is typically less than 1.

Unfortunately, the function of lizard limb structural texture on locomotion is less studied. Our primary geometric simulation suggested that $d_a < 1$ is beneficial for lizards with long legs. We hypothesize that as the size of limb decreases, the structural texture of limb should also change accordingly to generate the maximum self-propulsion.

Furthermore, sand swimming in sandfish the lizard no longer uses limbs for propulsion [72]. Instead, the limbs are folded as if it is one part of the undulatory body. Now that the limbs are immersed in sands, there is a emerged property of $d_a > 1$ due to the property of the granular media. The subtle difference between terrestrial-running and sand-swimming lizards is the duty factor: the fraction of a period that a limb is in contact with the substrate. The duty factor in terrestrial-running lizards is typically around 0.5. However, for sand swimming lizards, the quantification of duty factor can vary according to our definition of limb contact. If we define the limb contact as to provide additional thrust, then limbs of sand swimming lizards have duty factor 0; if we define the limb contact as to experience reaction force from interactions with substrates, then limbs of sand swimming lizards have duty factor 1. Our primary geometric model suggests that the importance of duty factor can be modulated by d_a . In the case where $d_a \sim 1$, locomotion performance will be sensitive to the choice of duty factor: typically lower duty factor leads to higher speed [17]. In the case where $d_a \gg 1$, the locomotion performance will be robust over the choice of duty factor. Inspired by this observation, we hypothesize that the duty factor also plays an important role in the correlation between limb size and structural texture.

8.2.2 Coding in matter transportation

In Chapter 7, we discussed the sufficiency to use spatially redundant modules to counter terrain rugosity. The rugosity is one of many challenges from natural complex terrains. In future work, we aim to extend the redundancy framework towards more general challenging

natural terrains.

Contact errors can have two types: unexpected contacts and missing steps. The locomotion response to these two types of errors are often different: unexpected contacts can introduce additional drag resistance whereas missing steps lead to thrust deficiency. For example, on rigid terrestrial surfaces, most contact errors result from missing steps. Whereas in complex natural substrates such as sand, dirt, and pine straw, it is often challenging to completely break contact with substrates and therefore unexpected contacts are likely inevitable.

Notably, robust locomotion over complex natural substrates with characteristic unexpected contact is particularly challenging. Our preliminary work showed that locomotion efficiency on loosely-packed granular media has been compromised for both conventional limbless and legged locomotors. We hypothesize that the compromised locomotion can be a result of poor robustness over unexpected contact from mechanical design.

In future work, we propose to establish a gait library where we can choose suitable gaits for environments with different contact error with different noise levels. While the multi-legged robot requires less complexity for environmental interactions, redundant legs introduce high-dimensional internal coordination space (e.g., joint angles and contact patterns). In other words, to fully exploit the potential in multi-legged robots, we require a systematic gait design framework to coordinate the high-dimensional internal degree-of-freedom (DoF). Therefore, in future work we can use a geometric mechanics framework to design a gait library ranging from low nominal speed but robust over noises to high nominal speed but sensitive to noises.

If we extend the analogy with information theory, then every pre-planned contact pattern corresponds to a binary code of dimension given by the number of legs of the robot. Specifically, a leg that is planned to make contact will be encoded as 1, and a leg that is not planning contact with the terrain is encoded as 0. The realized locomotion of this robot is analogous to transmitting the binary code over a noisy channel. To wit, the variations in

terrain height introduce channel noise, and every contact error corresponds to a “bit-flip” in this model. We then model channel noise as a stochastic process; a model terrain can be generated by sampling heights from a probability density function, and these terrain heights give some probability of introducing a contact error. The problem of robotic gait design now becomes a problem of encoding leg contact patterns. This formulation gives a lower bound on the amount of redundancy needed in the contact pattern, and this bound is formulated in terms of the entropy of the terrain [112]. The main benefit of this reformulation is that we can estimate the amount of redundancy required by computing the entropy of a randomly generated terrain.

REFERENCES

- [1] P. Holmes, R. J. Full, D. Koditschek, and J. Guckenheimer, “The dynamics of legged locomotion: Models, analyses, and challenges”, *SIAM review*, vol. 48, no. 2, pp. 207–304, 2006.
- [2] J. P. Nguyen, F. B. Shipley, A. N. Linder, G. S. Plummer, M. Liu, S. U. Setru, J. W. Shaevitz, and A. M. Leifer, “Whole-brain calcium imaging with cellular resolution in freely behaving *caenorhabditis elegans*”, *Proceedings of the National Academy of Sciences*, vol. 113, no. 8, E1074–E1081, 2016.
- [3] M. Raibert, K. Blankespoor, G. Nelson, and R. Playter, “Bigdog, the rough-terrain quadruped robot”, *IFAC Proceedings Volumes*, vol. 41, no. 2, pp. 10 822–10 825, 2008.
- [4] U. Saranli, M. Buehler, and D. E. Koditschek, “Rhex: A simple and highly mobile hexapod robot”, *The International Journal of Robotics Research*, vol. 20, no. 7, pp. 616–631, 2001.
- [5] P. F. Muir and C. P. Neuman, “Kinematic modeling for feedback control of an omnidirectional wheeled mobile robot”, in *Autonomous robot vehicles*, Springer, 1990, pp. 25–31.
- [6] M. H. Dickinson, “Unsteady mechanisms of force generation in aquatic and aerial locomotion”, *American zoologist*, vol. 36, no. 6, pp. 537–554, 1996.
- [7] M. E. Gurtin, *An introduction to continuum mechanics*. Academic press, 1982.
- [8] E. G. Drucker and G. V. Lauder, “Locomotor forces on a swimming fish: Three-dimensional vortex wake dynamics quantified using digital particle image velocimetry”, *Journal of Experimental Biology*, vol. 202, no. 18, pp. 2393–2412, 1999.
- [9] R. Dvořák, “Aerodynamics of bird flight”, in *EPJ Web of Conferences*, EDP Sciences, vol. 114, 2016, p. 01 001.
- [10] D. Torricelli, J. Gonzalez, M. Weckx, R. Jiménez-Fabián, B. Vanderborght, M. Sartori, S. Dosen, D. Farina, D. Lefeber, and J. L. Pons, “Human-like compliant locomotion: State of the art of robotic implementations”, *Bioinspiration & biomimetics*, vol. 11, no. 5, p. 051 002, 2016.
- [11] C. Li, T. Zhang, and D. I. Goldman, “A terradynamics of legged locomotion on granular media”, *science*, vol. 339, no. 6126, pp. 1408–1412, 2013.

- [12] J. Hwangbo, J. Lee, A. Dosovitskiy, D. Bellicoso, V. Tsounis, V. Koltun, and M. Hutter, “Learning agile and dynamic motor skills for legged robots”, *Science Robotics*, vol. 4, no. 26, eaau5872, 2019.
- [13] H. Kreutzmann, “The karakoram highway: The impact of road construction on mountain societies”, *Modern Asian Studies*, vol. 25, no. 4, pp. 711–736, 1991.
- [14] M. G. Bekker, “Off-the-road locomotion”, *Research and development in terramechanics*, 1960.
- [15] R. J. Full and D. E. Koditschek, “Templates and anchors: Neuromechanical hypotheses of legged locomotion on land”, *Journal of Experimental Biology*, vol. 202, no. 23, pp. 3325–3332, 1999.
- [16] H. C. Astley, C. Gong, J. Dai, M. Travers, M. M. Serrano, P. A. Vela, H. Choset, J. R. Mendelson, D. L. Hu, and D. I. Goldman, “Modulation of orthogonal body waves enables high maneuverability in sidewinding locomotion”, *Proceedings of the National Academy of Sciences*, vol. 112, no. 19, pp. 6200–6205, 2015.
- [17] M. Hildebrand, “Symmetrical gaits of horses”, *science*, vol. 150, no. 3697, pp. 701–708, 1965.
- [18] R. B. McGhee and G. I. Iswandhi, “Adaptive locomotion of a multilegged robot over rough terrain”, *IEEE transactions on systems, man, and cybernetics*, vol. 9, no. 4, pp. 176–182, 1979.
- [19] J. Z. Kolter, M. P. Rodgers, and A. Y. Ng, “A control architecture for quadruped locomotion over rough terrain”, in *2008 IEEE International Conference on Robotics and Automation*, IEEE, 2008, pp. 811–818.
- [20] J. Buchli, M. Kalakrishnan, M. Mistry, P. Pastor, and S. Schaal, “Compliant quadruped locomotion over rough terrain”, in *2009 IEEE/RSJ international conference on Intelligent robots and systems*, IEEE, 2009, pp. 814–820.
- [21] M. Kalakrishnan, J. Buchli, P. Pastor, M. Mistry, and S. Schaal, “Learning, planning, and control for quadruped locomotion over challenging terrain”, *The International Journal of Robotics Research*, vol. 30, no. 2, pp. 236–258, 2011.
- [22] M. Zucker, N. Ratliff, M. Stolle, J. Chestnutt, J. A. Bagnell, C. G. Atkeson, and J. Kuffner, “Optimization and learning for rough terrain legged locomotion”, *The International Journal of Robotics Research*, vol. 30, no. 2, pp. 175–191, 2011.
- [23] M. Buehler, R. Battaglia, A. Cocosco, G. Hawker, J. Sarkis, and K. Yamazaki, “Scout: A simple quadruped that walks, climbs, and runs”, in *Proceedings. 1998*

IEEE International Conference on Robotics and Automation (Cat. No. 98CH36146), IEEE, vol. 2, 1998, pp. 1707–1712.

- [24] J. G. Cham, J. K. Karpick, and M. R. Cutkosky, “Stride period adaptation of a biomimetic running hexapod”, *The International Journal of Robotics Research*, vol. 23, no. 2, pp. 141–153, 2004.
- [25] S. Bai, K. H. Low, G. Seet, and T. Zielinska, “A new free gait generation for quadrupeds based on primary/secondary gait”, in *Proceedings 1999 IEEE International Conference on Robotics and Automation (Cat. No. 99CH36288C)*, IEEE, vol. 2, 1999, pp. 1371–1376.
- [26] M. S. Kim and W. Uther, “Automatic gait optimisation for quadruped robots”, in *Australasian Conference on Robotics and Automation*, Citeseer, 2003, pp. 1–3.
- [27] M. J. Powell, “An efficient method for finding the minimum of a function of several variables without calculating derivatives”, *The computer journal*, vol. 7, no. 2, pp. 155–162, 1964.
- [28] N. Kohl and P. Stone, “Policy gradient reinforcement learning for fast quadrupedal locomotion”, in *IEEE International Conference on Robotics and Automation, 2004. Proceedings. ICRA'04. 2004*, IEEE, vol. 3, 2004, pp. 2619–2624.
- [29] P. Stone, K. Dresner, S. T. Erdogan, P. Fiedelman, N. K. Jong, N. Kohl, G. Kuhlmann, E. Lin, M. Sridharan, D. Stronger, *et al.*, “Ut austin villa 2003: A new robocup four-legged team”, 2003.
- [30] J. Tan, T. Zhang, E. Coumans, A. Iscen, Y. Bai, D. Hafner, S. Bohez, and V. Vanhoucke, “Sim-to-real: Learning agile locomotion for quadruped robots”, *arXiv preprint arXiv:1804.10332*, 2018.
- [31] S. Rossignol, R. Dubuc, and J.-P. Gossard, “Dynamic sensorimotor interactions in locomotion”, *Physiological reviews*, vol. 86, no. 1, pp. 89–154, 2006.
- [32] J. A. Nyakatura, K. Melo, T. Horvat, K. Karakasiliotis, V. R. Allen, A. Andikfar, E. Andrada, P. Arnold, J. Lauströer, J. R. Hutchinson, *et al.*, “Reverse-engineering the locomotion of a stem amniote”, *Nature*, vol. 565, no. 7739, pp. 351–355, 2019.
- [33] A. J. Ijspeert, “Amphibious and sprawling locomotion: From biology to robotics and back”, *Annual Review Of Control, Robotics, And Autonomous Systems, Vol 3, 2020*, vol. 3, no. ARTICLE, pp. 173–193, 2020.
- [34] S. Suzuki, T. Kano, A. J. Ijspeert, and A. Ishiguro, “Decentralized control with cross-coupled sensory feedback between body and limbs in sprawling locomotion”, *Bioinspiration & biomimetics*, vol. 14, no. 6, p. 066 010, 2019.

- [35] A. J. Ijspeert, A. Crespi, D. Ryczko, and J.-M. Cabelguen, “From swimming to walking with a salamander robot driven by a spinal cord model”, *science*, vol. 315, no. 5817, pp. 1416–1420, 2007.
- [36] A. Crespi, K. Karakasiliotis, A. Guignard, and A. J. Ijspeert, “Salamandra robotica ii: An amphibious robot to study salamander-like swimming and walking gaits”, *IEEE Transactions on Robotics*, vol. 29, no. 2, pp. 308–320, 2013.
- [37] T. Horvat and A. J. Ijspeert, “Spine-limb coordination controller for a sprawling posture robot”, in *8th International Symposium on Adaptive Motion of Animals and Machines (AMAM)(Sapporo)*, 2017.
- [38] P. Eckert, A. Spröwitz, H. Witte, and A. J. Ijspeert, “Comparing the effect of different spine and leg designs for a small bounding quadruped robot”, in *2015 IEEE International Conference on Robotics and Automation (ICRA)*, IEEE, 2015, pp. 3128–3133.
- [39] D. Owaki, T. Kano, K. Nagasawa, A. Tero, and A. Ishiguro, “Simple robot suggests physical interlimb communication is essential for quadruped walking”, *Journal of The Royal Society Interface*, vol. 10, no. 78, p. 20 120 669, 2013.
- [40] R. M. Alexander, *Principles of animal locomotion*. Princeton University Press, 2003.
- [41] S. Childress, A. Hosoi, W. W. Schultz, and J. Wang, *Natural locomotion in fluids and on surfaces: swimming, flying, and sliding*. Springer, 2012, vol. 155.
- [42] E. Muybridge, *Animal locomotion*. Da Capo Press, 1887, vol. 534.
- [43] S. Manton, “The evolution of arthropodan locomotory mechanisms—part 3. the locomotion of the chilopoda and pauropoda.”, *Zoological Journal of the Linnean Society*, vol. 42, no. 284, pp. 118–167, 1952.
- [44] H. C. Astley and B. C. Jayne, “Arboreal habitat structure affects the performance and modes of locomotion of corn snakes (*elaphe guttata*)”, *Journal of Experimental Zoology Part A: Ecological Genetics and Physiology*, vol. 311, no. 3, pp. 207–216, 2009.
- [45] H. Marvi, C. Gong, N. Gravish, H. Astley, M. Travers, R. L. Hatton, J. R. Mendelson, H. Choset, D. L. Hu, and D. I. Goldman, “Sidewinding with minimal slip: Snake and robot ascent of sandy slopes”, *Science*, vol. 346, no. 6206, pp. 224–229, 2014.

- [46] G. J. Stephens, B. Johnson-Kerner, W. Bialek, and W. S. Ryu, “Dimensionality and dynamics in the behavior of *c. elegans*”, *PLoS computational biology*, vol. 4, no. 4, e1000028, 2008.
- [47] J. Aguilar, T. Zhang, F. Qian, M. Kingsbury, B. McInroe, N. Mazouchova, C. Li, R. Maladen, C. Gong, M. Travers, R. L. Hatton, H. Choset, P. B. Umbanhowar, and D. I. Goldman, “A review on locomotion robophysics: the study of movement at the intersection of robotics, soft matter and dynamical systems”, *Reports on Progress in Physics*, vol. 79, pp. 1–35, Sep. 2016.
- [48] N. Gravish and G. V. Lauder, “Robotics-inspired biology”, *Journal of Experimental Biology*, vol. 221, no. 7, jeb138438, 2018.
- [49] P. Holmes, R. J. Full, D. Koditschek, and J. Guckenheimer, “The Dynamics of Legged Locomotion: Models, Analyses, and Challenges”, *SIAM Review*, vol. 48, no. 2, pp. 207–304, Jan. 2006.
- [50] E. Roth, S. Sponberg, and N. Cowan, “A comparative approach to closed-loop computation”, *Current opinion in neurobiology*, vol. 25, pp. 54–62, 2014.
- [51] N. J. Cowan, M. M. Ankarali, J. P. Dyhr, M. S. Madhav, E. Roth, S. Sefati, S. Sponberg, S. A. Stamper, E. S. Fortune, and T. L. Daniel, “Feedback control as a framework for understanding tradeoffs in biology”, *Integrative and Comparative Biology*, vol. 54, no. 2, pp. 223–237, 2014.
- [52] S. Sponberg, “The emergent physics of animal locomotion”, *Physics Today*, vol. 70, no. 9, pp. 34–40, 2017.
- [53] M. Srinivasan and A. Ruina, “Computer optimization of a minimal biped model discovers walking and running”, *Nature*, vol. 439, no. 7072, pp. 72–75, 2006.
- [54] Y. Ding, S. S. Sharpe, K. Wiesenfeld, and D. I. Goldman, “Emergence of the advancing neuromechanical phase in a resistive force dominated medium”, *Proceedings of the National Academy of Sciences*, vol. 110, no. 25, pp. 10 123–10 128, 2013.
- [55] U. Saranlı, Ö. Arslan, M. M. Ankaralı, and Ö. Morgül, “Approximate analytic solutions to non-symmetric stance trajectories of the passive spring-loaded inverted pendulum with damping”, *Nonlinear Dynamics*, vol. 62, no. 4, pp. 729–742, 2010.
- [56] R. Altendorfer, N. Moore, H. Komsuoglu, M. Buehler, H. Brown, D. McMordie, U. Saranlı, R. Full, and D. E. Koditschek, “Rhex: A biologically inspired hexapod runner”, *Autonomous Robots*, vol. 11, no. 3, pp. 207–213, 2001.

- [57] H.-M. Maus, J. Rummel, and A. Seyfarth, “Stable upright walking and running using a simple pendulum based control scheme”, *Advances in Mobile Robotics*, pp. 623–629, 2008.
- [58] I. Poulakakis and J. W. Grizzle, “The spring loaded inverted pendulum as the hybrid zero dynamics of an asymmetric hopper”, *IEEE Transactions on Automatic Control*, vol. 54, no. 8, pp. 1779–1793, 2009.
- [59] A. D. Kuo, J. M. Donelan, and A. Ruina, “Energetic consequences of walking like an inverted pendulum: Step-to-step transitions”, *Exercise and sport sciences reviews*, vol. 33, no. 2, pp. 88–97, 2005.
- [60] B. C. Jayne, “Muscular mechanisms of snake locomotion: An electromyographic study of lateral undulation of the florida banded water snake (*nerodia fasciata*) and the yellow rat snake (*elaphe obsoleta*)”, *Journal of Morphology*, vol. 197, no. 2, pp. 159–181, 1988.
- [61] J. Gray, “Undulatory propulsion”, *Journal of Cell Science*, vol. 3, no. 28, pp. 551–578, 1953.
- [62] P. E. Schiebel, A. M. Hubbard, and D. I. Goldman, “Comparative study of snake lateral undulation kinematics in model heterogeneous terrain”, *Integrative and Comparative Biology*, 2020.
- [63] P. E. Schiebel, J. M. Rieser, A. M. Hubbard, L. Chen, D. Z. Rocklin, and D. I. Goldman, “Mechanical diffraction reveals the role of passive dynamics in a slithering snake”, *Proceedings of the National Academy of Sciences*, vol. 116, no. 11, pp. 4798–4803, 2019.
- [64] “Sprawling locomotion in the lizard *sceloporus clarkii*: The effects of speed on gait, hindlimb kinematics, and axial bending during walking”, *Journal of Zoology*, vol. 243, no. 2, pp. 417–433, 1997.
- [65] R. Ritter, “Lateral bending during lizard locomotion”, *Journal of Experimental Biology*, vol. 173, no. 1, pp. 1–10, 1992.
- [66] S. Daan and T. Belterman, “Lateral bending in locomotion of some lower tetrapods. i.. 2.”, *Proceedings Of The Koninklijke Nederlandse Akademie Van Wetenschappen Series C-Biological And Medical Sciences*, vol. 71, no. 3, pp. 245–+, 1968.
- [67] J. L. Edwards, “The evolution of terrestrial locomotion”, in *Major patterns in vertebrate evolution*, Springer, 1977, pp. 553–577.
- [68] P. J. Bergmann, G. Morinaga, E. S. Freitas, D. J. Irschick, G. P. Wagner, and C. D. Siler, “Locomotion and palaeoclimate explain the re-evolution of quadrupedal body

form in brachymeles lizards”, *Proceedings of the Royal Society B*, vol. 287, no. 1938, p. 20 201 994, 2020.

- [69] R. M. Alexander, *Locomotion of animals*. Springer, 1982, vol. 163.
- [70] E. R. Westervelt, J. W. Grizzle, C. Chevallereau, J. H. Choi, and B. Morris, *Feedback control of dynamic bipedal robot locomotion*. CRC press, 2018.
- [71] D. Zhao and S. Revzen, “Multi-legged steering and slipping with low dof hexapod robots”, *Bioinspiration & biomimetics*, vol. 15, no. 4, p. 045 001, 2020.
- [72] R. D. Maladen, Y. Ding, C. Li, and D. I. Goldman, “Undulatory swimming in sand: Subsurface locomotion of the sandfish lizard”, *science*, vol. 325, no. 5938, pp. 314–318, 2009.
- [73] P. E. Schiebel, H. C. Astley, J. M. Rieser, S. Agarwal, C. Hubicki, A. M. Hubbard, K. Diaz, J. R. Mendelson III, K. Kamrin, and D. I. Goldman, “Mitigating memory effects during undulatory locomotion on hysteretic materials”, *Elife*, vol. 9, e51412, 2020.
- [74] C. Li, T. Zhang, and D. I. Goldman, “A terradynamics of legged locomotion on granular media”, *Science*, vol. 339, no. 6126, pp. 1408–1412, 2013.
- [75] R. L. Hatton, Y. Ding, H. Choset, and D. I. Goldman, “Geometric visualization of self-propulsion in a complex medium”, *Physical review letters*, vol. 110, no. 7, p. 078 101, 2013.
- [76] E. M. Purcell, “Life at low reynolds number”, *American journal of physics*, vol. 45, no. 1, pp. 3–11, 1977.
- [77] L. E. Becker, S. A. Koehler, and H. A. Stone, “On self-propulsion of micro-machines at low reynolds number: Purcell’s three-link swimmer”, *Journal of Fluid Mechanics*, vol. 490, pp. 15–35, 2003.
- [78] D. Tam and A. E. Hosoi, “Optimal stroke patterns for purcell’s three-link swimmer”, *Physical Review Letters*, vol. 98, no. 6, p. 068 105, 2007.
- [79] J. Ostrowski and J. Burdick, “The geometric mechanics of undulatory robotic locomotion”, *The international journal of robotics research*, vol. 17, no. 7, pp. 683–701, 1998.
- [80] A. Shapere and F. Wilczek, “Geometry of self-propulsion at low reynolds number”, *Journal of Fluid Mechanics*, vol. 198, pp. 557–585, 1989.

- [81] F. Wilczek and A. Shapere, *Geometric phases in physics*. World Scientific, 1989, vol. 5.
- [82] C. Gong, D. I. Goldman, and H. Choset, “Simplifying gait design via shape basis optimization.”, in *Robotics: Science and Systems*, 2016.
- [83] J. M. Rieser, C. Gong, H. C. Astley, P. E. Schiebel, R. L. Hatton, H. Choset, and D. I. Goldman, “Geometric phase and dimensionality reduction in locomoting living systems”, *arXiv preprint arXiv:1906.11374*, 2019.
- [84] L. M. Frolich and A. A. Biewener, “Kinematic and electromyographic analysis of the functional role of the body axis during terrestrial and aquatic locomotion in the salamander *ambystoma tigrinum*”, *Journal of Experimental Biology*, vol. 162, no. 1, pp. 107–130, 1992.
- [85] P. Roos, “Lateral bending in newt locomotion”, in *Proc Kon Ned Akad Wet (C)*, vol. 67, 1964, pp. 223–232.
- [86] A. Crespi and A. J. Ijspeert, “Online Optimization of Swimming and Crawling in an Amphibious Snake Robot”, *IEEE Transactions on Robotics*, vol. 24, no. 1, pp. 75–87,
- [87] C. T. Farley and T. C. Ko, “Mechanics of locomotion in lizards.”, *The Journal of experimental biology*, vol. 200, no. 16, pp. 2177–2188, 1997.
- [88] N. Kafkafi and I. Golani, “A traveling wave of lateral movement coordinates both turning and forward walking in the ferret”, *Biological cybernetics*, vol. 78, no. 6, pp. 441–453, 1998.
- [89] M. Hildebrand, “The adaptive significance of tetrapod gait selection”, *American Zoologist*, vol. 20, no. 1, pp. 255–267, 1980.
- [90] T. White and R. Anderson, “Locomotor patterns and costs as related to body size and form in teiid lizards”, *Journal of Zoology*, vol. 233, no. 1, pp. 107–128, 1994.
- [91] J. R. Hutchinson, D. Felkler, K. Houston, Y.-M. Chang, J. Brueggen, D. Kledzik, and K. A. Vliet, “Divergent evolution of terrestrial locomotor abilities in extant crocodylia”, *Scientific reports*, vol. 9, no. 1, pp. 1–11, 2019.
- [92] R. B. McGhee and A. A. Frank, “On the stability properties of quadruped creeping gaits”, *Mathematical Biosciences*, vol. 3, pp. 331–351, 1968.
- [93] M. Kalakrishnan, J. Buchli, P. Pastor, M. Mistry, and S. Schaal, “Fast, robust quadruped locomotion over challenging terrain”, in *2010 IEEE International Conference on Robotics and Automation*, IEEE, 2010, pp. 2665–2670.

- [94] C. D. Bellicoso, F. Jenelten, C. Gehring, and M. Hutter, “Dynamic locomotion through online nonlinear motion optimization for quadrupedal robots”, *IEEE Robotics and Automation Letters*, vol. 3, no. 3, pp. 2261–2268, 2018.
- [95] D. F. Hoyt and C. R. Taylor, “Gait and the energetics of locomotion in horses”, *Nature*, vol. 292, no. 5820, pp. 239–240, 1981.
- [96] M. Hildebrand, “Symmetrical gaits of primates”, *American Journal of Physical Anthropology*, vol. 26, no. 2, pp. 119–130, 1967.
- [97] ———, “Analysis of asymmetrical gaits”, *Journal of Mammalogy*, vol. 58, no. 2, pp. 131–156, 1977.
- [98] ———, “The quadrupedal gaits of vertebrates”, *BioScience*, vol. 39, no. 11, p. 766, 1989.
- [99] O. Rieppel, “A review of the origin of snakes”, *Evolutionary biology*, pp. 37–130, 1988.
- [100] B. F. Simões, F. Sampaio, C. Jared, M. Antoniazzi, E. Loew, J. Bowmaker, A. Rodriguez, N. Hart, D. Hunt, J. Partridge, *et al.*, “Visual system evolution and the nature of the ancestral snake”, *Journal of evolutionary biology*, vol. 28, no. 7, pp. 1309–1320, 2015.
- [101] J. J. Wiens, M. C. Brandley, and T. W. Reeder, “Why does a trait evolve multiple times within a clade? repeated evolution of snake-like body form in squamate reptiles”, *Evolution*, vol. 60, no. 1, pp. 123–141, 2006.
- [102] J. A. Nyakatura, E. Andrada, S. Curth, and M. S. Fischer, “Bridging “romer’s gap”: Limb mechanics of an extant belly-dragging lizard inform debate on tetrapod locomotion during the early carboniferous”, *Evolutionary Biology*, vol. 41, no. 2, pp. 175–190, 2014.
- [103] J. M. Rieser, J. L. Tingle, D. I. Goldman, J. R. Mendelson, *et al.*, “Functional consequences of convergently evolved microscopic skin features on snake locomotion”, *Proceedings of the National Academy of Sciences*, vol. 118, no. 6, 2021.
- [104] B. McInroe, H. C. Astley, C. Gong, S. M. Kawano, P. E. Schiebel, J. M. Rieser, H. Choset, R. W. Blob, and D. I. Goldman, “Tail use improves performance on soft substrates in models of early vertebrate land locomotors”, *Science*, vol. 353, no. 6295, pp. 154–158, 2016.
- [105] P. J. Bergmann and G. Morinaga, “The convergent evolution of snake-like forms by divergent evolutionary pathways in squamate reptiles”, *Evolution*, vol. 73, no. 3, pp. 481–496, 2019.

- [106] G. Morinaga and P. J. Bergmann, “Evolution of fossorial locomotion in the transition from tetrapod to snake-like in lizards”, *Proceedings of the Royal Society B*, vol. 287, no. 1923, p. 20 200 192, 2020.
- [107] B. Chong, T. Wang, J. M. Rieser, B. Lin, A. Kaba, G. Blekherman, H. Choset, and D. I. Goldman, “Frequency modulation of body waves to improve performance of sidewinding robots”, *The International Journal of Robotics Research*, vol. 40, no. 12-14, pp. 1547–1562, 2021.
- [108] E. A. Shammass, H. Choset, and A. A. Rizzi, “Geometric motion planning analysis for two classes of underactuated mechanical systems”, *The International Journal of Robotics Research*, vol. 26, no. 10, pp. 1043–1073, 2007.
- [109] ———, “Towards a unified approach to motion planning for dynamic underactuated mechanical systems with non-holonomic constraints”, *The International Journal of Robotics Research*, vol. 26, no. 10, pp. 1075–1124, 2007.
- [110] J. E. Colgate and K. M. Lynch, “Mechanics and control of swimming: A review”, *IEEE journal of oceanic engineering*, vol. 29, no. 3, pp. 660–673, 2004.
- [111] M. Hutter, C. Gehring, D. Jud, A. Lauber, C. D. Bellicoso, V. Tsounis, J. Hwangbo, K. Bodie, P. Fankhauser, M. Bloesch, *et al.*, “Anymal-a highly mobile and dynamic quadrupedal robot”, in *2016 IEEE/RSJ international conference on intelligent robots and systems (IROS)*, IEEE, 2016, pp. 38–44.
- [112] C. E. Shannon, “A mathematical theory of communication”, *The Bell system technical journal*, vol. 27, no. 3, pp. 379–423, 1948.
- [113] R. M. Murray, *A mathematical introduction to robotic manipulation*. CRC press, 2017.
- [114] S. Alben, “Efficient sliding locomotion of three-link bodies”, *Physical Review E*, vol. 103, no. 4, p. 042 414, 2021.
- [115] L. Koens and E. Lauga, “Rotation of slender swimmers in isotropic-drag media”, *Physical Review E*, vol. 93, no. 4, p. 043 125, 2016.
- [116] S. Berri, J. H. Boyle, M. Tassieri, I. A. Hope, and N. Cohen, “Forward locomotion of the nematode *c. elegans* is achieved through modulation of a single gait”, *HFSP journal*, vol. 3, no. 3, pp. 186–193, 2009.
- [117] J. Sznitman, X. Shen, R. Sznitman, and P. E. Arratia, “Propulsive force measurements and flow behavior of undulatory swimmers at low reynolds number”, *Physics of Fluids*, vol. 22, no. 12, p. 121 901, 2010. eprint: <https://doi.org/10.1063/1.3529236>.

- [118] R. L. Hatton and H. Choset, “Geometric motion planning: The local connection, stokes’ theorem, and the importance of coordinate choice”, *The International Journal of Robotics Research*, vol. 30, no. 8, pp. 988–1014, 2011.
- [119] Q. Guo, M. K. Mandal, and M. Y. Li, “Efficient hodge–helmholtz decomposition of motion fields”, *Pattern Recognition Letters*, vol. 26, no. 4, pp. 493–501, 2005.
- [120] J. Gray and G. Hancock, “The propulsion of sea-urchin spermatozoa”, *Journal of Experimental Biology*, vol. 32, no. 4, pp. 802–814, 1955.
- [121] T. Zhang and D. I. Goldman, “The effectiveness of resistive force theory in granular locomotion”, *Physics of Fluids*, vol. 26, no. 10, p. 101 308, 2014.
- [122] S. S. Sharpe, S. A. Koehler, R. M. Kuckuk, M. Serrano, P. A. Vela, J. Mendelson, and D. I. Goldman, “Locomotor benefits of being a slender and slick sand swimmer”, *Journal of Experimental Biology*, vol. 218, no. 3, pp. 440–450, 2015.
- [123] R. D. Maladen, Y. Ding, P. B. Umbanhowar, A. Kamor, and D. I. Goldman, “Mechanical models of sandfish locomotion reveal principles of high performance sub-surface sand-swimming”, *Journal of The Royal Society Interface*, vol. 8, no. 62, pp. 1332–1345, 2011.
- [124] B. Chong, Y. Ozkan Aydin, G. Sartoretti, J. M. Rieser, C. Gong, H. Xing, H. Choset, and D. I. Goldman, “A hierarchical geometric framework to design locomotive gaits for highly articulated robots”, in *Robotics: science and systems*, 2019.
- [125] S. Ramasamy and R. L. Hatton, “Geometric gait optimization beyond two dimensions”, in *2017 American Control Conference (ACC)*, IEEE, 2017, pp. 642–648.
- [126] H. C. Astley, J. R. Mendelson, J. Dai, C. Gong, B. Chong, J. M. Rieser, P. E. Schiebel, S. S. Sharpe, R. L. Hatton, H. Choset, *et al.*, “Surprising simplicities and syntheses in limbless self-propulsion in sand”, *Journal of Experimental Biology*, vol. 223, no. 5, 2020.
- [127] P. E. Schiebel, H. C. Astley, J. M. Rieser, S. Agarwal, C. Hubicki, A. M. Hubbard, K. Diaz, J. R. Mendelson III, K. Kamrin, and D. I. Goldman, “Mitigating memory effects during undulatory locomotion on hysteretic materials”, *eLife*, vol. 9, e51412, 2020.
- [128] S. S. Sharpe, Y. Ding, and D. I. Goldman, “Environmental interaction influences muscle activation strategy during sand-swimming in the sandfish lizard *scincus scincus*”, *Journal of Experimental Biology*, vol. 216, no. 2, pp. 260–274, 2013.

- [129] R. L. Hatton, T. Dear, and H. Choset, “Kinematic cartography and the efficiency of viscous swimming”, *IEEE Transactions on Robotics*, vol. 33, no. 3, pp. 523–535, 2017.
- [130] J. Korta, D. A. Clark, C. V. Gabel, L. Mahadevan, and A. D. Samuel, “Mechanosensation and mechanical load modulate the locomotory gait of swimming *c. elegans*”, *Journal of Experimental Biology*, vol. 210, no. 13, pp. 2383–2389, 2007.
- [131] J. Dai, H. Faraji, C. Gong, R. L. Hatton, D. I. Goldman, and H. Choset, “Geometric swimming on a granular surface.”, in *Robotics: Science and Systems*, 2016.
- [132] B. C. Jayne, “Kinematics of terrestrial snake locomotion”, *Copeia*, vol. 1986, pp. 915–927, 1986.
- [133] S. M. Secor, “Ecological significance of movements and activity range for the sidewinder, *Crotalus cerastes*”, *Copeia*, vol. 1994, no. 3, pp. 631–645, 1994.
- [134] H. C. Astley, J. M. Rieser, A. Kaba, V. M. Paez, I. Tomkinson, J. R. Mendelson, and D. I. Goldman, “Side-impact collision: Mechanics of obstacle negotiation in sidewinding snakes”, *Bioinspiration & Biomimetics*, vol. 15, no. 6, p. 065 005, 2020.
- [135] W. Mosauer, “A note on the sidewinding locomotion of snakes”, *The American Naturalist*, vol. 64, no. 691, pp. 179–183, Mar. 1930.
- [136] J. W. Burdick, J. E. Radford, and G. S. Chirikjian, “A “sidewinding” locomotion gait for hyper-redundant robots”, *Robotics and Automation*, vol. 3, pp. 101–106, 1993.
- [137] R. L. Hatton and H. Choset, “Sidewinding on slopes”, in *Proceedings of the IEEE International Conference on Robotics and Automation*, Anchorage, AK USA, May 2010, pp. 691–696.
- [138] R. Hatton and H. Choset, “Nonconservativity and noncommutativity in locomotion”, *The European Physical Journal Special Topics*, vol. 224, no. 17-18, pp. 3141–3174, 2015.
- [139] O. Wiezel and Y. Or, “Using optimal control to obtain maximum displacement gait for Purcell’s three-link swimmer”, in *2016 Conference on Decision and Control*, IEEE, 2016, pp. 4463–4468.
- [140] R. S. Millman and G. D. Parker, *Elements of differential geometry*. Prentice Hall, 1977.

- [141] M. McIntyre and G. Cairns, “A new formula for winding number”, *Geometriae Dedicata*, vol. 46, no. 2, pp. 149–159, 1993.
- [142] C. Gong, Z. Ren, J. Whitman, J. Grover, B. Chong, and H. Choset, “Geometric motion planning for systems with toroidal and cylindrical shape spaces”, in *Dynamic Systems and Control Conference*, American Society of Mechanical Engineers, vol. 51913, 2018, V003T32A013.
- [143] R. E. Williamson and H. F. Trotter, *Multivariable Mathematics*. Pearson Prentice Hall, 2004, ISBN: 9780130672766.
- [144] B. Lin, B. Chong, Y. Ozkan-Aydin, E. Aydin, H. Choset, D. I. Goldman, and G. Blekherman, “Optimizing coordinate choice for locomotion systems with toroidal shape spaces”, in *2020 IEEE/RSJ International Conference on Intelligent Robots and Systems (IROS)*, IEEE, 2020, pp. 7501–7506.
- [145] C. Gong, M. Travers, H. C. Astley, D. I. Goldman, and H. Choset, “Limbless locomotors that turn in place”, in *2015 IEEE International Conference on Robotics and Automation (ICRA)*, IEEE, 2015, pp. 3747–3754.
- [146] D. L. Hu, J. Nirody, T. Scott, and M. J. Shelley, “The mechanics of slithering locomotion”, *Proceedings of the National Academy of Sciences*, vol. 106, no. 25, pp. 10 081–10 085, 2009.
- [147] R. R. Selmic and F. L. Lewis, “Neural-network approximation of piecewise continuous functions: Application to friction compensation”, *IEEE transactions on neural networks*, vol. 13, no. 3, pp. 745–751, 2002.
- [148] S. Alben, “Efficient sliding locomotion with isotropic friction”, *Physical Review E*, vol. 99, no. 6, p. 062 402, 2019.
- [149] J. Aguilar, T. Zhang, F. Qian, M. Kingsbury, B. McInroe, N. Mazouchova, C. Li, R. Maladen, C. Gong, M. Travers, *et al.*, “A review on locomotion robophysics: the study of movement at the intersection of robotics, soft matter and dynamical systems”, *Reports on Progress in Physics*, vol. 79, no. 11, p. 110 001, 2016.
- [150] H. C. Astley, J. M. Rieser, A. Kaba, V. M. Paez, I. Tomkinson, J. R. Mendelson, and D. I. Goldman, “Side-impact collision: mechanics of obstacle negotiation in sidewinding snakes”, *Bioinspiration & Biomimetics*, vol. 15, no. 6, p. 065 005, 2020.
- [151] A. Schrijver, *Combinatorial optimization: polyhedra and efficiency*. Springer Science & Business Media, 2003, vol. 24.

- [152] B. Chong, T. Wang, *et al.*, “Optimizing contact patterns for robot locomotion via geometric mechanics”, *I. J. Robotic Res.* (submitted), 2022.
- [153] R. D. Maladen, Y. Ding, P. B. Umbanhowar, and D. I. Goldman, “Undulatory swimming in sand: experimental and simulation studies of a robotic sandfish”, *The International Journal of Robotics Research*, vol. 30, no. 7, pp. 793–805, 2011.
- [154] P. Liljebäck, K. Y. Pettersen, Ø. Stavdahl, and J. T. Gravdahl, “Lateral undulation of snake robots: A simplified model and fundamental properties”, *Robotica*, vol. 31, no. 7, pp. 1005–1036, 2013.
- [155] B. Chong, T. Wang, B. Lin, S. Li, G. Blekherman, H. Choset, and D. I. Goldman, “Moving sidewinding forward: Optimizing contact patterns for limbless robots via geometric mechanics”, in *Robotics: Science and Systems*, 2021.
- [156] R. Sedgewick and K. Wayne, *Algorithms: Algorithms_4*. Pearson Education, 2011, ISBN: 9780132762564.
- [157] P. Liljebäck, K. Y. Pettersen, Ø. Stavdahl, and J. T. Gravdahl, “Experimental investigation of obstacle-aided locomotion with a snake robot”, *IEEE Transactions on Robotics*, vol. 27, no. 4, pp. 792–800, 2011.
- [158] Z. Bien, M.-G. Chun, and H. Son, “An optimal turning gait for a quadruped walking robot”, in *Proceedings IROS’91: IEEE/RSJ International Workshop on Intelligent Robots and Systems’ 91*, IEEE, 1991, pp. 1511–1514.
- [159] D. Cho, J. Kim, and D.-G. Gweon, “Optimal turning gait of a quadruped walking robot”, *Robotica*, vol. 13, no. 6, pp. 559–564, 1995.
- [160] L. R. Palmer and D. E. Orin, “Attitude control of a quadruped trot while turning”, in *2006 IEEE/RSJ International Conference on Intelligent Robots and Systems*, IEEE, 2006, pp. 5743–5749.
- [161] R. M. Alexander, “The gaits of bipedal and quadrupedal animals”, *The International Journal of Robotics Research*, vol. 3, no. 2, pp. 49–59, 1984.
- [162] S. Hirose, H. Kikuchi, and Y. Umetani, “The standard circular gait of a quadruped walking vehicle”, *Advanced Robotics*, vol. 1, no. 2, pp. 143–164, 1986.
- [163] G. Dudek and M. Jenkin, *Computational principles of mobile robotics*. Cambridge university press, 2010.
- [164] G. Carbone and M. Ceccarelli, “Legged robotic systems”, in *Cutting Edge Robotics*, IntechOpen, 2005.

- [165] F. Qian, K. DAFFON, T. ZHANG, and D. I. Goldman, “An automated system for systematic testing of locomotion on heterogeneous granular media”, in *Nature-Inspired Mobile Robotics*, World Scientific, 2013, pp. 547–554.
- [166] C. Li, P. B. Umbanhowar, H. Komsuoglu, D. E. Koditschek, and D. I. Goldman, “Sensitive dependence of the motion of a legged robot on granular media”, *Proceedings of the National Academy of Sciences*, vol. 106, no. 9, pp. 3029–3034, 2009.
- [167] A. B. Ward and E. L. Brainerd, “Evolution of axial patterning in elongate fishes”, *Biological Journal of the Linnean Society*, vol. 90, no. 1, pp. 97–116, 2007.
- [168] G. Parra-Olea and D. B. Wake, “Extreme morphological and ecological homoplasy in tropical salamanders”, *Proceedings of the National Academy of Sciences*, vol. 98, no. 14, pp. 7888–7891, 2001.
- [169] M. C. Brandley, J. P. Huelsenbeck, and J. J. Wiens, “Rates and patterns in the evolution of snake-like body form in squamate reptiles: Evidence for repeated re-evolution of lost digits and long-term persistence of intermediate body forms”, *Evolution: International Journal of Organic Evolution*, vol. 62, no. 8, pp. 2042–2064, 2008.
- [170] E. A. Buchholtz, A. C. Booth, and K. E. Webbink, “Vertebral anatomy in the florida manatee, *trichechus manatus latirostris*: A developmental and evolutionary analysis”, *The Anatomical Record: Advances in Integrative Anatomy and Evolutionary Biology: Advances in Integrative Anatomy and Evolutionary Biology*, vol. 290, no. 6, pp. 624–637, 2007.
- [171] J. W. Sites Jr, T. W. Reeder, and J. J. Wiens, “Phylogenetic insights on evolutionary novelties in lizards and snakes: Sex, birth, bodies, niches, and venom”, *Annual Review of Ecology, Evolution, and Systematics*, vol. 42, pp. 227–244, 2011.
- [172] C. Gans, “Tetrapod limblessness: Evolution and functional corollaries”, *American Zoologist*, vol. 15, no. 2, pp. 455–467, 1975.
- [173] P. J. Bergmann and D. J. Irschick, “Vertebral evolution and the diversification of squamate reptiles”, *Evolution: International Journal of Organic Evolution*, vol. 66, no. 4, pp. 1044–1058, 2012.
- [174] T. Nath, A. Mathis, A. C. Chen, A. Patel, M. Bethge, and M. W. Mathis, “Using deeplabcut for 3d markerless pose estimation across species and behaviors”, *Nature protocols*, vol. 14, no. 7, pp. 2152–2176, 2019.
- [175] C. D. Siler and R. M. Brown, “Evidence for repeated acquisition and loss of complex body-form characters in an insular clade of southeast asian semi-fossorial

- skins”, *Evolution: International Journal of Organic Evolution*, vol. 65, no. 9, pp. 2641–2663, 2011.
- [176] B. Chong, Y. O. Aydin, C. Gong, G. Sartoretti, Y. Wu, J. M. Rieser, H. Xing, P. E. Schiebel, J. W. Rankin, K. B. Michel, *et al.*, “Coordination of lateral body bending and leg movements for sprawled posture quadrupedal locomotion”, *The International Journal of Robotics Research*, vol. 40, no. 4-5, pp. 747–763, 2021.
- [177] A. J. Ijspeert, “A connectionist central pattern generator for the aquatic and terrestrial gaits of a simulated salamander”, *Biological Cybernetics*, vol. 84, no. 5, pp. 331–348, Apr. 2001.
- [178] S. D. Kelly and R. M. Murray, “Geometric phases and robotic locomotion”, *Journal of Robotic Systems*, vol. 12, no. 6, pp. 417–431, 1995.
- [179] J. Cairns, S. Impa, J. O’Toole, S. Jagadish, and A. Price, “Influence of the soil physical environment on rice (*oryza sativa* l.) response to drought stress and its implications for drought research”, *Field Crops Research*, vol. 121, no. 3, pp. 303–310, 2011.
- [180] F. Qian, T. Zhang, W. Korff, P. B. Umbanhowar, R. J. Full, and D. I. Goldman, “Principles of appendage design in robots and animals determining terradynamic performance on flowable ground”, *Bioinspiration & biomimetics*, vol. 10, no. 5, p. 056014, 2015.
- [181] H. Bhatia, G. Norgard, V. Pascucci, and P.-T. Bremer, “The helmholtz-hodge decomposition—a survey”, *IEEE Transactions on visualization and computer graphics*, vol. 19, no. 8, pp. 1386–1404, 2012.
- [182] S. Renous, E. Hofling, and J. Gasc, “Respective role of the axial and appendicular systems in relation to the transition to limblessness”, *Acta biotheoretica*, vol. 46, no. 2, pp. 141–156, 1998.
- [183] A. Skinner, M. S. Lee, and M. N. Hutchinson, “Rapid and repeated limb loss in a clade of scincid lizards”, *BMC Evolutionary Biology*, vol. 8, no. 1, pp. 1–9, 2008.
- [184] S. Aoi, T. Tanaka, S. Fujiki, T. Funato, K. Senda, and K. Tsuchiya, “Advantage of straight walk instability in turning maneuver of multilegged locomotion: A robotics approach”, *Scientific reports*, vol. 6, p. 30199, 2016.
- [185] J. C. McKenna, D. J. Anhalt, F. M. Bronson, H. B. Brown, M. Schwerin, E. Shammass, and H. Choset, “Toroidal skin drive for snake robot locomotion”, in *2008 IEEE International Conference on Robotics and Automation*, IEEE, 2008, pp. 1150–1155.

- [186] J. Whitman, M. Travers, and H. Choset, “Learning modular robot control policies”, *arXiv preprint arXiv:2105.10049*, 2021.
- [187] C. Wright, A. Johnson, A. Peck, Z. McCord, A. Naaktgeboren, P. Gianfortoni, M. Gonzalez-Rivero, R. Hatton, and H. Choset, “Design of a modular snake robot”, in *2007 IEEE/RSJ International Conference on Intelligent Robots and Systems*, IEEE, 2007, pp. 2609–2614.
- [188] M. Tesch, K. Lipkin, I. Brown, R. Hatton, A. Peck, J. Rembisz, and H. Choset, “Parameterized and scripted gaits for modular snake robots”, *Advanced Robotics*, vol. 23, no. 9, pp. 1131–1158, 2009.
- [189] G. Sartoretti, W. Paivine, Y. Shi, Y. Wu, and H. Choset, “Distributed learning of decentralized control policies for articulated mobile robots”, *IEEE Transactions on Robotics*, vol. 35, no. 5, pp. 1109–1122, 2019.
- [190] N. Mazouchova, P. B. Umbanhowar, and D. I. Goldman, “Flipper-driven terrestrial locomotion of a sea turtle-inspired robot”, *Bioinspiration & biomimetics*, vol. 8, no. 2, p. 026007, 2013.
- [191] K. Byl, “Metastable legged-robot locomotion”, PhD thesis, Massachusetts Institute of Technology, 2008.
- [192] D. Wettergreen and C. Thorpe, “Gait generation for legged robots”, in *IEEE International Conference on Intelligent Robots and Systems*, 1992.
- [193] H. C. Sun and D. N. Metaxas, “Automating gait generation”, in *Proceedings of the 28th annual conference on Computer graphics and interactive techniques*, 2001, pp. 261–270.
- [194] A. Crespi, D. Lachat, A. Pasquier, and A. J. Ijspeert, “Controlling swimming and crawling in a fish robot using a central pattern generator”, *Autonomous Robots*, vol. 25, no. 1, pp. 3–13, 2008.
- [195] S. Dutta, A. Parihar, A. Khanna, J. Gomez, W. Chakraborty, M. Jerry, B. Grisafe, A. Raychowdhury, and S. Datta, “Programmable coupled oscillators for synchronized locomotion”, *Nature communications*, vol. 10, no. 1, pp. 1–10, 2019.
- [196] H.-W. Park, P. M. Wensing, and S. Kim, “High-speed bounding with the mit cheetah 2: Control design and experiments”, *The International Journal of Robotics Research*, vol. 36, no. 2, pp. 167–192, 2017.
- [197] M. B. Popovic, A. Goswami, and H. Herr, “Ground reference points in legged locomotion: Definitions, biological trajectories and control implications”, *The international journal of robotics research*, vol. 24, no. 12, pp. 1013–1032, 2005.

- [198] A. Shapere and F. Wilczek, *Geometric phases in physics*. World Scientific, 1989.
- [199] R. L. Hatton and H. Choset, “Nonconservativity and noncommutativity in locomotion”, *The European Physical Journal Special Topics*, vol. 224, no. 17-18, pp. 3141–3174, 2015.
- [200] S. Kuroda, I. Kunita, Y. Tanaka, A. Ishiguro, R. Kobayashi, and T. Nakagaki, “Common mechanics of mode switching in locomotion of limbless and legged animals”, *Journal of the Royal Society interface*, vol. 11, no. 95, p. 20140205, 2014.
- [201] V. B. Sukhanov, “General system of symmetrical locomotion of terrestrial vertebrates and some features of movement of lower tetrapods”, 1974.
- [202] B. Anderson, J. Shultz, and B. Jayne, “Axial kinematics and muscle activity during terrestrial locomotion of the centipede *scolopendra heros*”, *Journal of Experimental Biology*, vol. 198, no. 5, pp. 1185–1195, 1995.
- [203] S. Reilly and M. Delancey, “Sprawling locomotion in the lizard *sceloporus clarkii*: Quantitative kinematics of a walking trot”, *The Journal of experimental biology*, vol. 200, no. 4, pp. 753–765, 1997.
- [204] S. Reilly and M. Delancey, “Sprawling locomotion in the lizard *sceloporus clarkii*: The effects of speed on gait, hindlimb kinematics, and axial bending during walking”, *Journal of Zoology*, vol. 243, no. 2, pp. 417–433, 1997.
- [205] S. Hirose and H. Yamada, “Snake-like robots [tutorial]”, *IEEE Robotics & Automation Magazine*, vol. 16, no. 1, pp. 88–98, 2009.
- [206] B. Chong, T. Wang, E. Erickson, P. J. Bergmann, and D. I. Goldman, “Coordinating tiny limbs and long bodies: Geometric mechanics of diverse undulatory lizard locomotion”, *arXiv preprint arXiv:2201.09312*, 2022.
- [207] J. E. Marsden and T. S. Ratiu, *Introduction to mechanics and symmetry: a basic exposition of classical mechanical systems*. Springer Science & Business Media, 2013, vol. 17.
- [208] B. Zhong, Y. O. Aydin, C. Gong, G. Sartoretti, Y. Wu, J. Rieser, H. Xing, J. Rankin, K. Michel, A. Nicieza, *et al.*, “Coordination of back bending and leg movements for quadrupedal locomotion”, in *Robotics: Science and Systems*, 2018.
- [209] A. N. Burkitt, “A review of the integrate-and-fire neuron model: I. homogeneous synaptic input”, *Biological cybernetics*, vol. 95, no. 1, pp. 1–19, 2006.
- [210] S. Aoi, Y. Egi, and K. Tsuchiya, “Instability-based mechanism for body undulations in centipede locomotion”, *Physical Review E*, vol. 87, no. 1, p. 012717, 2013.

- [211] K. Yasui, T. Kano, E. M. Standen, H. Aonuma, A. J. Ijspeert, and A. Ishiguro, “Decoding the essential interplay between central and peripheral control in adaptive locomotion of amphibious centipedes”, *Scientific reports*, vol. 9, no. 1, pp. 1–11, 2019.
- [212] Y. Ozkan-Aydin, B. Chong, E. Aydin, and D. I. Goldman, “A systematic approach to creating terrain-capable hybrid soft/hard myriapod robots”, in *2020 3rd IEEE International Conference on Soft Robotics (RoboSoft)*, IEEE, 2020, pp. 156–163.
- [213] K. L. Hoffman and R. J. Wood, “Myriapod-like ambulation of a segmented micro-robot”, *Autonomous Robots*, vol. 31, no. 1, p. 103, 2011.
- [214] J. R. Usherwood and B. J. Smith, “The grazing gait, and implications of toppling table geometry for primate footfall sequences”, *Biology letters*, vol. 14, no. 5, p. 20180137, 2018.
- [215] S. Walker and R. Leine, “Set-valued anisotropic dry friction laws: Formulation, experimental verification and instability phenomenon”, *Nonlinear Dynamics*, vol. 96, no. 2, pp. 885–920, 2019.
- [216] A. A. Transteth, R. I. Leine, C. Glocker, and K. Y. Pettersen, “3-d snake robot motion: Nonsmooth modeling, simulations, and experiments”, *IEEE transactions on robotics*, vol. 24, no. 2, pp. 361–376, 2008.
- [217] R. M. Murray, Z. Li, S. S. Sastry, and S. S. Sastry, *A mathematical introduction to robotic manipulation*. CRC press, 1994.
- [218] J. Gray, “The mechanism of locomotion in snakes”, *Journal of experimental biology*, vol. 23, no. 2, pp. 101–120, 1946.
- [219] J. J. Socha, “Gliding flight in the paradise tree snake”, *Nature*, vol. 418, no. 6898, pp. 603–604, 2002.
- [220] R. L. Hatton and H. Choset, “Generating gaits for snake robots: Annealed chain fitting and keyframe wave extraction”, *Autonomous Robots*, vol. 28, no. 3, pp. 271–281, 2010.
- [221] H. Marvi and D. L. Hu, “Friction enhancement in concertina locomotion of snakes”, *Journal of the Royal Society Interface*, vol. 9, no. 76, pp. 3067–3080, 2012.
- [222] S. Kern and P. Koumoutsakos, “Simulations of optimized anguilliform swimming”, *Journal of Experimental Biology*, vol. 209, no. 24, pp. 4841–4857, 2006.
- [223] S. Jung, “Caenorhabditis elegans swimming in a saturated particulate system”, *Physics of Fluids*, vol. 22, no. 3, p. 031903, 2010.

- [224] L. E. Becker, S. A. Koehler, and H. A. Stone, “On self-propulsion of micro-machines at low reynolds number: Purcell’s three-link swimmer”, *Journal of fluid mechanics*, vol. 490, pp. 15–35, 2003.
- [225] J. Avron, O. Gat, and O. Kenneth, “Optimal swimming at low reynolds numbers”, *Physical review letters*, vol. 93, no. 18, p. 186 001, 2004.
- [226] H. C. Fu, T. R. Powers, and C. W. Wolgemuth, “Theory of swimming filaments in viscoelastic media”, *Physical review letters*, vol. 99, no. 25, p. 258 101, 2007.
- [227] D. Crowdy, S. Lee, O. Samson, E. Lauga, and A. Hosoi, “A two-dimensional model of low-reynolds number swimming beneath a free surface”, *Journal of Fluid Mechanics*, vol. 681, pp. 24–47, 2011.
- [228] F. Jing and S. Alben, “Optimization of two-and three-link snakelike locomotion”, *Physical Review E*, vol. 87, no. 2, p. 022 711, 2013.
- [229] S. Kajita, K. Kaneko, K. Harada, F. Kanehiro, K. Fujiwara, and H. Hirukawa, “Biped walking on a low friction floor”, in *2004 IEEE/RSJ International Conference on Intelligent Robots and Systems (IROS)(IEEE Cat. No. 04CH37566)*, IEEE, vol. 4, 2004, pp. 3546–3552.
- [230] A. J. Clark and T. E. Higham, “Slipping, sliding and stability: Locomotor strategies for overcoming low-friction surfaces”, *Journal of Experimental Biology*, vol. 214, no. 8, pp. 1369–1378, 2011.
- [231] D. S. Marigold, A. J. Bethune, and A. E. Patla, “Role of the unperturbed limb and arms in the reactive recovery response to an unexpected slip during locomotion”, *Journal of neurophysiology*, vol. 89, no. 4, pp. 1727–1737, 2003.
- [232] F.-J. Elmer, “Nonlinear dynamics of dry friction”, *Journal of Physics A: Mathematical and General*, vol. 30, no. 17, p. 6057, 1997.
- [233] Y. O. Aydin, J. M. Rieser, C. M. Hubicki, W. Savoie, and D. I. Goldman, “Physics approaches to natural locomotion: Every robot is an experiment”, in *Robotic Systems and Autonomous Platforms*, Elsevier, 2019, pp. 109–127.
- [234] B. Chong, Y. O. Aydin, J. M. Rieser, G. Sartoretti, T. Wang, J. Whitman, A. Kaba, E. Aydin, C. McFarland, H. Choset, *et al.*, “A general locomotion control framework for serially connected multi-legged robots”, *arXiv preprint arXiv:2112.00662*, 2021.
- [235] B. Chong, J. He, S. Li, E. Erickson, K. Diaz, T. Wang, D. Soto, and D. I. Goldman, *arXiv preprint arXiv:2207.10604*, 2022.

- [236] S. Kuroda, N. Uchida, and T. Nakagaki, “Gait switching with phase reversal of locomotory waves in the centipede scolopocryptops rubiginosus”, *Bioinspiration & Biomimetics*, vol. 17, no. 2, p. 026 005, 2022.
- [237] K. Yasui, K. Sakai, T. Kano, D. Owaki, and A. Ishiguro, “Decentralized control scheme for myriapod robot inspired by adaptive and resilient centipede locomotion”, *PloS one*, vol. 12, no. 2, e0171421, 2017.
- [238] A. Ridgel, R. Ritzmann, and P. Schaefer, “Effects of aging on behavior and leg kinematics during locomotion in two species of cockroach”, *Journal of Experimental Biology*, vol. 206, no. 24, pp. 4453–4465, 2003.
- [239] J. Gray and H. W. Lissmann, “The kinetics of locomotion of the grass-snake”, *Journal of Experimental Biology*, vol. 26, no. 4, pp. 354–367, 1950.
- [240] T. Majmudar, E. E. Keaveny, J. Zhang, and M. J. Shelley, “Experiments and theory of undulatory locomotion in a simple structured medium”, *Journal of The Royal Society Interface*, rsif20110856, 2012.
- [241] K. Kelley, S. Arnold, and J. Gladstone, “The effects of substrate and vertebral number on locomotion in the garter snake *thamnophis elegans*”, *Functional Ecology*, vol. 11, no. 2, pp. 189–198, 1997.
- [242] J. R. Pierce, *An introduction to information theory: symbols, signals and noise*. Courier Corporation, 2012.
- [243] A. Feinstein, “A new basic theorem of information theory”, *IEEE Transactions on Information Theory*, 1954.
- [244] M. C. Marchetti, J.-F. Joanny, S. Ramaswamy, T. B. Liverpool, J. Prost, M. Rao, and R. A. Simha, “Hydrodynamics of soft active matter”, *Reviews of modern physics*, vol. 85, no. 3, p. 1143, 2013.
- [245] S. Seok, A. Wang, M. Y. Chuah, D. Otten, J. Lang, and S. Kim, “Design principles for highly efficient quadrupeds and implementation on the mit cheetah robot”, in *2013 IEEE International Conference on Robotics and Automation*, IEEE, 2013, pp. 3307–3312.
- [246] E. Moore, D. Campbell, F. Grimmering, and M. Buehler, “Reliable stair climbing in the simple hexapod ‘rhex’”, in *Proceedings 2002 IEEE International Conference on Robotics and Automation (Cat. No. 02CH37292)*, IEEE, vol. 3, 2002, pp. 2222–2227.

- [247] J. Mi, Y. Wang, and C. Li, “Omni-roach: A legged robot capable of traversing multiple types of large obstacles and self-righting”, in *2022 International Conference on Robotics and Automation (ICRA)*, IEEE, 2022, pp. 235–242.
- [248] C. Ordonez, J. Shill, A. Johnson, J. Clark, and E. Collins, “Terrain identification for rhex-type robots”, in *Unmanned Systems Technology XV*, SPIE, vol. 8741, 2013, pp. 240–251.
- [249] X. A. Wu, T. M. Huh, R. Mukherjee, and M. Cutkosky, “Integrated ground reaction force sensing and terrain classification for small legged robots”, *IEEE Robotics and Automation Letters*, vol. 1, no. 2, pp. 1125–1132, 2016.
- [250] Y. Ozkan-Aydin and D. I. Goldman, “Self-reconfigurable multilegged robot swarms collectively accomplish challenging terradynamic tasks”, *Science Robotics*, vol. 6, no. 56, eabf1628, 2021.
- [251] D. Zhao, B. Bittner, G. Clifton, N. Gravish, and S. Revzen, “Walking is like slithering: A unifying, data-driven view of locomotion”, *Proceedings of the National Academy of Sciences*, vol. 119, no. 37, e2113222119, 2022.
- [252] A. Jacoff, A. Downs, A. Virts, and E. Messina, “Stepfield pallets: Repeatable terrain for evaluating robot mobility”, in *Proceedings of the 8th Workshop on Performance Metrics for Intelligent Systems*, 2008, pp. 29–34.
- [253] B. Chong, Y. O. Aydin, J. M. Rieser, G. Sartoretti, T. Wang, J. Whitman, A. Kaba, E. Aydin, C. McFarland, K. D. Cruz, *et al.*, “A general locomotion control framework for multi-legged locomotors”, *Bioinspiration & Biomimetics*, vol. 17, no. 4, p. 046015, 2022.
- [254] J. Whitman, N. Zevallos, M. Travers, and H. Choset, “Snake robot urban search after the 2017 mexico city earthquake”, in *2018 IEEE international symposium on safety, security, and rescue robotics (SSRR)*, IEEE, 2018, pp. 1–6.
- [255] N. D. Naclerio, A. Karsai, M. Murray-Cooper, Y. Ozkan-Aydin, E. Aydin, D. I. Goldman, and E. W. Hawkes, “Controlling subterranean forces enables a fast, steerable, burrowing soft robot”, *Science Robotics*, vol. 6, no. 55, eabe2922, 2021.
- [256] J. J. Abbott, Z. Nagy, F. Beyeler, and B. J. Nelson, “Robotics in the small, part i: Microbotics”, *IEEE Robotics & Automation Magazine*, vol. 14, no. 2, pp. 92–103, 2007.
- [257] D. S. Marigold, “Role of peripheral visual cues in online visual guidance of locomotion”, *Exercise and sport sciences reviews*, vol. 36, no. 3, pp. 145–151, 2008.

- [258] T. Krasovsky, A. Lamontagne, A. G. Feldman, and M. F. Levin, “Effects of walking speed on gait stability and interlimb coordination in younger and older adults”, *Gait & posture*, vol. 39, no. 1, pp. 378–385, 2014.
- [259] K. Diaz, E. Erickson, B. Chong, D. Soto, and D. I. Goldman, “Active and passive mechanics for rough terrain traversal in centipedes”, *bioRxiv*, 2022.
- [260] P. Wand, A. Prochazka, and K.-H. Sontag, “Neuromuscular responses to gait perturbations in freely moving cats”, *Experimental Brain Research*, vol. 38, no. 1, pp. 109–114, 1980.
- [261] B. Bläsing and H. Cruse, “Mechanisms of stick insect locomotion in a gap-crossing paradigm”, *Journal of Comparative Physiology A*, vol. 190, no. 3, pp. 173–183, 2004.
- [262] A. Mathis, P. Mamidanna, K. M. Cury, T. Abe, V. N. Murthy, M. W. Mathis, and M. Bethge, “DeepLabCut: Markerless pose estimation of user-defined body parts with deep learning”, *Nature neuroscience*, vol. 21, no. 9, pp. 1281–1289, 2018.
- [263] B. Gnedenko, A. Kolmogorov, B. Gnedenko, and A. Kolmogorov, “Limit distributions for sums of independent”, *Am. J. Math*, vol. 105, 1954.
- [264] L. E. Baum and M. Katz, “Convergence rates in the law of large numbers”, *Transactions of the American Mathematical Society*, vol. 120, no. 1, pp. 108–123, 1965.
- [265] S. N. Gorb, *Functional Surfaces in Biology: Little Structures with Big Effects Volume 1*. Springer Science & Business Media, 2009, vol. 1.
- [266] J. A. Dobson, D. L. Riddiford-Harland, and J. R. Steele, “Effects of wearing gumboots and leather lace-up boots on lower limb muscle activity when walking on simulated underground coal mine surfaces”, *Applied ergonomics*, vol. 49, pp. 34–40, 2015.